

A high-speed microscopy approach to single-
molecule studies of eukaryote signal
transduction

Erik Göran Hedlund

Doctor of Philosophy

University of York

Physics

September 2016

Abstract

Metabolic processes underlie all forms of life. An organism's ability to utilise chemical energy to stay alive and eventually reproduce is a central feature of life, regardless of organism length scale. To achieve this, an organism must be adaptable. That is, it must be able to adjust to varying surrounding environmental conditions. Cells must be able to sense this environment, 'transduce' the signal and bring about some cell level response. Cells respond to external stimuli by releasing chemical cascades along often intricate signalling pathways which regulate cellular function.

In this thesis, I have developed a novel optical microscopy system coupled to microfluidics and image analysis tools to help address challenging biological questions relating to metabolic sensing in eukaryotic life, using *Saccharomyces cerevisiae*, as a model system. A set of biophysical tools was developed to monitor signal transduction events in live yeast cells. A bespoke optical microscope was developed that can monitor single living cells and determine their response to controlled variations in environmental nutrient concentration at high sampling speeds comparable to the molecular diffusion time scale in a cells internal environment.

High-speed imaging at up to 200 frames per second and exposure times of 4.7 ms can be achieved. An electronic gain of 300x makes the camera system sensitive enough to track diffusion of single or small clusters of fluorescent protein molecules under physiological conditions. A high intensity laser excitation system was developed to deliver the light required to follow single fluorescent proteins in the living cells. A bespoke microfluidics system was built wherein cells can be exposed to rapidly changing extracellular environments and make it possible to follow individual cell responses to changing glucose conditions. Image analysis tools were adapted and developed to facilitate the automated measurement of protein mobility, stoichiometry and copy number, one cell at a time.

TABLE OF CONTENTS

Abstract	3
TABLE OF CONTENTS	5
Figures	8
Tables	17
Publications Arising from Doctoral Research	18
Acknowledgements	23
ISOLATE.....	24
Declaration.....	25
1 Introduction.....	27
2 A background to live cell experiments.....	30
2.1 Background to the use of <i>Saccharomyces cerevisiae</i> as a model organism	30
2.2 The glucose sensing system as a paradigm signal transduction pathway	34
2.3 Fluorescence imaging	37
2.4 The use of fluorescent proteins.....	40
3 Microfluidics	45
3.1 Preparing and using microfluidic chips	47
3.1.1 Liquid feed system	48
3.2 Mask design and flow channel production	56
3.2.1 Protocol for PDMS flow channel fabrication and preparation	57
4 Microscopy	62
4.1 The Microscope	66

4.1.1	Main microscope body modifications	66
4.1.2	The excitation module	68
4.1.3	The astigmatism module	73
4.1.4	Colour Splitter and Electron Multiplying CCD Camera.....	80
4.2	Controlling Software – The <i>CellBild</i> software suite	82
5	Experimental procedures and results	101
5.1	Preparation of cells for examination	103
5.2	Image processing for localising cell and nuclear membrane	105
5.3	Proof of concept – Steady state behaviour	111
5.4	Cells adapting to a new environment	113
5.4.1	There and back again – Imaging cells at a standard environment, an alternate environment and once again after return to the standard environment.....	117
5.4.2	There and staying there – Single transition experiments.....	121
5.4.3	Mutants used and their tagged transcription factors.....	122
5.5	Results – Dynamic environment	124
5.5.1	Single molecules and small clusters.....	134
5.5.2	Counting proteins in single cells	140
6	Conclusions, discussion and future work.....	143
6.1	Next steps.....	144
6.1.1	There is more to see in yeast.....	145
6.1.2	Microscope developments to consider	146
APPENDIX A – CellBild software excerpts.....		152
A.1	CellBild version 6.3.....	152
A.2	Pump control sub-VI structures.....	156
A.3	Mad City Labs nano-piezo positioning stage control	159

APPENDIX B.....	161
Transcription factor clusters regulate genes in eukaryotic cells.....	162
EXPERIMENTAL PROCEDURES.....	183
REFERENCES (APPENDIX B).....	184
SUPPLEMENTAL EXPERIMENTAL PROCEDURES	190
Strain construction and characterization.....	190
Microfluidics control of single cell imaging.....	194
Foci detection, tracking and stoichiometry determination.....	194
APPENDIX C.....	209
From <i>Animaculum</i> to singler molecules: 300 years of the light microscope.....	210
APPENDIX D – Growth media	221
List of abbreviations, acronyms, protein and gene names.....	222
References	224

Figures

Figure 2.1 – Yeast cells imaged using a Foldscope and an iPhone 6.	32
Figure 2.2 – The Foldscope. The 0.2 mm diameter sapphire sphere objective lens is mounted in the small black plastic bushing on the moveable paper slide. A light source is mounted on the bottom. The sample slide is inserted underneath the paper slide with the objective lens.	32
Figure 2.3 – Schematic of Mig1-Snf1 interaction upon exposure to glucose starvation in comparison to a glucose rich environment. Blue background on the right hand side indicates low glucose (0%) conditions, colourless on the left hand side indicate high glucose (4%). The Snf1 and Mig1 are phosphorylated under low glucose conditions.	35
Figure 2.4 – A Jablonski diagram showing the most important energy transitions in a fluorescent molecule. Vertical straight arrows are radiative transitions. Wiggly grey lines are non-radiative transitions. Coloured wiggly lines represent emitted photons.	38
Figure 2.5 – eGFP protein structure. The chromophore is visible in the centre of the barrel. Yellow are β -sheets and purple are α -helices.	40
Figure 2.6 – mCherry protein structure. The chromophore is visible in the centre of the barrel. Yellow are β -sheets and purple are α -helices.	42
Figure 3.1 – Laminar flow. Velocities in the height dimension of the channels used in this project.	46
Figure 3.2 – The layout of the experimental setup of the microfluidic chip. Flows of standard and alternate environments are supplied via the central channels. The side channels were used for wetting, Concanavalin A application and cell loading.	48

<i>Figure 3.3 – Simulated flow profile in the main channel. Top: Normalised and to scale flow profile from lowest (black), to max flow (white). Bottom right: Flow profile along the z axis at channel centre. Bottom left: Cross-sectional flow profile at cell mid-level (red level in the right-hand plot).</i>	54
Figure 3.4 – An example of the way the onset of alternate environment and the return to standard environment in the flow channel was measured. At 0 s a flow of a suspension of fluorescent beads was started in the alternate environment channel. The first frame with a visible bead is recorded as the onset and the last frame with a visible bead is recorded as the return time. The time code in the final frame is seconds after the pump has been stopped.	55
Figure 3.5 – A schematic representation of an imaging sequence with the changes between environments marked.	56
<i>Figure 3.6– The plunger method for degassing PDMS</i>	59
Figure 3.7 – The finished microfluidics chip, fused to a coverslip. The four inlets on the right side and the single outlet on the left.	61
Figure 4.1– The coarse and fine positioning stages mounted on the microscope.....	66
Figure 4.2 – Showing the excitation light intake of the microscope. On the left-hand side is the entrance box with a mirror directing the light down in the image. The distance from the back focal plane (BFP) focussing lens to the last beam steering lens (L_4) is 169.6 mm. The field diaphragm is located half way between the BFP lens and L_4	67
Figure 4.3 – A simplified schematic of the entirety of the optical beam path inside the Nikon microscope body	68
Figure 4.4 – A schematic of the excitation module components. The dichroic combining mirror is an FF495-Di03 filter. The half wave plate is mounted in a	

rotating holder and is used to adjust what proportion of light propagates through the widefield (main) path and how much goes through the FRAP path.....	69
Figure 4.5 – An image of a graticule used to measure the pixel size. Overlaid is the ROI used during experiments.	70
Figure 4.6 – Relative intensity excitation and emission spectra for the fluorescent proteins eGFP and mCherry and the transmission spectrum for the main imaging dichroic mirror, Di01–R488/561. Absorption, emission and transmission spectra from Chroma (https://www.chroma.com/products/fluorochrome). Note that the mCherry spectrum is about half the brightness of eGFP. The excitation laser lines are represented by the vertical blue and yellow dashed lines, 473 nm and 561 nm.	71
Figure 4.7 – A simulated two-dimensional Gaussian.	74
Figure 4.8 – The same simulated Gaussian as in figure 4.7 with overlaid noise.....	74
Figure 4.9 – The original astigmatism module geometry. Light path from left to right. Shown is the single 50 mm lens reforming the intermediate image in the intermediate image plane on the left-hand side at the one on the right-hand side. The cylindrical lens, L_{ast} , has a focal length of 1000 mm along one axis.....	76
Figure 4.10 – Left, the vignetting of the original geometry without colour splitting (DV^2 in bypass mode). Image showing yeast cells. Right, the vignetting in colour split mode. The curved cropping is clear at the centre of the image. Image showing a calibration graticule. The yellow box is the standard region of interest (ROI, 476 by 164 pixels) used.	78
Figure 4.11 – Left astigmatism disengaged. Right astigmatism engaged. The filter is a low pass emission filter with a 500 nm cut-off dealing with possible back reflections from the 561 nm laser.	79

Figure 4.12– From left to right, the microscope body, cylindrical lens (flipped out), colour splitter, EMCCD camera.	79
Figure 4.13 – The updated geometry as used in the work presented in this thesis. The colour splitter is to the right of the intermediate image plane. The intermediate plane is at the entrance to the colour splitter tube.....	80
Figure 4.14 – The spectral layout of the colour splitter filter set used. The emission filters are shown simplified showing centre wavelength and bandwidth as cyan and magenta verticals. The transmission characteristics of the GFP emission filter has been included. Absorption, emission and transmission spectra from Chroma (https://www.chroma.com/products/fluorochrome).	81
Figure 4.15 – A schematic representation of the optical paths in the DV ² colour splitter	81
Figure 4.16 – Physical control lines and data collection layout. The Trigger ready line hardware triggers the DAQ card counters internally on the card and is unaffected by software latencies once an acquisition is started.....	87
Figure 4.17 – Pulse synchronisation. Shown here is one period of a sequence with more than two frames to be acquired. All output pulses (the three bottom pulse trains) are synchronised to the first Trigger ready positive flank (not shown in this figure). The laser duty cycle is adjusted to correspond to the camera exposure time. In most situations described in this thesis, an exposure time of 4.7 ms was used.	88
Figure 4.18 – A full sequence of two time points, i.e. two frames each of 473 nm and 561 nm exposure. The initial two dark frames needed to avoid the inconsistencies in camera behaviour during the first two frames of any image sequence. Shown here is the minimal number of trigger pulses required. In normal operation, this	

is generally padded with extra trigger pulses, this simplifies acquisitions of slightly longer bright field sequences and avoids the possibility of a camera timing out due to a lost final frame never getting triggered. This can be safely added as trigger pulses are ignored if the Trigger ready is low, i.e. the camera is not set to acquire any images..... 89

Figure 4.19 – The main software user interface. Here shown in the start-up window.

On this pane, details of the experimental setup are entered. The white boxes are input fields and the grey boxes are indicator fields. The total number of Illuminated Frames entered is counting all frames from both lasers when running in A(F)LEX mode. Divide this by two to get the number of frames by laser wavelength. Note that this value is only fully tested and verified using even numbers (minimum one flash per laser). Other fields of importance are the framerate and laser pulse repetition rate fields. If the Link rates button is actuated, the laser repetition rate will be half the framerate for ALEX operation. The duty cycle of the laser can be adjusted (duty cycles of >50% will be flagged as incompatible with ALEX. The laser power can be attenuated electronically with the Power Denominator when the Power button is pressed..... 91

Figure 4.20– The pane for continuous imaging. When this panel is selected, an uninterrupted trigger pules train is started. The frame rate (pulse frequency) can be selected on the fly. The laser controls can also be operated from here. The lasers will be working in CW mode by default here unless otherwise selected with the AFLEX toggle..... 92

Figure 4.21– Settings pane. Here all references to DAQ input/output/counters are specified along with certain other settings required. Most of these settings can be set once and left in that state unless the hardware changes. 94

Figure 4.22 – The pump control pane. Flow rate and sequence setup is done from the middle and right hand boxes. Note that the total running time for a pumped sequence must be dialled in explicitly.	97
Figure 4.23 – Manual pump controls. This interface gives full control over the pump and volumes are translated into running times at selected flow rate. Note that the syringe size cannot be selected here. The syringe size will be whatever was chosen in the main pump control pane.	98
Figure 4.24 – The automatic pump sequence control interface. The only user control here is the Abort button.....	99
Figure 4.25 – The Mad City Labs nano-piezo stage control interface. Predefined adjustable offsets activated by button clicks are available on all axes.	100
Figure 5.1 – A red channel frame from a strain using Nrd1-mCherry as nuclear reporter. Notice that the middle cell does not have a clearly visible nucleus and the rightmost cell does not show the whole cell	106
Figure 5.2 – The green channel frame corresponding to the red channel in Figure 5.1. The green outline shows the found outer boundary of the cell envelopes.....	107
Figure 5.3 – Left, a cell with the focal volume bisecting the nucleus. Right, a cell with the nucleus offset from the focal volume.....	108
Figure 5.4 – The segmented cells. One colour per envelope.	109
Figure 5.5 – The binary masks of the cells from Figure 5.1 to Figure 5.4 with the nucleus superimposed as a black region. Note the middle cell with the under-sized nuclear segment (mask index 4). The membrane masks were always indexed from 2 and up, 1 being reserved for the surrounding area (blue in Figure 5.4). Nuclear masks were indexed from 1 and up, always one less than the corresponding membrane mask.	110

Figure 5.6 – A microscope slide with a GeneFrame attached.	112
Figure 5.7 – A differential interference contrast (DIC) image of a ROI as acquired with the 100 x 100-pixel region analysed marked with the yellow box. The box is 100x100 pixels, i.e. 9.3 μm sides.....	115
Figure 5.8 – First version of a There and back again protocol as used in the first successful alternating environment experiments. Every timepoint consisted of five illuminated frames. The delays are inserted between the timepoints and the frames within a timepoint are in sequence, back-to-back.....	118
Figure 5.9 – Second version of a There and back again protocol as used in subsequent experiments. This protocol was used for the Mig1-eGFP/Nrd1-mCherry experiments described here.....	119
Figure 5.10 – Frame disposition of two consecutive timepoints (T_1 and T_2). Showing an unproportioned delay (T_D) between the two timepoints. The R and G represent the red and green channels respectively. The red boxes are the guard frames, the unusable initial frames from every image acquisition being discarded.....	120
Figure 5.11 – Frame disposition of three consecutive timepoints (T_1 to T_3). Showing an unproportioned delay ($T_D = 30$ s) between the timepoints. The R and G represent the red and green channels respectively. The red boxes are the guard frames.....	122
Figure 5.12 – Cells acclimatised to a high glucose (+) environment exposed to a low glucose (-) environment and then returned to the original, high glucose (+) environment.	125
Figure 5.13– Cells acclimatised to a low glucose (-) environment exposed to a high glucose (+) environment and then returned to the original, low glucose (-) environment.	125

Figure 5.14 – Control experiment. Cells acclimatised to a high glucose (+) environment exposed continuously to this environment for the same duration as in Figure 5.12 and Figure 5.13. Note the mobile nucleus in the upper cell.	125
Figure 5.15 – Deletion mutant. The cells are acclimatised to a high glucose (+) environment and then exposed to a low glucose (-) environment. The transcription factor Snf1 has been deleted.	126
Figure 5.16 – Deletion mutant. The cells are acclimatised to a low glucose (-) environment and then exposed to a high glucose (+) environment. The transcription factor Snf1 has been deleted.	126
Figure 5.17 – Cells acclimatised to a high glucose (+) environment exposed to a low glucose (-) environment. The expected behaviour of Msn2 is approximately the inverse of that of Mig1, i.e. it should localise to the nucleus under low glucose conditions. The effect is not as dramatic as during a low to high transition (see Figure 5.18).	128
Figure 5.18 – Cells acclimatised to a low glucose (-) environment exposed to a high glucose (+) environment. The expected behaviour of Msn2 is approximately the inverse of that of Mig1, i.e. it should delocalise from the nucleus under low glucose conditions.	128
Figure 5.19 – Single transition sequence of the dual colour construct Mig1-eGFP and Reg1-mCherry. The Mig1 localisation under high glucose (+) conditions is used as a nuclear marker and is taken from the first frame.	129
Figure 5.20 – Single transition sequence of the dual colour construct Mig1-eGFP and Reg1-mCherry. The Mig1 localisation under high glucose (+) conditions is used as a nuclear marker and is taken from the first frame.	130

Figure 5.21 – Single transition sequence of the dual colour construct Mig1-eGFP and Snf1-mCherry in W303 background. The Mig1 localisation under high glucose (+) conditions is used as a nuclear marker and is taken from the first frame. .	130
Figure 5.22 – Single transition sequence of the dual colour construct Mig1-eGFP and Snf1-mCherry in W303 background. The Mig1 localisation under high glucose (+) conditions is used as a nuclear marker and is taken from the first frame. .	132
Figure 5.23 – Example of an in-vitro sample of mCherry during first illuminated frame. This frame is taken without astigmatism. The yellow box is the 100 x 100 (9.3 μm side) square used during live cell experiments. The dimmer spots visible are single molecules and the slightly larger, are clusters of two molecules.	136
Figure 5.24 – Kernel density estimates of single molecule intensities of eGFP and mCherry. HWHM for eGFP is $6.5 \cdot 10^3$ counts and for mCherry $4.5 \cdot 10^3$ counts. Note that the background is included in this count.....	137
Figure 5.25 – A baseline showing the background at $5 \cdot 10^3$ counts.....	137
Figure 5.26 – Tracking a spot identified as delocalised Mig1-eGFP in two consecutive frames after the cell having been transferred to a low glucose environment. The intensity plot is along the green line crosssection; the white circle pinpoints the spot tracked.	138
Figure 5.27 – Internal bleach correction for a data set with six timepoints of five frames.	141
Figure 5.28 – Total Mig1 content by compartment during a There-and-back-again type experiment, following the migration of Mig1-eGFP between the nucleus and the cytosol. (+) is 4% glucose and (-) is 0% glucose. The cells were transferred from a low glucose environment to high glucose after the first timepoint and were	

returned to the low glucose environment after 450 s. A final acquisition was made after 660 s, 210 s after the return to low glucose.	142
Figure 6.1 – Example of alternate frame timing with a 2:1 ratio of green to red frames. The rest of the sequence is based on the ‘one shot’ per timepoint method.	147
Figure 6.2 – Function of a Wollaston prism	149
Figure A.1 – CellBild main interface. Startup pane.....	152
Figure A.2 – Program start. Initialisation of various controls and constants.....	153
Figure A.3 – Further initialisation. Programmatically located directly below the region in Figure A.2.	154
Figure A.4 – CellBild 6.3, main loop.....	155
Figure A.5 – Closing down procedures. To avoid lingering handles or other references remaining in unused memory all Daq-card- and serial interfaces are gracefully closed and released before the application exits.	156
Figure A.6 – Automatic pump control interface	157
Figure A.7 – Manual pump control interface.....	158
Figure A.8 – Control interface for the nano-piezo positioning stage	159

Tables

Table 4.1 – Voltage calibration for laser power modulation – laser head output power.	93
Table 5.1 – Overview of <i>Saccharomyces cerevisiae</i> mutants used. Listed are the reporter fluorophore and which transcription factor or other component has been tagged using it. Also listed are deletions in the Other traits column.	123

Publications Arising from Doctoral Research

Erik G. Hedlund, Sviatlana Shashkova, Adam J. M. Wollman, Stefan Hohmann and Mark C. Leake **“Visualising Snf1/Mig1 signal transduction in *Saccharomyces cerevisiae* using high-speed single-molecule 4D astigmatic fluorescence microscopy”**

Biophysical Society Meeting, late abstract, poster presentation (2014)

Erik G. Hedlund, Sviatlana Shashkova, Adam J. M. Wollman, Stefan Hohmann and Mark C. Leake **“A novel approach to simultaneously tracking two species of single fluorescent molecules in 3D with high temporal resolution using astigmatic microscopy and its application to tracking Snf1/Mig1 signal transduction in *Saccharomyces cerevisiae*”**

The Microscience Microscopy Congress, Oral presentation (2015)

Adam J. M. Wollman, Sviatlana Shashkova, Erik Hedlund, Stefan Hohmann and Mark C. Leake **“Observing Signal Transduction Directly at the Single-Molecule Level in Live Eukaryotic Cells”**

Biophysical Journal, Volume 110, Issue 2 (2015), 570a (poster presentation)

Adam J. M. Wollman, Richard Nudd, Erik G. Hedlund and Mark C. Leake **”From Animaculum to single molecules: 300 years of the light microscope”**

Open Biology **5**:150019. (2015), doi: 10.1098/rsob.150019.

The paper is reprinted in its entirety as Appendix C

Erik G. Hedlund, Sviatlana Shashkova, Adam J. M. Wollman, Stefan Hohmann and Mark C. Leake **“Real-Time 3D Imaging at the Single Molecule Level of Signal Transduction in *Saccharomyces Cerevisiae* Responding to Environmental Changes”**

Biophysical Journal, Volume 110, Issue 3 (2016), 145a

Adam J. M. Wollman, Sviatlana Shashkova, Erik Hedlund, Rosmarie Friemann, Stefan Hohmann and Mark C. Leake “**Transcription factor clusters regulate genes in eukaryotic cells**”

Paper submitted and in review (2016)

The paper is reprinted in its entirety as Appendix B

Erik G. Hedlund, Sviatlana Shashkova, Adam J. M. Wollman, Stefan Hohmann and Mark C. Leake “**Single-Molecule Transcription Factor Dynamics in *Saccharomyces Cerevisiae* Glucose Sensing**”

Biophysical Journal, Volume 112, Issue 3 (2017), 282a

*If time stood still,
the World would be awfully dark*



Acknowledgements

Standing at the end of this road looking at the options that lie ahead I am immensely grateful to each and every one having helped me to get to where I am today. All who have pushed me and forced me to get through the tough times and kept me on the right path. This is for all of you who have supported and encouraged me through the years.

Mina hjärtligaste tack till mamma och pappa. Tack för allt ert stöd och framför allt för att jag finns.

All my love to Diana, my lovely wife. A force of nature in her own right. Standing by me or behind me if need be, pushing, shoving or kicking me in the right direction, no matter how obnoxious I may have been.

A giant Thank you Mark. For believing in me, inspiring me and helping me to reach this point. These few years has been the greatest time for me.

I am extremely grateful to the European Commission for giving me the opportunity to study biological physics in Oxford and York, for giving me the means to see Europe and beyond in my pursuit of knowledge.

I finally would like to show my gratitude for receiving stipendiary funding in my final year from the White Rose Consortium

ISOLATE

ISOLATE was a Marie Curie Actions Initial Training Network, funded and supervised by the European Union 7th Framework Programme. Grant agreement number: 289995.

The Network was coordinated at *Göteborgs Universitet* in Gothenburg, Sweden. The network had five university nodes located in the UK, Sweden, Denmark, the Netherlands and Switzerland and two commercial partners located in Denmark and the Czech Republic. Each of the nodes had a different focus, with the same overarching objective, to study molecular systems biology at the single cell and single molecule scale.

At *Göteborgs universitet* in Gothenburg, Sweden and at the *Rijksuniversiteit van Groningen* in the Netherlands, work was conducted on *Saccharomyces cerevisiae*, including specialised genetic modifications instrumental to the investigations conducted by the author at the *University of York*.

The purpose of the UK node, originally located in Oxford, but since 2013 in York, has been to develop novel microscopy methods to push the limit of microscopic imaging of living cells and their system level function in complex biological settings.

Declaration

I hereby declare that the work presented in this thesis, submitted for the degree of Doctor of Philosophy at the University of York, is that of me alone, except where so indicated in the text or described below. All sources are acknowledged as references.

* Genetic integration of fluorescent proteins into yeast strains was performed by Sviatlana Shashkova et al. in Gothenburg.

* The PSF finding and Gaussian fitting software is based on code originally developed by Isabel Llorente Garcia and refactored by Adam Wollman.

* The *CoPro* software for estimating protein copy numbers outside the microscope focal depth was developed by Adam Wollman

* The four-channel microfluidics channel design was based on designs and matrices previously used in Gothenburg by Anna-Karin Gustavsson et al.

* Appended papers were collaborative efforts

* The bespoke microscope modules described in this thesis are *based on* but *not identical* to the initial design developed during my first year in Oxford where the old design was included in a thesis submitted and examined for the degree of Master of Science by research.

I also declare that the work presented for examination in this thesis has not previously been submitted for examination for another degree at the University of York or elsewhere.

1 Introduction

At a first glance, life may appear both structured and neatly organised and chaotic. One species differ from the next and the animal kingdom is different from the plant kingdom and from the fungi. Looking at it again, one may start seeing how the perceived order start becoming fuzzy.

On the cellular length scale, i.e. from less than 1 μm , common for bacteria, to several 10s of μm for mammalian cells responses to interaction are not only a macroscopic one. Interaction between units as small as single molecules will play an important role in a cell. At this scale interactions are governed by atomic forces and free and directed diffusion processes are important for all aspects of the cells function: delivery of nutrients, oxygen and signal substances within the cell.

Any form of life is defined as units of single or multiple cells capable of autonomous reproduction (Leake 2013). They are physically active and require energy to get to the ultimate point of reproduction. The basis for the physical activity is the metabolic extraction of chemical energy from nutrients, organic compounds such as sugars, amino acids or fatty acids. The low temperature controlled oxidation of nutrients produces the energy rich molecule adenosine triphosphate (ATP) that acts as energy source for energy demanding processes within a cell. Many proteins will need to be phosphorylated by ATP to become active, an example being transcription factors binding and unbinding from the DNA to control the expression of genes. Other proteins such as *dyneins* and *kinesins* are motor proteins, proteins that by hydrolysing ATP gains energy to directionally move along structures, microtubules, within a cell (Michels 2002). Another category of proteins are kinases that are enzymes that mediates the transfer of the energy carrying phosphate group and are important parts of cellular signalling systems.

Every multicellular organism and several monocellular are eukaryotes. This domain of life is distinguished by the presence of a separate *nucleus* containing genetic material in the form of DNA. A eukaryote cell responds to external stimuli by triggering appropriate action by chemical signal cascades. Stimuli can be one or many external factors triggering action in cells, examples include chemical (e.g. nutrient gradients, oxygen levels, acidity, other chemicals), optical (e.g. photosynthesis, optical sensor cells in eyes) and mechanical action (e.g. sensory nerves). The response will be triggered by one or multiple sensory proteins and a signalling chain will follow. Kinases will eventually interact with transcription factors binding to the DNA and controlling transcription and thus in the next steps what proteins are produced to deal with the stimulus present. Other responses that do not involve transcription are also possible depending on the stimulus, but in this thesis the focus is on signal cascades resulting in regulation of transcription.

Eukaryotic signalling is a complicated and often convoluted, noisy affair, with pathways having multiple branches, crosstalk between pathways is common and other noise sources are ever present (Hartwell et al. 1999; Siso-Nadal et al. 2009; Saito 2010; Shashkova et al. 2015). An excellent eukaryotic model system is brewer's yeast, *Saccharomyces cerevisiae*, (more about this in chapter 2). In this thesis, I will describe novel techniques developed to achieve high resolution measurements of molecular signalling in living cells. The aim for my research was to improve the sensitivity of fluorescence microscopy and simultaneously introduce a method to in a controlled manner expose cells to different environments during a single experiment. Introducing high speed imaging and the use of novel image analysis, the Snf1/Mig1 glucose sensing pathway in yeast was targeted. The goal was to show interaction between transcription factors and downstream kinases.

This thesis is the product of a research project that has been part of a larger EC-financed consortium, the ISOLATE network. The network has been an initial training network for PhD candidates with an overarching goal of creating new tools for systems biology. The research presented here is based on specialised yeast strains developed in Gothenburg at Göteborgs universitet. The work performed by ISOLATE fellow Sviatlana Shashkova has been extremely important to me, providing functionalised yeast that could be analysed.

2 A background to live cell experiments

Cellular signal transduction is a fundamental part of life and any experiment intending to answer any questions on a systems level will need to be carried out on live cells. The project described here has focussed on eukaryotic cells and I have used *Saccharomyces cerevisiae* as a model organism.

2.1 Background to the use of *Saccharomyces cerevisiae* as a model organism

One of the most thoroughly studied eukaryotic organisms on the planet is the budding yeast known as brewer's yeast, *Saccharomyces cerevisiae*. The organism is one of the oldest uses of a microbial organism for a specific intentional purpose. Bread, wine, beer and mead have been important staples since antiquity. There are finds of wine production as far back as 7000 years ago (Berkowitz 1996) and the ancient Egyptians are known to have produced leavened bread. The oldest beer is almost as old, evidence of beer from 3000 BC has been found (Michel et al. 1992). Humans coexistence with yeast was for millennia an unknown partnership as the insight what specifically made the grape juice or mash become alcoholic or the bread rise was only properly understood with the rise of microbiology in the 19th century with the works of John Baptiste Desmazières, J. J. Colin and Louis Pasteur (Höxtermann 1996; Barnett 1998; Barnett 2000), but an empirical knowledge of how to treat the raw material to use the yeasts properties must have evolved long before humans even started to write in ancient Mesopotamia around the same time and place the first beer mentioned was brewed.

Wild yeast is found on ripe fruit such as grapes and the natural origin for wine production as such thus came directly with the raw material and certainly the earliest wines would have used wild yeasts, but early on, winemakers, beer brewers and bakers found the practice of using a sour dough or a small swig of prior batch added to a new batch immensely increased the efficiency of the process. Thus began the domestication of *Saccharomyces cerevisiae* (Gallone et al. 2016). Before the 19th century the living nature of yeast was not yet recognised, but the selection being unwittingly performed on the organism over the centuries led to the wide variety of different yeast strains we have access to today. Gallone et al. have traced the evolution of modern *S. cerevisiae* by following the many strains genetic ancestry. They show that the huge variety of yeasts, that today are specialised for use in baking, industrial ethanol production, wine making and especially beer brewing, has a relatively small number of ancestors that were domesticated early on.

The biochemistry of fermentation was discovered and characterised much earlier than the actual organism was found. It was known by the mid-1700s that “*ferment*” was essential to start a fermentation and in 1789 Antoine Lavoisier described fermentation of sugars into ethanol, acetic acid and carbon dioxide (Lavoisier 1789; Barnett 1998), work that was later revisited by later chemists, Louis Jacques Thenard, Joseph-Louis Gay-Lussac.

The earliest visual identification of *S. cerevisiae* as small ovoid bodies has been attributed to Antonie van Leeuwenhoek and his early experiments with microscopy in the 1670s and 1680s (van Leeuwenhoek 1680; Wollman et al. 2015). When he in a letter on the 14 June 1680 included drawn figures that look very similar to what we today know is yeast. However, this was disputed as early as 1838 by Louis Mandl (Barnett 2003). Nevertheless, it may very well have been true that Antonie actually



Figure 2.1 – Yeast cells imaged using a *Foldscope* and an iPhone 6.

saw yeast cells. A modern variant of the single-lens microscope, the *Foldscope* (Cybulski et al. 2014), has a construction very similar to the ones used by van Leeuwenhoek and is perfectly capable of resolving single yeast cells, see Figure 2.2. The images are small, but perfectly recognisable as *S. cerevisiae*. See Figure 2.1 for an image of *S. cerevisiae* taken with an iPhone 6 camera using a *Foldscope*.

As microscopy was continuously improved over the century and half following van Leeuwenhoek, by the early 1800s microscopes were reaching maturity levels suitable for proper microbiological investigations. Barnett mentions John Baptiste Desmazières as one of the earliest biologists studying yeast residue in the



Figure 2.2 – The Foldscope. The 0.2 mm diameter sapphire sphere objective lens is mounted in the small black plastic bushing on the moveable paper slide. A light source is mounted on the bottom. The sample slide is inserted underneath the paper slide with the objective lens.

1820s and during the 1830s the independent research of Charles Cagniard de la Tour, Friedrich Traugott Kützing and Theodor Schwann established that yeast was indeed a living organism (Höxtermann 1996; Barnett 1998). Later Cagniard de la Tour also described budding and bud scarring. Discovery of other yeast species continued during the following decades. In the 1850s and 60s the novel work of Louis Pasteur gives new insights into the differences between aerobic and anaerobic fermentation in yeast. At this time, the era of investigating yeast metabolism had started for real. For his microscopy studies, Pasteur used an early type of flow chamber, made by Heinrich Geissler, to achieve only a very thin layer of yeast containing medium that could be observed under a microscope while maintaining a well-defined surrounding environment (Barnett 2000). This could be considered the spiritual predecessor to the microfluidics system I have developed (see chapter 3) for the investigation of yeast metabolism.

As mentioned before, budding yeast *Saccharomyces cerevisiae* is only one of many yeasts of great economical value but it has come to be the go-to model organism for eukaryote studies. The species has some very beneficial traits that make it very suitable as a model organism. *S. cerevisiae* exists in both diploid (double chromosome sets) and haploid (single chromosome set) variants. Both of which have both commercial and scientific value.

The 16-chromosome genome of haploid *S. cerevisiae* was fully characterised by the mid-1990s and the organism's ~6000 genes were catalogued and made available to the scientific community in 1996 (Goffeau et al. 1996). The relatively small genome is well suited for a model organism. Many protein homologs, both expected and unexpected, between yeast and mammalian cells were also revealed in the process (Botstein et al. 1997), increasing the usability of yeast as a model organism for many

eukaryote processes. Extensive work has been conducted since, mapping many of the complicated interactions between genes and proteins in yeast. Analysing and building intricate interaction network graphs (Qin et al. 2003; Hin Yan Tong et al. 2004; Costanzo et al. 2010; Kaizu et al. 2010) laid the foundation for the type of investigations I have been conducting in the work presented here.

The use of a single cell organism provides the benefit of well compartmentalised life. One cell is one organism and, even if there can occur various cell to cell interactions, the cells are not differentiated as in a multicellular organism. Examples of cell to cell interactions are pheromone interactions, e.g. between diploid yeast cells seeking mating for sexual reproduction (Lin et al. 2004), inter-species communication (Hennig et al. 2015) and even artificial systems developed by researchers (Chen & Weiss 2005).

For my research the choice fell on using modified haploid yeast, a choice that has a few reasons. Most importantly a culture of haploid cells will produce genetically identical (clonal) individuals, which is important when following individual cells with the purpose of describing the cells response to environmental conditions. Other benefits are that they have a convenient size (around 5 μm diameter) and has a short doubling time (around 1-2 hours) (Wollman et al. 2016; Marks 2011).

2.2 The glucose sensing system as a paradigm signal transduction pathway

Yeast metabolism is an important research subject as many of the involved genes and proteins are conserved between eukaryotes and many have direct homologs in mammalian cells. Glucose is a preferred carbon source for yeast and a well-developed repression system has evolved to make the most efficient use of glucose when it is

available. The way this is done in living cells is to sense what available resources are present in the surrounding environment and if sufficient glucose is present, repress genes coding for proteins needed for the digestion of larger sugar molecules. A zinc finger protein called Mig1 is a major repressor and an important chain in the glucose signalling system. The protein has binding sites in the *SUC2* promoter and the *GAL* genes (Jan Olof Nehlin et al. 1991; Lutfiyya et al. 1998). It has been shown that Mig1 binding to the DNA is regulated by a pathway resulting in phosphorylation of the AMP kinase Snf1 (Lutfiyya et al. 1998; Ozcan & Johnston 1999; Patrick G. Needham & Trumbly 2006; Bendrioua et al. 2014; Almquist et al. 2015) when a cell is exposed to glucose starvation (Lutfiyya et al. 1998; Ozcan & Johnston 1999; Bendrioua et al. 2014; Almquist et al. 2015). Bendrioua and Almquist showed Mig1 bulk dynamics between nuclei and cytosol using fluorescently tagged Mig1. The approach they took was widefield fluorescence microscopy with exposure times around 30 s. In Figure 2.3

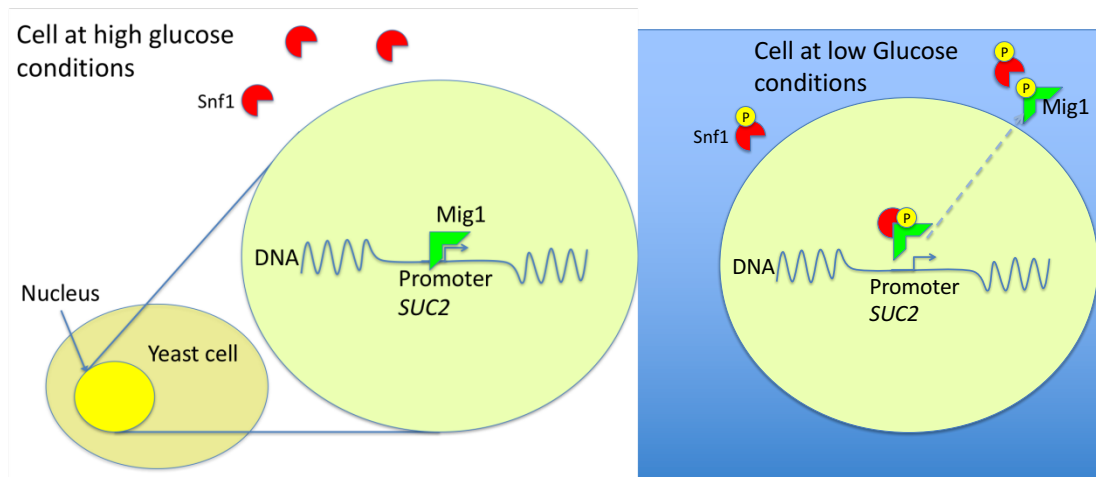


Figure 2.3 – Schematic of Mig1-Snf1 interaction upon exposure to glucose starvation in comparison to a glucose rich environment. Blue background on the right hand side indicates low glucose (0%) conditions, colourless on the left hand side indicate high glucose (4%). The Snf1 and Mig1 are phosphorylated under low glucose conditions.

a simplified schematic of how Snf1 shuttles between the nucleus and the cytosol and once phosphorylated, it mediates the phosphorylation of Mig1 that is consequently derepressed, released from the DNA, and is delocalised from the nucleus. Snf1 is conserved over all eukaryotes and has homologs in mammalian cells.

In this thesis for live cell experiments I used this Mig1 repression process as a model test system. In doing so, I have focussed on studying the instantaneous stoichiometry and dynamic relocation of key proteins which are part of the glucose sensing pathways in living yeast cells, which have been exposed to intermittent glucose rich and glucose starved environments. It is possible to expose cells to two precisely defined environments using a microfluidics system (see chapters 3 and 5). Haploid *S. cerevisiae* cells are around 5 μm in diameter, a convenient length scale for microscopy. As will be further elaborated in chapters 4 and 5, a small number (1-4 cells) can be imaged simultaneously and single molecules and small clusters of tagged proteins can be tracked with high accuracy within a cell. The separate nucleus in eukaryotes also provides a clear view of when interactions with the genome occurs.

The glucose sensing system is highly conserved amongst eukaryotes and have homologs in the plant and animal kingdoms. In mammalian cells the homolog of the instrumental Snf1 of yeast is the AMP-activated protein kinase (AMPK). The mammalian version just like Snf1 responds to low nutrition and oxygen levels. Thus, even if the nutrient and oxygen delivery system (blood circulation) is more complicated for mammalian cells, the Snf1-Mig1 interaction in yeast is still a good model for mammalian cell responses as well (Towle 2005).

Another transcription factor that responds to osmotic stress, but also changes in nutrition availability is Msn2 that is part of the general stress response (Babazadeh et

al. 2013; Lin et al. 2015). The response of Msn2 is almost the inverse of that of Mig1, as its localises to the nucleus upon glucose stress.

2.3 Fluorescence imaging

Fluorescence is the physical process in which energy in the form of light of one wavelength is absorbed by an atom or molecule and subsequently reemitted with an energy loss, i.e. the incoming light is down-converted to a longer wavelength. For the use in fluorescence imaging *in-vivo*, the fluorophores used will without exception be molecular. A fluorescent molecules internal energy state can be described as consisting of a set of electronic energy levels, which are further subdivided into vibrational energy levels. Put simply, the electronic states determine the photon energy needed to excite a molecule and the photon energy of emitted fluorescence; the vibrational states explain the width of absorption and emission bands (for examples of absorption/emission spectra, see Figure 4.6). The processes governing normal single-photon fluorescence can be illustrated using a Jablonski diagram, see Figure 2.4.

An incoming photon can excite the fluorophore to a higher electronic energy state, e.g. S_1 or S_2 in the figure. This absorption occurs over femtosecond timescales. Once in the excited state, vibrational losses or non-radiative conversion losses occur over picoseconds before any radiative transitions occurs. Finally, the energy can be released as a photon is emitted upon radiative relaxation to the ground state, the fluorescence lifetime, the time in the excited states, is in the order of nanosecond timescales. The efficiency of this process is commonly measured using the *quantum yield*, defined as the ratio between the number of emitted and absorbed photons:

$$\Phi = \frac{\text{Number of emitted photons}}{\text{Number of absorbed photons}} \quad (1)$$

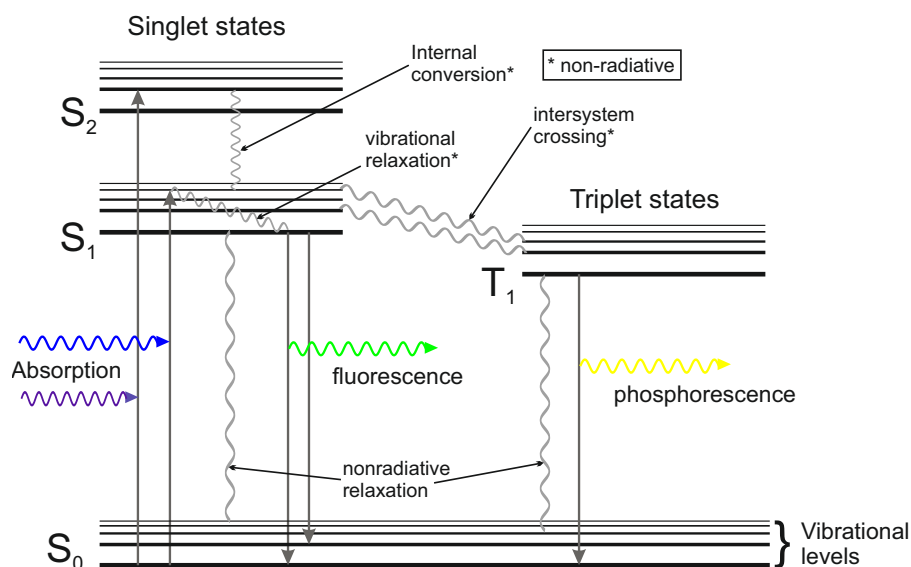


Figure 2.4 – A Jablonski diagram showing the most important energy transitions in a fluorescent molecule. Vertical straight arrows are radiative transitions. Wiggly grey lines are non-radiative transitions. Coloured wiggly lines represent emitted photons.

Normally the transitions are between singlet states, i.e. the electron spin pairing is not affected. However, there is a small possibility for an electron’s spin to flip and result in a formally forbidden intersystem crossing to a long-lived triplet state. The triplet state is metastable and the molecules lifetime in this state can be microseconds or longer. Transitions from a triplet state can be either directly to the ground state – phosphorescence, or via a return to an excited singlet state – delayed fluorescence. The ground state is also a singlet state, so a transition from a triplet state to the ground state is also a formally forbidden transition, hence the longer lifetime. Another downside of a triplet state, is that it is more likely to react with molecular oxygen, which is naturally in a triplet state. This can lead to the oxidation and destruction of the fluorophore, resulting in permanent *photobleaching* (Greenbaum et al. 2000).

It is also possible for a fluorophore to end up in more exotic non-fluorescent, “dark”, states that can be long-lived, and afterwards return to an emitting state. This is what is termed *photoblinking* since a single fluorophore can alternate between emitting and dark states (Adam et al. 2009; Roy et al. 2011).

Microscopic imaging of living yeast cells carry a few difficulties in brightfield, including low contrast between the cell and the surrounding medium, and imaging interaction processes between specific proteins within the cell is impossible with brightfield techniques. The proteins of interest are much smaller than the diffraction limit and there is need for a way to be able to distinguish the sought species. The need for specificity can be achieved by letting the proteins studied carry a fluorescent reporter that does not interfere with its function. The reporter will then be excited by light that is not passed through the optical system towards the detector. This means that the only thing in the field of view will be the fluorescence of the reporter fluorophore. This allows for down to single-molecule precision with modern detectors. In chapter 4 the microscope design used in this thesis is described.

2.4 The use of fluorescent proteins

In 1962, a green fluorescent protein was found in the jellyfish *Aequorea victoria* by Osamu Shimomura, Frank Johnson and Yo Saiga. They extracted what they found to be a protein that acted as a down-converter, producing a green light from the blue chemiluminescence produced by the Ca^{2+} activated protein aequorin (Shimomura et al. 1962; Shimomura 1995). In the wild, the two proteins are produced side by side and the energy from aequorin is resonantly transferred to the green fluorescent protein (GFP) allowing the jellyfish to emit green light. The fluorescent properties of GFP, meaning that it could be excited by incoming light in contrast to bioluminescent molecules needing chemical energy input, would eventually open the doors to a new world of microscopy and functional genetics.

After the genetic sequence of GFP had been fully mapped by 1992 (Prasher et

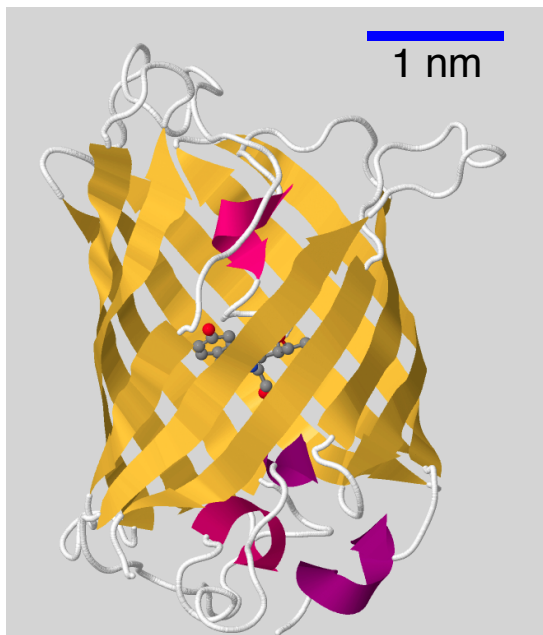


Figure 2.5 – eGFP protein structure. The chromophore is visible in the centre of the barrel. Yellow are β -sheets and purple are α -helices.

al. 1992) a new set of tools became available to biologists and biophysicists, as the proteins genome could now be introduced into other organisms so that it is produced together with other structures of interest (Tsien 1998; Leake 2013). The 26.9 kDa protein itself is a barrel-like structure 4.2 nm long, 2.4 nm in diameter with the chromophore being formed in the centre of the barrel (Ormö et al. 1996).

Since the 1990s, many variants of fluorescent proteins with varying excitation and emission wavelengths, based on the wild-type GFP has been developed by systematically introducing point mutations along the protein chain. Emission colours are now available varying from deep red to cyan (shortest wavelengths ~475 nm) and even blue (~448 nm) with excitation wavelengths ranging from yellow (~590 nm) to the near UV regime (< 400 nm) (Shaner et al. 2005; Shaner et al. 2007).

Early on point mutations found to improve the GFP performance was found by Roger Heim et al. in 1995 (Heim et al. 1995). And soon after that, another major improvement is made, the *Enhanced Green Fluorescent Protein* (eGFP, sometimes EGFP) with a 20-35 times increase in quantum yield (Cormack et al. 1996; Thastrup et al. 2001). This improved version (eGFP) is the protein that was chosen as a green reporter protein for the Mig1 and Msn2 transcription factors studied. The protein occurs as a weak dimer but can be found in monomeric state as well (Shaner et al. 2005). See Figure 2.5 for the protein structure of eGFP. The image was rendered using JSmol, an open-source HTML5 viewer for chemical structures in 3D. (<http://wiki.jmol.org/index.php/JSmol>).

A further improvement is a specifically monomeric version (mGFP) that has a point mutation preventing the protein from dimerising (Zacharias, Violin & Newton 2002).

Both eGFP and mGFP were indeed introduced into yeast for the investigations at hand. However, finding that the behaviour of the constructs using either GFP variant behaved similarly in yeast, the decision was made to concentrate on the mutants with eGFP reporters as not all mutants meant to utilise mGFP were viable. Using a consistent reporter protein throughout the experiments allowed for comparable fluorescent yield per traced protein.

Other fluorophores based on other base proteins has also been found. Of particular interest for the research presented here are the proteins based on a red fluorescent protein from *Discosoma* sp. An improved monomeric variant of a red fluorescent protein, called mCherry, was created by 2004 (Shaner et al. 2004). The protein mCherry has been extensively used as a red reporter protein in the work presented here. mCherry is a monomeric protein and it was used for tagging the many “second colour” proteins subjected to scrutiny in dual-colour experiments. The constructs used included dual-colour strains containing eGFP or mGFP tagged Mig1 and an mCherry tagged second protein. One key mutant used had the red tag on the RNA-polymerase subunit Nrd1, where it was used for clear nuclear localisation. Another had the mCherry tagging the AMP kinase Snf1.

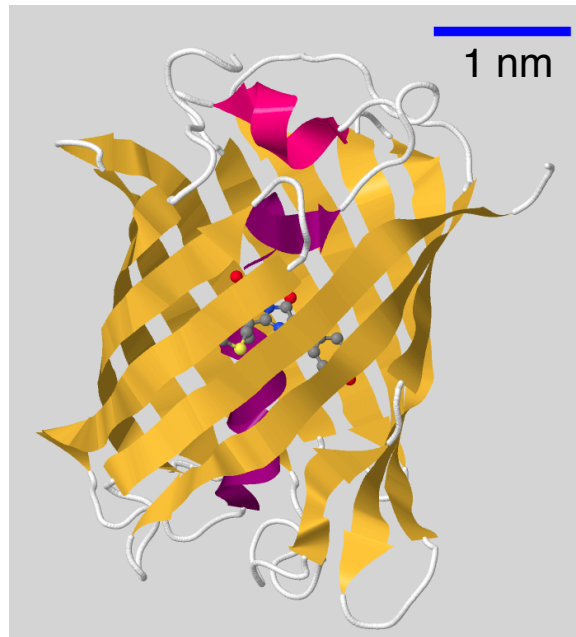


Figure 2.6 – mCherry protein structure. The chromophore is visible in the centre of the barrel. Yellow are β -sheets and purple are α -helices.

Fluorescent proteins are indeed not the most efficient fluorophores available having quantum efficiencies in general less than 40%, i.e. they are not very bright. (Shaner et al. 2005). The marker proteins used here, mCherry has a yield of ~20%, and that just slightly more than half as efficient as the eGFP (~35%). Fluorescent proteins also have poor photophysics. They are prone to quick photobleaching, and any one molecule will stochastically irreversibly photobleach after having emitted some $\sim 10^6$

photons (Leake 2013). This leaves the proteins under scrutiny in situ but dark and invisible to the observer. Other effects such as *blinking* can occur under high excitation intensities. Many available organic dyes have much better quantum yields and longer lifetimes before bleaching. Quantum dots is another relatively new addition to the range of available photo-excitabile markers. Quantum dots are semiconductor nanocrystals that is a bulk material that exhibit similar electronic energy level properties as single atoms due to their size and electronic properties (Reimann & Manninen 2002; Bawendi et al. 1990). They have a bleach time that can be thought of as nearly infinity in the type of experiments conducted here. However, the use of such external constructs pose several inconveniences. Many organic dyes are toxic in their own right and may interfere adversely with the cell. Quantum dots are large structures, 2-10 nm, sizes comparable to and larger than fluorescent proteins, and could lead to e.g. steric hindrance (any construct functionality will always need to be confirmed, regardless of fluorophore). Any dye or dot will also have to be introduced into the cell through the cell membrane, exposing the cell to acute stress and trauma.

In comparison, genetically integrated fluorescent protein markers will be integral parts of the cells, and as long as the marked proteins functions have been proven to not be impeded by the tag, the cell will be unscathed by the introduction of the marker. Upon production the proteins will have to mature, to fold into its active form, a process that takes around 15 minutes (in an *in-vitro* cell-free system)(MacDonald et al. 2012; Iizuka et al. 2011). A possible adverse effect could have been that due to the added fluorescent protein an instrumental protein (e.g. Snf1) becoming “too large” (steric hindrance) to enter the nuclear envelope and interact with the transcription factors there. This could be confirmed not to be the case both in bulk and microscopy assays.

Thus, despite the shortcomings of fluorescent proteins, they prove a good compromise for the type of investigations conducted.

3 Microfluidics

Visualising dynamic processes with high time resolution in living cells as they adapt to new environmental conditions is a nontrivial matter. The main problem is to apply the new environment to the cells while constantly be able to perform measurements on them. A simple assay in which steady state behaviour or very slow adaptation processes can be examined is easily achieved by stabilising a cell culture at some environmental condition and then immobilising the cells on a microscopy slide. This method could also be used for processes that take extended periods of time to follow its course, just transfer the cells from one state to another at the time of sample preparation and observe the changes.

For processes with a rapid response however, this is not an option. The way this issue has been dealt with in my work is by using a microfluidic chamber in which controlled flows of different environmental conditions can be rapidly changed and in doing so, exposing cells to a controlled environment change while continuously imaging one or a group of cells.

The flow-chamber used in the experiments described here is a cast polydimethylsiloxane (PDMS) slab featuring four 100 μm wide channels converging into one 400 μm wide channel, all channels are 27 μm deep. The channel design is of the same four-channel design that was used by Anna-Karin Gustavsson (Gustavsson et al. 2012) to visualise glycolytic oscillations in yeast. Figure 3.2 shows the four converging channels in the microscopes field of view. See also Figure 3.7 that shows the whole microfluidics chip: the PDMS slab bonded to a cover slip.

The flow through the channel is maintained in a low Reynolds number (eq. 3) regime, meaning that a liquid flowing through the channel will throughout exhibit a non-turbulent, laminar flow profile. This means that the flow with regards to the walls

will be governed by the no-slip condition, i.e. the liquid can be modelled as having zero velocity at the chamber boundary and then progressively faster “lamina” closer to the centre of the channel (see Figure 3.1 and subsection 3.1.1). In a laminar flow the flow velocities throughout the channel can be deterministically modelled, which is important to be able to know what environment a cell is exposed to.

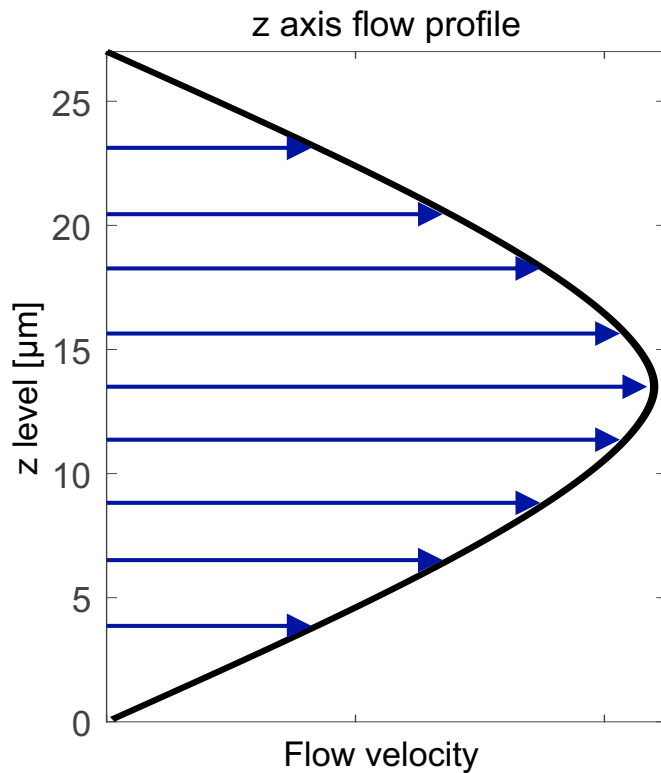


Figure 3.1 – Laminar flow. Velocities in the height dimension of the channels used in this project.

Several microchannel structures were considered, including a design using protruding pads for clamping down single cells (Huberts et al. 2013) and a design using pressure gradients to immobilise cells (Banaeiyan et al. 2013). However, the four-channel design is a simple structure with fairly large dimensions, compared to the other candidate flow channels. The dimensions are well suited for gravity fed operation and I have shown that even a simplistic bonding protocol works well for the type of experiments performed and presented here.

The onset of the alternate environment is within a second (see page 54 onwards). The new environment is synchronised with the imaging and it is possible to precisely time how long after an environment change an image is taken.

In the following subsections, the characterisation (section 3.1.1) and production (section 3.2) processes of flow channels are described. The protocol for immobilising cells in the flow channels is described in section 3.1.

3.1 Preparing and using microfluidic chips

During the experiments described in this thesis one of the two middle channels of a four-channel microfluidic chip was fed with a steady flow of a *standard environment*, while the second middle channel was fed with a controlled flow of an *alternate environment* for a designated time period. The two side channels were respectively used to wet and load the channels with cells, but were blocked for the duration of any experiment. One of the side channels was used to wet the channels with a 1 mg/ml solution of Concanavalin A in 10 mM Tris buffer with 100 mM NaCl at pH 8.0. The solution was manually pushed in using a 1 ml syringe attached to PTFE tubing. This pre-treatment was left to incubate for 15-30 minutes (Gustavsson used a consistent 30 minutes for a similar experimental setup).

Concanavalin A is a lectin used to immobilise the cells on the coverslip. The lectin binds non-specifically to the glass surface and specifically to α -mannose and α -glucose (Gustavsson et al. 2012; Lampen et al. 1971; Sigma-Aldrich n.d.). Sugars in the yeast cells membrane binds to the lectin and are held in place. This method of immobilising cells in liquid flows has been used successfully previously by Gustavsson et al. (Gustavsson et al. 2012; Gustavsson 2014).

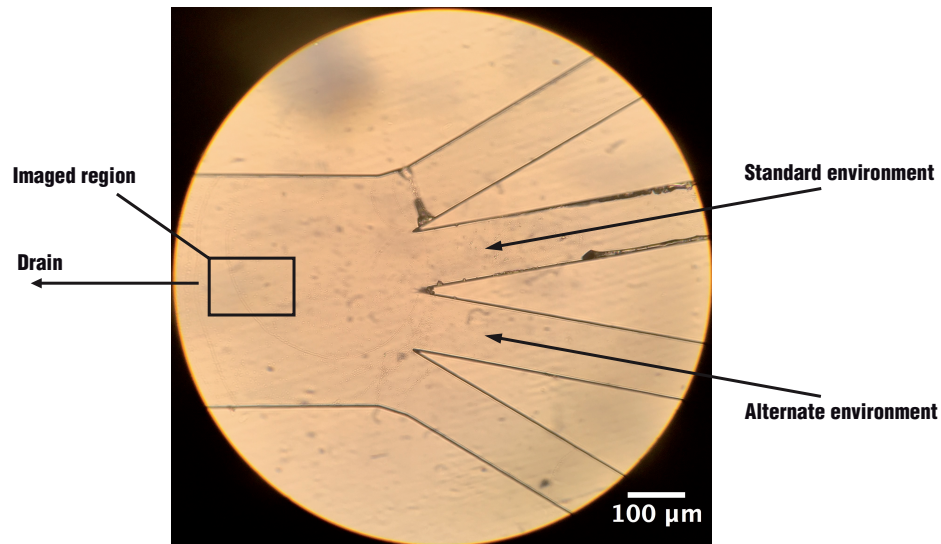


Figure 3.2 – The layout of the experimental setup of the microfluidic chip. Flows of standard and alternate environments are supplied via the central channels. The side channels were used for wetting, Concanavalin A application and cell loading.

The remaining lectin solution was then washed away by manually pushing through several 100 μl of the standard environment, followed by 10 μl of the alternate environment, ensuring that the alternate environment is positioned at the edge of the feed-channel.

3.1.1 Liquid feed system

The standard environment was fed to the microfluidics chip by means of a gravity feed. This was constructed as a scaffold holding a reservoir, a 10 ml syringe barrel without a plunger, elevated 60 cm above the chamber level. The reservoir is connected with #30 AWG PTFE tubing. The inner diameter is specified as 0.012 inches; this corresponds to a 0.3 mm bore. The (static) hydraulic head creates a head providing a pressure of:

$$P = \rho \cdot g \cdot h = 997.8 \cdot 9.82 \cdot (0.6 + 0.04) = 6.27 \text{ kPa} \quad (2)$$

calculated from the reservoir to the drain outlet (the additional 4 cm). Due to the very small flow through the system, this is assumed to be constant for the duration of an

experiment. The applied head pushes medium through the system at a rate of 0.50 mm/s through the PTFE tubes as measured at the outlet during wetting. The measured rate is thus the mean speed through the discharge tube measured after the outlet. The equivalent speeds running the pump only set to 10 $\mu\text{l}/\text{min}$ is 1.61 mm/s. With the combined flow of gravity feed and pumped flow set to 10 $\mu\text{l}/\text{min}$ the mean flow rate is 1.75 mm/s. The 0.3 mm (0.012'') inner diameter of the tube corresponds to a cross section of 73000 μm^2 , consequently this corresponds to a mean flow rate of 2.20 $\mu\text{l}/\text{min}$ delivered by the gravity feed. During experiments the syringe pump was set to pump 10 $\mu\text{l}/\text{min}$, using the feed tubes as a standard, assuming a uniform 0.3048 mm (0.012'') cross section, the measured mean flowrate from the pump only is 7.05 $\mu\text{l}/\text{min}$ and the measured mean flowrate from the combined gravity and pump feed is 7.66 $\mu\text{l}/\text{min}$. The discrepancy from the dialled in values is due to a standard library of syringe sizes and the syringe size used here was a 1 ml syringe, but the dimensions may have changed ever so slightly since the creation of the library. The pump provides a higher flowrate of the alternate environment. The higher flowrate driven by a higher pressure from the pump replaces the gravity feed while the pump is running, pushing the standard environment flow out towards the side.

The highest fluid resistance in the system is due to the microfluidic chip. The smallest cross section of the inlet channels is 100 by 27 μm , i.e. 2700 μm^2 to be compared to the 73000 μm^2 area of the feed and drain tubes.

The main assumption is that the flow through the channels is laminar. Generally, if the Reynolds number is less than 2300 the flow will be laminar and the flow will not be turbulent before the number passes 4000 (Hetsroni et al. 2005). The Reynolds numbers for the channels are calculated as:

$$Re = \frac{\rho \cdot u^2}{\mu \cdot \frac{u}{d_h}} = \frac{\rho \cdot u \cdot d_h}{\mu} \quad (3)$$

Where the first numerator, $\rho \cdot u^2$ is the dynamic pressure and the denominator, $\mu \cdot u/d_h$, is the shearing stress. The quantities are:

ρ : density [kg/m³]

u : velocity in the feedline or channel [m/s]

μ : dynamic viscosity [Ns/m² = Pa·s]

d_h : hydraulic diameter [m]

The properties of the minimal medium, YNB, used is almost identical to that of water so in the following the properties of water have been used (calculated at a room temperature of 22°C).

$$\rho = 998 \text{ kg/m}^3$$

$$\mu = 0.9544 \text{ mPa}\cdot\text{s}$$

The hydraulic diameter is defined as:

$$d_h = \frac{4 \cdot A}{p} \quad (4)$$

Where A is the area of the cross section and p is the length of the edge in contact with the fluid.

Thus, the expression for hydraulic diameter will be different for circular and rectangular cross sections. In a circular pipe, the hydraulic diameter will be simply the diameter and in a rectangular cross section channel it is given by the relationship:

$$d_h = \frac{2 \cdot w \cdot h}{w + h} \quad (5)$$

where w and h are the width (100 or 400 μm) and height (27 μm) of the channel.

Consequently, the feed tubes at a mean flow velocity of 0.5 mm/s have Reynolds numbers:

$$Re = \frac{998 \cdot (5 \cdot 10^{-4}) \cdot (3 \cdot 10^{-4})}{9.544 \cdot 10^{-4}} = 0.157 \quad (6)$$

Which is well below the critical value for non-laminar flow.

The narrowest channels have a cross section of 100 by 27 μm . Flow rates of 2.20 $\mu\text{l}/\text{min}$ corresponds to an average flow velocity of 3.4 mm/s in the main imaging channel and 13.6 mm/s in the feed channels. The higher rate of 7.7 $\mu\text{l}/\text{min}$ (the measured mean sum of the gravity fed flow and the pump flow) corresponds to 12 mm/s in the main channel and 47 mm/s in the inlet.

This corresponds to Reynolds numbers:

$$Re_{pump} = \frac{998 \cdot (1.2 \cdot 10^{-2}) \cdot (5.06 \cdot 10^{-5})}{0.9554 \cdot 10^{-3}} = 0.625 \quad (7)$$

in the imaging channel at the higher (pump fed) rate and:

$$Re_{gravity} = \frac{998 \cdot (3.4 \cdot 10^{-3}) \cdot (5.06 \cdot 10^{-5})}{0.9554 \cdot 10^{-3}} = 0.180 \quad (8)$$

at the lower (gravity fed) rate.

Here the d_h , the hydraulic diameter for the rectangular flow chip imaging channel has been calculated as:

$$d_h = \frac{2 \cdot 400 \cdot 27}{400} = 50.6 \mu\text{m} \quad (9)$$

The low Reynolds numbers for the channels and connecting tubing are consistent with laminar flow at the flow rates used in any experiment performed within the scope of this thesis, i.e. up to the very highest rate used, 7.7 $\mu\text{l}/\text{min}$.

The laminar flow through the system will allow the alternate environment to seamlessly replace the standard environment within seconds (further elaborated on later).

The flow in an enclosed channel is described in classical fluid mechanics by the Navier-Stokes equation for Newtonian and incompressible liquids:

$$\rho[\partial\mathbf{v} + (\mathbf{v} \cdot \nabla)\mathbf{v}] = -\nabla p + \eta\nabla^2\mathbf{v} + \rho\mathbf{g} \quad (10)$$

In the system used in this work, it can be assumed that all liquids involved are Newtonian and incompressible. Here using Bruus notation (Bruus 2015; Gustavsson et al. 2012).

From these the Hagen-Poiseuille equation can be derived which describe the pressure drop over a (long) section of pipe or duct, such as the feedline or the channels. This is needed when describing the gravity feed to the chip. The interesting number is the flow rate in the imaging channel at the level of the imaged cells, i.e. the first 5-10 μm above the channel floor. The simplifications in a Poiseuille flow are such that the three-dimensional flow field is reduced to a one-dimensional flow, there is no effect due to gravity. Another important assumption is the no-slip boundary condition. This is to say that the velocity of the flow drops to the velocity of the wall, i.e. 0, along the cross-sectional axes. Bruus has shown an analytical solution for the simple case of a rectangular channel with a width significantly larger than the height. The flow velocity profile in the x -direction is described by the equation:

$$v_x(y, z) = \frac{4h^2\Delta p}{\pi^3\mu L} \sum_{n=1,3,5\dots}^{\infty} \frac{1}{n^3} \left[1 - \frac{\cosh\left(n\pi\frac{y}{h}\right)}{\cosh\left(n\pi\frac{w}{2h}\right)} \right] \cdot \sin\left(n\pi\frac{z}{h}\right) \quad (11)$$

L is throughout these formulæ the length of the channel and is assumed to be much longer than the width and height. As of yet, there is no analytical solution to the expression for the *Volumetric flow* (Q) through a rectangular channel, being the same quantity as the mean flow measured and discussed earlier, but Bruus gives an estimation based on a situation where $h < w$. Bruus has shown that the error is less than 0.2% for a rectangular cross section where the height is half that of the width. The

error is also dropping as the aspect ratio between the two sides drops. Note that the number in brackets is a correction factor from an infinitely wide parallel plate situation.

$$Q_{rectangular} \approx \left(1 - 0.630 \frac{h}{w}\right) \cdot \frac{h^3 w}{12\mu L} \Delta p \quad (12)$$

Where Δp is the pressure drop over the channel. Knowing the initial pressure produced by the hydraulic head and the measured Q the microfluidics system can be modelled as a series of hydraulic resistances and the pressure drop over each section is given by the relations given. The final relation needed is the (analytical) expression for the relationship between volumetric flow and pressure drop in a circular cross section channel (the feed and discharge tubes).

$$Q_{circular} = \frac{\pi r^4}{8\mu L} \Delta p \quad (13)$$

Using a feed tube length of 72 cm (this is a length that is chosen for the calculations here as the reservoir holding the standard environment extends above the connection to the feed tube and some slack is needed to be able to connect the tubing), and a flow rate of $Q_{gravity} = 2.20 \mu\text{l}/\text{min}$, the pressure drop over the feed line is:

$$\Delta p_{feed} = Q_{gravity} \cdot \frac{8 \cdot \mu \cdot 0.72}{\pi r^4} = 9.3 \text{ Pa} \quad (14)$$

So, the pressure at the inlet is $6.27 \cdot 10^3 - 9.3 \text{ Pa} \approx 6.26 \text{ kPa}$. The next step is the pressure drop over the inlet channel. The channel is 23 mm long.

$$\Delta p_{inlet} \approx Q_{gravity} \cdot \left[\left(1 - 0.630 \frac{2.7 \cdot 10^{-5}}{10^{-4}}\right) \cdot \frac{(2.7 \cdot 10^{-5})^3 \cdot 10^{-4}}{12\mu \cdot 2.3 \cdot 10^{-2}} \right]^{-1} = 5.15 \text{ kPa} \quad (15)$$

Finally, the pressure drop over the 10 mm long imaging channel is:

$$\Delta p_{main} \approx Q_{gravity} \cdot \left[\left(1 - 0.630 \frac{2.7 \cdot 10^{-5}}{4 \cdot 10^{-4}}\right) \cdot \frac{(2.7 \cdot 10^{-5})^3 \cdot 4 \cdot 10^{-4}}{12\mu \cdot 10^{-2}} \right]^{-1} = 558 \text{ Pa} \quad (16)$$

This allows the use of the equation (11) to show the approximate flow velocity at an average $5 \mu\text{m}$ wide cell stuck to the channel floor.

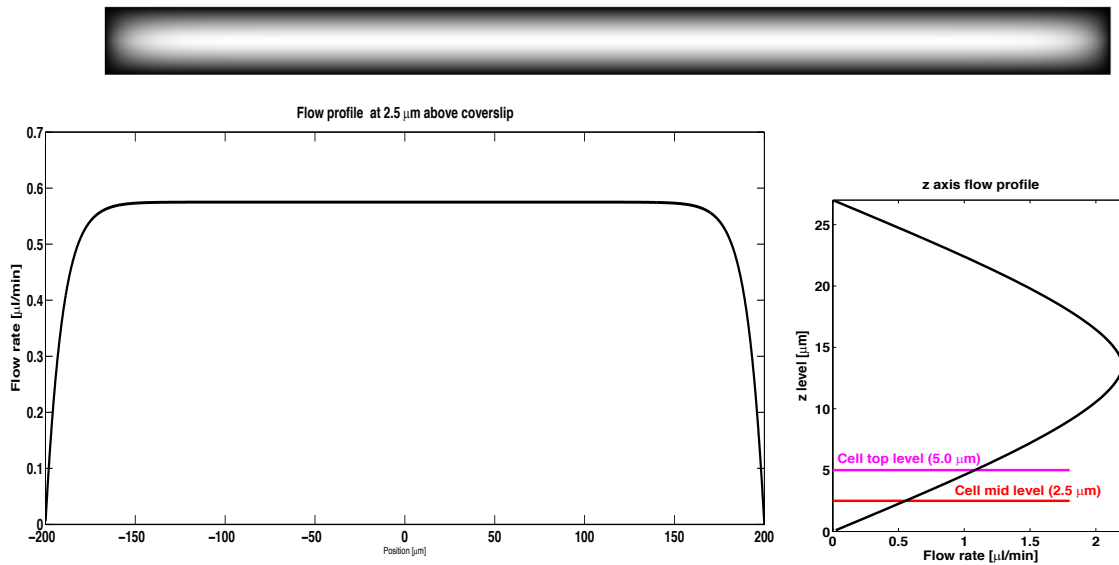


Figure 3.3 – Simulated flow profile in the main channel. Top: Normalised *and to scale* flow profile from lowest (black), to max flow (white). Bottom right: Flow profile along the *z* axis at channel centre. Bottom left: Cross-sectional flow profile at cell mid-level (red level in the right-hand plot).

The switchover between the gravity fed environment and the pump fed alternate environment is fast. In the system used it has been shown to occur over the first second after pump start. This was shown with the microscope in fluorescence mode using an unmarked standard environment (gravity fed) and an alternate environment with suspended 1 μm fluorescent beads. The microscope was then aimed at the region of interest where cells would be located during a live experiment and the laser was continuously turned on during acquisition. Acquiring at half the imaging rate as during a live cell experiment, i.e. an image interval of 10 ms (100 frames per second), the switch to the alternate environment could be seen by observing when beads appear in the field of view. To characterise the behaviour, the pump was started 500 frames (5 s) after imaging started and turned off again after 1500 frames (15 s). The microscope was focussed to the region 2-3 μm above the coverslip surface, the approximate mid-

point of a yeast cell deposited on the coverslip. The onset of the alternate environment was defined as the first frame in which an in-focus fluorescent bead first passes the field of view. This consistently happens between 0.6 s and 1.4 s after pump start, with little change in timing depending on imaging position. The return to the standard environment after pump stop takes somewhat longer time. The return, defined as the final frame in which an in-focus bead is visible in the field of view, occurs between 26 and 35 s after pump stop. See Figure 3.4 for an example of the appearance of a calibration assay. The difference in return time is also fairly consistent, adding 3 s per additional 20 μm from the inlets. The measurements were taken in 20 μm intervals from 20 to 60 μm from the point the inlets join in the main imaging channel.

A standard experimental sequence during live cell experiments consists of an initial sequence of one or several frames acquired before the pump is started and

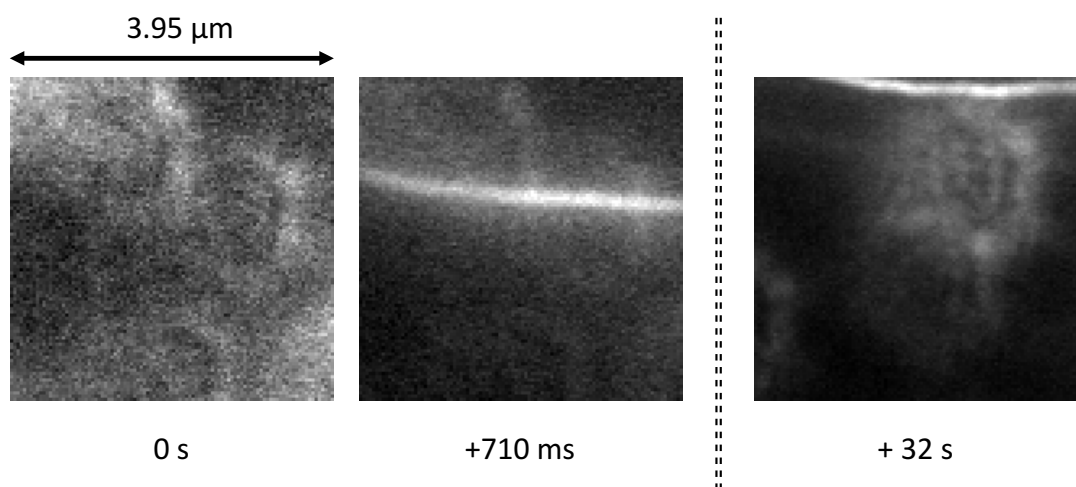


Figure 3.4 – An example of the way the onset of alternate environment and the return to standard environment in the flow channel was measured. At 0 s a flow of a suspension of fluorescent beads was started in the alternate environment channel. The first frame with a visible bead is recorded as the onset and the last frame with a visible bead is recorded as the return time. The time code in the final frame is seconds after the pump has been stopped.

then after a 30-60 s delay another burst of frames will be acquired. The intervals can be chosen to suit the experiment. By acquiring at least one burst before pump start a baseline in the standard environment is obtained and the fast switch ensures that the first burst in the alternate environment is of a cell that has been exposed to the new medium. In some experiments the behaviour was studied after a return to the standard environment. In these cases, the final measurement after the return, were always taken more than 30 s after the pump stop with a standard delay before final acquisitions having been 210 s. Some variations of this were used but there was always an allowance of a minimum delay of 30 s for experiments returning to the standard environment (see chapter 5 for detail on experimental protocols and Figure 3.5 for a schematic representation of a two-transition experiment).

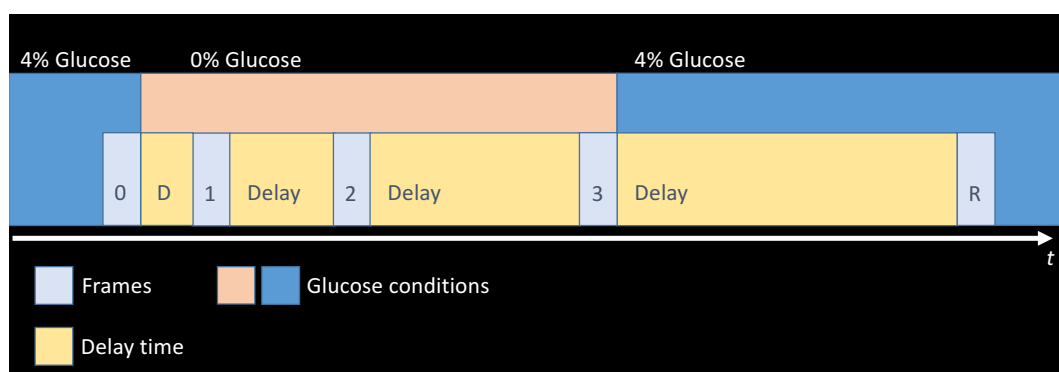


Figure 3.5 – A schematic *representation of an imaging sequence with the changes between environments marked.*

3.2 Mask design and flow channel production

To produce a microchannel, two parts are needed: a PDMS slab with a micro-imprint of the channels, that will act as the walls and ceiling of the channel, and a standard microscopy cover slip, large enough to cover the entirety of the channels and act as a floor in the chamber.

In section 3.2.1 the production of a master for channel casting on a silicon wafer and the use of such a master to produce a PDMS slab with an imprint of the channels is described.

The PDMS slab with the micro-imprint was bonded to a 25 by 50 mm microscopy coverslip through which the samples were imaged. Unfortunately, the flow channels used must be considered one time use only as the treatment with a lectin (see section 3.1, on sample preparation), will leave the channel with some cells so tightly bound to the channel walls they cannot be washed away with e.g. a high-pressure flow through the channels. Also, a new lectin treatment has proven not be effective in an already wetted channel in case sample cells fail to bond with the lectin.

3.2.1 Protocol for PDMS flow channel fabrication and preparation

The channels are cast using a master created on a wafer of monocrystalline silicon (as used in the production of e.g. micromechanics). The master preparation should be performed in a clean room. The master is constructed by spin-coating the wafer with a 27 μm thick layer of SU-8 negative photo-resist. Good practice is to pre-bake the wafer on a hot plate for circa 20 minutes at 150 $^{\circ}\text{C}$, the pre-bake dehydrates the wafer allowing the SU-8 to stick better to the wafer. After spin-coating the wafer is given a brief bake (2-3 minutes) at 95 $^{\circ}\text{C}$. A photo-lithographic procedure is then followed, using UV exposure (350-400 nm) through a transparency mask carrying the pattern of the 4-1 channel system. The UV exposure hardens the exposed pattern and the wafer is subsequently after-baked on a hot plate at 95 $^{\circ}\text{C}$ for a further 3 minutes and the process is followed by washing the unexposed photoresist away with SU-8 developer. Finally, the master is fixed by a 20-minute bake at 150 $^{\circ}\text{C}$. The resulting 27 μm tall ridges form the master on which the channels are cast. The channel dimensions are

ultimately determined by two factors: the transparency dimensions in the lateral plane and the spin-coating in the axial dimension. Such a master is durable, and during all experiments reported, a single master supplied all microfluidics chips used. It is crucial to be careful when separating the finished PDMS slab from the master as the silicon wafer is very fragile and can easily be cracked and consequently destroyed.

The following steps are then taken to produce the PDMS slab with microchannel imprints. 10 g raw PDMS (Sylgard elastomer) is measured and 1 g curing agent is added to it and the two components are mixed thoroughly together. After mixing the resulting mixture will be containing significant amounts of gas, mainly air introduced during the mixing. This means the mixture needs to be de-gassed before a slab can be cast. There are two main methods available to do this. Either the mixture is placed in a vacuum chamber such as a vacuum desiccator and exposed to a low-pressure environment for 15-30 minutes (the time may vary depending on how much air have been worked into the mixture and how quickly the foam formed subsides, best practice is to wait until the mixture is still and the foam has disappeared). A simple alternative to a vacuum chamber or desiccator is using 60 ml syringes as a one-time use vacuum chamber. This method was used successfully during the live cell experiments. The syringe is filled with the circa 10 ml PDMS/curing agent mixture and as much air as possible expunged from the system before sealing the tip. The plunger is then withdrawn, creating a vacuum in the syringe that degasses the mixture. The plunger is then held in place in the withdrawn position, circa 120 mm from the origin, for as long as it takes for the mixture to degas. As mentioned before this usually takes 15-30 minutes. An effective method of holding the plunger in position is to create 120 mm long struts, e.g. using optics mounting posts from Thorlabs. A pair constructed by combining two 100 mm posts with two 20 mm posts was used. The posts have a



Figure 3.6– The plunger method for degassing PDMS

good fit to the + shaped plunger shaft and hold the plunger securely in place during the de-gassing process (see Figure 3.6).

Following the degassing, the mixture is cast on the master inside a brass rim that is gently placed on top of the silicon wafer. The brass acts as walls during the casting and a specialised acrylic top with multiple holes positioned above the channels entrance points is fitted on top of the rim and used to hold several pins in place that serve as pre-fabricated inlets, thus no additional punching of holes is needed at a later time to introduce the feed-lines to the channels. If the master has not been used for some time it is beneficial to first wash it with isopropanol and blowing it dry with a particle free airflow. The PDMS is poured into the mould with the pins described in-situ and the whole package is pre-baked in an oven at 95 °C for at least one hour to allow the PDMS to settle and harden. The next step is to remove the inlet pins, the acrylic top and finally, the PDMS slab from the enclosure formed by the brass rim.

Depending on the time and temperature at which the extraction is done the procedure can be as simple as lifting the slab out together with the inlet pins if the finished cast has been allowed to cool to room temperature. A convenient choice of time during a day at which to prepare a new set of chips is making it the last thing done during a day and then a timed oven is used that turns off after a set time. The prebaked chip will then be waiting in the oven at room temperature when

arriving in the lab in the morning. If the package is hot it may be necessary to use a scalpel to pry the slab out of the mould. Care must then be taken not to crack the silicon wafer.

After removing the PDMS slab it needs to be fused with a microscopy cover slip. First, it is important to make sure that the inlets are fully open, a thin film of PDMS may form between the tip of the pins and the mask so a 27G injection needle is used to cut away any membranes at the feed tube in and outlets formed during the casting process.

The next step is to wash both the PDMS slab and a 25 by 50 mm coverslip with isopropanol, to make sure no fat deposits from fingerprints or other sources are found on the surfaces. The surfaces are blown dry with air and both the PDMS slab and the coverslip are treated in a plasma chamber (plasma from normal air mixture) for one minute. The procedure leaves the surfaces “activated”, i.e. they are having a higher than normal amount of surface charges. The treatment also makes the surface much more hydrophilic. The slab and the coverslip are put in place. If the cast is good and no dust or other impurities are present, they should easily form a nice and tight interface. This construct of a PDMS slab bound to a coverslip is what is referred to throughout this thesis as a *microfluidic chip*. If it is hard to aim properly on the first attempt, a drop of methanol can be used, it forms a thin film between the two components that evaporates within seconds to minutes, allowing for some position adjustment. This step is not essential, but can be used if needed by an inexperienced user.

The chip now has to after-bake at 95 °C for at least one hour for a permanent bond between the slab and the coverslip to form. *This step is essential*, as without this

baking step the chip will invariably leak due to coming wholly or partially loose from the coverslip.

With a limited number of moulds, good practice is to start a production line with one chip being after-baked while another is being pre-baked in the mould. The second, bonding after-bake is also fine to leave overnight.

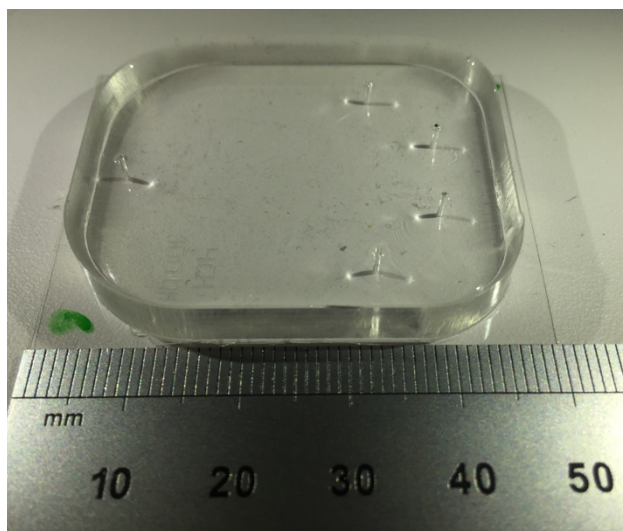


Figure 3.7 – The finished microfluidics chip, fused to a coverslip. The four inlets on the right side and the single outlet on the left.

To aid the wetting of channels during the setting up of an experiment the channels are treated once more in the plasma chamber for one minute, just before use (up to an hour beforehand). This makes the surfaces in the chip, including the channels, somewhat more hydrophilic. Allowing proper wetting of the channels.

To connect the chip to the outside world, micro-bore PTFE tubing was used. The tube is thin-walled tubing of #30 AWG, inner diameter 0.3 mm (Cole-Parmer). The tubing has an ideal dimension to be pushed directly into the chips in- and outlet wells. The tube fits snugly and the PDMS and PTFE tube themselves form an adequate seal for the flowrates used.

4 Microscopy

One of my key aims with this project been to image and describe metabolic processes in living *Saccharomyces cerevisiae* with precisions down to single-molecule interactions over short time scales. This is not a trivial task and the tools with which to image will have to be a compound system with various methods from different disciplines. In this chapter, the imaging aspects will be covered. The main imaging tool is a bespoke epifluorescence microscope built around a Nikon *Ti*-series inverted microscope. The system used for the work presented in this thesis is a further development from the modular microscope system with astigmatic imaging capabilities I developed and presented in my thesis *A Fourdimensional Microscope for Single Molecule Studies in Living Cells Using Astigmatic Axial Resolution Enhancement* (Hedlund 2015), submitted and examined as a separate course at the University of Oxford. The microscope has a number of bespoke modules used to control the sample position, illuminate it and acquire images of it. In this chapter, all the modules will be described in detail with their respective functions.

Also in this chapter, the software suite *CellBild* will be introduced. This specially designed piece of software controls most aspects of excitation light control, including mechanical and electronic shutters, camera triggering and synchronisation. It does also control the timing of the pump delivering the alternate environment in dual-environment microchannel experiments.

Super-resolution microscopy is a cover-all term for a wide range of techniques developed mainly since the 1990s to overcome the diffraction limit described by Ernst Abbe (Abbe 1873). The Abbe limit states that the smallest object that can be clearly resolved is determined by the imaging wavelength, the refractive index of the medium

through which the sample is viewed and the *Numerical Aperture*, another term coined by Abbe a few years later (Abbe 1881).

$$d = \frac{\lambda}{2 \cdot NA} \quad (17)$$

Where the NA , the numerical aperture is:

$$NA = n \cdot \sin \vartheta \quad (18)$$

Here n is the refractive index of the medium through which the sample is imaged. This is normally air ($n \approx 1$) or some immersion medium such as water or oil ($n > 1$). This means that e.g. a high- NA (say $NA = 1.5$) immersion objective lens cannot resolve structures separated by less than 200 nm when imaging with 600 nm light. Ever since Abbe's work in the late nineteenth century, microscopists have tried to push this boundary, but it largely remained the practical limit for the better part of the century to come as reviewed in the paper by Wollman, Nudd, Hedlund and Leake (Wollman et al. 2015). Apart from some dark-field techniques such as *Ultra-microscopy*, a technique proposed during the first decade of the twentieth century by Richard Zsigmondy (Mappes et al. 2012) that used scattering to image colloidal particles as small as 50 nm; an early proposed scanning near-field technique (Synge 1928); and a proposed 4π -technique in late 1970s (Cremer & Cremer 1978), most work in the field has been conducted from the 1990s onwards. In 1994 Stefan Hell ushered in the era of true super-resolution microscopy with *stimulated emission depletion microscopy*, (Hell & Wichmann 1994). STED microscopy is a scanning laser technique that allowed imaging of 35 nm fluorescent particles. A wide-field technique presented by H. Pin Kao and A.S. Verkman the same year showed how small (264 nm) single particles could be tracked in three dimensions with high spatial resolution along all axes by introducing asymmetric optics in the imaging path (Kao & Verkman 1994). Their new technique enhanced the axial resolution in their system to 12 nm compared

to a lateral resolution of 5 nm. This was the first use of the astigmatic approach to enhance the axial resolution, a method that was used in the work presented here, see section 4.1.3.

From that point on, many methods have evolved, for both scanning (confocal) and wide-field microscopy utilising the properties of fluorescence and optical enhancements to improve especially the axial resolution. In the realm of full frame imaging two major categories of enhancement methods have evolved. The astigmatism method mentioned above sorts itself to the same category as another method, biplane imaging. Both techniques rely on a slight defocussing of the image, i.e. having two focal planes at the sample, offset by a few nanometres, either in the entirety of the image (bi-plane) or along one lateral axis (astigmatism). The other major method category uses phase manipulation in the Fourier plane of an additional two-lens $4f$ imaging path to create images of point sources that have an asymmetric response to defocussing at the camera image plane. Effects sought after are e.g. multiple spots and rotation as in the *Double-Helix Point Spread Function* method developed by W.E. Moerner's group in 2008-2009 (Pavani & Piestun 2008; Pavani et al. 2009) and also in later developments such as the *Cork-Screw PSF* developed by the same group a few years later (Lew et al. 2011). These latter methods can indeed under some conditions be somewhat more accurate than the bi-plane or astigmatic methods (Badieirostami et al. 2010), but all (arguably except the bi-plane method, since it creates two independent images) suffer from slight distortion of an image in brightfield or fluorescence modes when the sample has a dense population of fluorophores. The phase manipulating methods use either fixed phase plates or a *Spatial Light Modulator* (SLM) and are more complicated to achieve. The phase retardation pattern is nontrivial to calculate and may need iterative optimisation if done from fundamental principles,

or the option is to buy a fixed phase plate from a commercial supplier. Other issues such as the necessity of precise alignment of phase modified PSF's and the mentioned distortion generally needs to be avoided in most cases when imaging in bright-field mode.

4.1 The Microscope

The bespoke microscope system I constructed is built around a Nikon *Ti*-series inverted microscope body with a mercury lamp attachment for epifluorescence microscopy. The build strategy is a modularised approach with the main module size being a 300 by 400 mm optical “bread-board”. The microscope body is mounted on one and the excitation module consists spreads out over two such units. On the microscope body a precision positioning stage from *Mad City Labs* is mounted on a coarse positioning stage (see Figure 4.1). The sample holder is a simplified flat surface to which the sample is affixed with tape. The use of tape instead of clamps is a purely practical decision as the narrow clearances did not allow for a practical clamp system to be mounted that can handle both standard samples and microfluidics chip style samples. The tape method worked well for all the use cases the microscope so far has been exposed to.

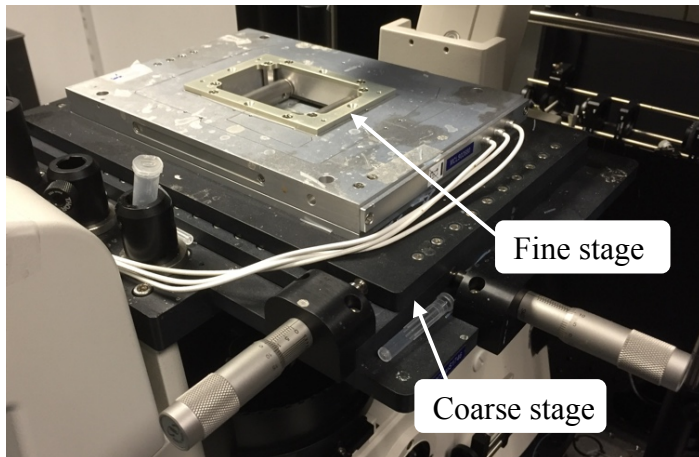


Figure 4.1– The coarse and fine positioning stages mounted on the microscope.

4.1.1 Main microscope body modifications

The main microscope body was only lightly modified in one aspect and that was in the light intake for excitation light for epi-fluorescence imaging. The original design was for use with a mercury lamp. The intake had a condenser and filter bank that was

omitted from the practical design used. The remaining Nikon original components used was the angled light intake that takes the form of a hollow lance holding a lens, on the far side focussing a collimated light beam on the back focal plane of the objective lens. The lance also holds the field diaphragm in the near focal plane. The lens has a focal length of 134.8 mm and after the field diaphragm a further focal length is just outside the angled light intake, at the point where the mercury lamp condenser and filters would be located. In Figure 4.2 the light intake is shown together with the final beam steering optics. The specifics of the beam steering will be covered in subsection 4.1.2 describing the excitation module.

In Figure 4.3 a schematic of the optical components of the Nikon microscope body is shown.

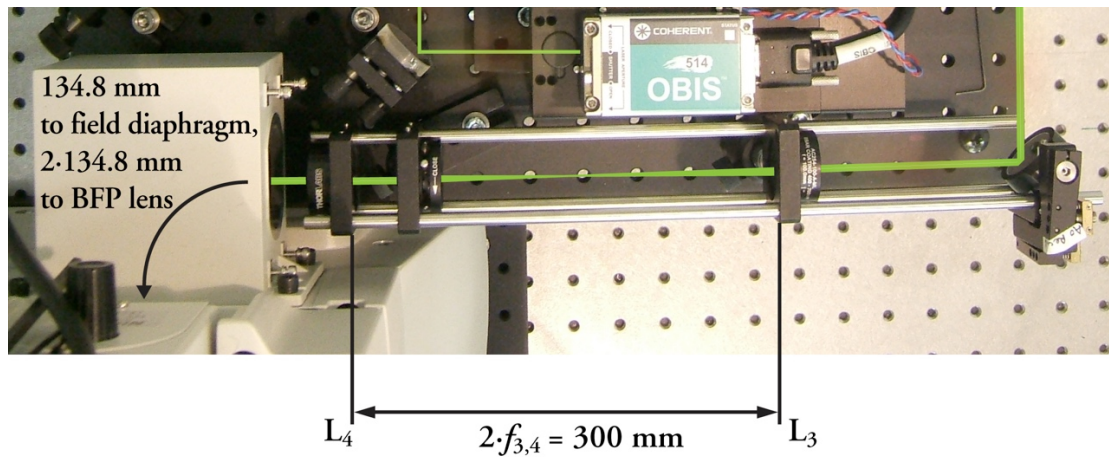


Figure 4.2 – Showing the excitation light intake of the microscope. On the left-hand side is the entrance box with a mirror directing the light down in the image. The distance from the back focal plane (BFP) focussing lens to the last beam steering lens (L_4) is 169.6 mm. The field diaphragm is located half way between the BFP lens and L_4 .

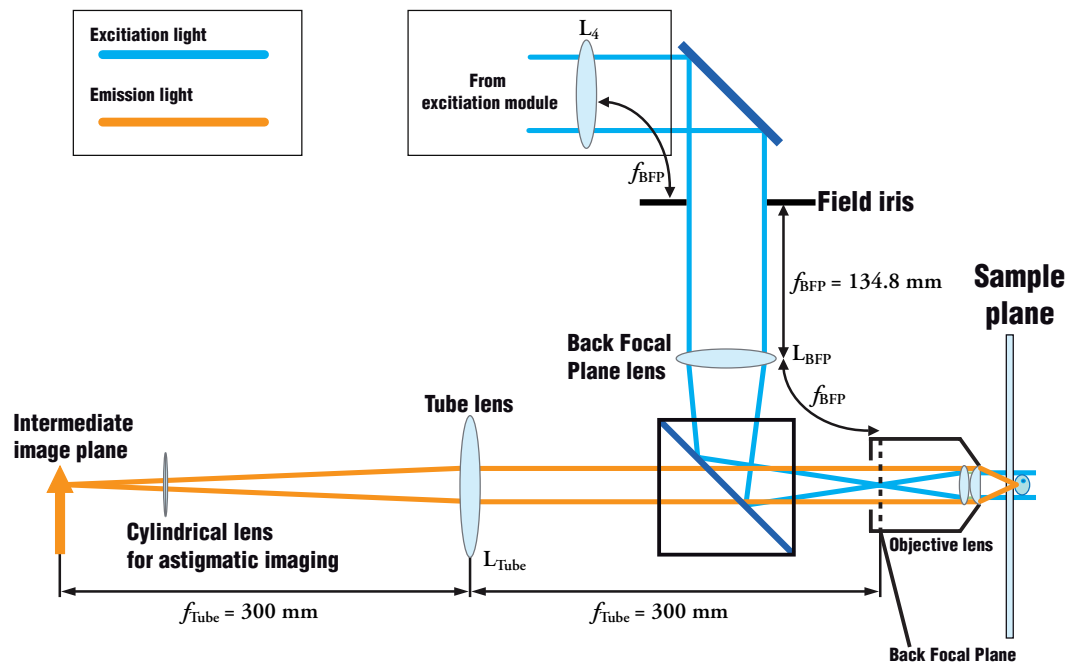


Figure 4.3 – A simplified schematic of the entirety of the optical beam path inside the Nikon microscope body

4.1.2 The excitation module

The most complex of the external modules is the excitation module. This module has been designed to have a small physical footprint and covers two standard module breadboards. The module has a set of distinct main purposes:

1. Generating the light of two different wavelengths used to excite two different fluorophores in a sample
2. Expansion and adjustment of the laser output beams to make the two match
3. Combining of the two light beams, and
4. Steering them to the sample
5. Shuttering the beams

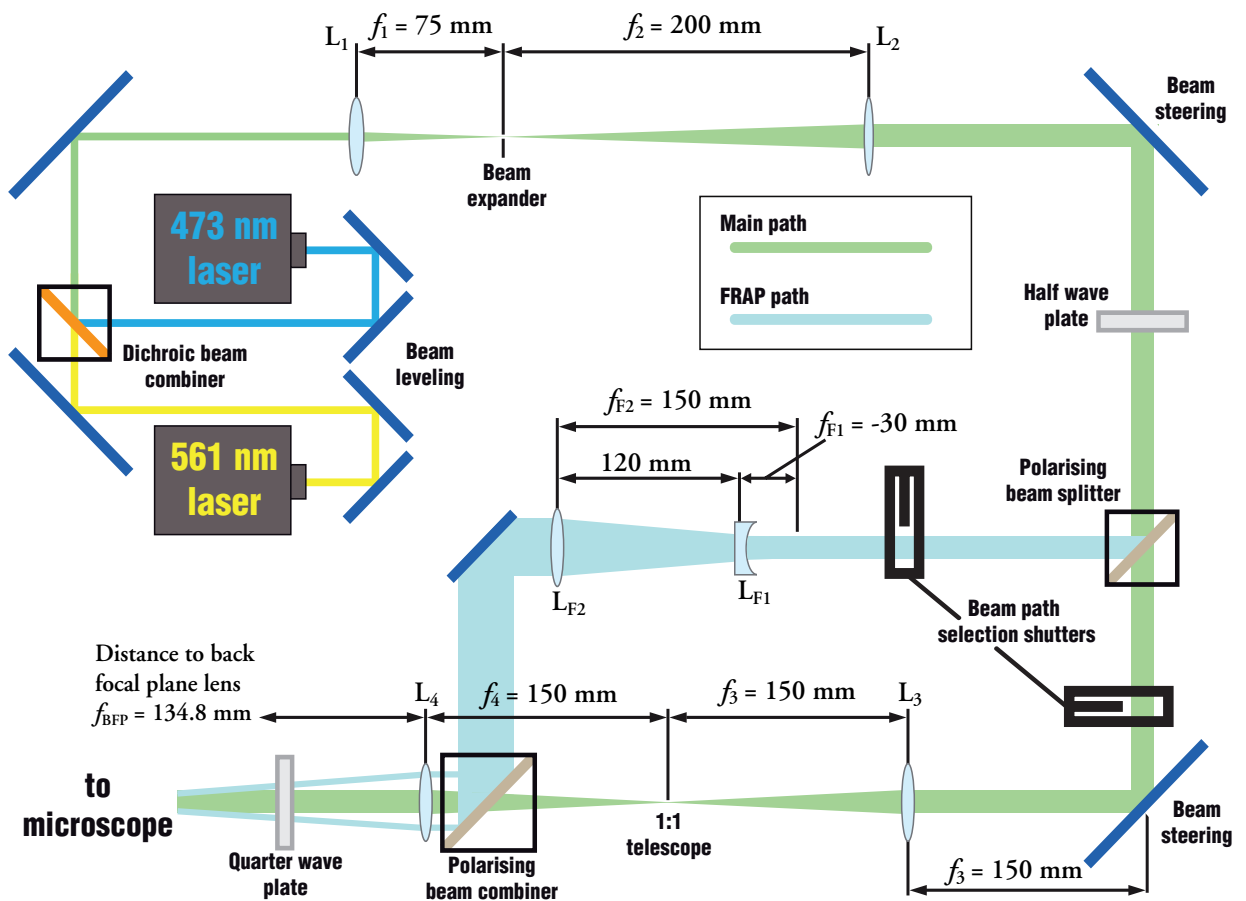


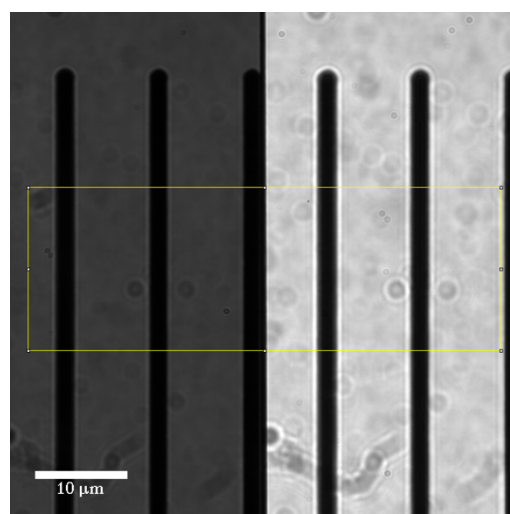
Figure 4.4 – A schematic of the excitation module components. The dichroic combining mirror is an FF495-Di03 filter. The half wave plate is mounted in a rotating holder and is used to adjust what proportion of light propagates through the widefield (main) path and how much goes through the FRAP path.

The primary illumination mode is an epi-fluorescence geometry. This means that the excitation light will fill the field of view in the sample plane. The back focal plane lens will focus a parallel beam of excitation light on the objective lens' back focal plane (see Figure 4.3), which in an infinity corrected microscope like the *Ti*-series, will result in a parallel beam through the sample plane. The width of the illuminated spot can be tuned using the field iris.

Secondary to the main purposes a secondary excitation path was built in that focusses the beams to a diffraction-limited spot at the sample plane. This mode is

useful for Fluorescence Recovery After Photobleaching (FRAP) type experiments. A technique first described in 1976 (Axelrod et al. 1976). A schematic of the components is shown in Figure 4.4. The FRAP path was implemented and verified that it produces a diffraction limited spot in the sample plane using fluorescent beads. However, it is worth noting, that the path was designed for experiments that yielded inconclusive results that eventually were not included in this thesis. Hence, this technique will not be further mentioned in this thesis. FRAP experiments were performed by Adam Wollman on another setup for some of the data reported in our paper (Wollman et al. 2016), see appendix B.

The light beam is first adjusted to the same height, 85 mm, and then passed through beam expanders to coordinate the beam waists of the two lasers to the same diameter and then they are combined with a dichroic mirror and once again passed through a beam expander to produce a beam of suitable size. The beam output by the laser heads is too narrow for the transmitted beam in through the epi-fluorescence path to



size.
Figure 4.5 – An image of a graticule used to measure the pixel size. Overlaid is the ROI used during experiments.

cover the region of interest imaged on the camera. Hence the requirement for a beam expander. As will be further explained in the section on the camera and acquisition limitations (see section 4.2 on page 77), the maximum size of a frame acquired at an actual frame rate of 200 frames per second is 476 by 164 pixels, which corresponds to a region of interest of 22.1 by 15.3 μm (note that the since a colour splitter is used

before the camera only half the width of a frame is actually being imaged) at the sample given the size of a single pixel corresponding to 93 nm as measured by imaging a standard graticule with 10 μm spacing. See Figure 4.5.

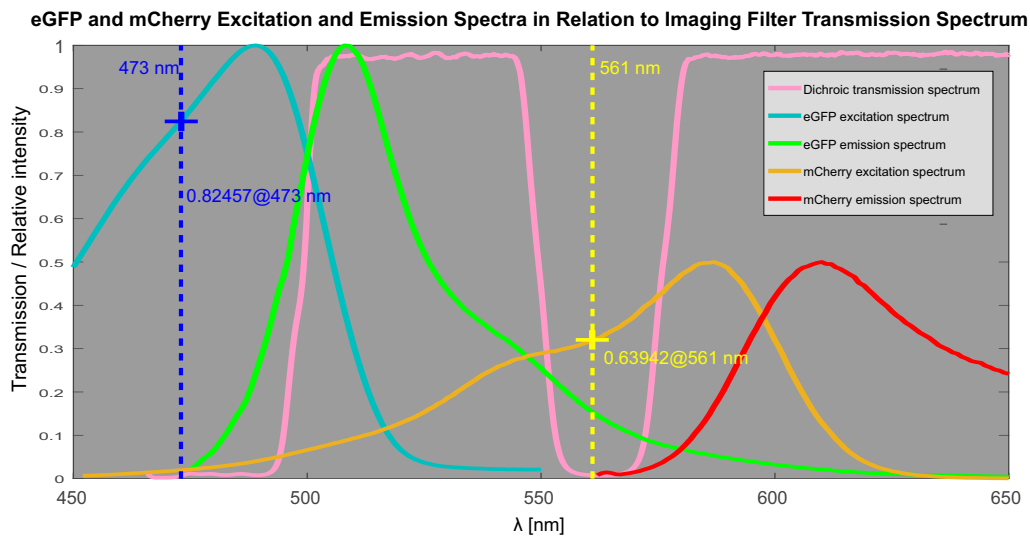


Figure 4.6 – Relative intensity excitation and emission spectra for the fluorescent proteins eGFP and mCherry and the transmission spectrum for the main imaging dichroic mirror, *Di01-R488/561*. Absorption, emission and transmission spectra from Chroma (<https://www.chroma.com/products/fluorochrome>). Note that the mCherry spectrum is about half the brightness of eGFP. The excitation laser lines are represented by the vertical blue and yellow dashed lines, 473 nm and 561 nm.

The beam waist was chosen so it would fill the shorter axis. Final adjustment of the light field at the sample was adjusted with the field iris. After adjustment with the field iris, the light field would have a diameter corresponding to the shortest axis, 15.3 μm , and any cells located in the dark corners would not be considered for analysis. Due to the Gaussian beam shape of the lasers only the centre portion is used and the beam flanks are cut out by the field iris to the 15.3 μm height of the region of interest (ROI).

Since the microscope is generally set up to work in an epifluorescence mode with light delivered on-axis to the sample in the opposite direction of imaging, the excitation light is coupled into the beampath by a dichroic mirror, selected with a

bandwidth wide enough to allow both 473 nm and 561 nm to be reasonably efficiently transmitted in the sample direction while transmitting the emission from the reporters. eGFP, the main GFP variant used has an emission peak at 507 nm and mCherry emits at 610 nm (Shaner et al. 2005). Note that this means that the dichroic selection by necessity will be non-ideally chosen for a single mirror to be able to deliver both the excitation and emission light. The filter solution in the imaging path was a *Di01-R488/561* dichroic mirror and a 25 nm wide *ZET473* notch filter centred at 473 nm was fitted in the imaging path. The dichroic has two stop-bands with high reflectivity, one below 499.0 nm and one between 549.5 and 576.0 nm (measured at 50% transmission, rounded to nearest half nanometre). Between 499.0 and 549.5 nm and from 576.0 nm and longer the mirror has very close to 100% transmission. For proper simultaneous imaging of the fluorescent proteins eGFP and mCherry, the proteins excitation bands must lie within the dichroic stop-bands and their emission bands must, at least in part, lie within its pass-bands. In Figure 4.6 the spectral layout of the excitation and emission bands of the fluorophores and the imaging dichroic is shown. Also shown are the two laser lines used for excitation. From the figure it is possible to see how the excitation lines unfortunately are not ideally situated. This was a trade-off coming down to practicalities such as the combined filter bank available and the lasers available. Nevertheless, excitation at the slightly short wavelength of 473 nm will still be absorbed at around 82% the rate of a laser trained at the absorption peak at 489 nm. A 488 nm line could possibly have been used, but was not available at the start of experimental work and for consistency, the line was kept. The longer, 561 nm line was harder to get around as the only single-line laser heads available at the time were 561 nm and lasers outside the necessary stop-band. The system was thus designed to accept the lower absorption at 561 nm as well (around 64% of the absorption at the peak at

587 nm). The emission peaks fall well within the pass-bands and a large portion of the eGFP emissions falls within the window between 499 and 549 nm and nearly all of the mCherry emissions are in the longer than 576 nm regime. Another thing that becomes obvious when viewing the spectra is that the eGFP has a long “tail” that stretches a bit into the mCherry emission peak, potentially introducing cross-talk between the two channels. In the practical work, this was never a significant problem. The alternating laser scheme that is introduced in detail in subsection 4.2 fully eliminates this issue. Any fluorescence in the red channel from species excited by the 473 nm line is disregarded as only the green channel is considered during 473 nm illumination (every other frame). The green channel is similarly disregarded during 561 nm illumination, and also the dichroic and emission filters hinder any cross-talk in the green channel from species excited by the 561 nm line.

4.1.3 The astigmatism module

Astigmatic imaging is a technique for super-resolving particles of sizes less than the diffraction limit introduced by H. Pin Kao and A. S. Verkman (Kao & Verkman 1994).

Astigmatic imaging result in a deformed image of the point spread function when imaging point sources. With the cylindrical lens in the imaging path the image of the point source comes to focus at two slightly different axial positions. An image without the asymmetric element will be an Airy disk with the width d given by Abbe’s $d = \frac{\lambda}{2 \cdot NA}$. The point spread function (PSF) is the transfer function that describes the optical system and will be the image itself when imaging a point source. The PSF can be written:

$$I(\rho) = \left[\frac{2J_1(\rho)}{\rho} \right]^2 \quad (19)$$

Where J_1 is a first order Bessel function (eq. 20).

$$J_1(\rho) = \frac{1}{2\pi} \int_{\tau=0}^{\pi} e^{-j(\tau - \rho \sin \tau)} d\tau \quad (20)$$

This image is rotationally symmetrical and has a prominent central peak containing most of the intensity with concentric rings around it with progressively less intensity. The centre peak can be closely modelled by a two-dimensional Gaussian and this is used when considering single molecule point sources.

With the cylindrical lens in the image path the image will show a slight deformation in either the x or y direction that is dependent on the offset from the focal plane. The deformation will manifest as an elongation along one axis for positive offsets and along the other for negative offsets. This is due to the fact that with the cylindrical lens one axis comes to focus at a slightly different plane than the other. The effect is that a new symmetry plane is created between the two actual focal planes, where the deformation is equal along both axes. The resulting image still resembles a 2D Gaussian, but with the major and minor axes carrying information about the axial position of the point source. See the simulated Gaussian in Figure 4.7 and Figure 4.8. By measuring the size of the axes on the

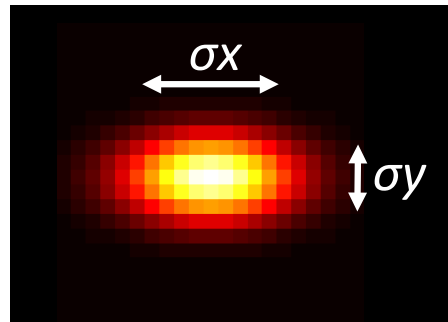


Figure 4.7 – A simulated two-dimensional Gaussian.

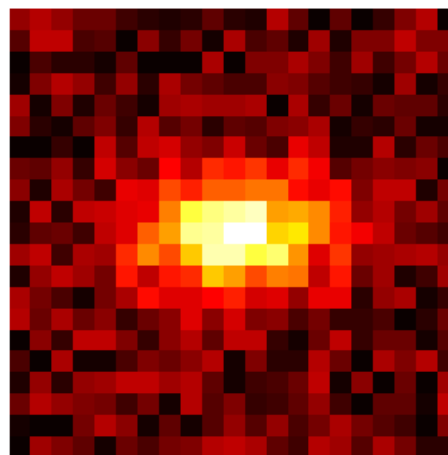


Figure 4.8 – The same simulated Gaussian as in figure 4.7 with overlaid noise

elliptical Gaussian and comparing them, z position can be decoded.

In some implementations of such a system the geometry of the imaging path includes a one-lens, $4f$ intermediate image translation. This method was described by Badieirostami et al. in a method review comparing astigmatism to the earlier mentioned DH-PSF and bi-plane methods (Badieirostami et al. 2010) and a similar geometry was used in an earlier iteration of the microscopy system as I have presented earlier in my thesis *A Fourdimensional Microscope for Single Molecule Studies in Living Cells Using Astigmatic Axial Resolution Enhancement* (Hedlund 2015). The geometry is shown in Figure 4.8 (image adapted from aforementioned thesis, used with the authors permission). The PSF deformation during defocussing along the two axes approximately follow a second-degree polynomial in either direction, slightly offset with the two curves overlapping at the symmetry point. The calibration of the system was done by fitting polynomials to measured shapes of fluorescent bead images in an image sequence of the beads being moved along the z-axis using the nano-piezo positioning stage. The process is described in-depth in (Hedlund 2015).

The astigmatic microscopy module is an asymmetric optical element, a cylindrical lens mounted in the emission path. The lens is mounted so that it can be flipped in and out of the imaging path, thus letting the microscope be used for standard non-astigmatic imaging as well. The Nikon microscope system is an infinity-corrected microscope, i.e. a point source at the sample will result in light focussed at a point located at infinity, meaning that the light will exit the objective lens as parallel beams (see Figure 4.3). After the objective lens, is the space called the *Tube*, which ends at the *Tube lens*. The Tube lens has a focal length of 200 mm, which is a standard used by Nikon. Also included in the tube section, is a flip-in optical component introducing a 1.5 times magnification. The optics of the flip-in component are not specified, which means that the internals of the microscope body has some “black-box” characteristics. However, this is not a big issue as the intermediate image plane location is retained and the optical system can be modelled as having a 1.5 times longer tube and tube lens focal length with the same intermediate image plane, i.e. the tube focal length will be

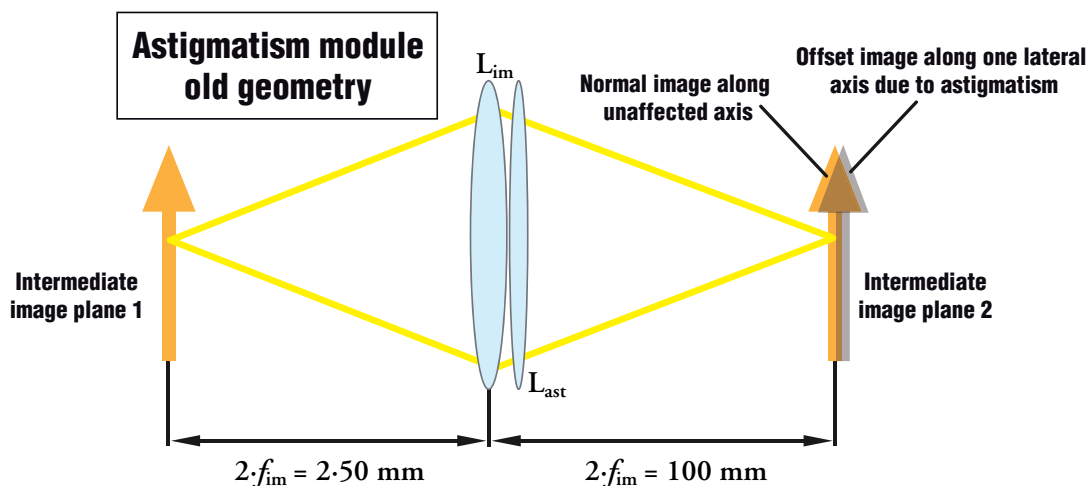


Figure 4.9 – The original astigmatism module geometry. Light path from left to right. Shown is the single 50 mm lens reforming the intermediate image in the intermediate image plane on the left-hand side at the one on the right-hand side. The cylindrical lens, L_{ast} , has a focal length of 1000 mm along one axis.

modelled as 300 mm. The astigmatic element will be inserted in the space outside the microscope body before the first intermediate image plane outside the body.

This method used a single 50 mm achromatic lens to reform the intermediate image just outside the imaging port of the microscope at the intermediate image plane of the colour splitter (see subsection 4.1.4). Next to this translation lens, the 1000 mm cylindrical lens could be inserted, providing the defocussing along one axis. The benefit of this was the use of a low power lens (implying less aberration) and the astigmatic element placed just next to an imaging element. The method worked well, but introduced excessive vignetting after the colour splitter, when working in splitting mode. Here vignetting refers to the unintended cropping of the field of view by the limitations of the optical components. The vignetting was not an issue while imaging single colour samples with the colour splitter in bypass mode. The image would have a slight circular cropping around the edges, but the ROI in the image centre would not be affected. See Figure 4.10.

With the colour splitter inserted unfortunately this resulted in a double arc cropping that could not be solved with a single lens imaging system. This cropping removed large portions of the useable image regions and a new design had to be developed.

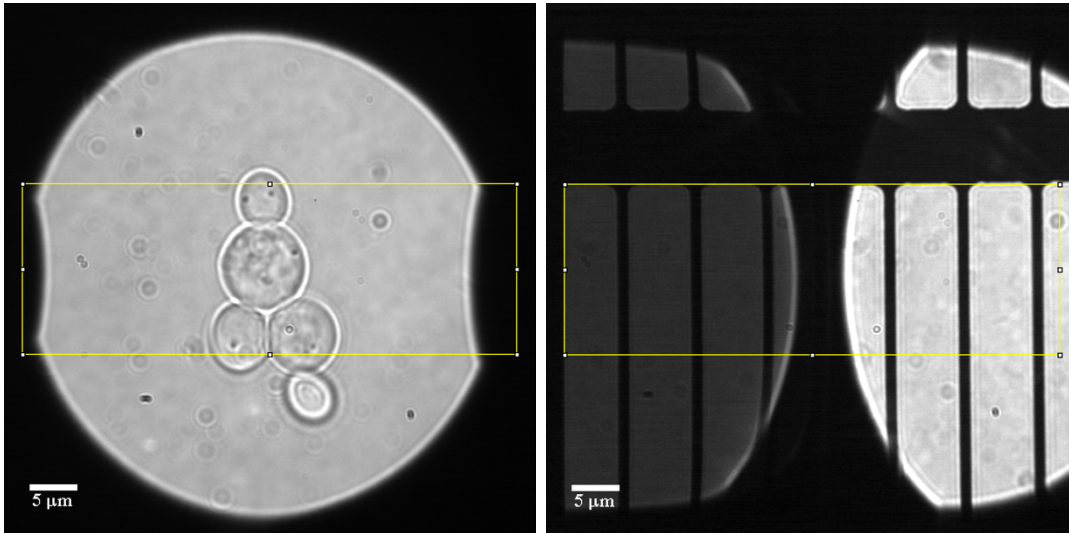


Figure 4.10 – Left, the vignetting of the original geometry without colour splitting (DV^2 in bypass mode). Image showing yeast cells. Right, the vignetting in colour split mode. The curved cropping is clear at the centre of the image. Image showing a calibration graticule. The yellow box is the standard region of interest (ROI, 476 by 164 pixels) used.

The solution developed during my work for this thesis, was to forego the additional imaging element (L_{im} in Figure 4.9) and place the first intermediate image plane after the tube lens directly at the colour splitters forward image plane. The position at which the image would normally be located if the DV^2 was directly mounted on the imaging port. This meant that the cylindrical element would have to be moved to a position not immediately adjacent an imaging element. The position available was right in front of the imaging port on the microscope, 15 mm from the body and 60 mm from the image plane in the colour splitter. The imaging element focussing on the DV^2 was now the tube lens and with the new position of the cylindrical lens, quite far from the imaging (tube) lens, it was necessary to change the focal length of the asymmetric element to get a comparable PSF deformation for the same offset in the axial direction. This geometry removed all the vignetting issues and this is the layout used henceforth. In the photograph in Figure 4.12, the colour splitter

is the blue tube and the astigmatic element is a 300 mm cylindrical lens on a flip mount next to the microscope body on the extreme left. The low-pass emission filter for the 561 nm laser with a cut-off at 500 nm is located just after the cylindrical lens and visible in the figures. In the detailed images in Figure 4.11 the mechanism used to switch between astigmatic and normal imaging is shown and the emission filter is clearly visible. A schematic of the new layout can be found in Figure 4.13.

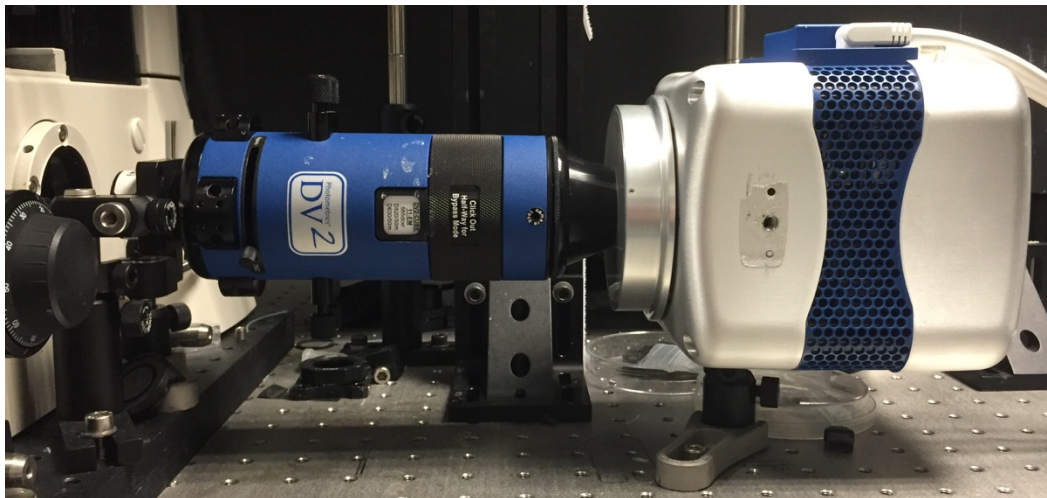


Figure 4.12– From left to right, the microscope body, cylindrical lens (flipped out), colour splitter, EMCCD camera.

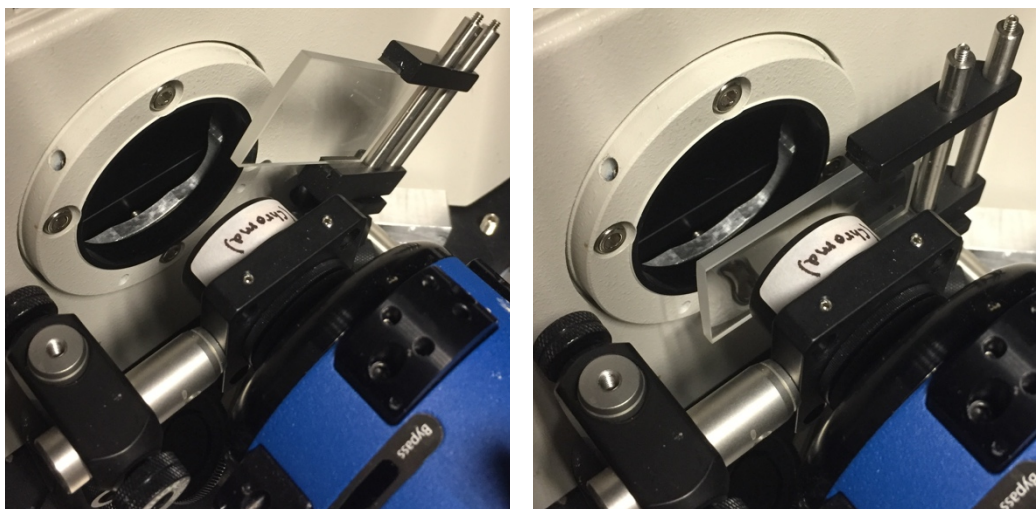


Figure 4.11 – Left astigmatism disengaged. Right astigmatism engaged. The filter is a low pass emission filter with a 500 nm cut-off dealing with possible back reflections from the 561 nm laser.

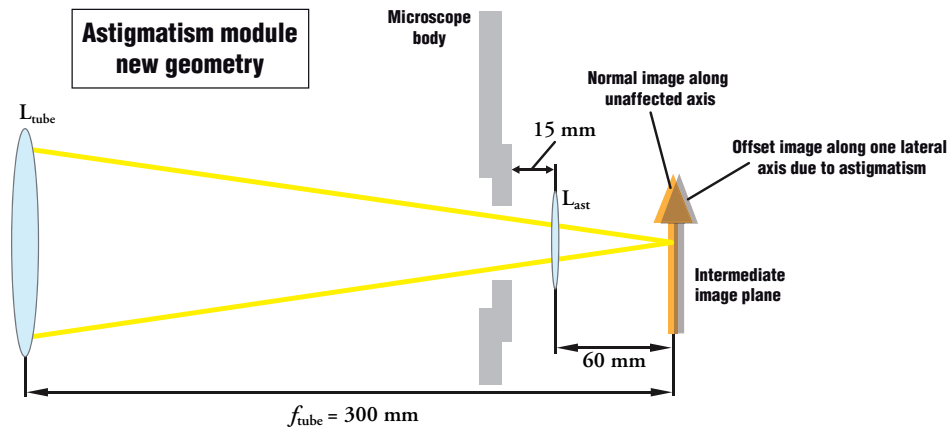


Figure 4.13 – The updated geometry as used in the work presented in this thesis. The colour splitter is to the right of the intermediate image plane. The intermediate plane is at the entrance to the colour splitter tube.

It is worth noting that even though the astigmatism module was implemented and characterised, eventually the system was not used in the data presented in this thesis. The deconvolution methods presented in chapter 5, provided the data sought and the astigmatism method was never used during these experiments.

4.1.4 Colour Splitter and Electron Multiplying CCD Camera

After the astigmatism module, the final module before the electron multiplying CCD (EMCCD) camera a commercial dual colour dichroic splitter was mounted. The splitter is a DV² module from Photometrics, who also supplied the EMCCD camera, an *Evolve Delta 512*. The splitter is contained in a 190 mm long tube with the dichroic mirror and emission filter sets mounted on a slide-in holder. A filter set using a 565dcsr dichroic mirror and a D520/30M emission filter in the short wavelength channel and a D630/50M in the long wavelength channel is used. In Figure 4.14 the spectral layout is shown. The emission filters transmission shown for reference in the figure are simplified versions showing only the centre wavelengths and their respective bandwidths. The filters are bespoke and are not available off the shelf.

The splitter is built around a 1:1 telescope with conjugate image planes just inside the entrance to the tube and just outside the exit. At this plane, the camera detector is placed.

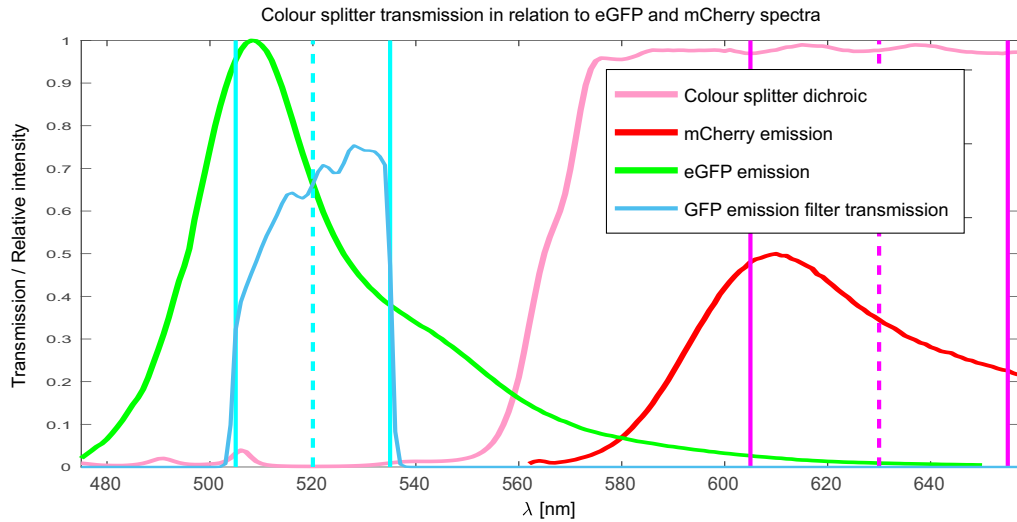


Figure 4.14 – The spectral layout of the colour splitter filter set used. The emission filters are shown simplified showing centre wavelength and bandwidth as cyan and magenta verticals. The transmission characteristics of the GFP emission filter has been included. Absorption, emission and transmission spectra from Chroma (<https://www.chroma.com/products/fluorochrome>).

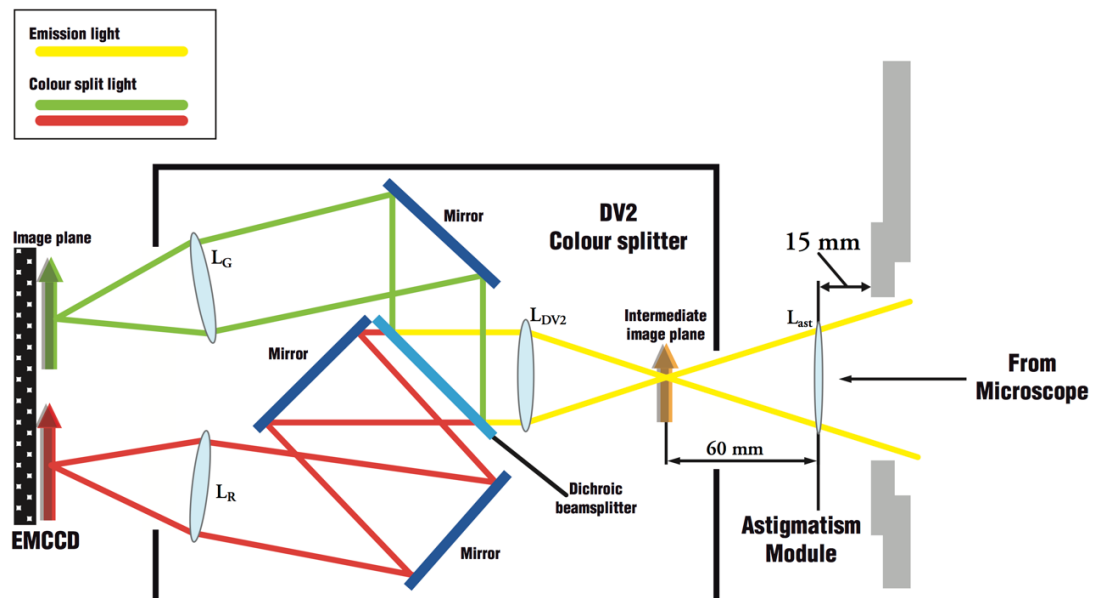


Figure 4.15 – A schematic representation of the optical paths in the DV² colour splitter

4.2 Controlling Software – The *CellBild* software suite

The requirements for image acquisition was that the system should be able to acquire at least 200 frames per second. 200 frames per second in order to be able to image 100 frames per second of either of the two colours when working in an alternating frame excitation mode. The main reporter fluorophores used in the research referenced here have been the red fluorescent protein, *mCherry* and the *Enhanced Green Fluorescent Protein* (eGFP). The specifics of the choice of these fluorophores are further elaborated in chapter 5. The two fluorophores are excited by a Vortran Stradus 561 nm laser (max 50 mW optical output) exciting *mCherry*, and Vortran Stradus 473 nm laser (max 80 mW optical output) exciting eGFP. Both lasers are linearly polarised (vertical). Both are controlled individually and can be used either alone or together. The blue excitation light from the 473 nm laser has some unintended side effects that adversely affects image acquisition in the red channel, so measures have to be taken to avoid these. Apart from exciting the eGFP, the blue light also excites a significant amount of autofluorescence in the red band selected by the dichroic and bandpass filters in the DV² colour splitter. The autofluorescence unfortunately is bright enough to drown the much dimmer emissions from the *mCherry* reporter to a point where it is impossible to extract useable data from the red channel. To remedy these issues, the decision was made to implement an alternating frame concept. By accepting an effective lower frame rate of 100 frames per second whilst retaining the 5 ms frame repetition rate, it was possible to implement an alternating frame laser excitation (Kapanidis et al. 2005)(AFLEX or ALEX, the latter acronym is more commonly used for this type of systems, but in the software suite “AFLEX” has been used) scheme where the sample was illuminated only every second frame by the 473 nm laser rather than continuously. This method allowed for every second frame to be analysed for GFP content and the

rest for mCherry content. This operation mode was accomplished incrementally and the initial step was to create software that could control both the camera and the lasers simultaneously.

The 473 nm laser had a directly available digital modulation provision. The laser output can be controlled by a TTL signal (0/+5 V). The laser emits when the TTL signal is high (+5V) and is dark when the signal is low (0 V). A 5 V TTL signal could easily be generated by using a counter on a Digital Acquisition (DAQ) card. A digital National Instruments card, model NI PCI-6602, was used. It has 8 counters, that can be individually controlled to either count incoming or generate outgoing pulses. The counter timing is by an 80 MHz joint time base, meaning that correctly set up, up to eight consecutive TTL controlled devices can be controlled with a minimum period of 12.5 ns. The time base oscillator is stable to within 50ppm (NI n.d.; NI 2009).

The initial implementation of an ALEX system was done using a continuously emitting 561 nm laser and a modulated 473 nm laser. In order to synchronise the imaging with the alternating laser illumination it is needed to control the camera as well with a series of trigger pulses that are synchronised with the laser control pulses. The DAQ card was controlled by software constructed in LabView. The original intention was to construct a fully contained software suite controlling all aspects of microscopy from sample positioning (precision positioning by the MCL nano-piezo stage), via laser control to image acquisition. Unfortunately, the third party API intended to provide LabView integration, allowing acquisition control of the camera had impractically large amounts of bugs and had lacking documentation. After initial development of a LabView based image capturing software created more problems than it solved, a new approach was needed. This prompted the use of the open-source alternative *μManager* (also styled *Micro-Manager*) for basic image collection and

camera initialisation (Edelstein et al. 2014). μ Manager supports the Evolve Delta-512 through the PVCAM driver. μ Manager also supports shutter solutions from Thorlabs, such as the SC10 shutter controller, two of which was used in the excitation module.

Thorlabs SH05 shutters were primarily used for beam path selection, but initially they were also for illumination timing control, a practice that was eventually abandoned as it proved that the actuation of the shutters introduced two major issues. When a mechanical SH05 shutter mounted to the optical table in any way opens, I measured vibrations that propagated through the optical table and introduced noticeable motion blur in the captured images for a duration of up to 3 frames (15 ms).

The second issue is the long actuation times being counted in the 10s of milliseconds. The shutter itself has a “Transfer Initialize” time of 8.0 ms, i.e. the time from applying the actuating voltage to the shutter blade starts moving. Next, the shutter has a “Transfer Open” time of 3.0 ms, this denotes the time it takes for the shutter to move from 20% to 80% open.

(<https://www.thorlabs.de/thorproduct.cfm?partnumber=SH05/M>)

Thus, the minimum time from application of a voltage to the shutter to the shutter being >80% open is >11 ms. To this should be added the, in these circumstances, negligible error introduced due to the accuracy of 200 μ s of the SC10 driver. Also adding to the delay is the latency of the serial interface (RS-232) if that is used as shutter trigger. It was further shown that due to the fairly long time it takes for the shutter blade to move past the beam, the first illuminated frame in an imaging sequence cannot be trusted to be fully open (the blade has fully opened the path for the beam) for the duration of the first or the second illuminated frame in any series. The beam diameter at the shutter is 3 mm and the shutters diameter is 12.7 mm (0.5”). As mentioned before the shutter takes 3 ms to move through 60% or 7.6 mm of the shutter

aperture. The conclusion is that the shutter blade will take: $3 \text{ ms} \cdot (3/7.6) = 1.2 \text{ ms}$ to traverse the beam. This is more than a fourth of a standard 4.7 ms exposure duration and it is longer than the readout allowance (300 μs , the time needed for the CCD to shift the acquired frame from the imaging sensor to the readout buffer) during a 5 ms frame period. So, not only were the actual laser exposure times for the initial two illuminated frames of any sequence unreliable (note that this is not counting the very first two frames of any sequence that are unreliable for other reasons, as covered in the section covering the camera specifics, but with some fine-tuning of the timing they could be made to coincide with the shutter opening), but also several frames were disturbed by the vibrations the shutter action couples to the table. A bespoke scaffolding solution where the shutter was entirely decoupled from the table was designed and built. The scaffold was a separate floor stand with an arm holding the shutter in place from above. This solution ended up being short-lived as a method of modulating the 561 nm laser electronically was found and subsequently all experimental shuttering was done electronically, though the mechanical shutters had to be left in place in order to allow beam path selection (epi-fluorescence or FRAP path).

The early iterations of the software used a simple two-counter solution with one counter output controlling the laser and the other counter, timed at double the frequency of the laser counter but with a short duty cycle, acting as a camera trigger. The camera was set to what is known as “*Strobe mode*” in Photometrics vernacular, meaning that the camera will enter an idle state and wait for TTL pulses on the trigger pin (pin 1) on the camera I/O port. Once pin 1 receive a high (+5 V) signal it will expose one frame and re-enter the idle state and once readout and resetting is done it will respond to the next raising flank on the trigger pin. So, as long as an exposure plus

reset time kept within the frame period the frame rate would be consistent. The reset time required is not well documented and depends on the frame cropping (the region of interest, ROI). In order to attain 200 frames per second (5 ms frame period) it is necessary to crop the frame to a region no larger than 476 by 164 pixels and allow no less than 290 μ s reset time. The readout time and maximum ROI size is imposed by the camera CCD hardware. A narrower field can be shifted into the readout buffer faster and the maximum framerate is mainly determined by the width in the fast (shifting) direction and a maximum of 164 pixels can be used. There is also a minor dependency on the width in the slow direction, and hence the full 512-pixel width of the sensor cannot be used and the width in this direction is limited to 476 pixels. It turns out that 290 μ s in this case is at the very edge of what is possible to use, so in the experiments conducted the exposure time was set to 4.7 ms allowing a full 300 μ s reset time. It is possible to use I/O pin 6 that goes high once the camera is ready to be triggered to dynamically sense when the camera is ready and trigger immediately. This is done when internal triggering is performed, allowing slightly longer exposure times while still retaining the frame rate. However, this would have complicated the laser control system that will be described further on.

The first versions of the control software, using only the two counters triggering the camera and controlling the blue laser were not perfectly synchronised, due to the way it was initialised in software. The software latency could result in several hundred microsecond discrepancies between actual starting points of the two pulse trains. This proved largely unproblematic due to the reset time mentioned before. It turned out the discrepancy between the starting times was fairly consistent but occasionally it was larger. This was entirely down to computer scheduling as could be shown by stopping

the software and restarting it, which usually (but not always) resulted in reverting to another delay.

To combat this issue an internal triggering approach on the DAQ card was first introduced. μ Manager was set up to provide a shutter event on a digital out pin on the DAQ card. The pins can be internally routed to trigger the start of one or multiple counters. This allowed the two counters to be perfectly synchronised. This also allowed the introduction of a third counter controlling the 561 nm laser at a 5 ms offset. Thus, a true alternating laser system could be built. The synchronisation issue thus having been solved and the two lasers emissions now being individually controlled, the only remaining issue was the shuttering. The next step was to introduce full electronic control of the imaging cycle.

Eventually, for the final iterations of the synchronisation modules, a multi-layered trigger approach was taken, in which no software triggering was performed at

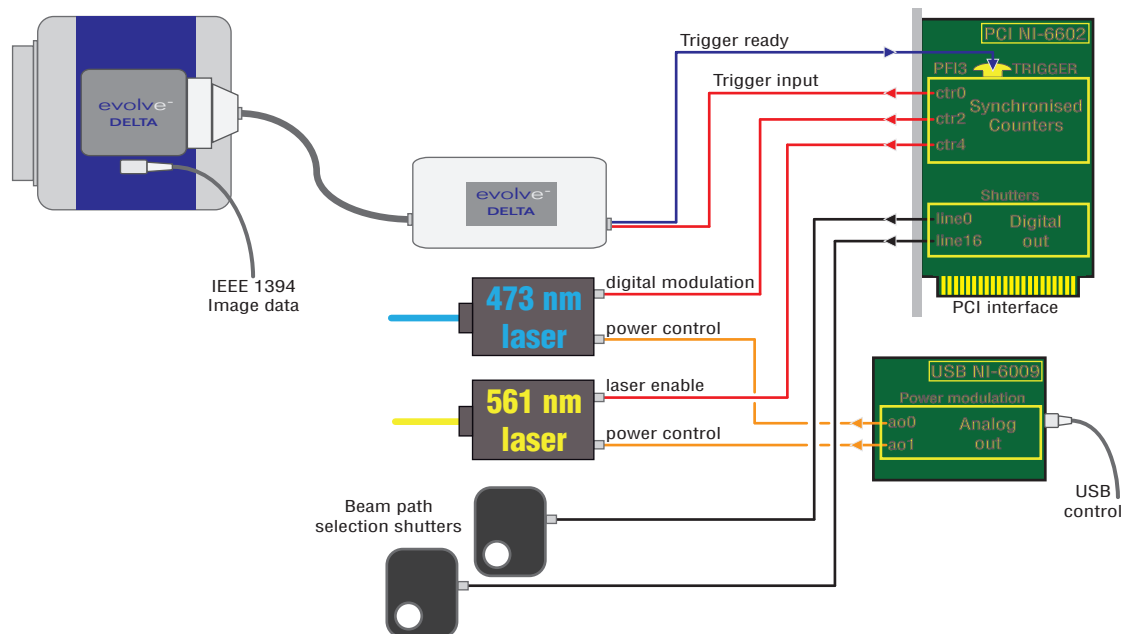


Figure 4.16 – Physical control lines and data collection layout. The *Trigger ready* line hardware triggers the DAQ card counters internally on the card and is unaffected by software latencies once an acquisition is started.

all. When starting an acquisition sequence, the camera would simply be put into the idle state in the strobe mode, in which it would remain for a set time before throwing a timeout exception if it did not receive a trigger pulse. Then the aforementioned pin 6 goes high when the camera is ready to acquire and this signal is routed back to a digital in pin on the DAQ card which is again internally routed to trigger the counters. See Figure 4.16 for the physical layout of signal routing and Figure 4.17 for pulse synchronisation.

Thus, all components can be synchronised, the lasers can be set to illuminate a precise number of frames, and the exact frame where either laser should for the first

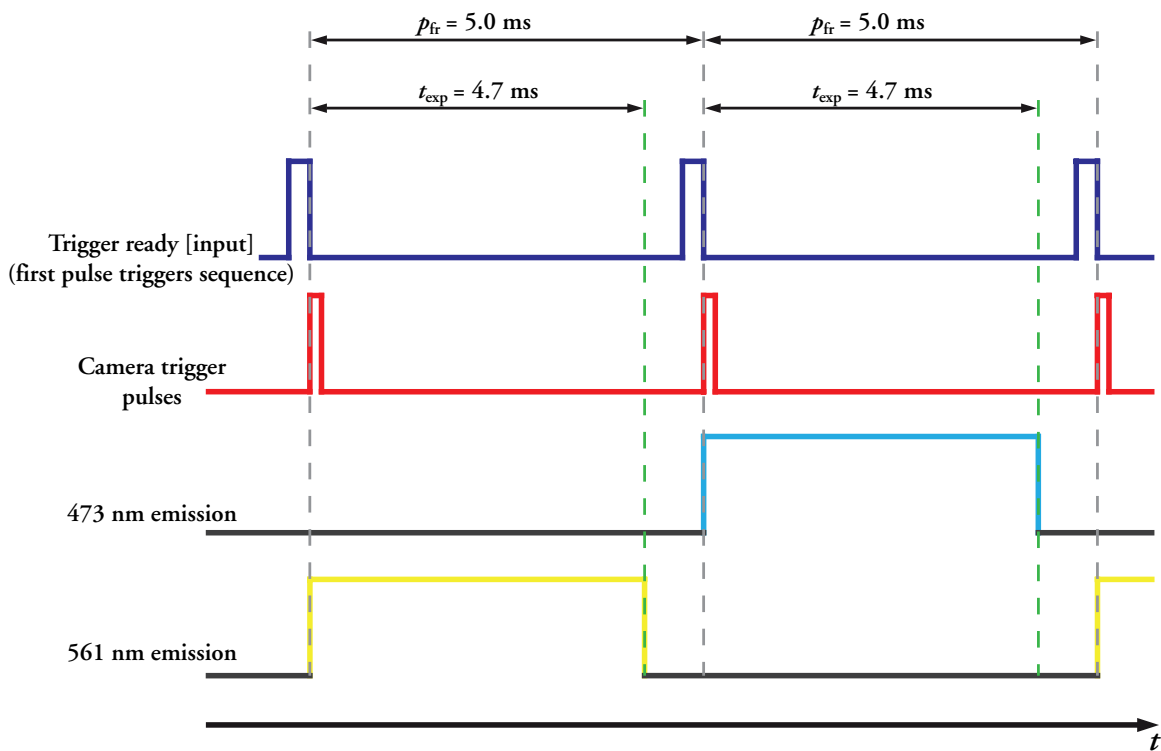


Figure 4.17 – Pulse synchronisation. Shown here is one period of a sequence with more than two frames to be acquired. All output pulses (the three bottom pulse trains) are synchronised to the first *Trigger ready* positive flank (not shown in this figure). The laser duty cycle is adjusted to correspond to the camera exposure time. In most situations described in this thesis, an exposure time of 4.7 ms was used.

time illuminate, can be set explicitly. The normal designation would be to specify frame 3, the first well defined frame. Something worth noting is that due to the internal hardware implementation of the camera, the first two frames in any sequence taken will not be consistent with regards to exposure times and readout values, and will have to be discarded. This will be especially important to remember when acquiring bursts of frames with long waits in between the frames as described in chapter 5.4 – an

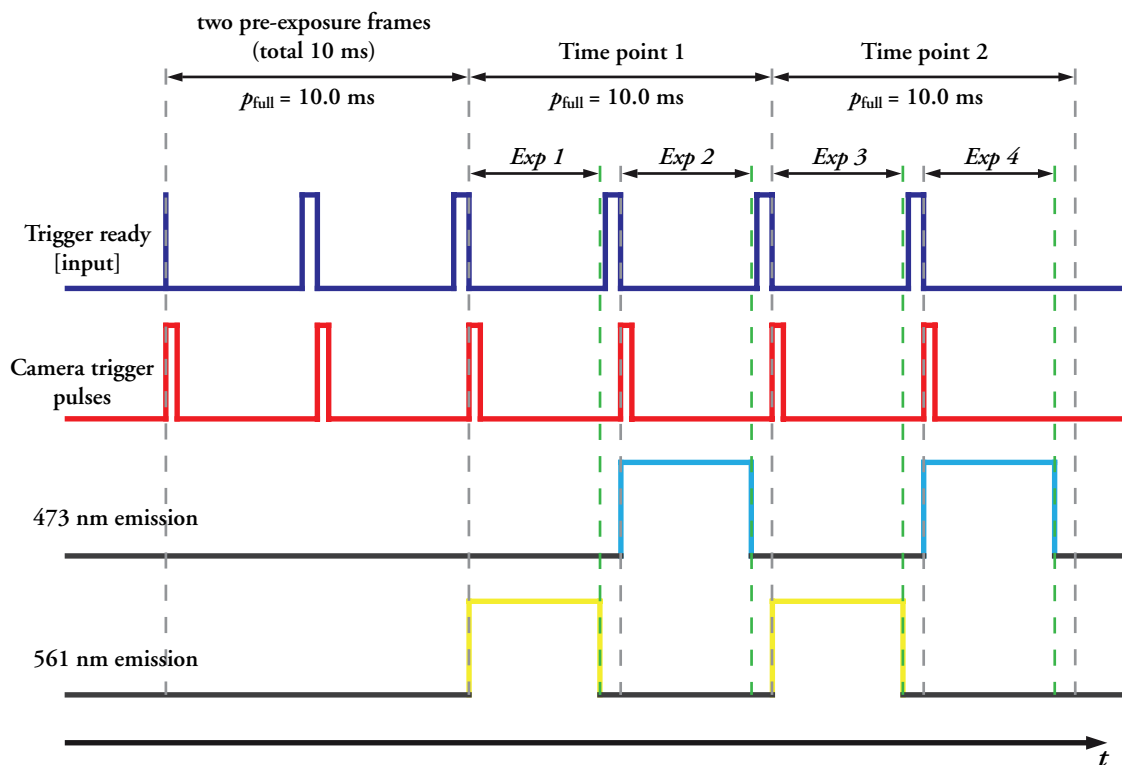


Figure 4.18 – A full sequence of two time points, i.e. two frames each of 473 nm and 561 nm exposure. The initial two dark frames needed to avoid the inconsistencies in camera behaviour during the first two frames of any image sequence. Shown here is the *minimal number* of trigger pulses required. In normal operation, this is generally padded with extra trigger pulses, this simplifies acquisitions of slightly longer bright field sequences and avoids the possibility of a camera timing out due to a lost final frame never getting triggered. This can be safely added as trigger pulses are ignored if the *Trigger ready* is low, i.e. the camera is not set to acquire any images.

additional two frames should always be prepended the actual burst and the lasers should normally wait for the first valid frame (frame 3 of the burst).

At this point the alternating laser control had reached maturity and the synchronisation subsystem was retained for future versions of the software. A user interface was built to provide primarily the two main modes of operation – Finite pulse sequences for fluorescence experiments and continuous trigger pulses for focussing and brightfield acquisitions.

These two primary front panels are shown in Figure 4.19 and 4.20. In the *Finite sequences* panel the frame number selections and the fine-tuning of starting points is done. Selection of the *Continuous camera triggering* pane automatically starts the trigger pulse train at selected frame rate.

Additional features that proved necessary or just useful were simultaneously introduced. Control of the mechanical shutters for beam path selection was introduced early on and relied on digital outputs from the DAQ card being used on the external trigger input on the two SC10 shutter drivers. The lasers can also be controlled at any point to emit continuously or pulsed, either alternating or simultaneously, duty cycles individually adjustable.

Two methods of controlling laser power delivered to a sample were implemented. The first uses a ratio based method where the light dose is determined by the duty cycle of the laser. This is achieved by reducing the duty cycle by a set ratio (e.g. $\frac{1}{2}$ or $\frac{1}{10}$) from the original setting. E.g. if the laser is set to a standard duty cycle of 50%, a $\frac{1}{10}$ reduction, effectively a virtual ND1 filter, would result in a 5% duty cycle with attenuation selected. However, this method is not ideal, as the exposure time for an attenuated frame will still be the same as for an unattenuated frame. This means that for most of the exposure, the camera will not collect anything but background.

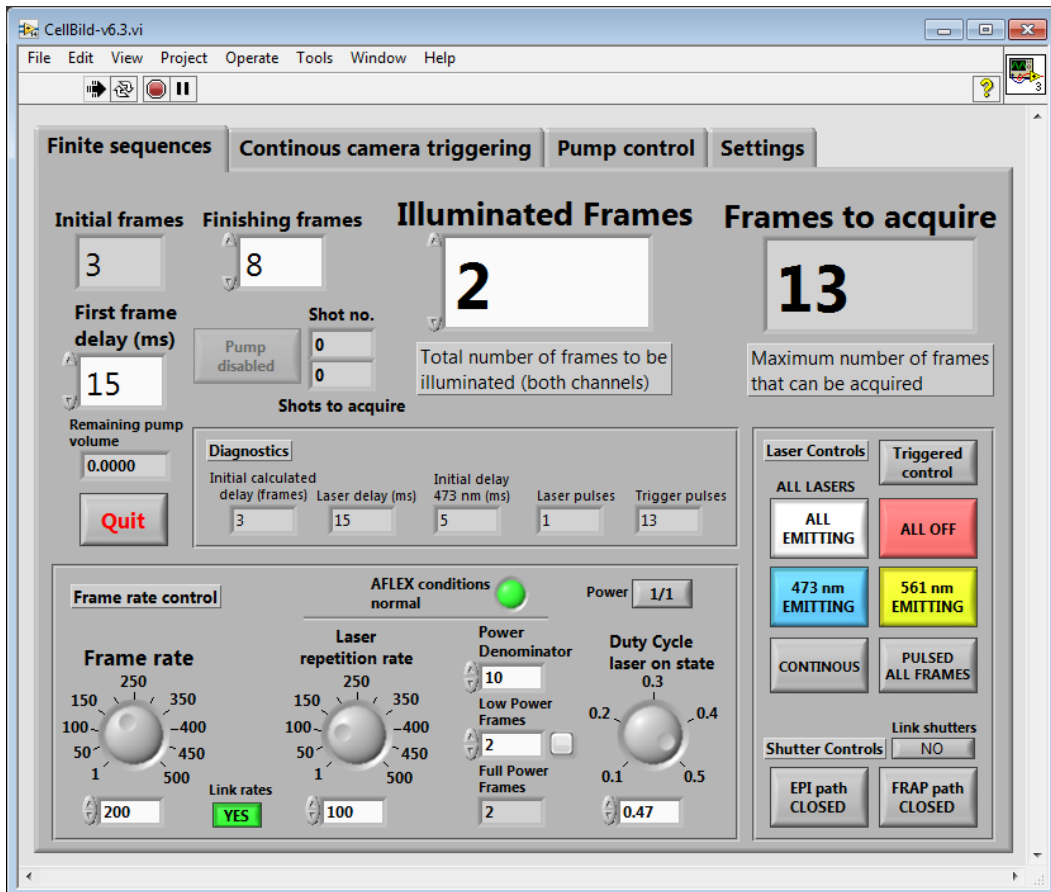


Figure 4.19 – The main software user interface. Here shown in the start-up window. On this pane, details of the experimental setup are entered. The white boxes are input fields and the grey boxes are indicator fields. The total number of Illuminated Frames entered is counting all frames from both lasers when running in A(F)LEX mode. Divide this by two to get the number of frames by laser wavelength. Note that this value is only fully tested and verified using even numbers (minimum one flash per laser). Other fields of importance are the framerate and laser pulse repetition rate fields. If the Link rates button is actuated, the laser repetition rate will be half the framerate for ALEX operation. The duty cycle of the laser can be adjusted (duty cycles of >50% will be flagged as incompatible with ALEX). The laser power can be attenuated electronically with the Power Denominator when the Power button is pressed.

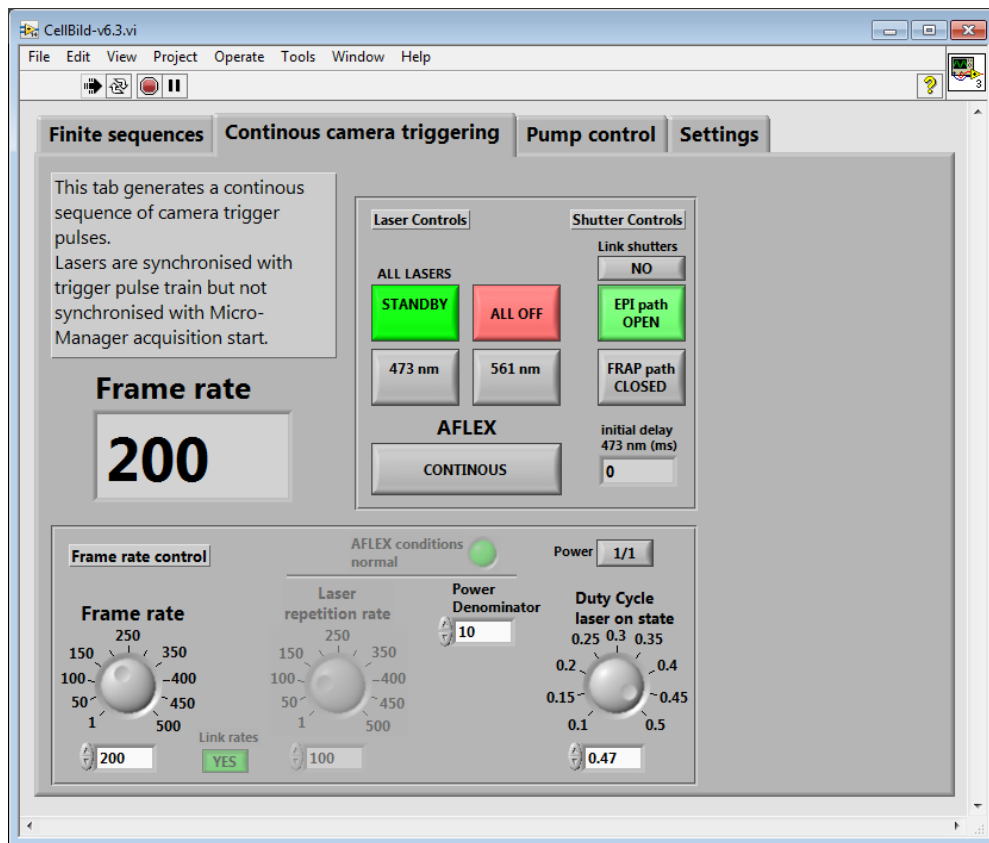


Figure 4.20– The pane for continuous imaging. When this panel is selected, an uninterrupted trigger pulses train is started. The frame rate (pulse frequency) can be selected on the fly. The laser controls can also be operated from here. The lasers will be working in CW mode by default here unless otherwise selected with the *AFLEX* toggle.

The second method implemented provides true power modulation, made possible by a secondary DAQ card that can output an analogue voltage, 0 to 5 V with 12-bit accuracy. The secondary DAQ card is a USB controlled National Instruments NI USB-6009. As no experiments that were performed needed any prompt and synchronised power modulation on a frame-to-frame basis the latency introduced by the USB interface can be disregarded. The lasers external power control interfaces are proportional voltage controls. The laser output power is controlled by applying a

voltage from minimum 0 V, corresponding to minimum laser power out, to +5 V, corresponding to max power out.

The response over this range is proportional over the full range (with very minor non-linearity close to the max and min voltages). To calibrate the laser output power, the max output power measured by an external Thorlabs power meter was set to be at the highest voltage available that produced a correctly attenuated output when the dialled in voltage was respectively, halved or reduced by 90%. The resulting voltages was selected as max values for full range operation and entered on the *Settings* pane on which there is an option to select between the duty cycle attenuation mode and the true power modulation mode. The calibrated power levels can be found in Table 4.1.

Table 4.1 – Voltage calibration for laser power modulation – laser head output power.

Laser	Level at max	Laser power out (full range)	Laser power out (attenuation: 1/2)	Laser power out (attenuation: 1/10)
561 nm	4.25 V	36.3 mW	18.2 mW	3.7 mW
473 nm	4.22 V	59.7 mW	30.0 mW	6.2 mW

The power levels were chosen so that the power delivered to the sample would be equal. The levels in Table 4.1 translated to power densities of 2.96 kW/cm² for the 561 nm laser and 2.75 kW/cm² for the 473 nm laser.

The final main panel of the user interface is the settings pane, see figure 4.21. The duty cycle of the trigger pulses is specified here as well as the selection of laser attenuation/power control mode and calibrated voltage values if the proportional (“External”) mode of attenuation control is selected. Of particular importance is the selection of the correct “Trigger ready source”, this must be set to correspond to the DAQ pin that receives the sequence start signal. It should either be the pin (physically)

connected to the cameras “Trigger ready” line or the pin internally routed to receive a triggering signal from μ Managers shutter control. μ Manager can be made to operate a digital line on a DAQ card as shutter control, this can be used to trigger the counters on the DAQ card instead of physically actuating a shutter. This mode of operation was abandoned when the “Trigger ready” pin was connected to and directly sensed by the DAQ card.

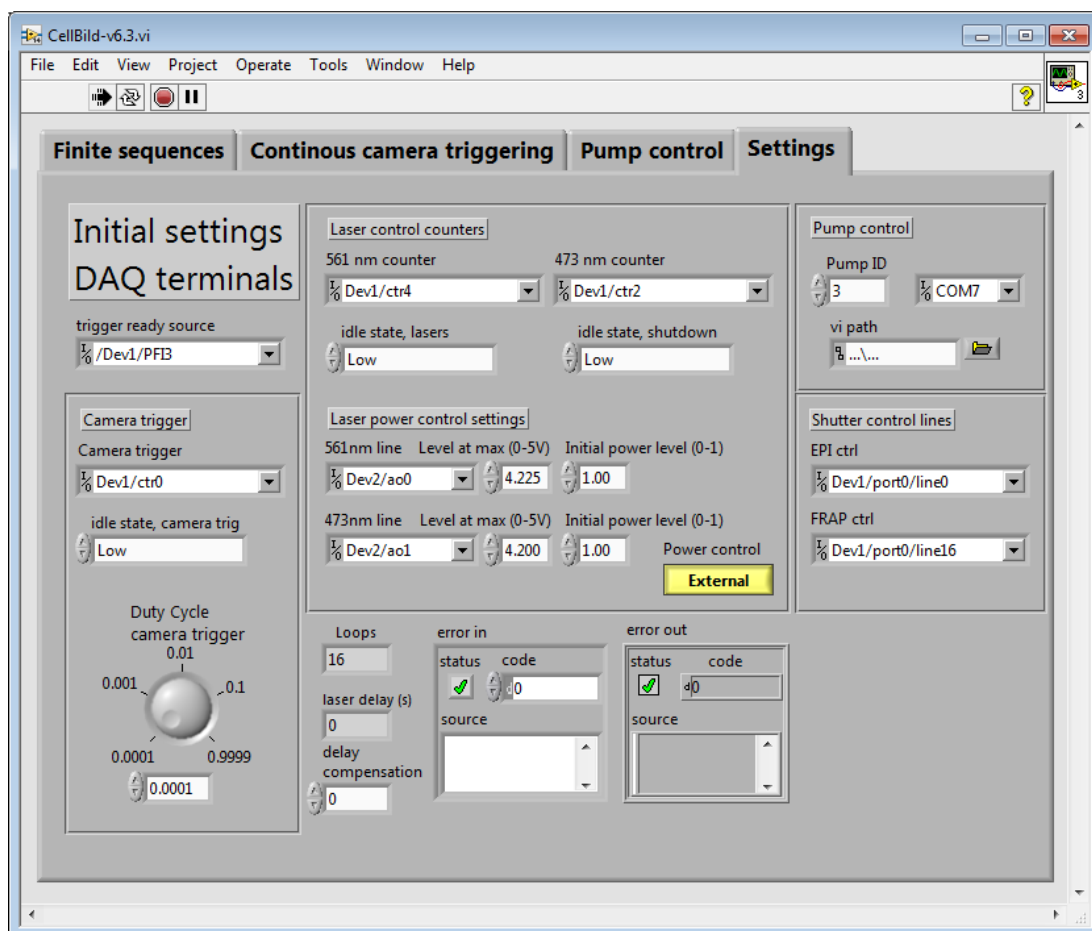


Figure 4.21– Settings pane. Here all references to DAQ input/output/counters are specified along with certain other settings required. Most of these settings can be set once and left in that state unless the hardware changes.

The settings as shown in figure 4.21 are set up for three counter outputs, one for camera trigger (Dev1/ctr0) and two for laser control (Dev1/ctr2,4), two TTL channels for shutter control (Dev1/port0/line0,16)), two analogue voltage channels for laser power control (Dev2/ao0,1) and one digital input for trigger sensing (Dev1/PFI3).

The setting also present in the upper right corner on this pane are the settings for pump control. The most recent iterations of the software include the ability to control a syringe pump from the CellBild suite and synchronise the pump action with finite image sequences. The pump is controlled by a serial interface through a USB to RS-485 converter and the corresponding device name needs to be entered. The COM-port when the software is used on a Windows system, substitute with the corresponding device path if used on other systems. The communication with the pump is via a standard VISA clear text protocol with a very simple syntax: [pumpID]V[Speed]. The number before the 'V', the pump id is a number identifying the pump, as several pumps of this model can be daisy-chained and the serial commands are then fed through to all pumps and the id is used to identify which pump in a chain should react to the command. The number after the 'V' is the desired pump speed. This is the only recognised command. The way to stop the pump is to issue the command "3V0" (using the pump id 3 as is the case with the pump used here).

A real world example is that if the pump with id 3 should infuse at 10 $\mu\text{l}/\text{min}$ using a standard 1 ml syringe the command would be "3V-4397". Note that infusion means negative direction of the pump motor. The actual value needed at this point depends on the infusion rate and the syringe geometry, specifically the barrel inner diameter. A library of various syringes may be needed if syringes of different sizes or from different makers and distributors are used in order to accurately calculate the correct speed needed.

Pump control is managed from the fourth pane of the main interface, shown in figure 4.22. On this pane experiments requiring environment change are programmed. In the rightmost box, the volumetric flow rate is entered. The size of the syringe used must be chosen from a drop-down menu with a library of a few commonly used syringe sizes. Also included in this box is a safety feature that prevents overrunning the pump capacity. The pump does not have built-in interlocks to stop it at the endpoints. So, to prevent the motor from running the plunger block into the end stops, potentially damaging the equipment, it is important to set a limit to the deliverable volume. This can be manually set but it is automatically updated when the manual controls are used. The manual controls can be accessed by the button in the leftmost box. The enable button in the same box enables the pump enable *button* on the Finite sequences pane. This extra enable button was included to avoid unintended effects arising from the accidental activation of pump sequences when acquiring finite sequences without the intent to use pumped environment.

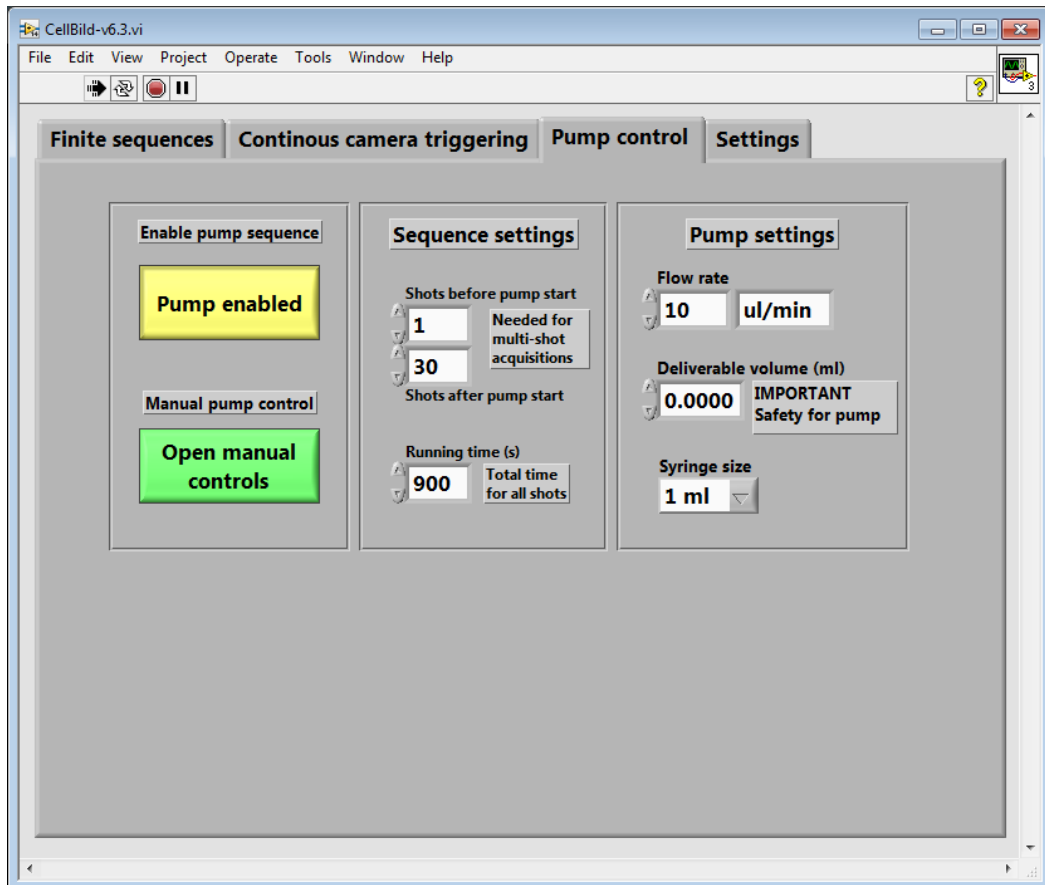


Figure 4.22 – The pump control pane. Flow rate and sequence setup is done from the middle and right hand boxes. Note that the total running time for a pumped sequence must be dialled in explicitly.

A sequence is programmed as two numbers: how many frame bursts should be acquired before the pump is started, and how many should be acquired after the pump is started (i.e. in the alternate environment). The total running time of the pump must be explicitly set and should span all time-points to be acquired in the pumped environment.

The *Open manual controls* button starts a modal pump control window. From this window, the pump can be controlled in order to perform tasks such as filling a syringe, wetting microfluidics channels or feed-tubes and similar tasks. The volume difference in the syringe due to actions performed with the manual controls updates

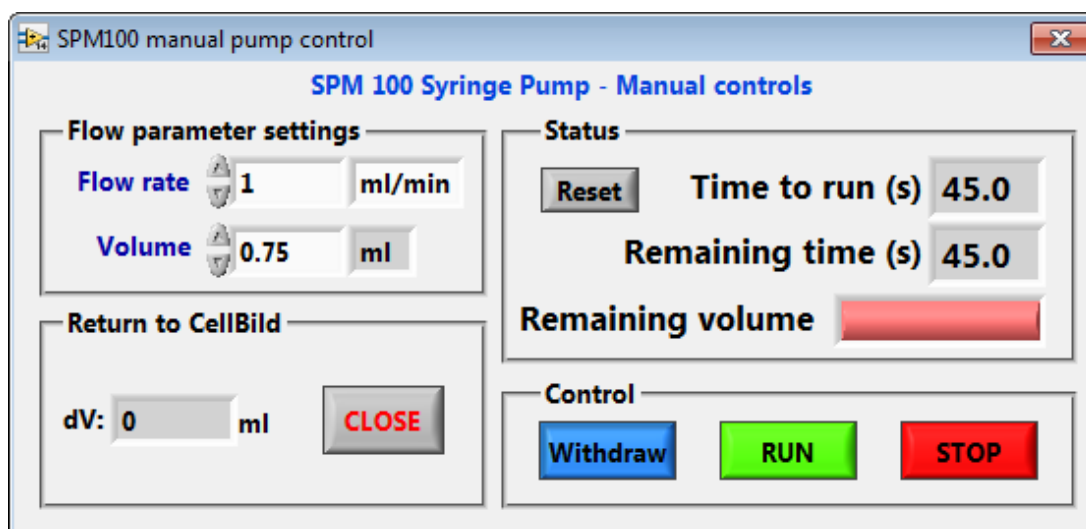


Figure 4.23 – Manual pump controls. This interface gives full control over the pump and volumes are translated into running times at selected flow rate. Note that the syringe size cannot be selected here. The syringe size will be whatever was chosen in the main pump control pane.

the *Deliverable volume* field in the Pump control pane upon closing of the manual control window.

The pump sequences will be run if the *Pump enabled* button on the Finite sequences pane is activated. When a sequence run is activated, CellBild will allow the number of camera activations (frame bursts) specified in “*Shots before pump start*” to be run before activating the pump. After pump activation the number of frame bursts are counted and when the number specified in “*Shots after pump start*” is reached the main interface is reset and readied for new sequences. The pump enable button needs to be activated in advance of every sequence start. The counter is not automatically reset if a pump sequence is aborted early, either manually or due to the pump reaching the end stop (as specified by the *Deliverable volume*), and a double actuation of the enable pump button is required to reset the sequence if desired. A corresponding sequence must be set up in the data acquisition software, which could be e.g. μ Manager as in all experiments reported here. During pump activation, a modal window (see

figure 4.24) is started with a countdown to pump deactivation. This window counts down from the time specified in the *Running time* field on the *Pump control* pane in the main interface, or from a time calculated to prevent the pump from overrunning the deliverable volume in the event the remaining volume in the syringe is not enough for a full sequence.

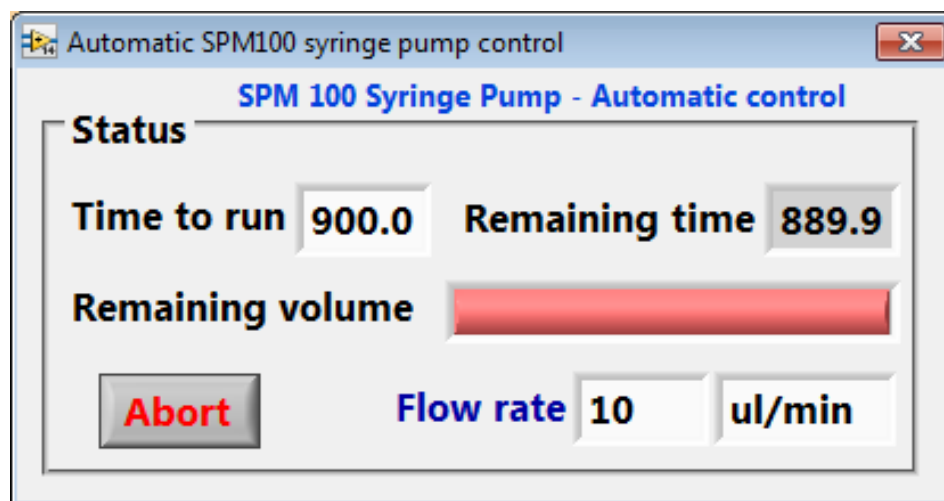


Figure 4.24 – The automatic pump sequence control interface. The only user control here is the *Abort* button.

In addition to the main CellBild software a separate LabVIEW VI, see figure 4.25 was constructed to control the nano-piezo positioning stage. The stage can be moved within a $300^3 \mu\text{m}^3$ box with nanometre precision (Mad City Labs: <http://www.madcitylabs.com/nanolpseries.html>), and it is used for fine-tuning of the samples lateral position and focus. This VI is not a part of the main CellBild application, but is run as a separate entity. This arrangement has the additional benefit of modal pop-ups, like the automatic pump control, will not be blocking access to the stage control interface.

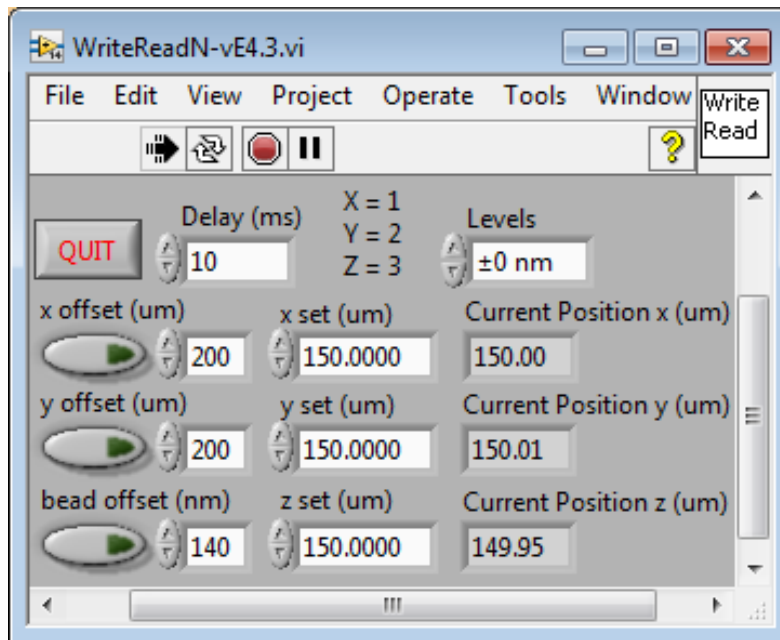


Figure 4.25 – The Mad City Labs nano-piezo stage control interface. Predefined adjustable offsets activated by button clicks are available on all axes.

LabVIEW source code for several crucial components are listed in appendix A and the full source code is also available for download from Sourceforge at:

<https://sourceforge.net/projects/york-biophysics/files/CellBild/>

5 Experimental procedures and results

One of the key goals in my project has been to monitor signal transduction in *Saccharomyces cerevisiae* in real time and at a single-molecule precision level. This is a challenging task. The approach has been to use optical fluorescence microscopy as described in chapter 4 combined with genetically integrated reporter proteins bound to signalling proteins of interest. Two reporter strategies were used during the investigations presented here:

1. Single tagged dynamic protein (Mig1) with eGFP reporter and a dedicated nuclear reporter: NRD1-mCherry to infer the position of the nuclear envelope directly.
2. Dual tagged dynamic proteins with eGFP and mCherry reporters. with the eGFP acting as a nuclear reporter. With the position of the nuclear envelope being inferred directly from the eGFP fluorescence signal.

The first approach was initially used to confirm the behaviour of Mig1 localisation at a given steady state environment and correlate this with the nuclear position. Further on, it was used to follow the dynamic translocation of Mig1 molecules to and from the nucleus as the environmental conditions were changed during microfluidics experiments.

Nrd1 is an RNA polymerase component that is only present in any significant abundance in the cell nucleus, with a copy number of around 2000 molecules (Adam J. M. Wollman & Leake 2015). An mCherry tag was genetically attached to functional Nrd1 and could be used as a standard for nuclear location during imaging as it does not leave the nucleus. Due to its high abundance the nuclear location can be followed even during experiments with longer duration. Despite the lower photo-stability of mCherry compared to eGFP (Shaner et al. 2005; Shaner et al. 2007) the large number

of available fluorophores allow for a clear tracking for the duration of any experiment conducted and described here.

The second approach could be used once it had been shown that the Mig1 content in a yeast cell is so clearly localised to the nucleus in a glucose rich environment that it is possible to use Mig1-eGFP localisation as a reporter for nuclear position under these conditions. This approach to nuclear localisation could of course only be used in steady state experiments at glucose rich conditions so it was a secondary method only for such experiments, but for dynamic experiments the method proved ideal.

5.1 Preparation of cells for examination

The purpose of the project has been to investigate the translocation of certain transcription factors and upstream kinases involved in yeast response to variations in environmental glucose concentration. For this end, several mutant strains incorporating fluorescent protein tags on the proteins being investigated, have been developed to allow specificity in fluorescence microscopy.

The development of all mutants was made by the ISOLATE partners at Göteborgs universitet in Gothenburg, Sweden, many of them were created by Sviatlana Shashkova. The procedure of procuring cells was to have the mutants produced in Gothenburg and a plate culture shipped to us on YPD-agar plates (see appendix D for formulae of various solid and liquid media used). To produce fresh and viable cells for examination these plates were then used to create a base stock to be stored at a temperature of -80°C and subsequent cultures for examination were either set from cells taken directly from the frozen stock or from fresh YPD-agar plates streaked and grown from the frozen stock or, in the case of recent arrival of new plates, streaks taken directly from the transported plate.

The overarching purpose of all the steps described here is to have as uniform a distribution of viable cells as possible. *Saccharomyces cerevisiae* has a doubling time of somewhere in the region of 1.5 to 2 hours (Marks 2011) in a rich medium such as YPD.

From the received plates, an overnight culture was grown in YPD, 2% glucose, and cells from this culture were separated from the overnight medium by centrifugation at 3000-3500 rpm for 50 s and washed by resuspension in fresh YPD and the centrifugation repeated. The pellet after the second spin is then resuspended in

YP (without glucose) with added glycerol for a final concentration of 20% glycerol and then immediately frozen to 80°C for storage.

Cells for investigations can be prepared in a few different ways but the method used for the experiments presented in this thesis were all grown according to the following protocol (unless otherwise stated) for consistency.

Sterile YNB minimal medium with 4% glucose was prepared in 2 ml aliquots in 15 ml Falcon tubes. A scraping was made by a sterile pipette tip of the frozen stock required and the scraping was placed in the YNB prepared and left in a shaker at 30°C overnight (normal incubation time 12-15 hours). The culture is grown to a density high enough to easily generate roughly 2-3 bound cells per 338 μm^2 (equivalent to the area of the imaged region of interest) in the microfluidic channel. Cell cultures were grown from a small number of initial cells in a relatively glucose rich environment. The conditions were such that the cells did not deplete the growth media of glucose during overnight incubation. After 12-15 hours, the cells are separated from the overnight medium by centrifugation at 3000-3500 rpm for 50 s and then washed in the same manner as described before in fresh YNB at the glucose concentration (and other conditions) intended for the actual investigation. If the investigation is to be conducted at either continuous or initial low glucose conditions, the cells were allowed to acclimatise to the new environment normally for about one hour, comparable to the time it takes to prepare a microfluidics chip for use (for chip preparation protocol, see chapter 3.2).

5.2 Image processing for localising cell and nuclear membrane

The imaging was done using alternating frame excitation (ALEX, see chapter 4) to avoid the excessive red channel autofluorescence excited by the 473 nm laser. The implementation is further elaborated in chapter 4.2 and in appendix A. The resulting image sequences were initially cropped to a square 100 x 100 pixels, equivalent to a 9.3 by 9.3 μm , region of interest (ROI) at the sample plane, aligned to the centre of the laser excitation field. 2-4 yeast cells could fit within this region of interest and a suitable cell group was selected and positioned during sequence setup.

To determine the tagged transcription factor abundance “compartment by compartment” for each cell, it is necessary to find the location of the nuclear envelope and the cell membrane. To find the compartments is a multi-step procedure. The cell membrane position is determined first using binary masking based on a threshold selected to include all intended fluorescence and autofluorescence in one of the image channels (usually the green channel as used in most of the experiments described in this thesis, but there are no reasons in principle why the red channel could not be used). At this point the only objective is to determine the boundaries of the cells and their respective nuclei. A method that gives a reasonable starting point for determining a suitable threshold to find the cell envelope is to take the full width at half maximum of a histogram of the natural logarithm of intensity distribution of the pixels in the ROI. For many cells this value could be used directly, but many ROIs had to be manually adjusted.

The image is first converted to a binary image with the determined threshold deciding which pixels are allocated ‘1’ and ‘0’ respectively. To avoid small spots of the “wrong” value within the segmented regions, first the “holes”, i.e. dark (‘0’) pixels surrounded by light (‘1’) pixels in the image are filled in using the MATLAB `imfill`

function. Next, the image is morphologically opened by the MATLAB `imopen` function. The opening function itself performs two operations, first it erodes the image and then it dilates it again using the same structuring element. The element used here is a disk with a radius of 4 pixels. This removes objects smaller than the disk and the result is a binary image without stray zeroes among ones and vice versa.

This procedure is followed twice during the segmentation, once to find the cell membranes, and once to find the nuclear envelopes.

In Figure 5.2 a boundary of the cells in the ROI has been found using this method and is represented by the green outline.

The next step is to determine the nuclear envelope. The same masking procedure is followed with a suitable threshold at a timepoint, frame and channel selected to show either a dedicated nuclear reporter (e.g. Nrd1-mCherry that was used in several experiments described, using the red channel, see an example of a response in Figure 5.1) or a highly localised transcription factor (e.g. Mig1-eGFP that was used in dual-colour experiments, see section 5.5). The thresholds were adjusted manually on a ROI by ROI basis as due to cell heterogeneity a robust, coverall algorithm to determine the nuclear threshold of any given cell proved excessively hard.

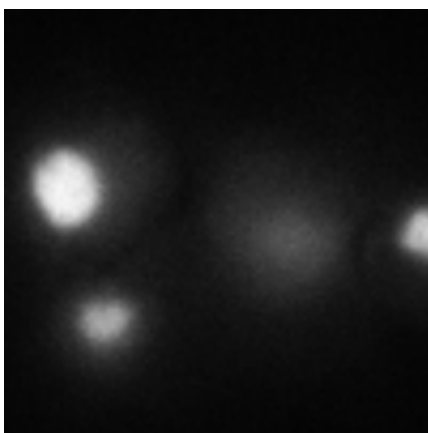


Figure 5.1 – A red channel frame from a strain using Nrd1-mCherry as nuclear reporter. Notice that the middle cell does not have a clearly visible nucleus and the rightmost cell does not show the whole cell

Once the two boundaries have been determined one of two methods was used to determine the full geometry, represented as multiple binary masks (see Figure 5.5), one set delimiting the nuclei and one set the whole cells minus the nuclei.

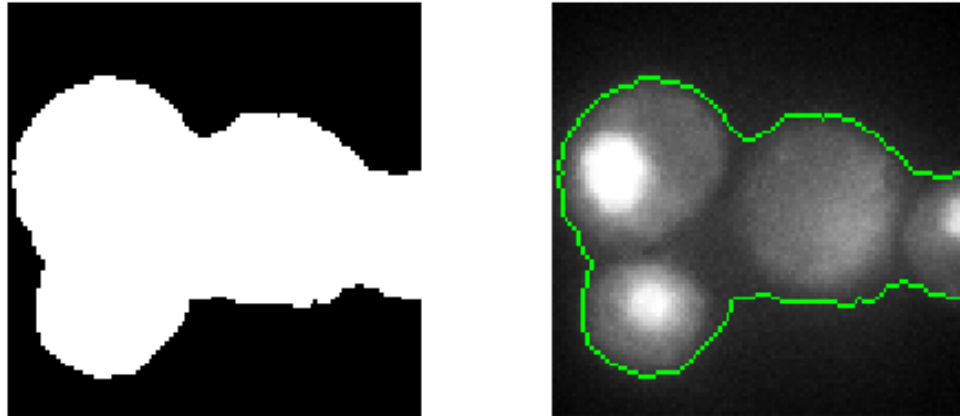


Figure 5.2 – The green channel frame corresponding to the red channel in Figure 5.1. The green outline shows the found outer boundary of the cell envelopes.

A watershed algorithm (Beucher & Lantuejoul 1979; Otsu 1979; Vincent & Soille 1991; Meyer 1994; Xue et al. 2010) was used to find the boundaries *between* adjacent cells. The algorithm works by considering a greyscale image as a topology. An imagined drop of water, a seed, is dropped on the hills representing the image and it flows towards minima in the topology. By planting seeds, one per cell, within the outer boundary (the green border in Figure 5.2), the outside of which is defined as a maximum height region and any flows cannot enter this region, the boundaries between the cells can be found.

As seeds for the algorithm the preferred source was the cell nuclei, but in some instances the dynamic range was too low and this yielded unpredicted results. A manual selection of one point per cell was used as seed and the process was otherwise identical. The figures shown here is a good example of a situation where it is hard to

find a good segmentation for the nucleus for one cell. The middle cell has a very dim (possibly due to being further from the focal plane than other nuclei, it may have been near the top of the cell rather than in the same in-focus mid-section as the other clearly visible nuclei). The *depth of field*, the axial distance over which a point is clearly resolved is described by the equation (Spring & Davidson 2016):

$$d_{\text{tot}} = \frac{\lambda \cdot n}{\text{NA}^2} + \frac{n}{M \cdot \text{NA}} \cdot e \quad (20)$$

Where λ is the wavelength imaged (i.e. the emission wavelengths of the fluorophores), n is the refractive index of the immersion oil ($n = 1.518$ for Immersol 518 N), NA the numerical aperture of the objective lens ($\text{NA} = 1.49$), M the magnification of the lens (100x) and e the smallest resolvable distance given by the sensor (93 nm for the system used, see chapter 4.1). This means that the focal depth is between 348 and 418 nm (at the emission peaks for eGFP and mCherry respectively, 508 and 610 nm). In Figure 5.3 possible geometries for the leftmost and middle cells are shown.

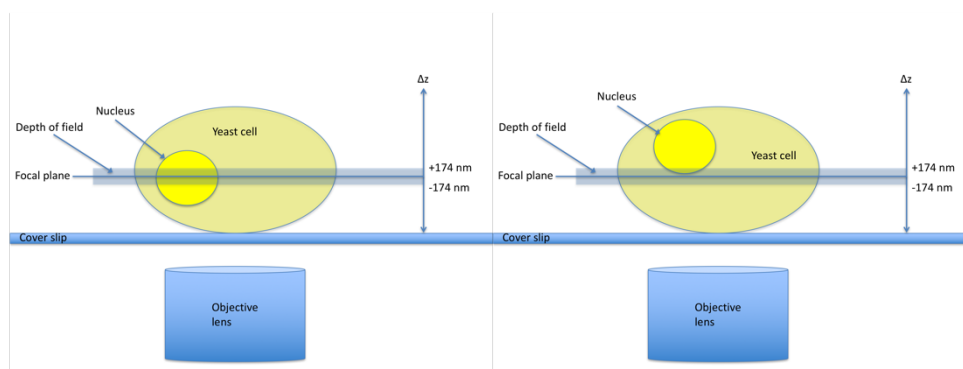


Figure 5.3 – Left, a cell with the focal volume bisecting the nucleus. Right, a cell with the nucleus offset from the focal volume.

In Figure 5.2 the initial outer limit of cell extent in a ROI is shown and the resulting binary mask. This shows how the cell membrane boundary to the surrounding

unpopulated medium can be found using the general and autofluorescence. In Figure 5.4 the situation is shown after applying the watershed algorithm using the nuclei as seeds.

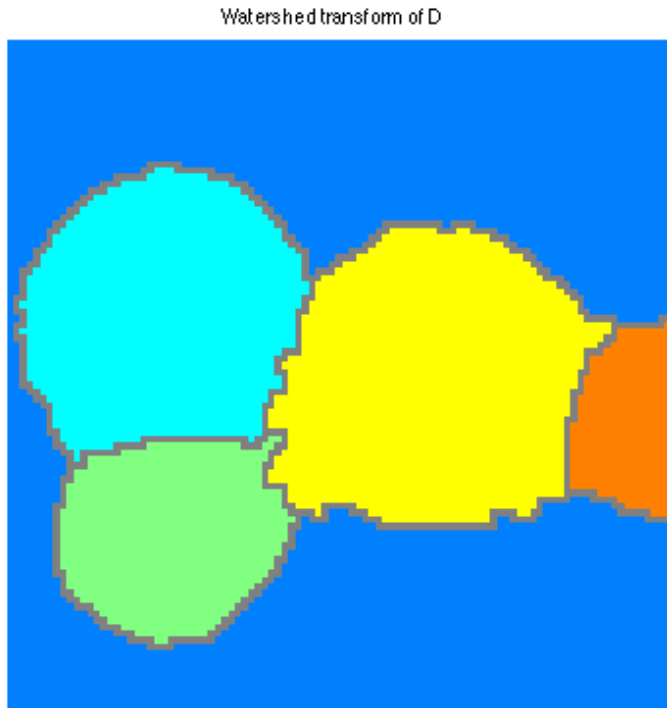


Figure 5.4 – The segmented cells. One colour per envelope.

The dim nucleus in the middle cell did indeed produce a nuclear segment as can be seen in Figure 5.5 (index 4) showing the three initially selected cell segments with the nuclear segments overlaid, but it was smaller than the other segments and the decision was later made to not include this cell in the analysis as a clearly defined nucleus is a prerequisite to be able to show signal transduction between cytosol and nucleus. However, its use as a seed for the segmentation is perfectly acceptable.

These masks were subsequently used to determine how transcription factors migrate throughout the cells and to differentiate between cytosolic and nuclear content.



Figure 5.5 – The binary masks of the cells from Figure 5.1 to Figure 5.4 with the nucleus superimposed as a black region. Note the middle cell with the under-sized nuclear segment (mask index 4). The membrane masks were always indexed from 2 and up, 1 being reserved for the surrounding area (blue in Figure 5.4). Nuclear masks were indexed from 1 and up, always one less than the corresponding membrane mask.

5.3 Proof of concept – Steady state behaviour

I first investigated steady state behaviour with regards to the yeast extracellular glucose concentration, before studying transient, dynamic effects following sudden changes in glucose concentration. The steady states, the known characteristics of which were introduced in chapter 2 were the first images acquired using the improved imaging and illumination setup. Both bulk behaviour and average single cell behaviour has been studied before in similar studies (Bendrioua et al. 2014; Almquist et al. 2015). These studies showed the distribution (measured as fluorescence intensity) by compartment of Mig1 in a cell in response to environmental glucose concentration. It is established that Mig1 is highly localised to the nucleus under glucose rich conditions and that it is highly delocalised during glucose starvation.

Earlier investigations using fluorescent proteins as reporters used relatively long integration times (i.e. camera exposure times), many 10s of milliseconds up to several seconds (e.g. 27-300 ms in Bendrioua's 2014 paper). A new approach in the imaging taken in the work presented here is to use short exposure times facilitated with high intensity excitation light, to enable tracking over a time scale comparable to the diffusional time scale of individual protein molecules in a yeast cell. At exposure times as short as 4.7 ms, the cytosolic diffusion rates in a living yeast cell, a few $\mu\text{m}^2/\text{s}$ (Adam J. M. Wollman & Leake 2015), can be resolved and singular proteins or small clusters of proteins be pinpointed within a cell without motion blur artefacts.

Initial investigations were conducted on cells at steady state. The cells were acclimatised to a specific glucose concentration and other conditions and a sample for imaging was prepared by immobilising cells on a pad of agarose with the same environmental conditions as the cells are exposed to in the acclimatisation stock. A

sample for imaging was prepared by using a GeneFrame, a shallow plastic rim attached with an adhesive to a microscope slide.



Figure 5.6 – A microscope slide with a GeneFrame attached.

The GeneFrame is stuck onto the slide and melted agarose at $\sim 50^{\circ}\text{C}$, with environment adjusted as desired in this case to include a minimal cell growth medium (YNB) and an appropriate amount of glucose, is poured into the well created by the frame. The level of liquid agarose is adjusted to reach the rim of the frame and left to cool and set. After the agarose has set and cooled to safe temperatures for yeast, the yeast is applied by smearing a few microliters on the top of the agarose pad and a plasma cleaned coverslip is pressed down to hold the cells in place. The GeneFrame has double sided adhesive so at this point the second sticky side is exposed and used to hold the coverslip in place.

This method of preparing slides for microscopy was used throughout for experiments conducted at steady state conditions (except for microfluidics control experiments where cells were exposed to identical conditions in standard and alternate environments). The results of the GeneFrame experiments and the steady state control experiments in the flow cells exhibited the same behaviour with regards to protein distribution in the cells, proving that the two methods were interchangeable to provide control data. They also confirm Almquist and Bendrioua's finds.

5.4 Cells adapting to a new environment

After having shown the ability to visualise transcription factor and kinase localisation behaviour in cells at steady state as described in section 5.3, the next step was to follow the behaviour of single cells that were exposed to glucose concentrations which were varied rapidly and dynamically and visualise cell signalling. To be able to show responses to a change in environmental glucose conditions the microfluidics protocol described in chapter 3.2 was used. Once a freshly prepared cell culture has acclimatised to the conditions in the standard environment and a microfluidics chamber has been prepared, a small amount of cell suspension is injected manually into the microfluidics chamber by a 1 ml syringe and allowed to sediment on the chamber floor.

If the Concanavalin A treatment has been successful, a number of cells will have been bound to the channel floor by the lectin. The standard environment flow is started and unbound cells are washed away. At this point the chamber is checked for bound cells and if the density is deemed high enough (a full experimental set with ten regions of interest will require cells bound in as many locations). The number of cells per region of interest should ideally be as high as possible to collect a larger data set, but the practical limit is 3-4 cells per 100 x 100-pixel region. It is not desirable to have a carpet of cells but a small cluster of 2-4 cells is ideal for imaging. Also, chemical communication between adjacent cells in large cell carpets and difficulty providing a good flow of medium around the cells providing fresh environment and washing residual metabolites away are reasons for avoiding too dense coverage. If the surface coverage is deemed dense enough, and the cells' bonds to the Concanavalin A covered microchannel surface are stable enough that the gravity fed standard environment flow does not flush the cells away, immediately or within a few minutes, the sample is good

to use and the experiment can proceed. Allowing 3-5 minutes before taking a decision of whether to proceed or not gives a good indication as to how well the cells have been bound. If the number of cells bound is too low, i.e. it can be surmised that it will be hard to find enough fields of view with cells for a full set of data, the gravity fed standard environment flow is stopped and a new dose of cell suspension is added and the above process is repeated. This could be tried a third time as well, but if at that point not enough cells can be found, two routes can be taken depending on if any cells at all have bound. If a smaller set of cells have bound, and seem to be bound firmly enough (a simple manual push on an attached syringe will generate a high flow and if the cells stay bound despite this it is possible to proceed), a smaller data set can still be acquired, simply reducing the number of ROIs imaged. If this is not the case, it may be that the lectin has not bound properly to the coverslip or perhaps something with the surface chemistry of the cells and if so, it is unlikely that any further actions will produce better results. The best option is to write the microfluidics chip off and proceed with a new chip. Also discard the chip in the case of excessive amounts of cells being firmly bound to the channels. A reasonably populated field of view is shown in Figure 5.7

If imaging at initially glucose rich environment, it is beneficial to entirely disconnect the loading syringe from the needle and connecting tubing. In a glucose rich environment, the cell culture develops significant amounts of gas (carbon dioxide) that raises the pressure in the loading channel and may, if still connected, push additional cell culture into the imaging channel, risking to rip the cells imaged of the channel floor. Even worse, the gas can form bubbles that are pushed into the main channel where it can disrupt the media flows and/or rip cells from the floor. With the

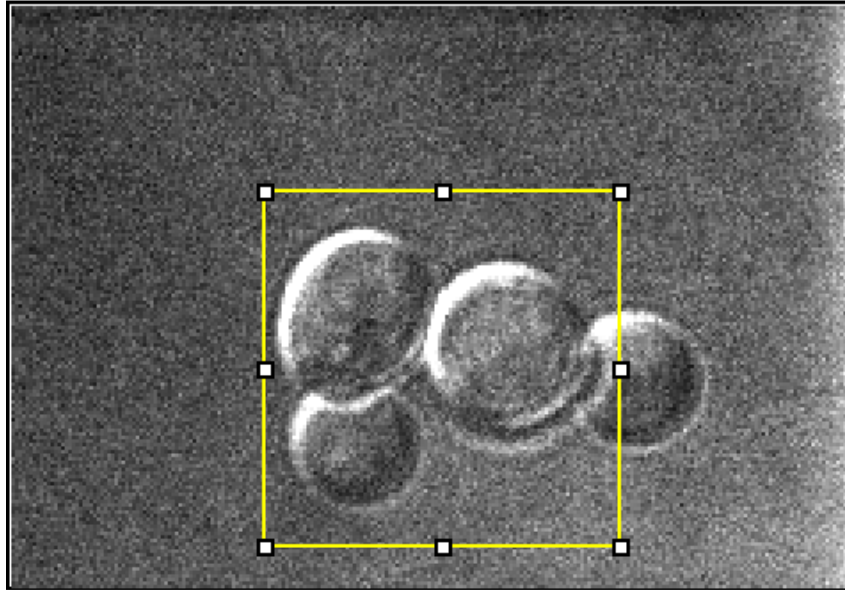


Figure 5.7 – A differential interference contrast (DIC) image of a ROI as acquired with the 100 x 100-pixel region analysed marked with the yellow box. The box is 100x100 pixels, i.e. 9.3 μm sides.

syringe disconnected, the risk for such occurrences is minimised. Practical trials showed that there is no backflow into the loading channel using the standard gravity feed and pump feed flow rates with the loading syringe disconnected.

One thing that quickly proved important, was to use a freshly defrosted aliquot of Concanavalin A stock for every chip used. It seems as if the stock solution degrades quickly even if kept in a refrigerator at $\sim 5^{\circ}\text{C}$. Also, a one minute (air-) plasma treatment of the chip before wetting the channels in preparation for imaging should be performed to facilitate wetting and binding of lectin to the channel walls.

Once a chip has been prepared according to this protocol, a steady flow of standard environment is allowed to flow for about ten minutes before any environment changes are introduced. This is about the time it took for me to locate a region on the sample with well distributed cells as described above. The selected cells are centred within the 100 x 100-pixel focus region and two sets of bright-field images are taken. All brightfield image sequences are using the camera set to expose using an external

trigger just like fluorescent frames. The CellBild controls (see chapter 4.2) are set to *Continuous camera triggering*, which starts a continuous pulse train with a predefined frame period – unless otherwise stated it is 5 ms in all experiments described in this thesis.

First a Differential Interference Contrast (DIC) image set is acquired (3-5 frames is standard) in order to get high contrast images of the cells imaged. DIC has to be acquired first, as the Wollaston prism in the imaging path has to be removed before fluorescence imaging can be conducted as otherwise the image will be distorted. A Wollaston prism divides an incoming light beam with arbitrary polarisation into two outgoing beams, an ordinary and an extraordinary beam with orthogonal polarisation. Any single fluorescent molecule will emit polarised light and, in the general case of there being no fixed electric dipole orientations of any two fluorescent proteins, the image position will be randomly distorted depending on the orientation of the fluorophore if the prism is left in situ. The process of removing the prism may minutely disturb the focus and alignment of the field of view as a result of the mechanical manipulation of the prism, so a readjustment is necessary after the process.

Second, after any necessary re-centring and refocussing, a standard transmission brightfield reference image sequence (3-5 frames is standard) is acquired. This procedure mirrors the pre-fluorescence protocol for the steady state acquisitions. The reason for a minimum of 3 frames, as mentioned in chapter 4.2, is due to the inconsistencies during the first two frames of any sequence acquired by the camera, and so the first two frames must be discarded.

At this point the experiment is prepared for fluorescence imaging. The CellBild controls are set to *Finite sequences*, the brightfield lamp is turned off and the cameras

electronic gain is set for fluorescence imaging (300x has been used for fluorescence imaging during the experiments presented here).

A final pre-bleach step is followed before imaging the main data series for all data sets to conserve the number of unbleached proteins available at the start of the main imaging series. If imaging e.g. Mig1-eGFP that is highly localised to the nucleus, the camera will saturate the first few frames before the fluorophores have photobleached to an unsaturated level. To counter this effect a 5-frame per channel image sequence is acquired at 1/10 laser power, low enough to not cause saturation and get data from the unbleached fluorophores. Then a burst of a further 5 frames at full power is shot for the green channel (the unsaturated red channel is not treated). The photobleaching during the five frames brings the fluorescence down to nonsaturating levels. After the pre-bleach the following protocols were followed.

5.4.1 There and back again – Imaging cells at a standard environment, an alternate environment and once again after return to the standard environment

To show the behaviour when cells are exposed to two subsequent environmental shifts an experimental protocol was designed that could do this. Earlier results by Almquist et al. (Almquist et al. 2015) using the same and similar cell strains, shows that fluorescent intensity, indicative of protein localisation shift between cytosol and nucleus, occur over the space of two minutes. Thus, initially the protocol shown in Figure 5.8 was followed.

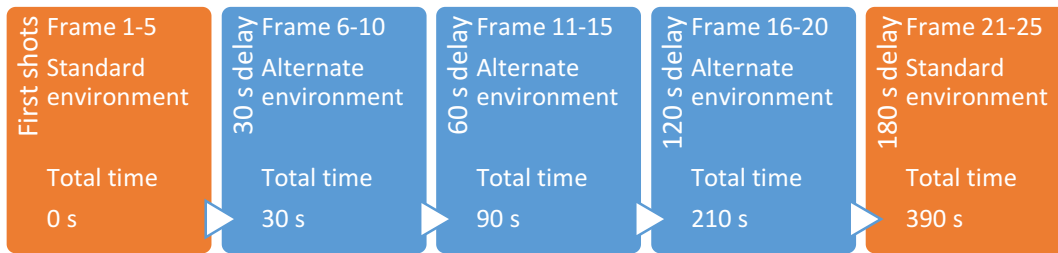


Figure 5.8 – First version of a *There and back again* protocol as used in the first successful alternating environment experiments. Every timepoint consisted of five illuminated frames. The delays are inserted between the timepoints and the frames within a timepoint are in sequence, back-to-back.

The initial protocol is designed to acquire five frames each of green and red channel for a total of ten frames, alternating channel excitation. This means that the frame interval per channel is 10 ms and the actual frame interval (red to green and vice versa) is 5 ms. With a 5 ms frame interval the longest possible exposure time is 4.7 ms and this is used throughout. The delays noted in Figure 5.8 are the delays between the timepoint before and the current one. The first timepoint is acquired in the standard environment before the pump delivering the alternate environment is started. Thus, the cumulative time in the alternate environment is $30 + 60 + 120 = 210$ s and then a three-minute delay before the final timepoint, once again in the standard environment was acquired.

Using this protocol, while showing the cells response to environmental change the time allowed for adaptation is short and the return to standard environment after 210 s shows the readaptation response from a point where the initial adaptation may still be in progress (noting Almquist et al. results).

An extended protocol version was introduced to allow more time for cells to acclimatise to the new, alternate environment, by inserting another timepoint before the return to initial conditions. The logarithmic lengthening of delay times was retained and a 240 s delay was introduced before the new final timepoint at alternate environment, see Figure 5.9. The delay after return to the standard environment before the final frames were acquired, was also lengthened to 210 s. The reason for using longer times in the protocol was that, after experimenting with the delay times I found that the maximum response to the environmental change seemed to occur around ~210 s after the environment was changed, and so allowing the cells to reacclimatise to the standard environment for this time would result in a more complete “reset” to the original state compared to the shorter 180 s used in the first protocol version.



Figure 5.9 – Second version of a *There and back again* protocol as used in subsequent experiments. This protocol was used for the Mig1-eGFP/Nrd1-mCherry experiments described here.

The standard and alternate environments were chosen to be either of the two conditions:

- High Glucose (+) – YNB medium with 4% glucose
- Low Glucose (-) – YNB medium with 0% glucose (i.e. glucose free)

As mentioned the cells would always be grown overnight in the first type of environment and before investigations transferred into a fresh batch of medium with

the appropriate glucose concentration for the initial condition intended. A proper washing is particularly important if the initial conditions, the standard environment, is intended to be low (-) glucose. The acclimatisation period is also important in this case.

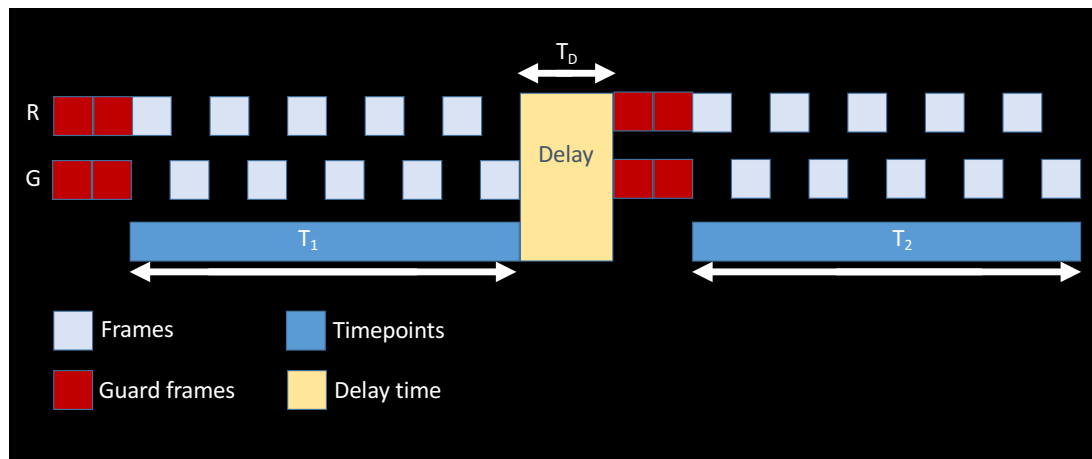


Figure 5.10 – Frame disposition of two consecutive timepoints (T_1 and T_2). Showing an unproportioned delay (T_D) between the two timepoints. The R and G represent the red and green channels respectively. The red boxes are the guard frames, the unusable initial frames from every image acquisition being discarded.

In Figure 5.10 the disposition of data collection is shown. The images acquired are in reality stored in one large TIFF-stack file for later analysis. The images are divided into a right and a left side, corresponding to the red and green channel respectively, and in post-processing, the frames are divided accordingly. Every other frame is illuminated with either laser (ALEX operation) and the corresponding frames from the divided stack are extracted, and the discarded guard frames (the two inconsistent initial frames of any image sequence) are removed to produce two stacks

of consecutive frames. In post-processing, it is necessary to further divide the stack up into five-frame blocks, the timepoints.

This protocol uses timepoints consisting of five frames per channel (in total ten frames) with a frame period (per channel) of 10 ms. The five frames were chosen to allow tracking of particles over the 50 ms duration of a timepoint.

5.4.2 There and staying there – Single transition experiments

A third imaging protocol was introduced, designed to allow following the behaviour over longer time periods with more densely spaced timepoints. The protocol also introduces a standardised cycle time. After an experiment is started the cells are exposed to 15 minute cycles of standard and alternate environment.

Due to the lower intensity and the poorer photostability of mCherry, a limited number of frames are possible to acquire before the available molecules have irreversibly photobleached. However, using a single illuminated frame pair for every image exposure, instead of five it was possible to acquire 1 + 30 timepoints without reaching completely photobleaching the mCherry content, with the caveat of sacrificing the ability to track single particles. The delays between timepoints was chosen to a linear regime with 30 s between consecutive timepoints for a total of 15 minutes. The frame disposition is shown in Figure 5.11. Note that every timepoint still require two guard frames before any illuminated frames.

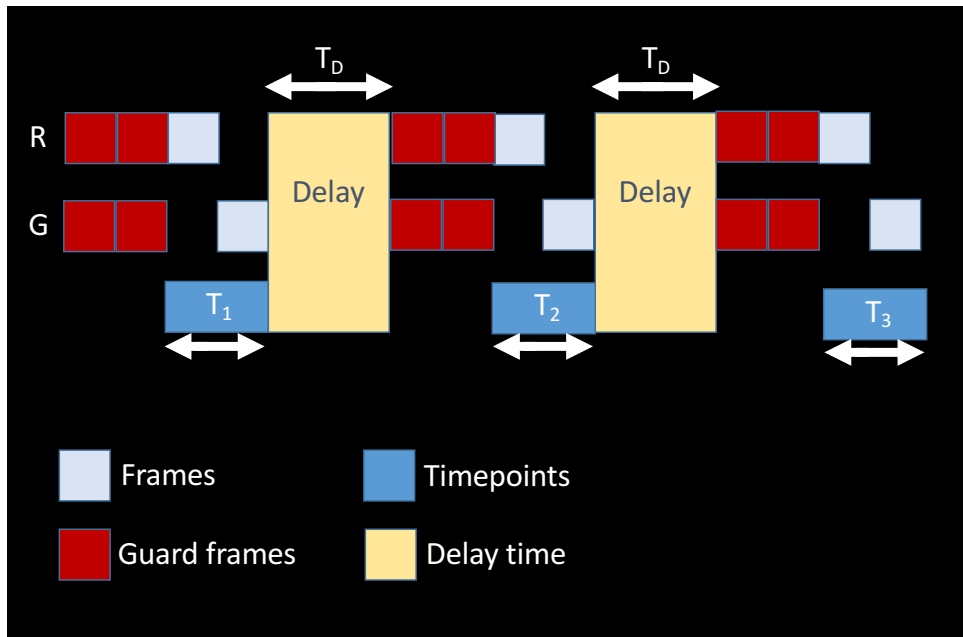


Figure 5.11 – Frame disposition of three consecutive timepoints (T_1 to T_3). Showing an unproportioned delay ($T_D = 30$ s) between the timepoints. The R and G represent the red and green channels respectively. The red boxes are the guard frames.

A further limitation was also imposed, a maximum of four cycles per experiment (some exceptions were made, allowing a fifth cycle) leading to a total duration of any one experiment using this protocol of two hours, approximately corresponding to the doubling time of haploid yeast in a minimal medium (Marks 2011).

5.4.3 Mutants used and their tagged transcription factors

Several mutants of the background strains W303 and BY4741 were used for the investigations presented here. Both are well defined variants of haploid yeast. They behave in a very similar manner with regards to Mig1 localisation behaviour as a function of extracellular glucose concentration, but the W303 variant has some problems due to an adenosine deficiency, manifesting as the production of a red pigment that add greatly to the general autofluorescence in the cells. So, in order to

use this cell strain, an addition of adenosine hemisulphate to the growth medium is necessary. As the BY4741 background does not have these issues, this variant was preferred over the W303 in most experiments. The only time the W303 was used were for certain mutation combinations that we only had access to in W303 background.

The varieties that were used are listed in Table 5.1.

Table 5.1 – Overview of Saccharomyces cerevisiae mutants used. Listed are the reporter fluorophore and which transcription factor or other component has been tagged using it. Also listed are deletions in the Other traits column.

Background strain	eGFP	mCherry	Other traits
BY4741	eGFP / Mig1	Nrd1	
BY4741	eGFP / Mig1	Nrd1	<i>snf1</i> Δ
BY4741	eGFP / Msn2	Nrd1	
BY4741	eGFP / Mig1	Reg1	
W303	eGFP / Mig1	Snf1	

5.5 Results – Dynamic environment

The cell strains listed in Table 5.1 long sequences were studied according to the two protocols listed in section 5.4.1. In this section, all references to “High glucose (+)” should be understood as 4% glucose content (by weight) and all references to “Low glucose (-)” should be understood as 0% glucose (no glucose present). All results represented in this section have been imaged using either of the protocols in section 5.4.1 or 5.4.2 for environmental control and imaging using either the five frames per timepoint protocol (5.4.1) or the single-frame protocol (5.4.2) described in corresponding sections.

The first three results shown here are the Mig1-eGFP/Nrd1-mCherry strain being imaged using the second version of the *There and back again*-protocol from subsection 5.4.1. In Figure 5.12 the effect to the transcription factor Mig1 from bringing the cells environment from a high glucose (+) environment to a low glucose (-) environment and back again to high (+) is shown. The Mig1 responds promptly to the new, low glucose environment by unbinding from the DNA and delocalising from the nucleus. Upon returning to the high concentration, the Mig1 starts to localise again. The Nrd1 remains localised to the nucleus (not shown in the figure). In Figure 5.13 the inverse is shown, cells acclimatised to a low glucose environment is taken from the low (-) glucose concentration to high (+) and back to low (-). The response is a localisation to the nucleus of Mig1 in the glucose rich environment, and a subsequent delocalisation upon return to low glucose concentrations. In the final panel, Figure 5.14, a control experiment, shows the behaviour when exposed to continuously high glucose conditions using the same medium in both standard and alternate environment feeds. The Mig1 remains localised to the nucleus for the duration of the experiment. Every timepoint in these experiments consist of five consecutive frames of either

colour interleaved, with a 5 ms frame period. Shown in the figures are the first frame in every burst of five frames, making these figures comparable to the experiments shown in the figures from Figure 5.15 onwards. The initial frame is always red followed by a green and every timepoint is divided into an equal number of red and green frames, always ending with a green frame.

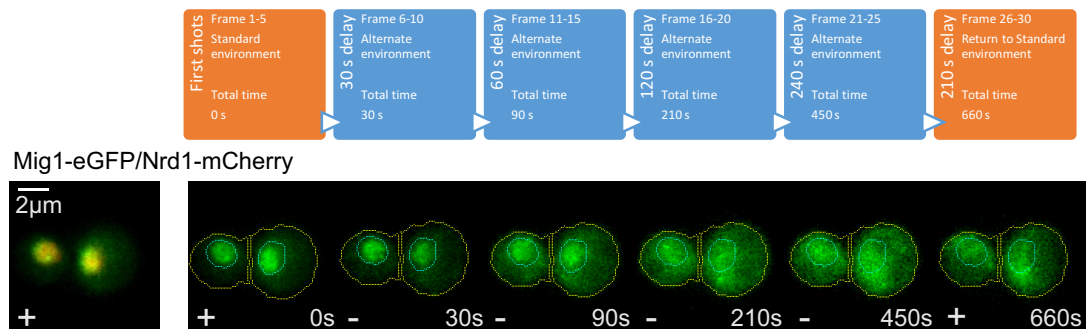


Figure 5.12 – Cells acclimatised to a high glucose (+) environment exposed to a low glucose (-) environment and then returned to the original, high glucose (+) environment.

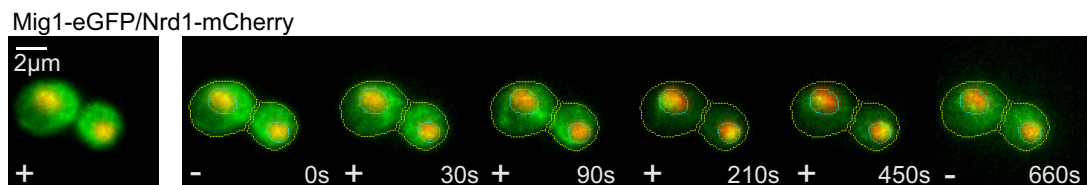


Figure 5.13– Cells acclimatised to a low glucose (-) environment exposed to a high glucose (+) environment and then returned to the original, low glucose (-) environment.

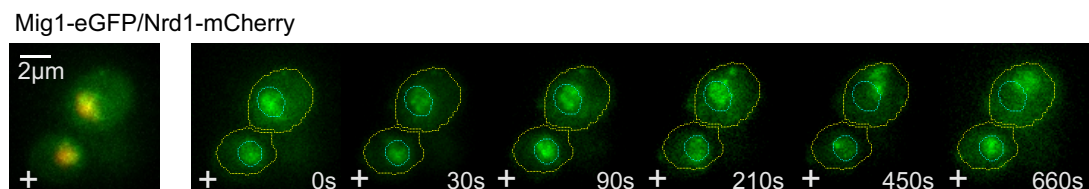


Figure 5.14 – Control experiment. Cells acclimatised to a high glucose (+) environment exposed continuously to this environment for the same duration as in Figure 5.12 and Figure 5.13. Note the mobile nucleus in the upper cell.

In Figure 5.14 an example of a nucleus moving relative to the cell envelope is shown, demonstrating the importance of being careful during the masking and watershed procedure. This type of nuclear shift was uncommon but did occur occasionally.

The following results were acquired using the *There and staying there* protocol from subsection 5.4.2. In the following figures, the timepoints represented are chosen to be the same or close to the equivalent timepoints during the experiments shown in Figure 5.12 to Figure 5.14 in order for the two methods to be visually comparable. The slightly altered protocol allows for more timepoints while retaining the same accumulated exposure time and light dose over the duration of an experiment. The order of the experiments shown follows the one in Table 5.1.

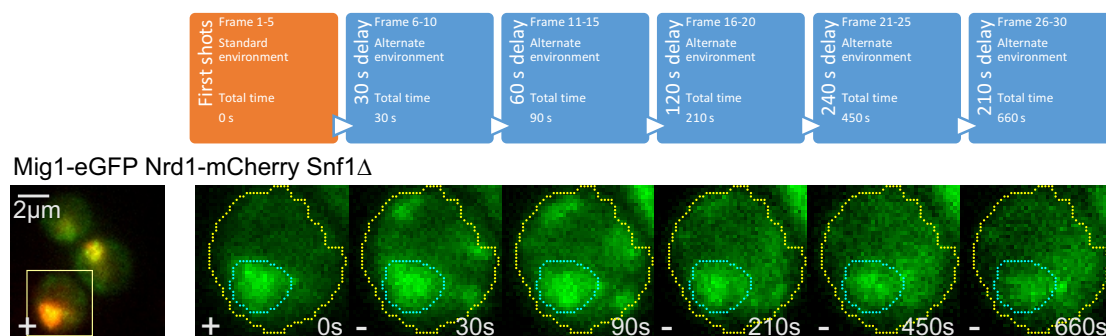


Figure 5.15 – Deletion mutant. The cells are acclimatised to a high glucose (+) environment and then exposed to a low glucose (-) environment. The transcription factor Snf1 has been deleted.

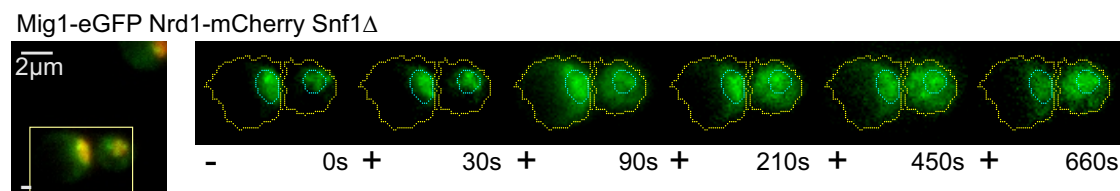


Figure 5.16 – Deletion mutant. The cells are acclimatised to a low glucose (-) environment and then exposed to a high glucose (+) environment. The transcription factor Snf1 has been deleted.

In the experiments shown in Figure 5.15 and Figure 5.16 a deletion mutant was used in which Snf1 was not expressed. It can be noted that in the absence of snf1 the expected behaviour is for the Mig1 is to stay mostly localised to the nucleus as snf1 is believed to be intimately involved in the phosphorylation and release of Mig1 from its binding sites on the DNA. The results from the deletion mutant seems to corroborate this. The Mig1 localised to the nucleus tend to remain localised. However, an increase in *localised* GFP fluorescence *outside* the nucleus can be seen though. Mig1 will be present throughout the cell under any condition, but will preferentially bind to the DNA unless acted upon by Snf1. As of yet, no other pathways potentially acting on Mig1 in response to glucose variations are known.

Especially in the high (+) to low (-) experiment (Figure 5.15) extranuclear localisation in foci (i.e. the large spots that can be seen in the cytoplasm) are clearly visible. The reason for these large clusters is unknown, but as mentioned in the paper by Wollman, Shashkova, Hedlund et al. (Wollman et al. 2016) clustering seem to be a common occurrence.

In the following Figure 5.17 and Figure 5.18, another transcription factor, Msn2, has been tagged with eGFP. Msn2 is expected to behave approximately inversely compared to Mig1. The protein is expected to localise to the nucleus under low glucose (-) and to delocalise under high glucose (+) conditions. This behaviour could be confirmed.

Msn2-eGFP Nrd1-mCherry

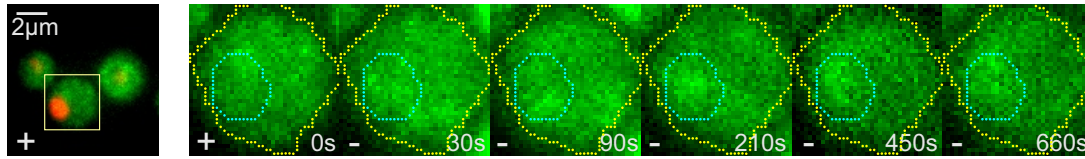


Figure 5.17 – Cells acclimatised to a high glucose (+) environment exposed to a low glucose (-) environment. The expected behaviour of Msn2 is approximately the inverse of that of Mig1, i.e. it should localise to the nucleus under low glucose conditions. The effect is not as dramatic as during a low to high transition (see Figure 5.18).

Msn2-eGFP Nrd1-mCherry

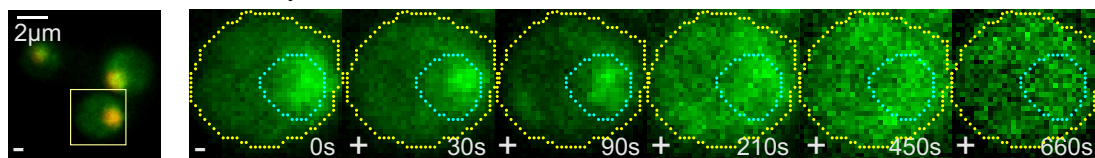


Figure 5.18 – Cells acclimatised to a low glucose (-) environment exposed to a high glucose (+) environment. The expected behaviour of Msn2 is approximately the inverse of that of Mig1, i.e. it should delocalise from the nucleus under low glucose conditions.

The experiments described up to this point all used the mCherry-tagged RNA-polymerase component Nrd1 as a reporter for the location of the cell nucleus. This is a very convenient way of knowing where the nucleus is as the Nrd1 will be confined to the nucleus in a living and healthy cell. An alternative method to localise the nucleus uses the intrinsic localisation of certain transcription factors under certain conditions. As was shown in the Mig1-eGFP/Nrd1-mCherry experiments (see Figure 5.12 and Figure 5.13), Mig1 is highly localised to the nucleus under high glucose conditions, so clearly in fact, that the intensity excess in the nucleus can be used in the same manner as the Nrd1-mCherry localisation strategy. This enables dual-colour analysis of strains not containing the nuclear specific marker Nrd1-mCherry so long as the cells are

exposed to the localising conditions for long enough. The same effect could be used for the Msn2-eGFP strain or any other cell strain that exhibits clear localisation. However, the only dual-colour systems analysed with this technique described in this thesis are relying on the Mig1-eGFP localisation.

In Figure 5.19 and Figure 5.20 dual colour behaviour is shown for the BY4741 variety with Mig1 tagged with eGFP and Reg1 tagged with mCherry. Reg1 is a subunit of the complex Reg1-Glc7 that regulates the phosphorylation state of Snf1, an active Reg1-Glc7 antagonises phosphorylation of Snf1 (Zhang et al. 2011; Towle 2005; Almquist et al. 2015). The Mig1 localisation at high glucose (+) is used as nuclear marker. The marking is taken either at the beginning of the sequence in the case of environment shift from high (+) to low (-) glucose conditions, or after 180 s in the case of shift from low (-) to high (+), i.e. when the localisation is expected to be reaching steady state behaviour.

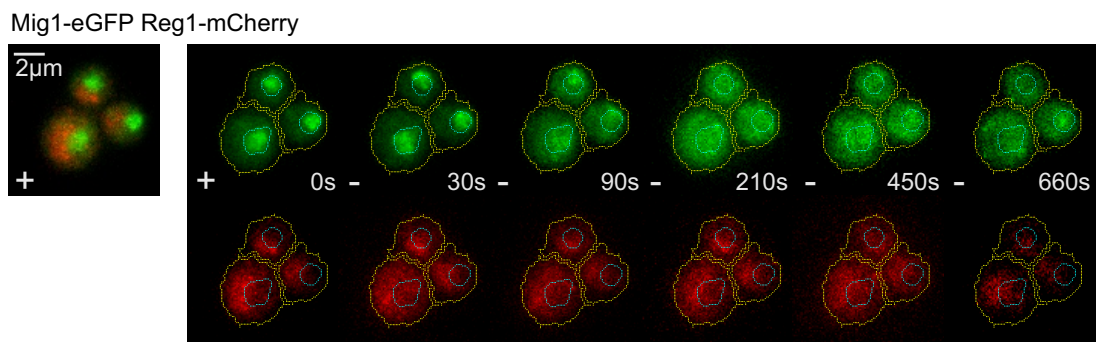


Figure 5.19 – Single transition sequence of the dual colour construct Mig1-eGFP and Reg1-mCherry. The Mig1 localisation under high glucose (+) conditions is used as a nuclear marker and is taken from the first frame.

Mig1-eGFP Reg1-mCherry

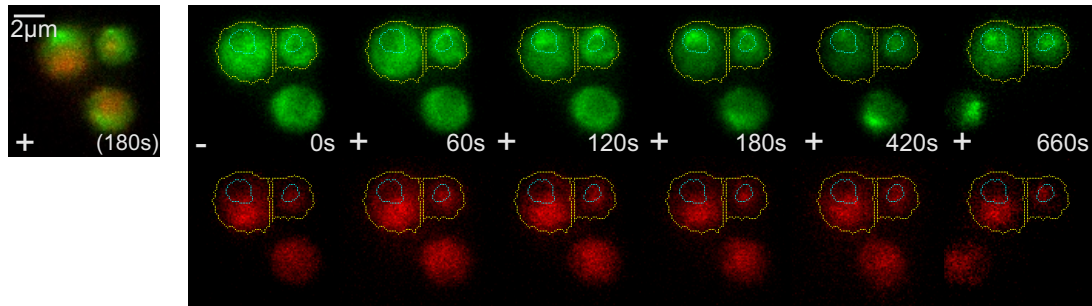


Figure 5.20 – Single transition sequence of the dual colour construct Mig1-eGFP and Reg1-mCherry. The Mig1 localisation under high glucose (+) conditions is used as a nuclear marker and is taken from the first frame.

In the following figures, a W303 variant using Mig1 with eGFP tags and Snf1 with mCherry tags is shown. The reason for using cells with an alternative background for these specific experiments is that the all attempts to create a cell strain in the BY4741 background that simultaneously express Mig1-eGFP (or Mig1-mGFP) and Snf1-mCherry failed. However, if W303 cells are grown and kept in medium with appropriate adenosine hemisulphate supplement (4 µg/ml) present, they behave well and do not produce excessive autofluorescence in the red channel.

Mig1-eGFP Snf1-mCherry

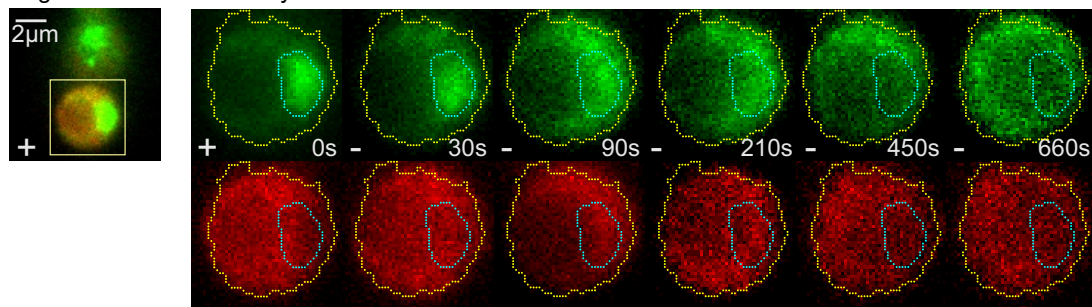


Figure 5.21 – Single transition sequence of the dual colour construct Mig1-eGFP and Snf1-mCherry in W303 background. The Mig1 localisation under high glucose (+) conditions is used as a nuclear marker and is taken from the first frame.

The Snf1 is mostly absent from the nucleus under high glucose (+) conditions. As the environment is shifted to low glucose (-) content, the Snf1 begin to migrate into nucleus. The apparent behaviour is that the Snf1 becomes more evenly spread throughout the cell from having been absent from the nucleus under (+) conditions. This behaviour is expected given the results from earlier research (Bendrioua et al. 2014; Almquist et al. 2015). In these images, every timepoint is a single frame per colour, taken in sequence, the red frame first and the green 5 ms afterwards (see section 5.4.2, specifically Figure 5.11).

In the following figure, cells from the same strain are transferred from low to high glucose conditions. An issue with this specific strain that proved harder to find a simple solution to is that they were particularly prone to being washed away during low to high glucose sequences. One hypothesis that has not been confirmed is that this may be due to a lower concentration of carbohydrates in the cell membrane that can bind to the Concanavalin A used to bind the cells down during experiments. The problem was not present in experiments commencing at a high glucose concentration so a less than ideal solution to the problem was to initiate the experiments at high glucose, allowing cells to bind to the coverslip and then letting them acclimatise to a low glucose environment *in* the microchannel and commence the experiment first after that. The cells were prepared for experiments using the same protocol as for a high to low experiment until the point that the cells have been loaded into the microfluidics chip and stuck to the surface, i.e. they are *not* transferred into a low glucose environment during the initial washing stage after extraction from the overnight cultures but will be exposed to the new environment just prior to the imaging.

Mig1-eGFP Snf1-mCherry

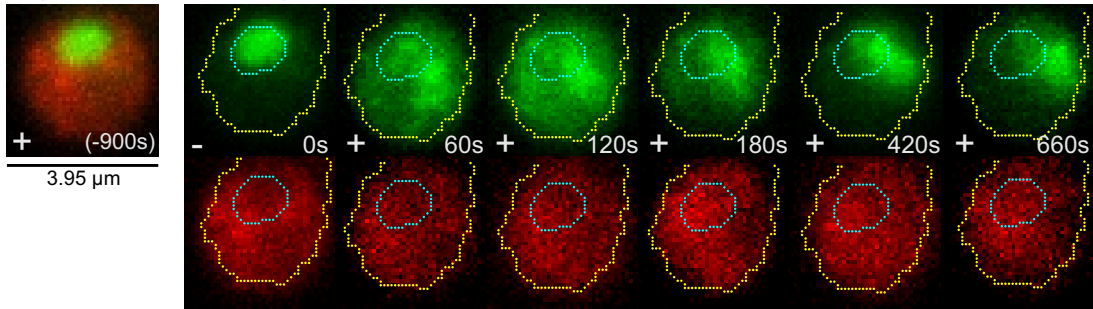


Figure 5.22 – Single transition sequence of the dual colour construct Mig1-eGFP and Snf1-mCherry in W303 background. The Mig1 localisation under high glucose (+) conditions is used as a nuclear marker and is taken from the first frame.

The procedure is very similar to the high to low glucose sequence described before, with the difference that the first full power frame is taken after the first pump cycle has concluded. After this point, the same frame sequences are followed as before, but using the gravity fed environment (high glucose, 4%) rather than the pumped flow (low glucose, 0%) to act as the de facto *alternate* environment.

A further set of issues that proved important to take into account over long imaging sequences, are that the cells *may* move ever so slightly over the duration of an experiment and the focus may drift, especially during the first moments after physically letting go of the focussing knobs (the focussing issue can easily be remedied by introducing an autofocus mechanism, but had to be done manually on the setup used here). So whenever possible, the preferred focussing technique used was to first focus on the sample and let the sample rest for a few minutes after which the only focus adjustment made were done using the nano-piezo stage and *not* the microscope focussing knobs. In practise this meant that initial coarse and fine focussing with knobs were done while acquiring pre-sequence brightfield images and subsequent fine adjustments were made using the nano-piezo stage.

The first issue, cells moving during the course of an imaging sequence required a similar approach but slightly complicates the analysis stage. The cells are bound to the by the Concanavalin A during an experiment. However, a cell may move slightly between two timepoints. This can be seen e.g. in Figure 5.20, notice how the third cell (bottom of field of view, without superimposed outline) moves towards the left, the effect is particularly visible in the last timepoint shown (+660 s). The migration is invariably in the direction of the media flow and observations indicate that it seems as if the cells may be rolling along the surface.

The cells moving is mainly an issue for the type of investigations conducted here if the nuclear reporter is mobile, as in the dual-colour experiments described here. If the cell rolls over the surface and the nuclear reporter is delocalised in either endpoint, it is not possible to determine the position of the nucleus with any appreciable accuracy for the entire duration of the experiment which poses a problem if the goal is to determine the distribution of transcription factors with regard to the nucleus. The movement poses less of a problem when using a permanent nuclear reporter, such as the Nrd1-mCherry construct described before. However, care must be taken to create appropriate masks and segmentations for every frame for a cell that has moved.

If the movement is excessive it is possible to track them between timepoints by briefly switching to brightfield mode and reposition and refocus in the time in between the fluorescent frames. This method was rarely used in practice, but was useful for some cells that did not bind very well to the lectin coating. As mentioned, the W303 variant was problematic in this respect, but still bound well enough so that a proper analysis could be performed. The only W303 strain used was the dual-colour Mig1-eGFP, Snf1-mCherry with mobile nuclear marker (Mig1-eGFP).

5.5.1 Single molecules and small clusters

By measuring the characteristic fluorescence intensity emitted from single molecules of the fluorescent markers used, single molecules and up to small clusters of the fluorophores can be localised and counted within the focal volume. An excited single fluorescent protein molecule will emit a deterministic number of photons and this results in a characteristic intensity at the camera. This also means that following a photobleach trace of a sample will show a step-wise bleaching discernible when approaching the final few molecules still emitting (Leake 2013). These properties are used to determine the characteristic intensity by letting a known set of molecules be exposed to the same imaging conditions as the live cells. In-vitro samples were prepared of the fluorophores that were encountered: The two GFP varieties available, eGFP and mGFP, and the red mCherry. As in the end only eGFP was used in the data providing strains, mGFP is not covered here, but have comparable characteristics to eGFP.

The in-vitro assays used a solution of purified diluted protein bound to a coverslip surface. The coverslip was first treated for about one minute in a plasma cleaner and then a simple flow channel was made using the same method I used in my previous work (Hedlund 2015). A simple flow chamber is made by two strips of double sided tape is attached to a microscope slide with a 1.5-2 mm gap in between them. The plasma treated coverslip is attached as a bridge between the two strips and the tape is trimmed to the extent of the coverslip. Next a solution of eGFP or mCherry antibodies (1 $\mu\text{g/ml}$) was flowed into the chamber and left to incubate for ~ 5 minutes. After this time, the chamber was washed thoroughly with ~ 200 μl phosphate buffered saline (PBS). At this point only antibodies bound to the surfaces would remain in the flow chamber. Next, a dilute solution of the marker protein used in-vivo, in this case eGFP

or mCherry (1 $\mu\text{g/ml}$), was wicked through the flow chamber and left to incubate for a further 5 minutes. During this time, a brief check was performed to confirm that there was indeed the expected fluorescence in the sample. Also included in the protein solution were 300 μm latex beads, to be used as aides for finding the correct focal plane. The slide was placed on the microscope and focussed using the tape edges as reference. A brief flash of laser illumination was given and if something resembling a bright cloud was present the sample could be confirmed good. Incubation was done with the sample chamber in the direction the lens would be once mounted on the microscope, so that beads could settle on the surface. At the end of the second incubation with fluorescent protein constructs, a second wash was performed and the slide was remounted on the microscope. The tape edge was again used as initial reference, and then a bead was used to find the correct focal plane. The mid plane of the bead was found and then the plane was shifted to 20 nm above the surface, the approximate height of the bound fluorophores, using the nano-piezo translation stage. Finally, an area with surface bound protein is sacrificed for fine-tuning of the focus and finally, after moving to a fresh region, an image sequence is acquired.

With proper dilution, the sample will be sufficiently sparse and the fluorophores imaged will be single molecules. This can be confirmed by analysing the intensities recorded and considering the distribution of intensities.

The same spot localising software used to pinpoint single molecules and clusters in living cells, ADEMS (Adam J. M. Wollman & Leake 2015), was used to find spots (single molecules) in the field of view. The software uses the integrated intensity over a small area so the same values will be valid for both astigmatic and regular imaging provided the whole astigmatic PSF is included in the analysed area. In figure 5.23 a

field of view of an mCherry *in vitro* sample is shown with a 100 x 100-pixel box indicated.

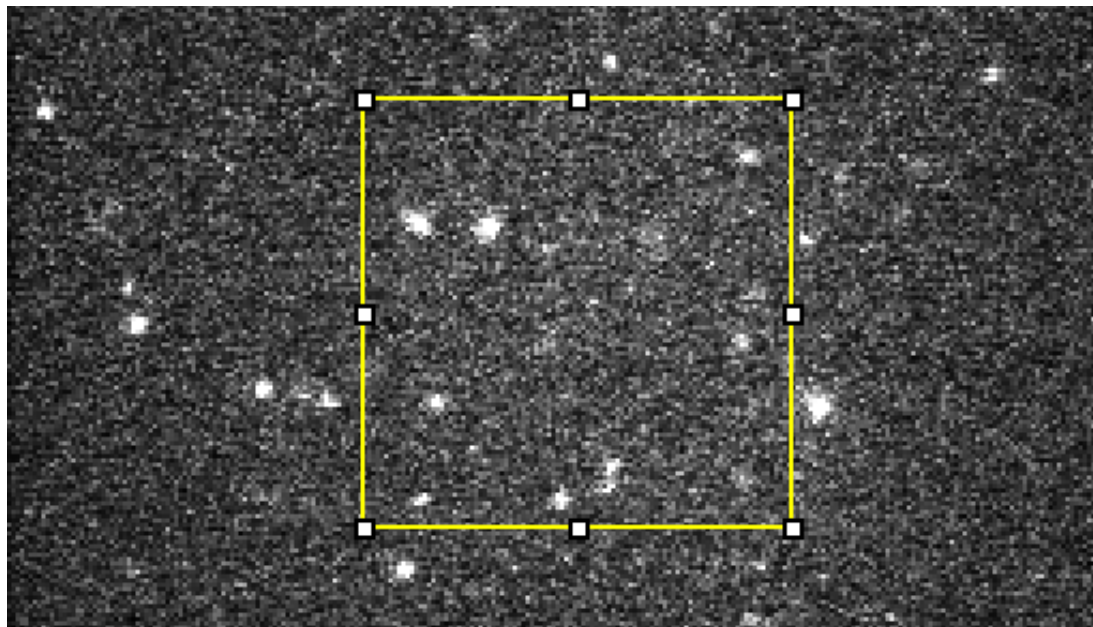


Figure 5.23 – Example of an in-vitro sample of mCherry during first illuminated frame. This frame is taken without astigmatism. The yellow box is the 100 x 100 (9.3 μm side) square used during live cell experiments. The dimmer spots visible are single molecules and the slightly larger, are clusters of two molecules.

The integrated intensities of the spots found in the frame were recorded and their relative intensities were presented as a Kernel Density Estimate (KDE), presenting the probability density a point has a certain intensity. A histogram would serve a similar purpose, but seeing the actual number of counts collected has a distribution, a density estimate is a good way of representing this data. The MATLAB standard function “ksdensity” was used. The result is, provided the sample is sparse enough to isolate enough fluorophores as single spots, a clear density peak around the intensity of a single fluorophore, and also much lower peaks at integer multiples of this value, corresponding to analysed spots that initially contained more than one fluorophore. The assay is designed to generate a sample sparse enough to generate mainly spots containing single fluorophores. However, the step-wise bleaching of single fluorophores allows this type of analysis, as spots containing more than a single

molecule initially can be distinguished by their peaks in the KDE. The result is shown in Figure 5.24. The integrated intensity as captured by the camera is $1.5 \cdot 10^4 \pm 6.5 \cdot 10^3$ counts for eGFP and $6.1 \cdot 10^4 \pm 4.5 \cdot 10^3$ counts for mCherry. The error being calculated as the half width at half maximum (HWHM) of the peak. This number is including the background.

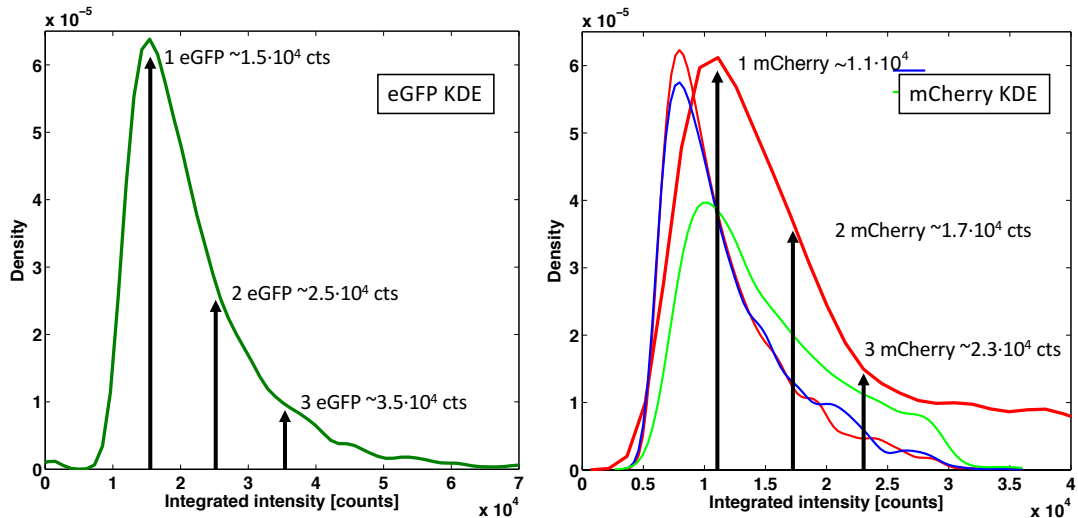
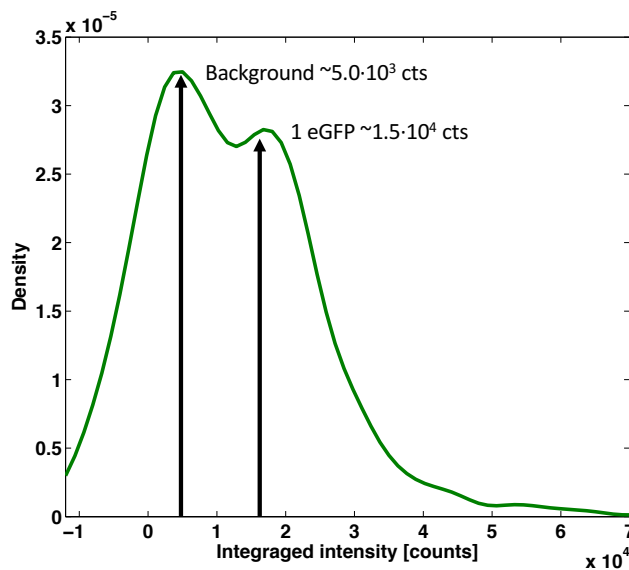


Figure 5.24 – Kernel density estimates of single molecule intensities of eGFP and mCherry. HWHM for eGFP is $6.5 \cdot 10^3$ counts and for mCherry $4.5 \cdot 10^3$ counts. Note that the background is included in this count.

The background is confirmed by similarly analysing the spots using a baseline approach. By including the same spot locations used to produce the results in Figure 5.24, but also including ten frames past the located spot had bleached. This results in



a KDE with a peak centred at the background intensity. As shown in figure 5.25 this gives an integrated background intensity of $5.0 \cdot 10^3$ counts.

Figure 5.25 – A baseline showing the background at $5 \cdot 10^3$ counts

The conclusion is that an eGFP molecule has a characteristic integrated intensity of $1.0 \cdot 10^4 \pm 6.5 \cdot 10^3$ counts and an mCherry molecule has a characteristic integrated intensity of $6.1 \cdot 10^3 \pm 4.5 \cdot 10^3$ counts.

With the knowledge of the characteristic intensity of the fluorescent proteins used as markers, it is possible to determine if a spot detected in a living cell is a single or a small cluster of fluorophores. In Figure 5.26 a diffusing spot identified as Mig1-eGFP is shown in two consecutive frames, separated by 10 ms, as it is tracked using the ADEMS software.

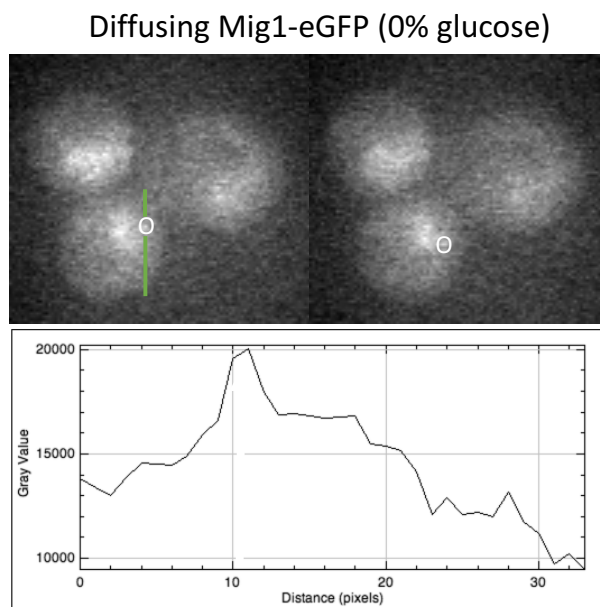


Figure 5.26 – Tracking a spot identified as delocalised Mig1-eGFP in two consecutive frames after the cell having been transferred to a low glucose environment. The intensity plot is along the green line cross-section; the white circle pinpoints the spot tracked.

The cell has been transferred to a low glucose environment from having been in a high glucose environment. The spot was found outside the nucleus. The two frames were taken from a dynamic environment experiment with multi-frame timepoints. In practice, few trajectories are longer than 2-3 frames owing to the fast photobleaching of the fluorophores and to the inherent four-dimensional nature of the experiments. Only fluorophores within the relatively shallow depth of field (~ 350 nm as mentioned in section 5.2, see Figure 5.3) can be resolved, so if a detected spot diffuses out of this volume between frames, it will not be marked as a trajectory.

Astigmatism as described in chapter 4 can be used to track fluorophores some distance outside this narrow slice through an up to $\sim 5 \mu\text{m}$ diameter cell to counter the effect of this limitation.

However, a different approach (Adam J. M. Wollman & Leake 2015) was developed in our group during the course of my work that suited the single frame technique described in section 5.4.2 well. The technique is called *CoPro* (Concentration of Proteins). If the diffusion of specific proteins is ignored the actual number of molecules in a cell can still be estimated. The extended number of timepoints gives an insight into the dynamics over time.

5.5.2 Counting proteins in single cells

The next natural step was to follow the flows of proteins as a function of the environmental transitions. The CoPro approach was used to follow the stoichiometry of Mig1 in the BY4741 strain as a function of glucose concentration.

CoPro estimates the number of molecules in a cell by knowing the characteristic intensity of a single molecule, first finding spots in a field of view, counting them separately and then using an estimate of how many are out of the depth of field volume by analysing the added background from the out-of-plane molecules. The properties of this addition are calculated by using a simulated PSF of a fluorescent molecule and its contribution depending on its position in the cell and then use this as the basis for the estimate of what is called *the Pool*, i.e. any fluorescent molecule that cannot be directly observed as a spot.

However, as due to photobleaching, the number of bright proteins will not remain constant it is necessary to compensate for the photobleaching. The duration of an experiment is only 15 minutes and during that period the number of proteins that are degraded and the number of new proteins maturing is low so the assumption is that the number of proteins in any one cell is constant for the duration of the experiment and the first frame is used as the baseline and subsequent frames are corrected to this number.

An effect that is only important when imaging bursts of more than one frame per channel at a timepoint is the photobleaching within one frame may be to some extent reversible (Remington 2006) and it is necessary to create a correction curve for every time point. See Figure 5.27 for an example of correction factors for a data set with six timepoints of five frames each.

Internal bleach correction using the first frame of the first timepoint as the baseline. X-axis here is time exposed. Every point here is calculated from the mean of the sum of the copy numbers in the compartments within a frame.

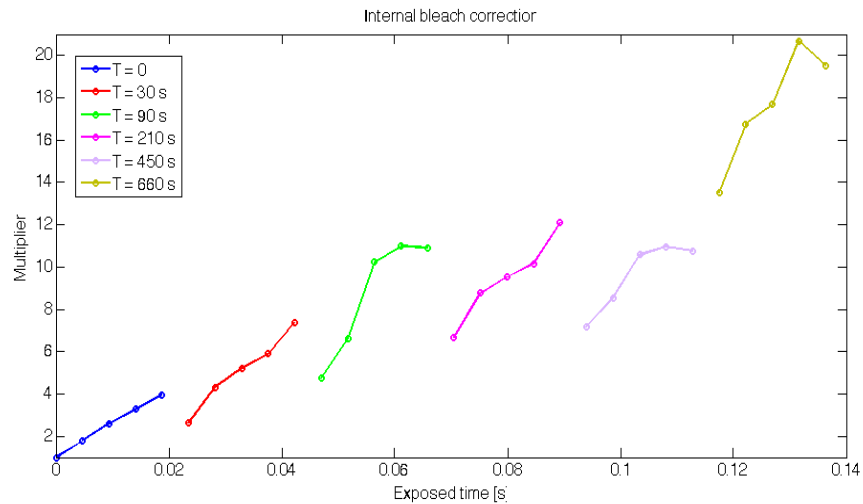


Figure 5.27 – Internal bleach correction for a data set with six timepoints of five frames.

In Figure 5.28 an experiment is shown where a mutant BY4741 is having Mig1-eGFP moving between the cytosol and the nucleus upon being subjected to a high glucose environment after having been acclimatised to a low glucose environment. This data is also presented in our paper “Transcription factor clusters regulate genes in eukaryotic cells” (Wollman et al. 2016), see appendix B.

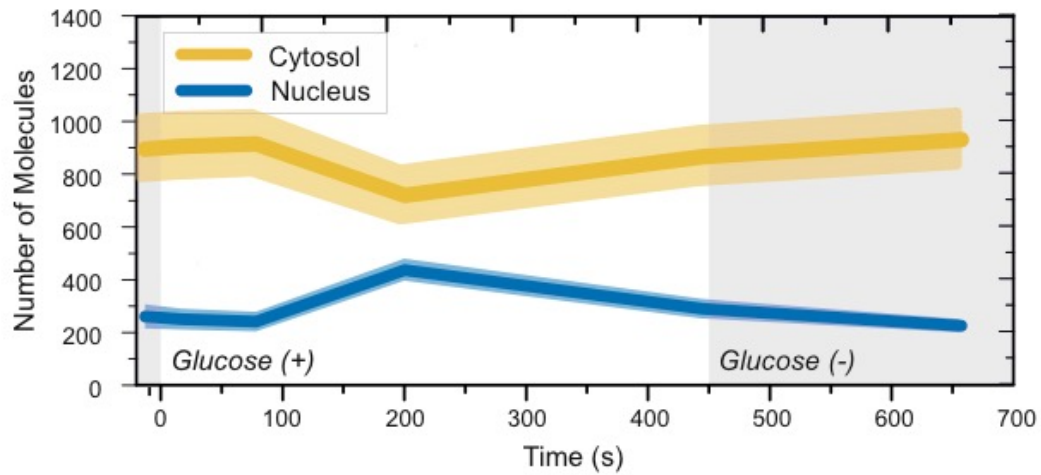


Figure 5.28 – Total Mig1 content by compartment during a There-and-back-again type experiment, following the migration of Mig1-eGFP between the nucleus and the cytosol. (+) is 4% glucose and (-) is 0% glucose. The cells were transferred from a low glucose environment to high glucose after the first timepoint and were returned to the low glucose environment after 450 s. A final acquisition was made after 660 s, 210 s after the return to low glucose.

6 Conclusions, discussion and future work

With the research presented in this thesis I have shown how it is possible to build a bespoke single-molecule fluorescence microscope system capable of imaging dynamic signalling processes in living eukaryote cells. Here the model organism *Saccharomyces cerevisiae* was used. I have here shown how several techniques can be combined to achieve high-quality imaging of transcription factor translocation in living eukaryotic cells with a high enough sampling speed to capture diffusion events at physiological rates and simultaneously estimate the absolute number of up to two different types of proteins and their location by intra-cellular compartment – nuclear and cytosolic content.

The benefits of being able to image protein-protein and protein-DNA interactions in real time are many and the potential is immense. By focussing on signalling pathways that are conserved between eukaryotes, a better understanding of mammalian signalling is on the horizon and potential near future medical benefits are not an impossibility.

The microscope system I developed has been proven to be capable of imaging at full frame rates of up to 200 frames per second with single colour laser illumination and half that, 100 frames per second, with true dual colour alternating frame laser excitation (ALEX). Technically, the potential exists to image even faster. Rates of near double that frame rate may be theoretically possible, but the camera is nearing its practical limits at this point, as the possible region of interest is diminishing for every speed increase in this regime. Also, the fluorescent proteins used here are nearing their useful limits even at the rates used in this thesis with the Evolve 512 delta EMCCD camera acquiring with an electronic gain of 300x, due to their photophysical

limitations in emitting only a finite number of photons, typically $\sim 10^6$ for GFP, before irreversibly photobleaching.

The microscope system also has an axial resolution enhancement modification with an astigmatic imaging module. The way the system was built, the microscope can easily be switched between a high-speed 4D microscopy mode with superresolution capabilities and a conventional high-resolution, high-speed mode.

The data acquired confirms translocation behaviour of the studied kinases and transcription factors of *S. cerevisiae* which was reported previously but using bulk ensemble biochemical methods or slow and imprecise fluorescence imaging (Lutfiyya et al. 1998; Ahuatzki et al. 2007; Bendrioua et al. 2014; Almquist et al. 2015). Using the novel *CoPro* method, a new level of precision in determining the instantaneous copy number of tagged proteins has been achievable, on a cell by cell basis. It has also shown some so far undocumented clustering effects in cells that are both fully functional and deletion mutants. The larger clustering found specifically in *snf1Δ*-deletion mutants is much different from the clustering in the undeleted strains and would benefit from future further examination.

6.1 Next steps

There are two intimately interconnected aspects of the research presented in this thesis that will be interesting to follow up in order to gain further knowledge: (i) the continuing investigation of various aspects of yeast signalling, and (ii) the improvement of the microscope system. To gain further insight into the biology of eukaryote metabolic processes both aspects will prove important. The outlook is best divided into the following two categories, where the furthering of biological research is the goal for which the microscope development is a means. A wide variety of new

lines of inquiry can easily be followed directly using the same methodology described here with little or no tinkering with the microscope system. With some minor improvements, in software, hardware or both, the microscope can be made even more useful and its capabilities enhanced to capture images of behaviour yet unknown.

Examples of software improvements include modified image sequence timing. Hardware improvement examples include added autofocus and imaging of polarisation components of fluorescence images.

6.1.1 There is more to see in yeast

The novel concept of combining techniques to get true transcription factor stoichiometry from image data gathered while cells are adapting to new conditions will prove an important step in understanding how cell adaptation in response to signalling is functioning *in vivo*.

The near future has a set of experiments lined up that will complement the set that has been presented here. A range of *S. cerevisiae* mutants with proteins related to the pathways studied here is already available and awaits investigation. New research would ideally involve probing the interaction of other repressor proteins with DNA, other upstream kinases and other transcription factors.

One set of experiments that potentially will be very interesting will involve the use of specific mutant strains sensitive to chemical inhibitors acting on key interactions in the signalling chain. A series of investigations of the dynamic behaviour of cells being exposed to inhibitors at varying points during the adaptation process might give further insight into the mechanisms responsible for cell adaptation to new environments.

Further investigations of the clustering effect found (Wollman et al. 2016) should be pursued. The finding of very large clusters in the Snf1 Δ deletion mutant is interesting and merits an in-depth study. These clusters are much larger than the functional clusters found and described here and in the paper and may very well have fundamentally different origins. Only a proper investigation and analysis can shed light on this matter.

6.1.2 Microscope developments to consider

A few improvements to the microscopy system can with varying degrees of ease be implemented on the current setup. Modifications that could potentially improve several aspects of its performance.

A modified illumination sequence could be beneficial. Having a multitude of fluorescent proteins will result in targets with varying photostability. A clear example was shown in this thesis, with eGFP being more stable than mCherry. A modified sequence in which the alternating illumination timing sequence is not 1:1 but adjusted e.g. to offset differences in photostability. Using e.g. a 2:1 green to red frame interval would offset the difference between eGFP and mCherry (Shaner et al. 2005). The trade-off is a lower spatiotemporal resolution of red particle localisation having a 15 ms frame period with a retained total of 200 frames per second. A bonus would be the *higher* spatiotemporal resolution of the green channel tracking having two green frames back to back between every two red frames. An example frame disposition is shown in Figure 6.1. The example is matching the single frame per timepoint disposition used in chapter 5.4 (c.f. figure 5.11).

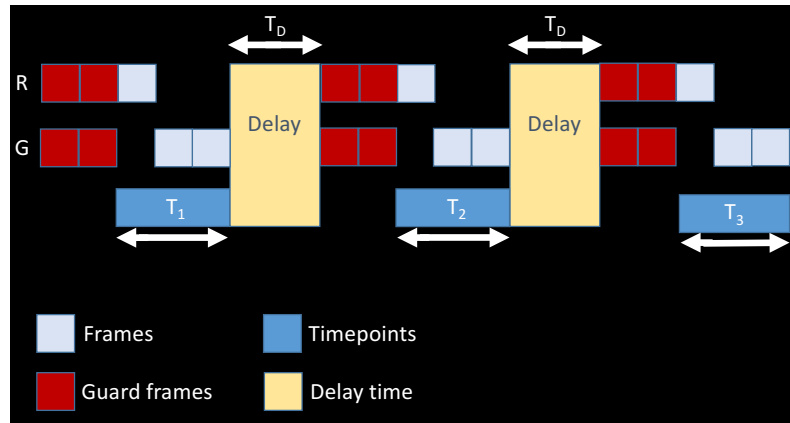


Figure 6.1 – Example of alternate frame timing with a 2:1 ratio of green to red frames. The rest of the sequence is based on the ‘one shot’ per timepoint method.

Many other sequence timings can be envisioned, with the frame ratios, duty cycles and power levels adjusted to specific tasks. Proteins known to be bound or confined may not need to be probed as frequently. One example of this is the use of Nrd1-mCherry as a nuclear marker. The localization of proteins with high diffusion rates could be sampled more frequently to provide better trajectories for analysis.

The microscope has a secondary beam path, initially adjusted to provide a diffraction limited spot in the sample plane. This can be used to perform fluorescence recovery after photobleaching (FRAP) type experiments. At present this feature is manually controlled with little synchronisation with the rest of the system. By evolving the CellBild control software to incorporate timed excitation path selection with the laser pulse control, a high precision FRAP imaging system could be integrated with diffusion tracing experiments.

Potentially the secondary path can further be repurposed for e.g. total internal reflection fluorescence (TIRF) microscopy, a mode that is useful for investigating

surface proteins. In the scope of glucose sensing, it could be used for probing e.g. a tagged hexose transport protein (Hxt) (Bendrioua et al. 2014).

For longer time series one addition to the setup that would greatly improve the results is to implement an autofocus method. Introducing this would remove the issues with axial drift that are hard to avoid during longer time series. The drift normally occurs during the first few minutes, so the method of focussing early and leaving the microscope to “settle” and then adjust the focus with the nano-piezo stage has proven a good first step. However, an automatic system would remove the need for waiting and the inaccuracies of the human eye and provide a well-defined focal level. An infrared sensing system could be fitted to the microscope in its current state and use the nano-piezo stage to make necessary axial corrections.

A major improvement in tracking and counting molecules could potentially be made by integrating astigmatic imaging with CoPro estimation. This would require a reworking of the CoPro code base to use modified point spread function models that take into account the astigmatic effects on the image.

An untested idea for future trials is introducing imaging of the polarisation direction of emitted fluorescence. An unconstrained fluorescent protein in solution will rotate within nanoseconds and the emitted light from such a molecule is not possible to analyse with respect to polarisation at millisecond range exposure times used in the type of experiments described here. However, with sufficient stiffening of the linker between the fluorescent proteins and the active proteins (e.g. Mig1), the orientation of a construct may last for long enough for valid data to be acquired. The effect of clustering, dwell times before nuclear membrane passage (Wollman et al.

2016) and binding to DNA, all lowers the motility of the target proteins and also potentially the attached fluorescent protein.

Wollaston or Nomarski prisms (see Figure 6.2) are two of the key components in DIC imaging and a slider holder for such a prism is integrated into the objective lens turret. Such a prism divides incoming light into an ordinary and an extraordinary path. The effect is that an unpolarised point source imaged through the prism will be deformed into an image resembling a figure ‘8’. If the light is polarised, depending on the orientation of the polarisation the image is expected to be varying between top heavy to bottom heavy with a symmetric appearance upon 45° or circular polarisation.

It may be possible to image fluorescence through a DIC prism slide and achieve this effect on the emission. This approach could provide insight into the structure of clusters and the location and direction of nuclear binding sites by measuring the weights of the two ends of the image of a spot. If fluorophore alignment can be made to last long enough, this approach may prove very useful to investigate e.g. conformational changes in clusters.

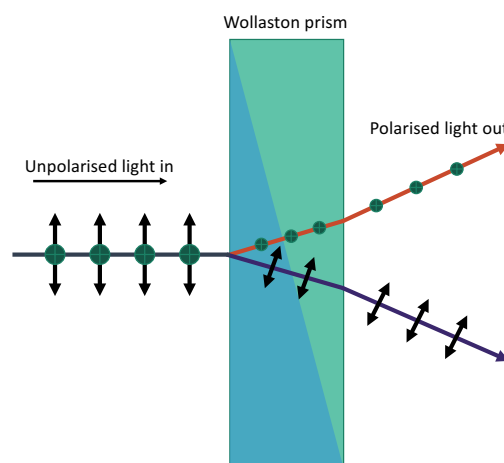


Figure 6.2 – Function of a Wollaston prism

My research leading up to this thesis has by necessity been divided into two eras: the first year, spent in Oxford where I developed the outline of the microscope system that after a physical relocation of all lab equipment to York, marking the beginning of the second era, evolved into the high precision instrument it is today. The move necessitated the disassembly of the microscope to move the equipment to York. A fresh start could be had upon arrival and once all equipment could be reassembled, a new instrument grew out of the old machine. Several improvements, necessary to allow the dual colour capabilities to achieve their full potential, to increase the frame rate and to introduce secondary illumination modes could be naturally factored into the new assembly.

Appendices

APPENDIX A – CellBild software excerpts

In this appendix, some key areas of the LabView source code for microscope control are reproduced. For a full overview the sourcecode is available and can be downloaded from: <https://sourceforge.net/projects/york-biophysics>

This appendix will use the following structure: Any software layouts will follow programmatic flow which is generally from left to right. There are a few instances when this cannot be followed and any convolutions will be commented whenever the flow is nontrivial.

The main application (CellBild v6.3) is covered first and then follows the Camtech pump control subroutines and finally the Mad City Labs nano-piezo positioning stage control interface.

A.1 CellBild version 6.3

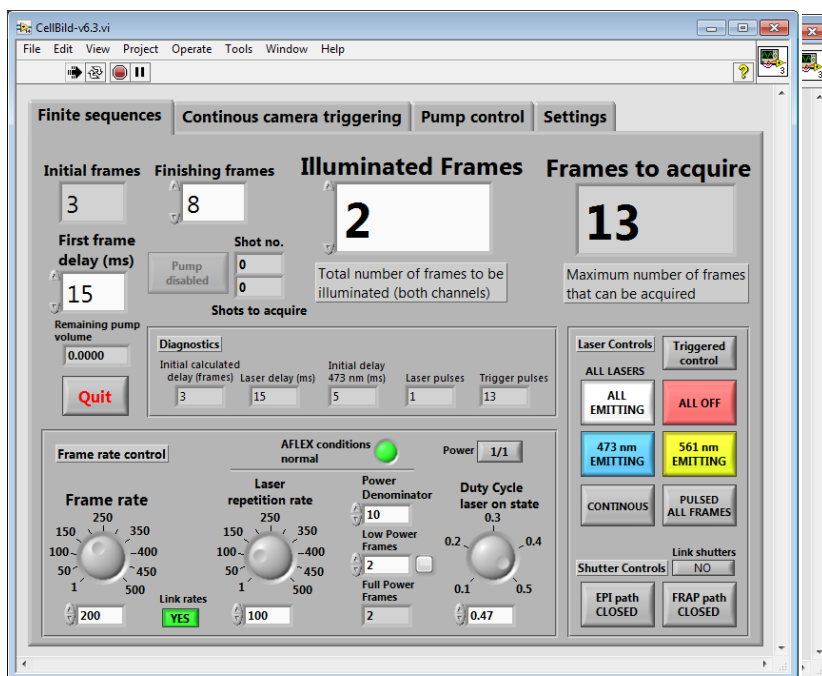


Figure A.1 – CellBild main interface. Startup pane.

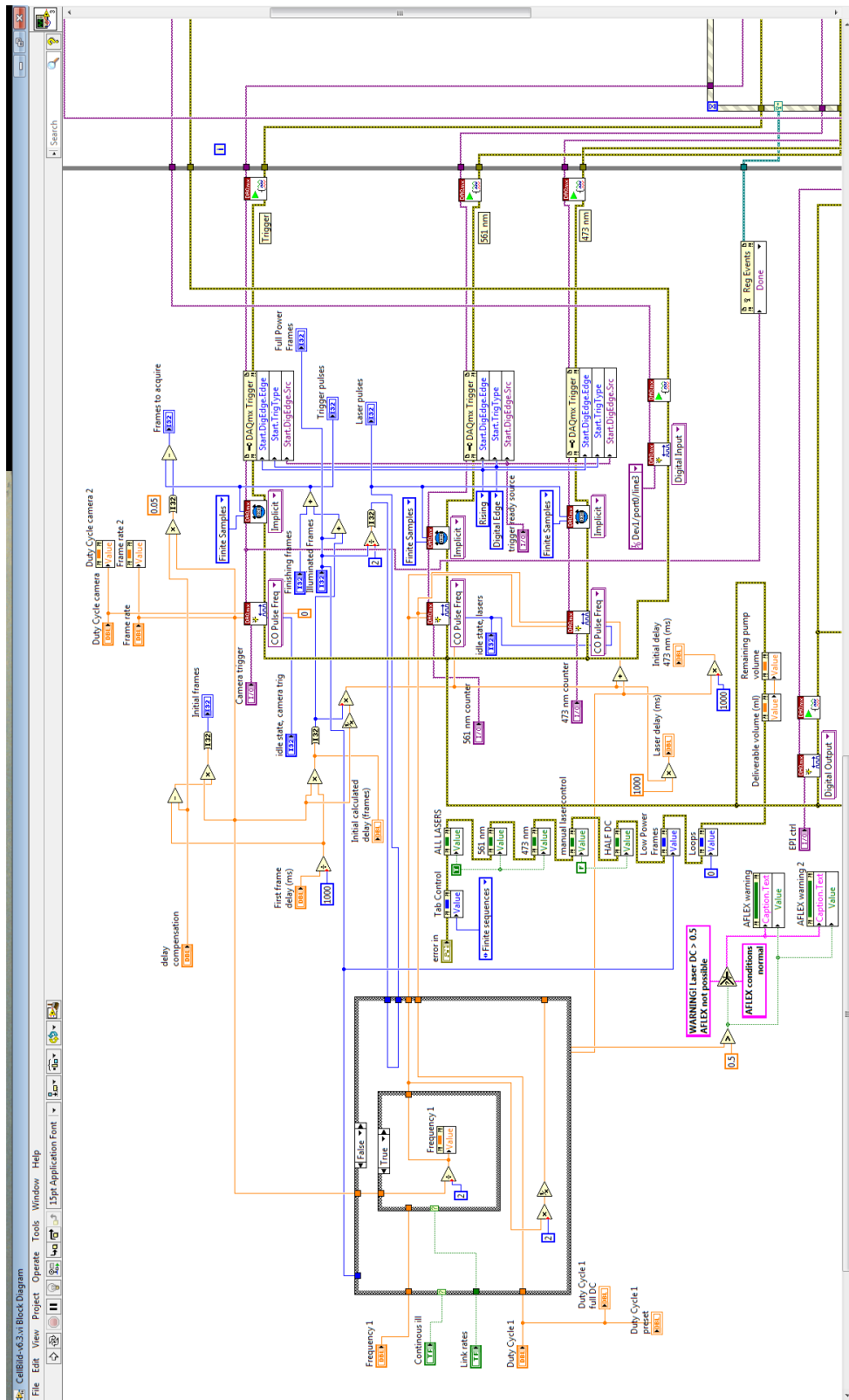


Figure A.2 – Program start. Initialisation of various controls and constants.

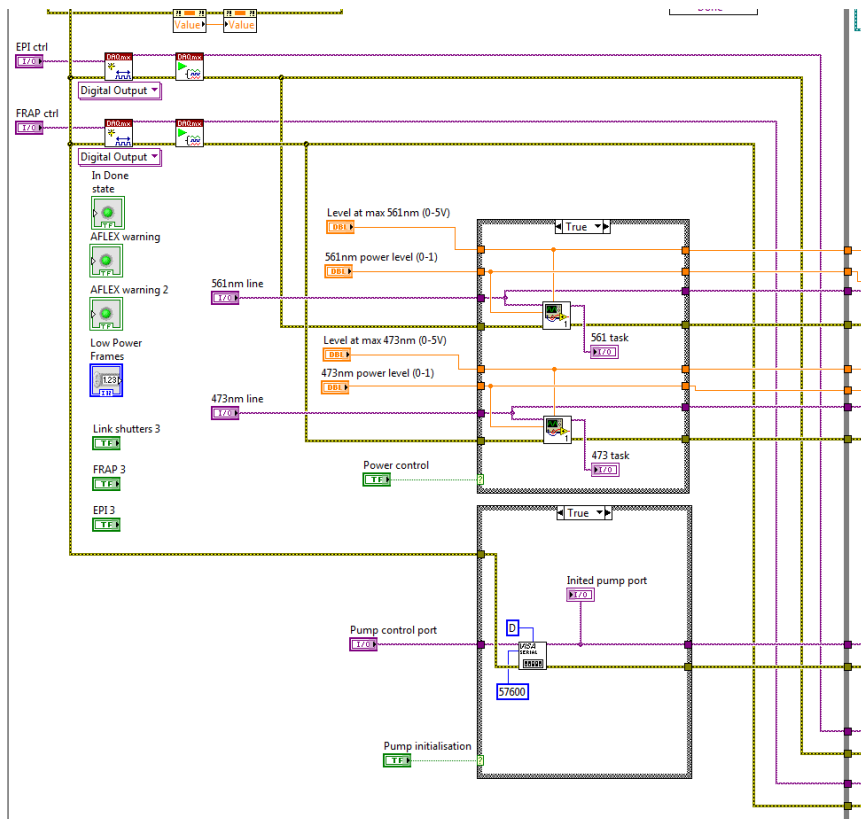


Figure A.3 – Further initialisation. Programmatically located directly below the region in Figure A.2.

After the initialisation shown in Figure A.2-Figure A.3 The program enters the main control loop shown in the following figure. Prominent features are from top to bottom: The case structure triggering the automatic pump control; one of the case structures controlling the laser emission state, this structure makes sure that the emission state is updated if any input is made since the last iteration since; the bottom shows the event triggered state dependent case structure. The whole interface is highly modal so much of the stateful control is based on the 37 events handled here.

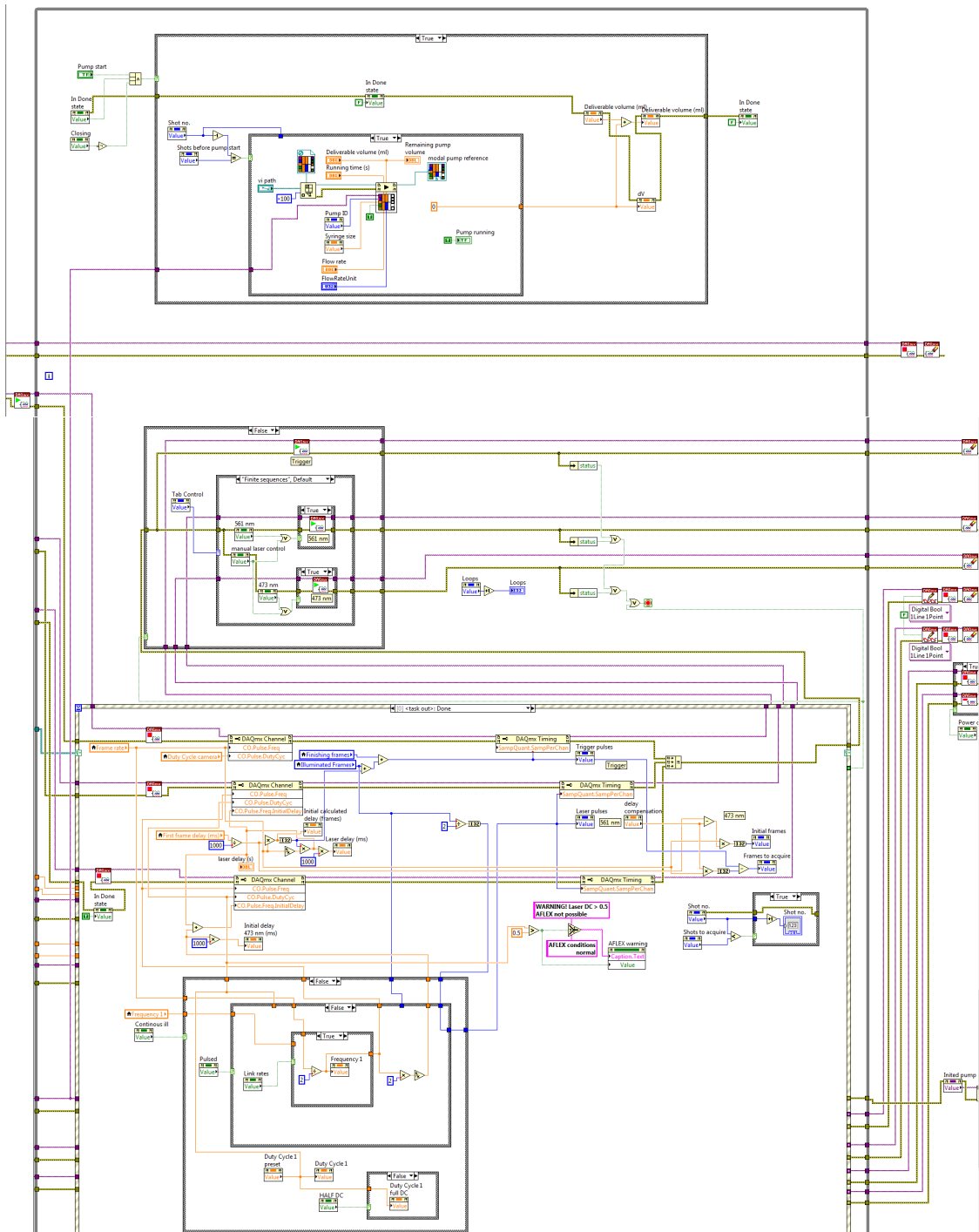


Figure A.4 – CellBild 6.3, main loop.

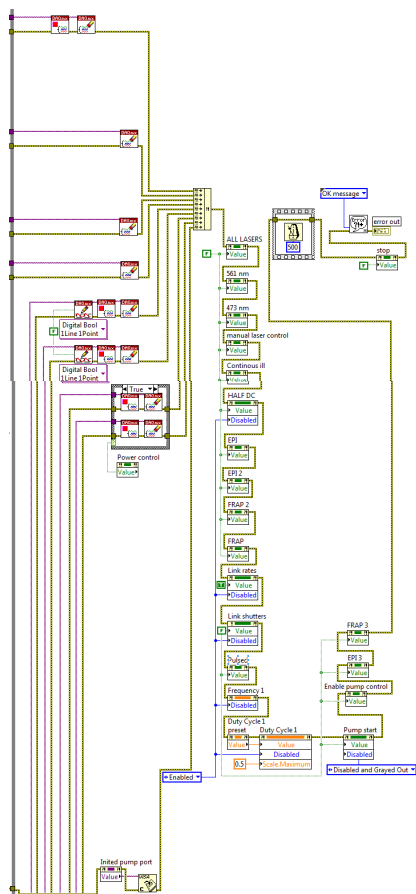


Figure A.5 – Closing down procedures. To avoid lingering handles or other references remaining in unused memory all Daq-card- and serial interfaces are gracefully closed and released before the application exits.

A.2 Pump control sub-VI structures

CellBild has two specialised control VI that handles interactions with the SPM100 syringe pump used for microfluidics experiments. They are similar in internal structure, but one is intended for the automatic control of infusion and its only user accessible feature is an Abort button. The second is intended for manual control and has a full set of controls, letting the user change infusion speed and direction. The following Figure A.6 and Figure A.7 are the program structures for the pump controls.

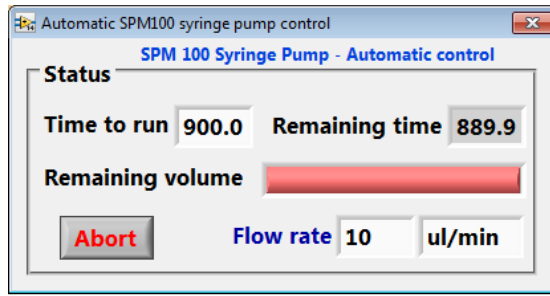
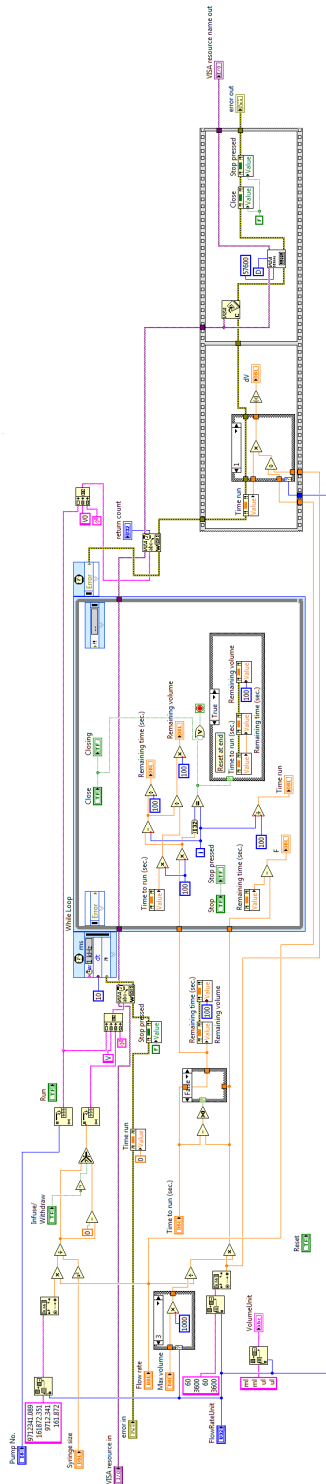


Figure A.6 – Automatic pump control interface

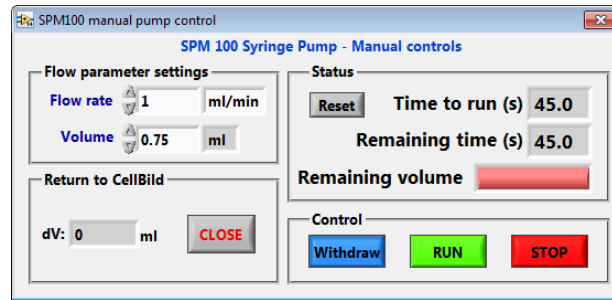
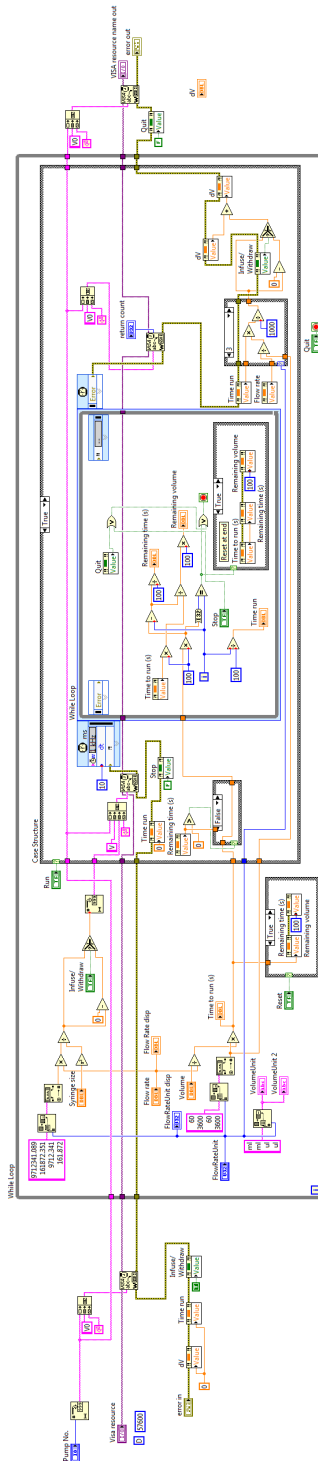
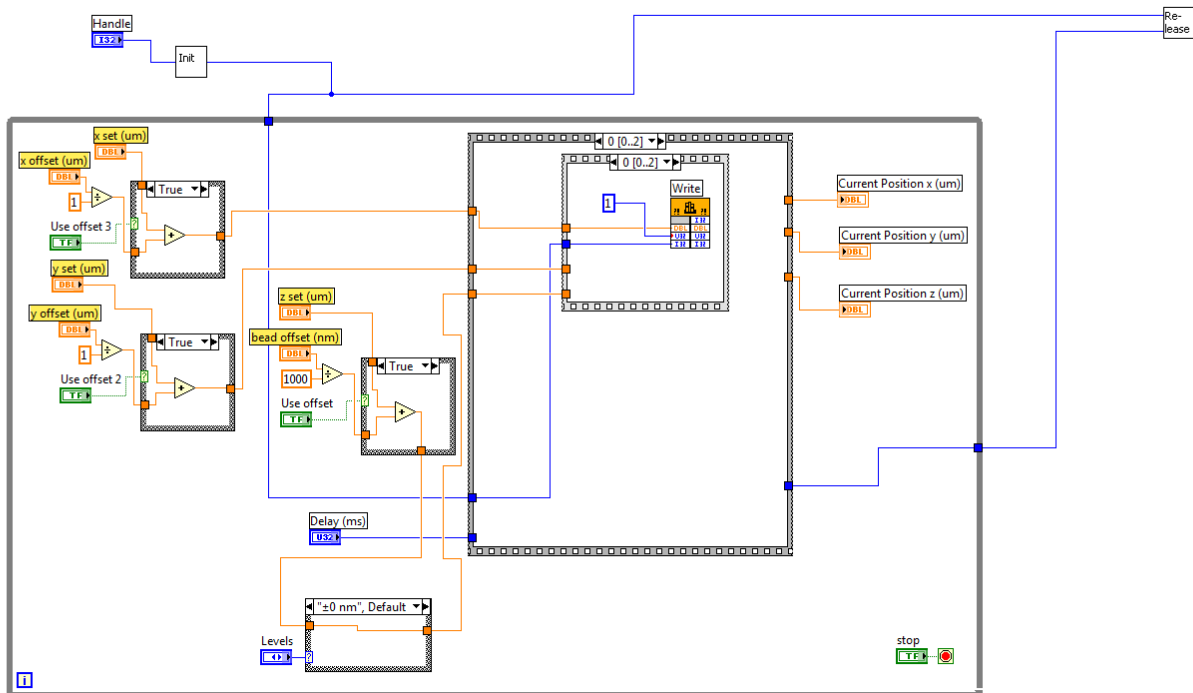
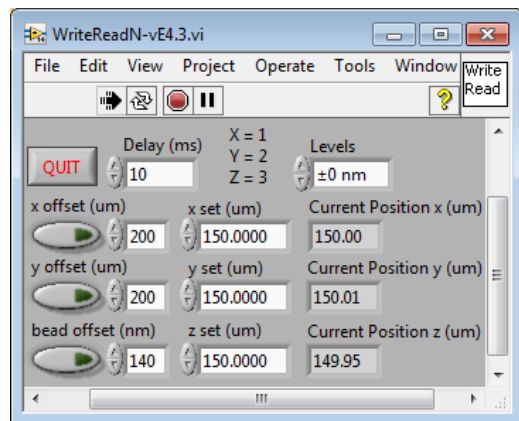


Figure A.7 – Manual pump control interface

A.3 Mad City Labs nano-piezo positioning stage control

The nano-piezo stage used for fine positioning and focussing is controlled from a separate piece of software shown here. The offset buttons can be adjusted to move the stage a preset distance at the touch of a button.

Figure A.8 – Control interface for the nano-piezo positioning stage



APPENDIX B

Transcription factor clusters regulate genes in eukaryotic cells

Adam J. M. Wollman, Sviatlana Shashkova, Erik G. Hedlund,
Rosmarie Friemann, Stefan Hohmann, Mark C. Leake

Paper submitted and in review

My own unique contributions to this work were: (i) Design, planning and execution of microfluidics experiments; (ii) Analysis of data from these experiments. (iii) I wrote the corresponding section.

Transcription factor clusters regulate genes in eukaryotic cells

Adam J. M. Wollman^{1,4}, Sviatlana Shashkova^{2,4}, Erik G. Hedlund¹, Rosmarie Friemann², Stefan Hohmann^{2,3}, Mark C. Leake^{1*}

¹Biological Physical Sciences Institute, University of York, York YO10 5DD, UK

²Department of Chemistry and Molecular Biology, University of Gothenburg, 40530 Göteborg, Sweden.

³Department of Biology and Biological Engineering, Chalmers University of Technology, 41296 Göteborg, Sweden.

⁴Authors contributed equally.

*Correspondence: mark.leake@york.ac.uk.

SUMMARY

Transcription is regulated through binding factors to a gene's promoter to activate or repress expression; however, the mechanisms by which factors find targets and regulate expression remain unclear. Using single-molecule fluorescence microscopy, we determined *in vivo* stoichiometry and spatiotemporal dynamics of a genomically encoded GFP tagged repressor at wild type levels from a paradigm signal transduction pathway of *Saccharomyces cerevisiae*. We observe oligomeric repressor clusters localize dynamically from the cytoplasm and bind to nuclear promoter targets upon extracellular signal detection, correlated to repression of target genes. Our results indicate a clear functional link between transcription factor clusters and gene regulation. *In vitro* and structural analysis on reconstituted repressor indicate clusters are stabilized by depletion forces between intrinsically disordered sequences. We observed similar clusters of a co-regulatory activator of a different pathway. This supports a generalized cluster model that can reduce promoter search times through intersegment transfer while stabilizing gene expression.

INTRODUCTION

Cells respond to their environment through gene regulation involving transcription factors. Those factors bind to DNA targets of a few tens of base pairs (bp) length inside ~500-1,000bp promoter sequences to repress/activate expression, involving single (Jacob & Monod 1961) and multiple (Gertz et al. 2009) factors, culminating in regulating target genes. The mechanism for finding targets in a genome ~six orders of magnitude larger is unclear since free diffusion followed by capture is too slow to account for observed search times (Berg et al. 1981). Target finding may involve heterogeneous mobility including nucleoplasmic diffusion, sliding and hops along DNA up to ~150bp, and longer jumps separated by hundreds of bp called intersegment transfer (Mahmutovic et al. 2015; Halford & Marko 2004; Gowers & Halford 2003).

In eukaryotes, factor localization is dynamic between nucleus and cytoplasm (Whiteside & Goodbourn 1993). Although target binding sites in some cases are known to cluster in hotspots (Harbison et al. 2004) the assumption has been that factors themselves do not function in clusters but as single molecules. Realistic simulations of diffusion and binding in the complex milieu of nuclei suggest a role for multivalent factors to facilitate intersegment transfer by enabling DNA segments to be connected by a single factor (Schmidt et al. 2014).

The use of single-molecule fluorescence microscopy to monitor factor localization in live cells has resulted in functional insight of gene regulation (Li & Xie 2011). Fluorescent protein reporters in particular have revealed complexities in mobility and kinetics in bacterial (Hammar et al. 2012) and mammalian cells (Gebhardt et al. 2013) suggesting a revised view of target finding (Mahmutovic et al. 2015).

Key features of gene regulation in eukaryotes are exemplified by glucose sensing in budding yeast, *Saccharomyces cerevisiae*. Here, regulation is achieved by factors which include a repressor called Mig1, a Zn finger DNA binding protein (J O Nehlin et al. 1991) that acts on targets including *SUC2* and *GAL* genes (Frolova 1999; Lutfiyya et al. 1998). Mig1 is known to localize to the nucleus in response to increasing extracellular glucose (De Vit et al. 1997), correlated to its dephosphorylation (Bendrioua et al. 2014). Glucose sensing is particularly valuable for probing gene regulation since the activation status of factors such as Mig1 can be controlled reproducibly by varying extracellular glucose. Genetic manipulation of the

regulatory machinery is also tractable, enabling native gene labeling with fluorescent reporters for functioning imaging studies.

We sought to explore functional spatiotemporal dynamics and kinetics of gene regulation in live *S. cerevisiae* cells using its glucose sensing pathway as a model for signal transduction. We used single-molecule fluorescence microscopy to track functional transcription factors with millisecond sampling to match the mobility of individual molecules. We were able to quantify composition and dynamics of Mig1 under physiological and perturbed conditions which affected its ability to alter its phosphorylation state. Similarly, we performed experiments on a protein called Msn2 (Lin et al. 2015), which functions as an activator for Mig1 target genes but controlled by a different pathway. By modifying the microscope, we were also able to determine turnover kinetics of transcription factors at their nuclear targets.

The results, coupled to models we developed using chromosome structure analysis, indicated unexpectedly that the functional component which binds to promoter targets operates as a cluster of transcription factor molecules with stoichiometries of ~6-9 molecules, as opposed to individual molecules. We speculated that these functional clusters in live cells were stabilized through interactions of intrinsically disordered sequences which we identified both in the repressor and activator, facilitated through cellular depletion forces. We were able to mimic those depletion forces in *in vitro* single-molecule and circular dichroism experiments using a molecular crowding agent. Our novel discovery of factor clustering has a clear functional role in facilitating factors finding their binding sites through intersegment transfer, as borne out by simulations of multivalent factors (Schmidt et al. 2014); this addresses a long-standing question of how transcription factors efficiently find their targets. This clustering also functions to reduce off rates from targets compared to simpler monomer binding. This effect improves robustness against false positive detection of extracellular chemical signals, similar to observations for the monomeric but multivalent bacterial LacI repressor (Mahmutovic et al. 2015). Our findings potentially reveal an alternative eukaryotic cell strategy for achieving this effect but using an entirely different structural mechanism.

RESULTS

Single-molecule imaging reveals *in vivo* clusters of functional Mig1

To explore the mechanisms of transcription factor targeting we used millisecond Slimfield single-molecule fluorescence imaging (Plank et al. 2009; Reyes-Lamothe et al. 2010a; Badrinarayanan et al. 2012) on live *S. cerevisiae* cells (Figure 1A and S1). We prepared a genomically encoded green fluorescent protein (GFP) reporter for Mig1 (Table S1). To enable nucleus and cell body identification we employed mCherry on the RNA binding nuclear protein Nrd1. We measured cell doubling times and expression to be the same, within experimental error, as the parental strain containing no fluorescent protein (Figure S2A), indicating functional fusions similar to previous Mig1-GFP fusions (De Vit et al. 1997). We optimized Slimfield for single-molecule detection sensitivity with an *in vitro* imaging assay of surface-immobilized purified GFP (Leake et al. 2006) indicating a brightness for single GFP molecules of ~5,000 counts on our camera detector (Figure S2B). To determine any fluorescent protein maturation effects we performed cell photobleaching while using antibiotic-mediated suppression of expression of additional fluorescent protein, and measured subsequent recovery of cellular fluorescence <15% for fluorescent protein components, corrected for any native autofluorescence, over the timescale of imaging experiments (Figures S2C and S2D).

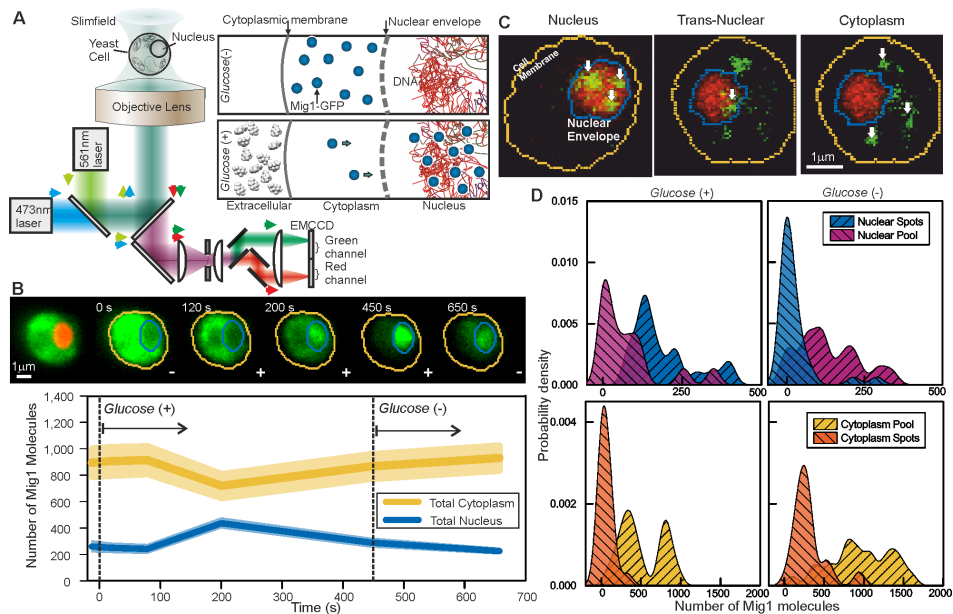


Figure 1. Single-molecule Slimfield microscopy of live cells reveals Mig1 clusters. (A) **Dual-color fluorescence microscopy assay.** (B) **Example of change of Mig1-GFP localization (cyan, upper panel) with glucose for the same cell, Nrd1-mCherry indicated (red, left) mean and SEM errorbounds of total cytoplasmic (yellow) and nuclear (blue) contributions shown (lower panel), n=15 cells.** (C) **Example cells showing nuclear (left), trans-nuclear (center) and cytoplasmic (right) Mig1-GFP localization (green, distinct foci white arrows), Nrd1-mCherry (red) and segmented cell body (yellow) and nuclear envelope (blue) indicated.** (D) **Kernel density estimations for Mig1-GFP content in pool and foci for cytoplasm and nucleus at glucose (+/-), n=30 cells.**

Under depleted (0-0.2%)/elevated (4%) extracellular glucose (-/+), we measured cytoplasmic and nuclear Mig1 localization bias respectively, as reported previously (De Vit et al. 1997), visible by rapidly exchanging extracellular fluid using microfluidics, while observing the same cell (Figure 1B; Supplementary Experimental Procedures). However, our ultrasensitive imaging resolved two novel components under both conditions consistent with a diffuse monomer pool and distinct multimeric foci which could be tracked up to several hundred milliseconds (Figure 1C; Movies S1 and S2; Supplementary Experimental Procedures). We wondered if the presence of foci was an artifact due to GFP oligomerization. To discourage artifactual aggregation we performed a control using another type of GFP containing an A206K mutation (denoted GFPmut3 or mGFP) known to inhibit oligomerization (Zacharias, Violin, Newton, et al. 2002). However, both *in vitro* experiments using purified GFP and mGFP (Figure S2B; Supplementary

Experimental Procedures) and live cell experiments at *glucose* (-/+ (Figures S2E and S2F) indicated no significant difference to foci brightness values (Pearson's χ^2 test, $p < 0.001$). We also developed a genomically encoded Mig1 reporter using green-red photoswitchable fluorescent protein mEos2 (McKinney et al. 2009). Super-resolution stochastic optical reconstruction microscopy (STORM) from thousands of individual photoactivated tracks indicated the presence of foci (Supplemental Experimental Procedures), clearly present in nuclei hotspots in live cells at *glucose* (+) (Figure S1). These results strongly argue that foci formation is not dependent on hypothetical fluorescent protein oligomerization.

We implemented nanoscale tracking based on automated foci detection which combined iterative Gaussian masking and fitting to foci pixel intensity distributions to determine the spatial localization to a lateral precision of 40nm (Miller et al. 2015; Llorente-Garcia et al. 2014). Tracking was coupled to stoichiometry analysis using single GFP photobleaching of foci tracks (Leake et al. 2006) and single cell copy number quantification (Adam J M Wollman & Leake 2015). These methods enabled us to objectively quantify the number of Mig1 molecules associated with each foci, its effective microscopic diffusion coefficient D and spatiotemporal dynamics in regards to its location in the cytoplasm, nucleus or translocating across the nuclear envelope, as well as the copy number of Mig1 molecules associated with each subcellular region and in each cell as a whole. These analyses indicated ~850-1,300 Mig1 total molecules per cell, dependent on extracellular glucose (Figure 1D; Table S2).

At *glucose* (-) we measured a mean ~950 Mig1 molecules per cell in the cytoplasmic pool (Figure 1D) and 30-50 multimeric foci in total per cell, based on interpolating the observed number of foci in the microscope's known depth of field over the entirety of the cell volume. These foci had a mean stoichiometry of 6-9 molecules and mean D of 1-2 $\mu\text{m}^2/\text{s}$, extending as high as 6 $\mu\text{m}^2/\text{s}$. In nuclei, the mean foci stoichiometry and D was the same as the cytoplasm to within experimental error (Student t -test, $p < 0.05$), with a similar concentration. Trans-nuclear foci, those entering /leaving the nucleus during observed tracking, also had the same mean stoichiometry and D to cytoplasmic values to within experimental error ($p < 0.05$). However, at *glucose* (+) we measured a considerable increase in the proportion of nuclear foci compared to *glucose* (-), with up to 8 foci per nucleus of mean apparent

stoichiometry 24-28 molecules, but D lower by a factor of 2, and 0-3 cytoplasmic/trans-nuclear foci per cell (Figures 2A and 2B).

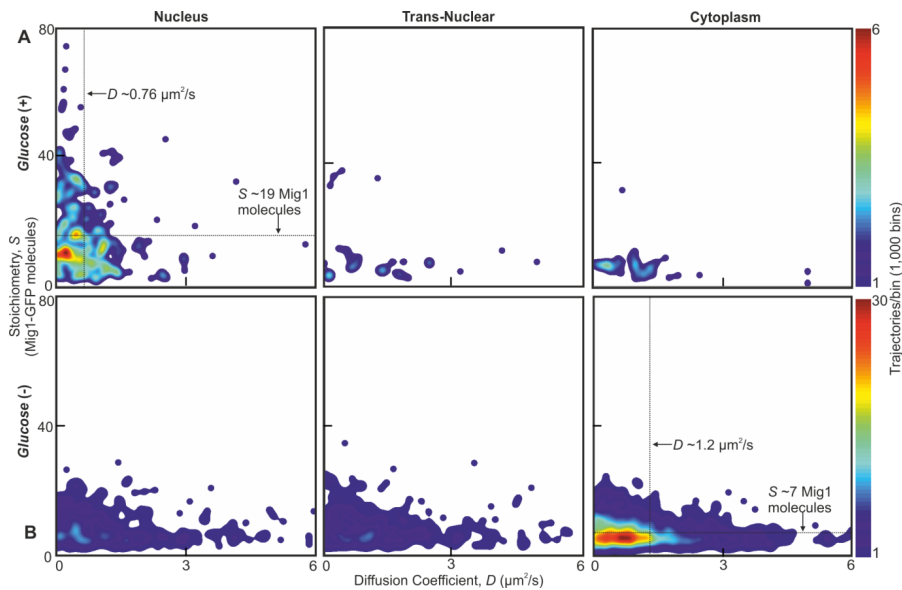


Figure 2. Mig1 foci stoichiometry, mobility and localization depends on glucose. **Heat map** showing dependence of stoichiometry of detected GFP-labeled Mig1 foci with D under (A) glucose (+) and (B) glucose (-) extracellular conditions. Mean values for glucose (+) nuclear and glucose (-) cytoplasmic foci indicated (arrows).

Mig1 cluster localization is dependent on phosphorylation status

To understand how Mig1 clustering was affected by its phosphorylation, without mutating the protein, we deleted the *SNF1* gene which encodes the Mig1-interacting Snf1 kinase, a key regulator of Mig1 phosphorylation. Under Slimfield imaging this strain indicated Mig1 clusters with similar stoichiometry and D as for the wild type strain at *glucose* (+), but with a significant insensitivity to depleting extracellular glucose (Figures 3A, 3B and S1). We also used a yeast strain in which the kinase activity of Snf1 could be controllably inhibited biochemically by addition of cell permeable PP1 analog 1NM-PP1. Slimfield imaging indicated similar results in terms of the presence of Mig1 clusters, their stoichiometry and D , but again showing a marked insensitivity towards depleted extracellular glucose indistinguishable from the wild type *glucose* (+) phenotype (Figure 3C, 3D and S1; Table S2). These results demonstrate that the state of Mig1 phosphorylation does not affect its ability to form

functional clusters, but does alter their localization bias between nucleus and cytoplasm.

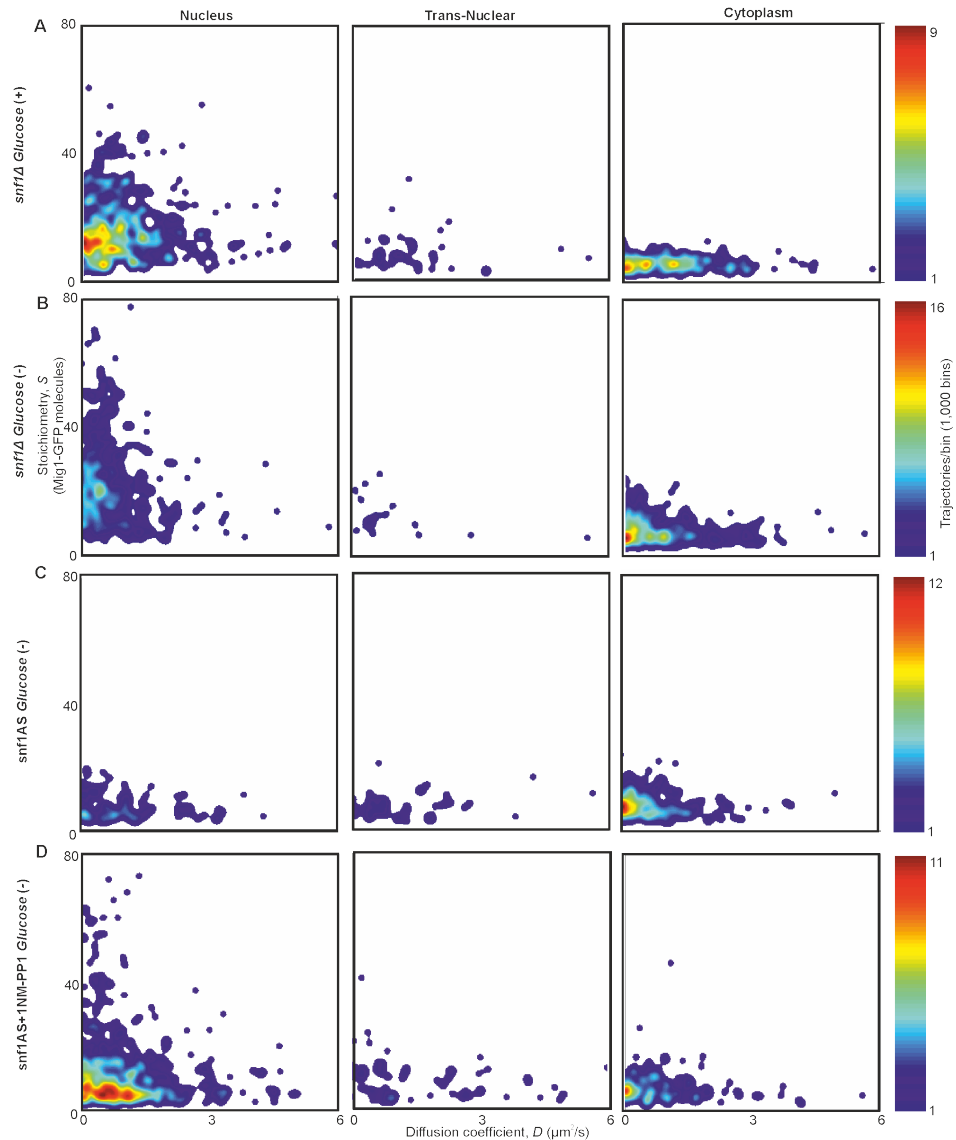


Figure 3. Mig1 phosphorylation does not affect clustering but regulates localization. SNF1 deletion strain under (A) glucose (+) and (B) glucose (-) conditions and the ATP analog INM-PP1 sensitive strain at glucose (-), in the absence (C) and presence (D) of INM-PP1, heat maps showing dependence of stoichiometry of detected GFP-labeled Mig1 foci with D .

Cytoplasmic Mig1 is mobile but nuclear Mig1 has mobile and immobile states

The dynamics of Mig1 between cytoplasm and nucleus is critically important to its role in gene regulation. We therefore interrogated tracked foci mobility. We

quantified cumulative distribution functions (CDFs) for all nuclear and cytoplasmic tracks (Gebhardt et al. 2013) allowing characterization of the diffusional modes underlying the microscopic diffusion coefficients. A CDF signifies the probability that a foci will be a certain distance from its starting point as a function of time while it is tracked, and a mixed mobility population can be modeled as the weighted sum of multiple CDFs characterized by different D (Supplemental Experimental Procedures). Cytoplasmic foci at *glucose* (+/-), and nuclear foci at *glucose* (-), were consistent with just a single mobile population (Figure S3) whose D of 1-2 $\mu\text{m}^2/\text{s}$ was consistent with earlier observations. However, nuclear foci at *glucose* (+) indicated a mixture of mobile and immobile components (Figure 4A). These results, substantiated by fitting two Gamma functions to the distribution of estimated D (Stracy et al. 2015) for *glucose* (+) nuclear foci (Figure 4A, inset), indicate 20-30% of nuclear foci are immobile, consistent with a DNA-bound state, as previously demonstrated for other nuclear transcription factors (Gebhardt et al. 2013). Mean square displacement analysis of foci tracks sorted by stoichiometry indicated Brownian diffusion over short timescales of a few tens of ms but anomalous diffusion over longer timescales $>30\text{ms}$ (Figure 4B; Supplementary Experimental Procedures). These results are consistent with *glucose* (+) Mig1 cluster diffusion being restrained by interactions with nuclear structures and binding to DNA, similar to that reported for other transcription factors (Izeddin et al. 2014; Gebhardt et al. 2013). Here however this interaction is dependent on extracellular glucose despite Mig1 requiring a pathway of proteins to detect its extracellular analyte, unlike the more direct detection mechanism of the prokaryotic *lac* repressor. We conclude that Mig1 clusters bind to the DNA with direct glucose dependence.

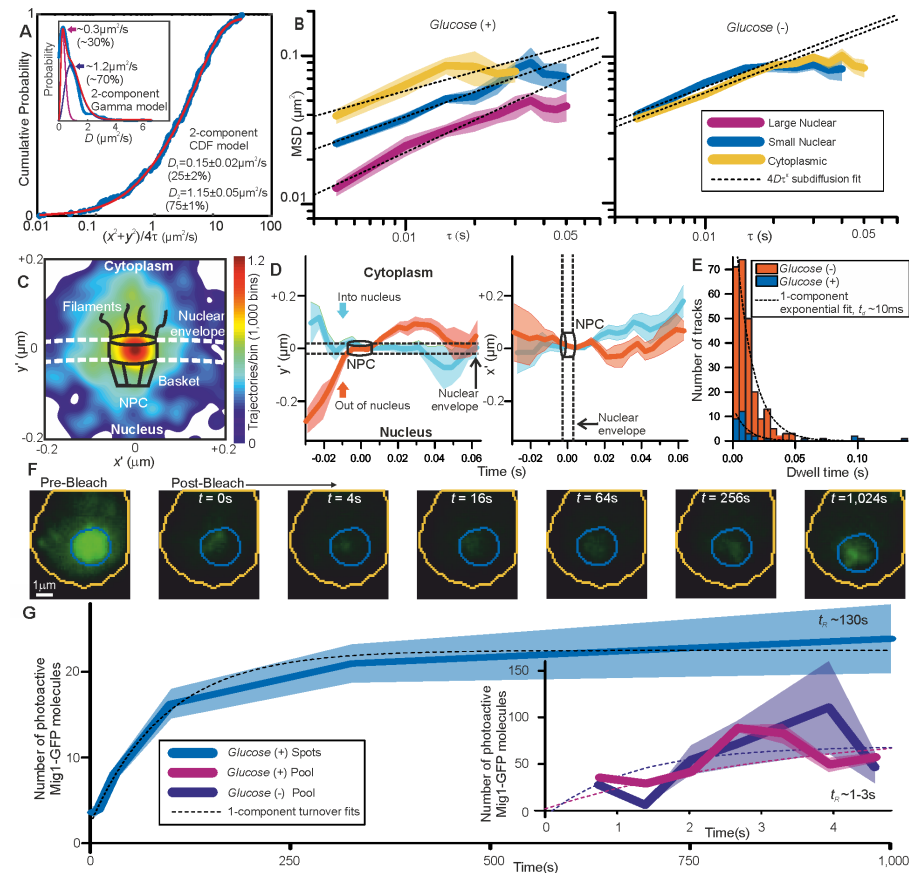


Figure 4. Repressor clusters have heterogeneous mobility depending on localization. (A) Cumulative probability, glucose (+) nuclear tracks, dual Gamma fit to D (inset). (B) Mean MSD from cytoplasmic (yellow), small (blue, stoichiometry ≤ 20 Mig1-GFP molecules) and large nuclear (purple, stoichiometry > 20 Mig1-GFP molecules) foci, SEM indicated, $n=30$ cells. Subdiffusion fits to time intervals ≤ 30 ms (dashed), anomalous coefficient $\alpha=0.4-0.8$. (C) Heat map for trans-nuclear tracks, (D) distance perpendicular and parallel to nuclear envelope with time, (E) dwell times and single exponential fits (dotted). (F) Example glucose (+) single cell FRAP, (G) mean and SEM indicated, $n=5$ and 7 cells for glucose (-/+) respectively.

Mig1 nuclear translocation selectivity does not depend on glucose but is mediated by interactions away from the nuclear envelope

Due to the marked localization of Mig1 towards nucleus/cytoplasm at glucose (+/-) respectively, we asked whether this spatial bias was due to selectivity initiated during translocation at the nuclear envelope, specifically, does the nuclear envelope function as a gate for Mig1? By converting trans-nuclear tracks into coordinates parallel and perpendicular to the measured nuclear envelope position, and synchronizing origins to be the nuclear envelope crossing point, we could compare spatiotemporal

dynamics of different Mig1 clusters during translocation. A heat map of spatial distributions of translocating clusters indicated a hotspot of comparable volume to that of structures of budding yeast nuclear pore complexes (Adam 2001) and accessory nuclear structures of cytoplasmic nucleoporin filaments and nuclear basket (Strambio-De-Castillia et al. 2010), with some nuclear impairment to mobility consistent with restrained mobility (Figure 4C). We observed a dwell in cluster translocation across the 30-40nm width of the nuclear envelope (Figure 4D). At *glucose* (-) the proportion of detected trans-nuclear foci was significantly higher compared to *glucose* (+), consistent with Mig1's localization dynamics. The distribution of dwell times could be fitted using a single exponential function with ~10ms time constant similar to previous estimates for transport factors (Yang et al. 2004). However, although the relative proportion of trans-nuclear foci was much lower at *glucose* (+) compared to *glucose* (-), the dwell time constant was found to be insensitive to glucose (Figure 4E). This insensitivity to extracellular chemical signal demonstrates, surprisingly, that there is no direct selectivity on the basis of transcription factor phosphorylation state by nuclear pore complexes themselves, suggesting that cargo selectivity mechanisms of nuclear transport (Lowe et al. 2010), as reported for a range of substrates, is blind to the phosphorylation state – the nuclear envelope does not function as a gate for phosphorylated Mig1. Coupled with our observation that Mig1 at *glucose* (-) does not exhibit immobility in the nucleus, this suggests that Mig1 localization is driven by changes in Mig1 binding affinity not involving the nuclear pore complex such as to the DNA or to other proteins within or outside the nucleus.

Mig1 nuclear foci bound to targets turn over slowly as whole clusters in >100s

To further understand the mechanisms of Mig1 binding/release during gene regulation we sought to quantify these kinetics at its targets. By modifying our microscope, we could implement an independent focused laser path using the same laser source, enabling us to use fluorescence recovery after photobleaching (FRAP) to probe nuclear Mig1 turnover (Supplementary Experimental Procedures). The focused laser rapidly photobleached GFP content in cell nuclei in <200ms (Figure 4F). We could then monitor recovery of any fluorescence intensity by illuminating with millisecond Slimfield stroboscopically as opposed to continuously to extend the

observation timescale to $>1,000$ s. Using automated foci detection, we could separate nuclear pool and foci content at each time point for each cell. These analyses demonstrated measurable fluorescence recovery for both components, which could be fitted by single exponentials indicating fast recovery of pool at both *glucose* (-) and (+) with a time constant <5 s but a larger time constant at *glucose* (+) for nuclear foci >100 s (Figure 4G). Further analysis of intensity levels at each time point revealed a stoichiometry periodicity in nuclear foci recovery equivalent to 7-9 GFP

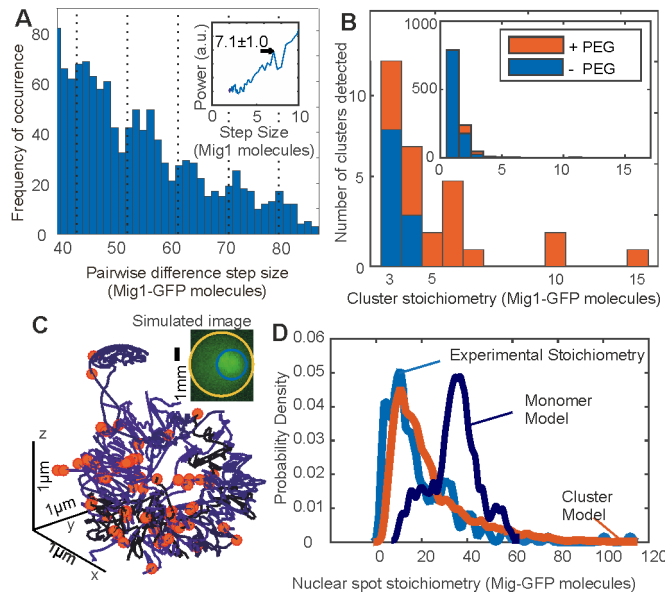


Figure 5. Mig1 clusters are stabilized by depletion forces and bind to promoter targets. (A) Zoom-in on pairwise difference distribution for stoichiometry of Mig1-GFP foci, 7-mer intervals (dashed) and power spectrum (inset), mean and Gaussian sigma error (arrow). (B) Stoichiometry for Mig1-GFP clusters in vitro in PEG absence (blue)/presence (red). (C) 3C model (blue) with overlaid Mig1 promoter binding sites from bioinformatics (red), simulated image based on model with realistic signal and noise added (inset). (D) Cluster (red) and monomer (dark blue) model (goodness-of-fit $R^2 < 0$) for Mig1-GFP stoichiometry compared against experimental data (cyan, $R^2 = 0.75$).

molecules (Figure S4A), but no obvious periodicity in stoichiometry measurable from pool recovery. An identical periodicity to within experimental error was measured from nuclear foci at *glucose* (+) in steady-state (Figure 5A). These periodicity values in Mig1 stoichiometry were consistent with earlier observations for cytoplasmic and trans-nuclear clusters at *glucose* (+/-), and in the nucleus at *glucose* (-), with mean stoichiometry ~ 7 molecules. These data taken as a whole clearly suggest that molecular turnover at nuclear foci of Mig1 bound to its target genes occurs in units of single clusters, as opposed to single Mig1 monomers.

Mig1 clusters are spherical, a few tens of nm wide

Our observations from stoichiometry, dynamics and kinetics, which supported the hypothesis that functional clusters of Mig1 perform the role of gene regulation, also suggested an obvious prediction in terms of the size of observed foci: the physical diameter of a multimeric cluster should be larger than that of a single Mig1 monomer. We therefore sought to quantify foci widths from Slimfield data by performing intensity profile analysis on background-corrected pixel values over each foci image (Supplementary Experimental Procedures). The diameter was estimated from the measured width corrected for motion blur due to particle diffusion in the sampling time of a single image frame, minus that measured from single purified GFP molecules immobilized to the coverslip surface in separate *in vitro* experiments. This analysis revealed diameters of 15-50nm at *glucose* (-), which showed an increase with foci stoichiometry S that could be fitted with a power law dependence S^a (Figure S4B) with optimized exponent a of 0.32 ± 0.06 (\pm SEM). A heuristic tight packing model for GFP labeled Mig1 monomers in each cluster predicts that, in the instance of an idealized spherical cluster, $a = 1/3$. Our data at *glucose* (-) thus supports the hypothesis that Mig1 clusters have a spherical shape. For nuclear foci at *glucose* (+) we measured larger apparent diameters and stoichiometries, consistent with >1 individual Mig1 cluster being separated by less than our measured ~ 200 nm optical resolution limit. This observation agrees with earlier measurements of stoichiometry periodicity for nuclear foci at *glucose* (+). In other words, that higher apparent stoichiometry nuclear foci are consistent with multiple individual Mig1 clusters each containing ~ 7 molecules separated by a nearest neighbor distance < 200 nm and so detected as a single fluorescent foci.

Clusters are stabilized by depletion forces

Since we observed Mig1 clusters in live cells using Slimfield imaging we wondered if these could be detected and further quantified using other methods. However, native gel electrophoresis on extracts from Mig1-GFP cells (Figure S5A) indicated a single stained band for Mig1, which was consistent with denaturing SDS-PAGE combined with western blotting using recombinant Mig1-GFP, and of extracts from the parental cells which included no fluorescent protein reporter (Figure S5B and S5C). Using Slimfield imaging on purified Mig1-GFP *in vitro* under identical

imaging conditions for live cells similarly indicated monomeric Mig1-GFP foci in addition to a small fraction of brighter foci which were consistent with predicted random overlap of monomer images (Supplementary Experimental Procedures). However, on addition of low molecular weight polyethylene glycol (PEG) at a concentration known to mimic small molecule ‘depletion’ forces in live cells (Phillip & Schreiber 2013) we detected significant numbers of multimeric foci (Figure 5B). Depletion is an entropic derived attractive force which results from osmotic pressure between particles suspended in solution that are separated by distances short enough to exclude other surrounding smaller particles. Using purified GFP alone under identical conditions showed no such effect (Figure S5D). These results suggest a hypothesis that clusters present in live cells are stabilized by depletion components that are lost during biochemical purification.

Chromosome structure modeling supports a cluster binding hypothesis

We speculated that Mig1 cluster-mediated gene regulation had testable predictions in regards to the nuclear location of Mig1 at elevated extracellular glucose. We therefore developed quantitative models to simulate the appearance of realistic images of genome-bound Mig1-GFP at *glucose* (+). We used sequence analysis to infer locations of Mig1 binding sites in the yeast genome (Supplementary Experimental Procedures), based on alignment matches to previously identified 17bp Mig1 target patterns (Lundin et al. 1994) which comprised conserved AT-rich 5bp and GC-rich 6bp sequences. In scanning the entire *S. cerevisiae* genome we found >3,000 hits though only 112 matches for likely gene regulatory sites located in promoter regions (Table S3). We mapped these candidate binding sites onto specific 3D locations (Figure 5C) obtained from a consensus structure for budding yeast chromosomes based on 3C data (Duan et al. 2010). We generated simulated images, adding experimentally realistic levels of signal and noise, and ran these synthetic data through the same tracking software as for experimental data. We used identical algorithm parameters throughout and compared these predictions to the measured experimental stoichiometry distributions.

In the first instance we used these locations as coordinates for Mig1 monomer binding, assuming that just a single Mig1 molecule binds to a target. Copy number analysis of Slimfield data (Table S2) indicated a mean ~190 Mig1 molecules per cell

associated with nuclear foci, greater than the number of Mig1 binding sites in promoter regions. In the first instance we assigned 112 molecules to target promoter binding sites, then assigned the remaining 78 molecules randomly to non-specific DNA coordinates of the chromosomal structure. We included effects of different orientations of the chromosomal structure relative to the camera by generating simulations from different projections and included these all in compiled synthetic datasets.

We then contrasted monomer binding to a cluster binding model, which assumed that a whole cluster comprising 7 GFP labeled Mig1 molecules binds a single Mig1 target. Here we randomly assigned the 190 Mig1 molecules into just 27 (i.e. $\sim 190/7$) 7-mer clusters to the set of 112 Mig1 target promoter sites. We also implemented improvements of both monomer and cluster binding models to account for the presence of trans-nuclear tracks. Extrapolating the number of detected trans-nuclear foci in our microscope's depth of field over the whole nuclear surface area indicated a total of ~ 130 Mig1 molecules at *glucose* (+) inside the nucleus prior to export across the cytoplasm. We simulated the presence of these trans-nuclear molecules either using 130 GFP-labeled Mig1 molecules as monomers, or as 18 (i.e. $\sim 130/7$) 7-mer clusters at random 3D coordinates over the nuclear envelope surface (Figure S6).

We discovered that a cluster binding model which included the presence of trans-nuclear foci generated excellent agreement to the experimental foci stoichiometry distribution ($R^2=0.75$) compared to a very poor fit for a monomer binding model ($R^2<0$) (Figure 5D). The optimized cluster model fit involved on average $\sim 25\%$ of promoter loci to be bound across a population of simulated cells by a 7-mer cluster with the remaining clusters located non-specifically, near the nuclear envelope, consistent with nuclear transit. This structural model supports the hypothesis that the functional unit of Mig1-mediated gene regulation is a cluster of Mig1 molecules, as opposed to Mig1 acting as a monomer.

The activator Msn2 also forms functional clusters

We wondered if the discovery of transcription factor clusters was unique to specific properties of the Mig1 repressor, as opposed to being a more general feature of other eukaryotic Zn finger transcription factors. To address this question we prepared a similar genomically encoded green fluorescent protein (GFP) reporter to the Zn

finger protein Msn2 at functional wild type expression levels. Nrd1-mCherry was again used as a nuclear marker (Figure S1). Msn2 acts as an activator and not a repressor, which co-regulates several Mig1 target genes but with the opposite nuclear localization response to glucose (Lin et al. 2015). On performing *in vivo* Slimfield imaging under identical conditions to the Mig1-GFP strain we again observed a significant population of fluorescent Msn2 foci, which had comparable D and stoichiometry to those estimated earlier for Mig1, with a minimum measured foci stoichiometry of ~ 6 molecules (Table S2), implying that Msn2 also operates as a cluster. The key difference with the data from the Mig1-GFP strain was that Msn2, unlike Mig1, demonstrated high apparent foci stoichiometry values and lower values of D at *glucose* (-), which was consistent with its role as an activator of the same target genes as opposed to a repressor (Figure 6). These results suggest that two different eukaryotic transcription factors that have antagonist effects on the same target genes operate as molecular clusters.

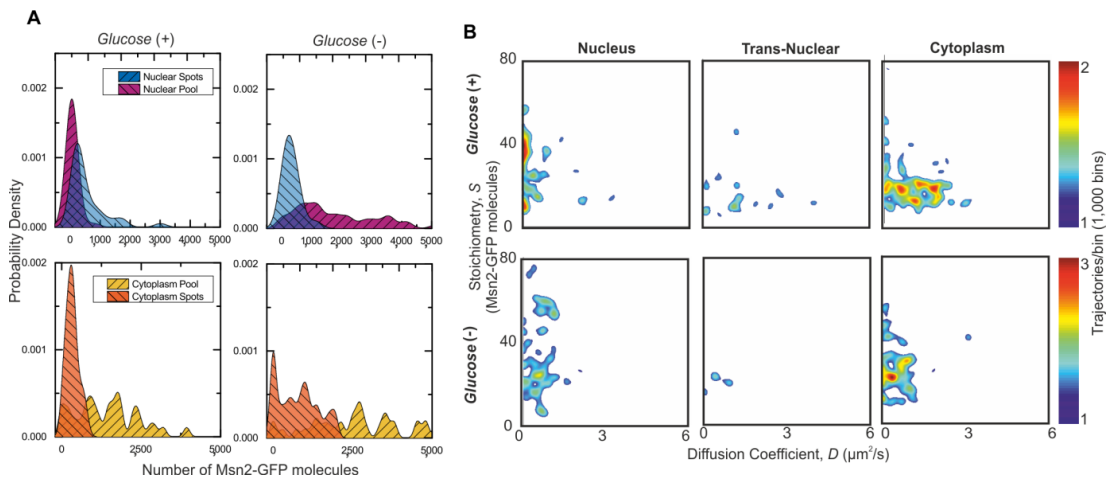


Figure 6. Activator Msn2 also forms functional clusters but with a reverse dependence on glucose for localization. (A) Kernel density estimations for Msn2-GFP in pool and foci for cytoplasm and nucleus at glucose (+/-). (B) Heat maps showing dependence of stoichiometry and D of detected Msn2-GFP foci, $n=30$ cells.

Mig1 and Msn2 possess intrinsic disorder which may favor clustering

Since both Mig1 and Msn2 demonstrate significant populations of clustered molecules in functional cell strains we asked the question if there were features common to the sequences of both proteins which might explain this behavior. To address this question we used multiple sequence alignment to determine conserved structural features of both proteins, and secondary structure prediction tools with

disorder prediction algorithms. As expected, sequence alignment indicated the presence of the Zn finger motif in both proteins, with secondary structure predictions suggesting relatively elongated structures (Figure 7A). However, disorder predictions indicated multiple extended intrinsically disordered regions in both Mig1 and Msn2 sequences with an overall proportion of disordered content >50%, as high as 75% for Mig1 (Figure 7B; Table S4). We measured a trend from a more structured region of Mig1 towards the N-terminus and more disordered regions towards the C-terminus. Msn2 demonstrated a similar bipolar trend but with the structured Zn finger motif towards the C-terminus and the disordered sequences towards the N-terminus. We then ran the same analysis as a comparison against the prokaryotic transcription factor LacI, which represses expression from genes of the *lac* operon as part of the prokaryotic glucose sensing pathway. The predicted disorder content in the case of LacI was <50%. In addition, further sequence alignment analysis predicted that at least 50% of candidate phosphorylation sites in either Mig1 or Msn2 lie within these intrinsically disordered sequences (Table S4; Figure 7A). An important observation reported previously is that the comparatively highly structured LacI exhibits no obvious clustering behavior from similar high-speed fluorescence microscopy tracking on live bacteria (Mahmutovic et al. 2015). Intrinsically disordered proteins are known to undergo phase transitions which may enable cluster formation and increase the likelihood of binding to nucleic acids (Uversky et al. 2015; Toretsky & Wright 2014). We measured significant changes in circular dichroism (Supplemental Experimental Procedures) of the Mig1 fusion construct upon addition of PEG in the wavelength range 200-230nm (Figure 7C) known to be sensitive to transitions between ordered and intrinsically disordered states (Sode et al. 2007; Avitabile et al. 2014). Since the Zn finger motif lies towards the opposite terminus to the disordered content for both Mig1 and Msn2 this may suggest a molecular bipolarity which could stabilize a cluster core while exposing Zn fingers on the surface enabling interaction with accessible DNA. This structural mechanism has analogies to that of phospholipid interactions driving micelle formation, however mediated here through disordered sequence interactions as opposed to hydrophobic forces (Figure 7C). The prevalence of phosphorylation sites located in disordered regions may also suggest a role in mediating affinity to target genes, similar to protein-protein binding by phosphorylation and intrinsic disorder coupling (Nishi et al. 2013).

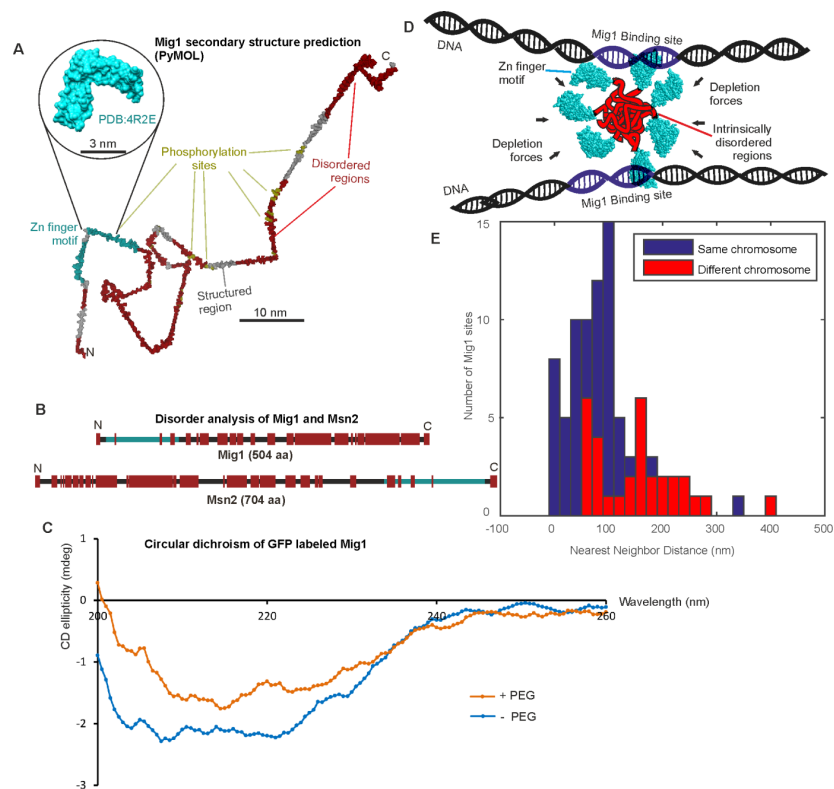


Figure 7. *Mig1* and *Msn2* contain disordered sequences which may mediate cluster formation. (A) Structural prediction for *Mig1*; Zn finger motif (cyan), disordered sections (red) from PyMOL, beta sheet (gray), phosphorylation sites (yellow); zoom-in indicates structure of conserved Zn finger from PSI-BLAST to PDB ID: 4R2E (Wilms tumor protein, WT1). (B) DISOPRED prediction for *Mig1* and *Msn2*; disordered regions (red), Zn finger regions (cyan). (C) Circular dichroism of *Mig1*-GFP in vitro in PEG absence (blue)/presence (red) (D) Schematic of depletion-stabilized *Mig1* cluster bound to multiple promoter targets (Zn finger PDB ID: 4R2E). (E) Distribution of nearest neighbor distances for *Mig1* sites within promoters on same (blue) or different (red) chromosome.

DISCUSSION

Our findings address a totally underexplored and novel aspect of gene regulation with technology that has not been available until recently. In summary, we observe that the repressor protein *Mig1* forms clusters which, upon extracellular glucose detection, localize dynamically from the cytoplasm to bind to locations in the genome which are consistent with the locations of the *Mig1* nuclear promoter targets determined from structural and bioinformatics analysis. These dynamic localization events of the clusters are correlated to biochemical measurements of repression from the *Mig1* target genes. Our results therefore strongly support a functional link between *Mig1* transcription factor clusters and *Mig1* target gene regulation. The physiological role of multivalent transcription factor clusters has been elucidated through simulations

(Schmidt et al. 2014) but unobserved until now. These simulations show that intersegmental transfer between sections of nuclear DNA was essential for factors to find their binding sites within physiologically relevant timescales and requires multivalency. Our findings address the longstanding question of how transcription factors find their targets in the genome so efficiently. Evidence for higher molecular weight Mig1 states from biochemical studies has been suggested previously (Patrick G Needham & Trumbly 2006). A Mig1-His-HA construct was overexpressed in yeast and cell extracts run in different glucose concentrations through sucrose density centrifugation. In western blots, a higher molecular weight band was observed, attributed to a hypothetical cofactor protein. However, no cofactor was detected and none reported to date. The modal molecular weight observed was ~four times that of Mig1 but with a wide observed distribution consistent with our mean detected cluster size of ~7 molecules. The authors only reported detecting higher molecular weight states in the nucleus in repressing conditions.

Our measured turnover of genome-bound Mig1 has similar timescales to that estimated for nucleoid-bound LacI (Mahmutovic et al. 2015), but similar rates of turnover have also been observed in yeast for a DNA-bound activator (Karpova et al. 2008). Faster off rates have been observed during single particle tracking of the DNA-bound fraction of the glucocorticoid receptor (GR) transcription factor in mammalian cells, equivalent to a residence time on DNA of just 1s (Gebhardt et al. 2013). Single GR molecules appear to bind as a homodimer complex on DNA, and slower Mig1 off rates may suggest higher order multivalency, consistent with Mig1 clusters.

Estimating nearest-neighbor distances between Mig1 promoter sites in the *S. cerevisiae* genome from the 3C model (Figure 7D) indicates 20-30% are <50 nm, small enough to enable different DNA segments to be linked though intersegment transfer by a single cluster (Gowers & Halford 2003; Schmidt et al. 2014). This separation would also enable simultaneous binding of >1 target (Figure 7C). The proportion of loci separated by <50nm is also consistent with the estimated proportion of immobile foci and with the proportion of cluster-occupied sites predicted from our structural model. Such multivalency chimes with the tetrameric binding of prokaryotic LacI leading to similar low promoter off rates (Mahmutovic et al. 2015). Extensive bioinformatics analysis of proteome disorder across a range of species suggests a sharp increase from prokaryotes to eukaryotes (Xue et al. 2012),

speculatively due to the prokaryotic absence of cell compartments and regulated ubiquitination mechanisms lowering protection of unfolded disordered structures from degradation (Ward et al. 2004). Our discovery in yeast may reveal a eukaryotic adaptation that stabilizes gene expression. Our findings address the longstanding question of how gene expression in eukaryotes is robust against stochastic noise in the extracellular signal. The slow off rate we measure would result in insensitivity to high frequency stochastic noise which could otherwise result in false positive detection and an associated wasteful expression response. We also note that long turnover times may facilitate modulation between co-regulatory factors by maximizing overlap periods, as suggested previously for Mig1/Msn2 (Lin et al. 2015).

Our results suggest that cellular depletion forces due to crowding enable cluster formation. Crowding is known to increase oligomerization reaction rates for low association proteins but slow down fast reactions due to an associated decrease in diffusion rates, and have a more pronounced effect on higher order multimers rather than dimers (Phillip & Schreiber 2013). It is technically challenging to study depletion forces *in vivo*, however there is growing *in vitro* and *in silico* evidence of the importance of molecular crowding in cell biology. A particularly striking effect was observed previously in the formation of clusters of the bacterial cell division protein FtsZ in the presence of two crowding proteins – hemoglobin and BSA (Rivas et al. 2001). Higher order decamers and multimers were observed in the presence of crowding agents and these structures are thought to account for as much as 1/3 of the *in vivo* FtsZ content. Similarly, two recent yeast studies of the high-osmolarity glycerol (HOG) pathway also suggest a dependence on gene expression mediated by molecular crowding (Babazadeh et al. 2013; Miermont et al. 2013).

The range of GFP labeled Mig1 cluster diameters *in vivo* of 15-50nm is smaller than the 80nm diameter of yeast nuclear pore complexes (Ma & Yang 2010), not prohibitively large as to prevent intact clusters from translocating across the nuclear envelope. An earlier *in vitro* study using sucrose gradient centrifugation suggested a Stokes radius of 4.8 nm for the Mig1 fraction, i.e. diameter 9.6nm, large for a Mig1 monomer (Patrick G Needham & Trumbly 2006) whose molecular weight is 55.5kDa, e.g. that of monomeric bovine serum albumin (BSA) at a molecular weight of 66kDa is closer to 3.5nm (Axelsson 1978). The authors ascribed this effect to a hypothetical elongated monomeric structure for Mig1. The equivalent Stokes radius for GFP has

been measured at 2.4nm (Hink et al. 2000), i.e. diameter 4.8nm. Also, for our Mig1-GFP construct there are two amino acids residues in the linker region between the Mig1 and GFP sequences (i.e. additional length 0.7-0.8nm). Thus the anticipated hydrodynamic diameter of Mig1-GFP is 15-16nm. The mean observed ~7-mer cluster diameter from Slimfield data is ~30nm, which, assuming a spherical packing geometry, suggests a subunit diameter for single Mig1-GFP molecules of $\sim 30/7^{1/3} \approx 15.6\text{nm}$, consistent with that predicted from the earlier hydrodynamic expectations. Using Stokes law this estimated hydrodynamic radius indicates an effective viscosity for the cytoplasm and nucleoplasm as low as 2-3cP, compatible with earlier live cell estimates on mammalian cells using FCS (Liang et al. 2009).

One alternative hypothesis to that of intrinsically disordered sequences mediating Mig1 cluster formation is the existence of a hypothetical cofactor protein to Mig1. However, such a cofactor would be invisible on our Slimfield assay but would result in a larger measured hydrodynamic radius than we estimate from fluorescence imaging, which would be manifest as larger apparent viscosity values than those we observe. Coupled to observations of Msn2 forming clusters also, and the lack of any reported stable cofactor candidate to date, limits the cofactor hypothesis. Pull down assays do suggest that promoter bound Mig1 consists of a complex which includes the accessory proteins Ssn6 and Tup1 (Treitel & Carlson 1995), however this would not explain the observation of Mig1 clusters outside the nucleus.

There may be other advantages in having a different strategy between *S. cerevisiae* and *E. coli* to achieve lowered transcriptional regulator off rate. A clue to these may lie in phosphorylation. We discovered that at least 50% of candidate serine or threonine phosphorylation sites in Mig1 and Msn2 lie in regions with high intrinsic disorder, which may have higher sequence-unspecific binding affinities to DNA (Uversky et al. 2015; Toretsky & Wright 2014). Thus phosphorylation at sites within these regions may potentially disrupt binding to DNA, similar to observed changes to protein-protein affinity being coupled to protein phosphorylation state (Nishi et al. 2013). Previous studies indicate that dephosphorylated Mig1 binds to its targets (Schüller 2003). Thus, intrinsic disorder may be required for bistability in affinity of Mig1/Msn2 to DNA.

Wide scale bioinformatics screening reveals a significant prevalence of intrinsic disorder in eukaryotic transcription factors (Liu et al. 2006), though our discovery is the first, to our knowledge, to make a link between predicted disorder and the ability

to form higher-order clusters in transcription factors, addressing the longstanding question of why there is so much predicted disorder in eukaryote transcription factors. Our observations that protein interactions based on weak intracellular forces and molecular crowding has direct functional relevance may stimulate new research lines in several areas of cell biology. For example, our findings may have important mechanistic implications for other aggregation processes mediated through intrinsic disorder interactions, such as those of amyloid plaques found in neurodegenerative disorders. Increased understanding of the clustering mechanism may not only be of value in understanding such diseases, but could enable future novel synthetic biology applications to manufacture gene circuits with, for example, a range of bespoke response times.

EXPERIMENTAL PROCEDURES

Strain construction

We developed Mig1 fluorescent protein strains based on strain YSH1351 (Bendrioua et al. 2014) using eGFP in the first instance and also mGFP/GFPmut3 designed to inhibit oligomerization (Zacharias, Violin, Newton, et al. 2002), and photoswitchable mEos2 (McKinney et al. 2009), fully detailed in Supplementary Experimental Procedures.

Single-molecule imaging

A dual-color bespoke laser excitation single-molecule fluorescence microscope was used (Badrinarayanan et al., 2012) utilizing narrow epifluorescence excitation of 10 μ m full width at half maximum (FWHM) in the sample plane to generate Slimfield illumination, fully detailed in Supplementary Experimental Procedures.

Foci tracking and copy number analysis

Foci were automatically detected using software written in MATLAB (Mathworks) (Miller et al., 2015), lateral localization \sim 40nm, enabling estimates of D and stoichiometry. Copy numbers for individual cells were estimated using image convolution (Adam J M Wollman & Leake 2015). Full details can be found in the Supplementary Experimental Procedures.

SUPPLEMENTAL INFORMATION

Supplemental Information includes Supplemental Experimental Procedures, six figures, four tables and two movies.

ACKNOWLEDGMENTS

Supported by the Biological Physical Sciences Institute, Royal Society, MRC (grant MR/K01580X/1), Swedish Research Council and European Commission via Marie Curie-Network for Initial training ISOLATE (Grant agreement nr: 289995). We thank Magnus Alm Rosenblad and Sarah Shammam for assistance with RNABOB and PONDR, Marija Cvijovic and Michael Law for help with qPCR data analysis. M.C.L. and S.H. planned/designed project; A.J.M.W., S.S. E.G.H. and R.F. collected data and performed analyses; all authors wrote the paper and discussed results.

REFERENCES

- Adam, S.A. (2001). The nuclear pore complex. *Genome Biol.* 2, REVIEWS0007.
- Avitabile, C., D'Andrea, L.D., Romanelli, A., Yount, N.Y., Yeaman, M.R., Schuerholz, T., Brandenburg, K., Marx, G., Zasloff, M., Yang, L., et al. (2014). Circular Dichroism studies on the interactions of antimicrobial peptides with bacterial cells. *Sci. Rep.* 4, 337–360.
- Axelsson, I. (1978). Characterization of proteins and other macromolecules by agarose gel chromatography. *J. Chromatogr. A* 152, 21–32.
- Babazadeh, R., Adiels, C.B., Smedh, M., Petelenz-Kurdziel, E., Goksör, M., and Hohmann, S. (2013). Osmostress-induced cell volume loss delays yeast Hog1 signaling by limiting diffusion processes and by Hog1-specific effects. *PLoS One* 8, 1–12.
- Badrinarayanan, A., Reyes-Lamothe, R., Uphoff, S., Leake, M.C., and Sherratt, D.J. (2012). In vivo architecture and action of bacterial structural maintenance of chromosome proteins. *Science* 338, 528–531.
- Bendrioua, L., Smedh, M., Almquist, J., Cvijovic, M., Jirstrand, M., Goksör, M., Adiels, C.B., and Hohmann, S. (2014). Yeast AMP-activated protein kinase monitors glucose concentration changes and absolute glucose levels. *J. Biol. Chem.* 289, 12863–

12875.

Berg, O.G., Winter, R.B., and Von Hippel, P.H. (1981). Diffusion-driven mechanisms of protein translocation on nucleic acids. 1. Models and theory. *Biochemistry* *20*, 6929–6948.

Duan, Z., Andronescu, M., Schutz, K., McIlwain, S., Kim, Y.J., Lee, C., Shendure, J., Fields, S., Blau, C.A., and Noble, W.S. (2010). A three-dimensional model of the yeast genome. *Nature* *465*, 363–367.

Frolova, E. (1999). Binding of the glucose-dependent Mig1p repressor to the GAL1 and GAL4 promoters in vivo: regulation by glucose and chromatin structure. *Nucleic Acids Res.* *27*, 1350–1358.

Gebhardt, J.C.M., Suter, D.M., Roy, R., Zhao, Z.W., Chapman, A.R., Basu, S., Maniatis, T., and Xie, X.S. (2013). Single-molecule imaging of transcription factor binding to DNA in live mammalian cells. *Nat. Methods* *10*, 421–426.

Gertz, J., Siggia, E.D., and Cohen, B.A. (2009). Analysis of combinatorial cis-regulation in synthetic and genomic promoters. *Nature* *457*, 215–218.

Gowers, D.M., and Halford, S.E. (2003). Protein motion from non-specific to specific DNA by three-dimensional routes aided by supercoiling. *EMBO J.* *22*, 1410–1418.

Halford, S.E., and Marko, J.F. (2004). How do site-specific DNA-binding proteins find their targets? *Nucleic Acids Res.* *32*, 3040–3052.

Hammar, P., Leroy, P., Mahmutovic, A., Marklund, E.G., Berg, O.G., and Elf, J. (2012). The lac repressor displays facilitated diffusion in living cells. *Science* *336*, 1595–1598.

Harbison, C.T., Gordon, D.B., Lee, T.I., Rinaldi, N.J., Macisaac, K.D., Danford, T.W., Hannett, N.M., Tagne, J.-B., Reynolds, D.B., Yoo, J., et al. (2004). Transcriptional regulatory code of a eukaryotic genome. *Nature* *431*, 99–104.

Hink, M.A., Griep, R.A., Borst, J.W., van Hoek, A., Eppink, M.H., Schots, A., and Visser, A.J. (2000). Structural dynamics of green fluorescent protein alone and fused with a single chain Fv protein. *J. Biol. Chem.* *275*, 17556–17560.

Izeddin, I., Récamier, V., Bosanac, L., Cissé, I.I., Boudarene, L., Dugast-Darzacq, C., Proux, F., Bénichou, O., Voituriez, R., Bensaude, O., et al. (2014). Single-molecule

tracking in live cells reveals distinct target-search strategies of transcription factors in the nucleus. *Elife* 3.

Jacob, F., and Monod, J. (1961). Genetic regulatory mechanisms in the synthesis of proteins. *J. Mol. Biol.* 3, 318–356.

Karpova, T.S., Kim, M.J., Spriet, C., Nalley, K., Stasevich, T.J., Kherrouche, Z., Heliot, L., and McNally, J.G. (2008). Concurrent fast and slow cycling of a transcriptional activator at an endogenous promoter. *Science* 319, 466–469.

Leake, M.C., Chandler, J.H., Wadhams, G.H., Bai, F., Berry, R.M., and Armitage, J.P. (2006). Stoichiometry and turnover in single, functioning membrane protein complexes. *Nature* 443, 355–358.

Li, G.-W., and Xie, X.S. (2011). Central dogma at the single-molecule level in living cells. *Nature* 475, 308–315.

Liang, L.-F., Da, X., Chen, T.-S., and Pei, Y.-H. (2009). [Nucleoplasmic viscosity of living cells investigated by fluorescence correlation spectroscopy]. *Guang Pu Xue Yu Guang Pu Fen Xi* 29, 459–462.

Lin, Y., Sohn, C.H., Dalal, C.K., Cai, L., and Elowitz, M.B. (2015). Combinatorial gene regulation by modulation of relative pulse timing. *Nature* 527, 54–58.

Liu, J., Perumal, N.B., Oldfield, C.J., Su, E.W., Uversky, V.N., and Dunker, A.K. (2006). Intrinsic disorder in transcription factors. *Biochemistry* 45, 6873–6888.

Llorente-Garcia, I., Lenn, T., Erhardt, H., Harriman, O.L., Liu, L.-N., Robson, A., Chiu, S.-W., Matthews, S., Willis, N.J., Bray, C.D., et al. (2014). Single-molecule in vivo imaging of bacterial respiratory complexes indicates delocalized oxidative phosphorylation. *Biochim. Biophys. Acta - Bioenerg.* 1837, 811–824.

Lowe, A.R., Siegel, J.J., Kalab, P., Siu, M., Weis, K., and Liphardt, J.T. (2010). Selectivity mechanism of the nuclear pore complex characterized by single cargo tracking. *Nature* 467, 600–603.

Lundin, M., Nehlin, J.O., and Ronne, H. (1994). Importance of a flanking AT-rich region in target site recognition by the GC box-binding zinc finger protein MIG1. *Mol. Cell. Biol.* 14, 1979–1985.

Lutfiyya, L.L., Iyer, V.R., DeRisi, J., DeVit, M.J., Brown, P.O., and Johnston, M.

- (1998). Characterization of three related glucose repressors and genes they regulate in *Saccharomyces cerevisiae*. *Genetics* *150*, 1377–1391.
- Ma, J., and Yang, W. (2010). Three-dimensional distribution of transient interactions in the nuclear pore complex obtained from single-molecule snapshots. *Proc. Natl. Acad. Sci. U. S. A.* *107*, 7305–7310.
- Mahmutovic, A., Berg, O.G., and Elf, J. (2015). What matters for lac repressor search in vivo--sliding, hopping, intersegment transfer, crowding on DNA or recognition? *Nucleic Acids Res.* *43*, 3454–3464.
- McKinney, S.A., Murphy, C.S., Hazelwood, K.L., Davidson, M.W., and Looger, L.L. (2009). A bright and photostable photoconvertible fluorescent protein. *Nat. Methods* *6*, 131–133.
- Miermont, A., Waharte, F., Hu, S., McClean, M.N., Bottani, S., Léon, S., and Hersen, P. (2013). Severe osmotic compression triggers a slowdown of intracellular signaling, which can be explained by molecular crowding. *Proc. Natl. Acad. Sci. U. S. A.* *110*, 5725–5730.
- Miller, H., Zhaokun, Z., Wollman, A.J.M., and Leake, M.C. (2015). Superresolution imaging of single DNA molecules using stochastic photoblinking of minor groove and intercalating dyes. *Methods*.
- Needham, P.G., and Trumbly, R.J. (2006). In vitro characterization of the Mig1 repressor from *Saccharomyces cerevisiae* reveals evidence for monomeric and higher molecular weight forms. *Yeast* *23*, 1151–1166.
- Nehlin, J.O., Carlberg, M., and Ronne, H. (1991). Control of yeast GAL genes by MIG1 repressor: a transcriptional cascade in the glucose response. *EMBO J.* *10*, 3373–3377.
- Nishi, H., Fong, J.H., Chang, C., Teichmann, S.A., and Panchenko, A.R. (2013). Regulation of protein-protein binding by coupling between phosphorylation and intrinsic disorder: analysis of human protein complexes. *Mol. Biosyst.* *9*, 1620–1626.
- Phillip, Y., and Schreiber, G. (2013). Formation of protein complexes in crowded environments--from in vitro to in vivo. *FEBS Lett.* *587*, 1046–1052.
- Plank, M., Wadhams, G.H., and Leake, M.C. (2009). Millisecond timescale slimfield imaging and automated quantification of single fluorescent protein molecules for use

in probing complex biological processes. *Integr. Biol. (Camb)*. *1*, 602–612.

Reyes-Lamothe, R., Sherratt, D.J., and Leake, M.C. (2010). Stoichiometry and architecture of active DNA replication machinery in *Escherichia coli*. *Science* *328*, 498–501.

Rivas, G., Fernández, J.A., and Minton, A.P. (2001). Direct observation of the enhancement of noncooperative protein self-assembly by macromolecular crowding: indefinite linear self-association of bacterial cell division protein FtsZ. *Proc. Natl. Acad. Sci. U. S. A.* *98*, 3150–3155.

Schmidt, H.G., Sewitz, S., Andrews, S.S., and Lipkow, K. (2014). An Integrated Model of Transcription Factor Diffusion Shows the Importance of Intersegmental Transfer and Quaternary Protein Structure for Target Site Finding. *9*.

Schüller, H.-J. (2003). Transcriptional control of nonfermentative metabolism in the yeast *Saccharomyces cerevisiae*. *Curr. Genet.* *43*, 139–160.

Sode, K., Ochiai, S., Kobayashi, N., and Usuzaka, E. (2007). Effect of reparation of repeat sequences in the human alpha-synuclein on fibrillation ability. *Int. J. Biol. Sci.* *3*, 1–7.

Stracy, M., Lesterlin, C., Garza de Leon, F., Uphoff, S., Zawadzki, P., and Kapanidis, A.N. (2015). Live-cell superresolution microscopy reveals the organization of RNA polymerase in the bacterial nucleoid. *Proc. Natl. Acad. Sci. U. S. A.* *112*, E4390-9.

Strambio-De-Castillia, C., Niepel, M., and Rout, M.P. (2010). The nuclear pore complex: bridging nuclear transport and gene regulation. *Nat. Rev. Mol. Cell Biol.* *11*, 490–501.

Toretsky, J.A., and Wright, P.E. (2014). Assemblages: functional units formed by cellular phase separation. *J. Cell Biol.* *206*, 579–588.

Treitel, M.A., and Carlson, M. (1995). Repression by Ssn6-Tup1 is directed by Mig1, a repressor/activator protein. *Proc. Natl. Acad. Sci. U. S. A.* *92*, 3132–3136.

Uversky, V.N., Kuznetsova, I.M., Turoverov, K.K., and Zaslavsky, B. (2015). Intrinsically disordered proteins as crucial constituents of cellular aqueous two phase systems and coacervates. *FEBS Lett.* *589*, 15–22.

De Vit, M.J., Waddle, J. a, and Johnston, M. (1997). Regulated nuclear translocation of the Mig1 glucose repressor. *Mol. Biol. Cell* *8*, 1603–1618.

Ward, J.J., Sodhi, J.S., McGuffin, L.J., Buxton, B.F., and Jones, D.T. (2004). Prediction and functional analysis of native disorder in proteins from the three kingdoms of life. *J. Mol. Biol.* *337*, 635–645.

Whiteside, S.T., and Goodbourn, S. (1993). Signal transduction and nuclear targeting: regulation of transcription factor activity by subcellular localisation. *J. Cell Sci.* *104* (Pt 4, 949–955.

Wollman, A.J.M., and Leake, M.C. (2015). Millisecond single-molecule localization microscopy combined with convolution analysis and automated image segmentation to determine protein concentrations in complexly structured, functional cells, one cell at a time. *Faraday Discuss.* *184*, 401–424.

Xue, B., Dunker, A.K., and Uversky, V.N. (2012). Orderly order in protein intrinsic disorder distribution: disorder in 3500 proteomes from viruses and the three domains of life. *J. Biomol. Struct. Dyn.* *30*, 137–149.

Yang, W., Gelles, J., and Musser, S.M. (2004). Imaging of single-molecule translocation through nuclear pore complexes. *Proc. Natl. Acad. Sci. U. S. A.* *101*, 12887–12892.

Zacharias, D.A., Violin, J.D., Newton, A.C., and Tsien, R.Y. (2002). Partitioning of lipid-modified monomeric GFPs into membrane microdomains of live cells. *Science* *296*, 913–916.

SUPPLEMENTAL EXPERIMENTAL PROCEDURES

Strain construction and characterization

Mig1-mGFP and Mig1-mEos2 fusions were constructed by introducing into YSH1351 (BY4741 wild type) cells the *mGFP-HIS3* or *mEos2-HIS3* PCR fragment flanked on its 5' end with 50bp sequence of *MIG1* 3' end and 50bp downstream of *MIG1* excluding the STOP codon. The *mEos2-HIS3* and *mGFP-HIS3* fragment was amplified from mEos-his plasmid (GeneArt, Life Technologies) and pmGFP-S plasmid designed for this study by inserting into plasmid YDp-H. Modified strains in which the *SNF1* gene was deleted, *snf1Δ*, were prepared by compromising the gene with an auxotrophic marker providing into cells the *LEU2* PCR product amplified from plasmid YDp-L and flanked with 50bp of *SNF1* upstream and downstream sequence on 5' and 3' ends, respectively. Strains in which Snf1 kinase activity can be inhibited by 25μM 1NM-PP1 were prepared by introducing into cells a plasmid with an ATP analog-sensitive version of Snf1 with *I132G* mutation (Rubenstein et al. 2008). All transformations were performed using the lithium-acetate protocol (Gietz & Schiestl 2007).

Cell doubling times of all strains were calculated (Warringer et al. 2011) (fig. S2) based on OD₆₀₀ values obtained during cultivation (Bioscreen analyser C). We quantified mRNA relative expression of the *MIG1* gene using qPCR against the constitutive actin gene *ACT1* in the wild type and the Mig1-mGFP strain in cells pre-grown in 4% glucose and then shifted to elevated (4%) and depleted (0.2%) extracellular glucose for 2 h. mRNA isolation and cDNA synthesis were performed as described previously (Geijer et al. 2013).

For Msn2-GFP experiments we used the YSH2350 strain (*MATa msn2-GFP-HIS3 nrd1-mCherry-hphNT1 MET LYS*) in BY4741 background.

Protein production and purification

His-tagged *mCherry*, *eGFP* and *mGFP* genes were amplified by PCR and cloned into pET vectors. An expression pRSET A plasmid containing 6xHis-Mig1-mGFP was obtained commercially (GeneArt, Life Technologies). *Escherichia coli* strain BL21(DE3) carrying the expression plasmid was grown in LB with 100μg/ml ampicillin and 34μg/ml chloramphenicol at 37°C to OD₆₀₀ 0.7. Protein expression was induced by adding isopropyl-β-D-thiogalactopyranoside (IPTG) at final concentration

of 1mM for 3h at 30°C. Cells were suspended in 50mM NaH₂PO₄, 10mM Tris, 300mM NaCl, 2mM EDTA, 0.2mM PMSF, 0.1% β-mercaptoethanol, pH 8.0, and lysed by sonication or by three passages through a chilled Emulsiflex (Avestin). Extracts were cleared (24,000g, 30min) and filtered (pore diameter 0.45µm; Millipore, Bedford). All proteins were purified using Ni²⁺ affinity chromatography on a 5ml HisTrap FF column (GE Healthcare). Mig1-mGFP was eluted with a linear gradient 0 - 0.4 M imidazole in lysis buffer. Mig1-mGFP was further purified by size-exclusion chromatography (Superdex 200 Increase 10/300, GE Healthcare) and concentrated (50 kDa molecular weight cutoff VIVASPIN 20 concentrator). Purity of the sample was confirmed by Coomassie stained SDS-PAGE gels (Simply Blue Safe Stain, Life Technologies).

Media and growth conditions

Cells from frozen stocks were grown on plates with standard YPD media (10 g/l yeast extract, 20 g/l bacto-peptone, 20 g/l agar) supplemented with 4% glucose (w/v) at 30°C overnight. For the liquid cultures, the YPD was prepared as above but without agar, and the cells were grown at 30°C while shaking (180 rpm).

For transformants that carried a plasmid with mutated *SNF1* (p*SNF1-II132G*), minimal YNB media with –URA amino acid supplement was applied. For the growth rate experiments cells were grown on 100 well plates in YNB with complete amino acid supplement and 4% glucose (w/v) until logarithmic phase, subcultured into fresh medium on a new 100 well plate and grown until logarithmic phase again. 10 µl of each culture was resuspended in 250 µl of fresh YNB medium with 4% or 0.2% glucose (w/v) on a new plate and cultivated in Bioscreen analyser C for 96 h at 30°C or 22°C. OD measurements at 600 nm were taken every 10 min with prior shaking. Each strain was represented in sextuplicates.

For microscopy experiments on the BY4741 wild type and/or cells with genetically integrated fluorescent proteins, minimal YNB media (1.7 g/l yeast nitrogen base without amino acids and (NH₄)₂SO₄, 5 g/l (NH₄)₂SO₄, 0.79 g/l complete amino acid supplement as indicated by manufacturer) with appropriate glucose concentrations was used. In brief, cells were first streaked onto YPD plates, grown overnight at 30°C prior to culturing in liquid minimal YNB media with complete amino acid supplement and 4% glucose overnight, then sub-culturing into fresh YNB with 4% glucose for 4h with shaking at 30°C. Cultures were spun at 3,000rpm, re-

suspended into fresh YNB with or without glucose, immobilized in 1 μ l spots onto an 1% agarose well perfused with YNB minimal media with an appropriate glucose concentration enclosed between a plasma-cleaned BK7 glass microscope coverslip and slide, which permitted cells to continue to grow and divide (Reyes-Lamothe et al. 2010b; Badrinarayanan et al. 2012) while being observed for up to several hours if required.

SDS-PAGE

50 ml cultures of YSH1703 transformed with centromeric pMig1-HA and pSNF1-I132G-TAP or pSNF1-TAP plasmids were grown until mid-log phase in yeast nitrogen base, 4% glucose, uracil and histidine deficient. Each culture was separated into two new cultures with 4% and 0.05% glucose, respectively, and incubated for 30 min. The following procedure was adapted from Bendrioua et al. (Bendrioua et al. 2014). Cells were harvested by centrifugation (3,000rpm, 50s), suspended in 1 ml of 0.1M NaOH for 5 min and spun down. Pellets were suspended in 2 ml of 2M NaOH with 7% β -mercaptoethanol for 2 min and then 50% trichloroacetic acid was added. Samples were vortexed and spun down at 13,000rpm. The pellets were washed in 0.5 ml of 1M Tris-HCl (pH 8.0), resuspended in 50 μ l of 1x SDS sample buffer (62.5 mM Tris-HCl (pH 6.8), 3% SDS, 10% glycerol, 5% β -mercaptoethanol, and 0.004% bromophenol blue) and boiled for 5 min. The protein extracts were obtained by centrifuging at the maximal speed and collecting the supernatants. For western blotting, 50 μ g of extracted proteins were resolved on a Criterion TGX 10% precast polyacrylamide gel, then transferred onto a nitrocellulose membrane (Trans-Blot Turbo Transfer Pack, Bio-Rad) using Trans-Blot Turbo Transfer System (Bio-Rad). After transfer, the membrane was blocked in Odyssey Blocking buffer (LI-COR Biosciences). Mig1 was detected by using primary mouse anti-HA (1:2000) antibodies (Santa Cruz), then secondary goat anti-mouse IRDye-800CW (1:5000) antibodies (LI-COR Biosciences). The result was visualized by using an infrared imager (Odyssey, LI-COR Biosciences), 800nm channel.

Native PAGE

A 50 ml culture of the YSH2862 strain was grown until mid-log phase in rich media with 4% glucose, then, 25 ml of the culture was transferred into fresh YPD with 4% glucose, and the rest into YPD with 0.05% glucose for 30 min. The cultures were

harvested by centrifugation, suspended in 0.1ml of solubilization buffer (100 mM Tris-HCl, pH 6.8, 0.1 mM Na₃VO₄, 1x protease inhibitor cocktail (Roche), 0.1% Triton-X100). 400µl of glass beads were added, and cells were broken by FastPrep, 6m/s, 20 s. Protein extracts were obtained by adding 150 µl of solubilization buffer, centrifugation at 13,000 rpm, 5min and collecting the supernatant. Protein quantification was performed by using Bradford with BSA standard (Bio-Rad). 250 µg of total protein extracts were run on a Criterion TGX Stain Free 10% precast polyacrylamide gel (Bio-Rad). Samples were diluted 1:1 with 2x Native Sample Buffer (Bio-Rad). Electrophoresis was performed at 4⁰C starting at 100V until the bromophenol blue line reached the end of the gel. The gel was transferred onto a nitrocellulose membrane (Trans-Blot Turbo Transfer Pack, Bio-Rad) using Trans-Blot Turbo Transfer System (Bio-Rad). After transfer, the membrane was blocked in Odyssey Blocking buffer (LI-COR Biosciences), analyzed by immunoblotting with mouse anti-GFP (1:500) antibodies (Roche) and visualized with goat anti-mouse IRDye-800CW (1:5,000) antibodies (LI-COR Biosciences) by using an infrared imager (Odyssey, LI-COR Biosciences), 800nm channel. As a molecular weight reference, a NativeMark Unstained Protein Standards (Invitrogen) were used.

Slimfield microscopy

GFP and mCherry excitation used co-aligned linearly polarized 488 nm and 561 nm wavelength 50 mW lasers (Coherent Obis) respectively which could be attenuated independently via neutral density filters followed by propagation through an achromatic $\lambda/2$ plate to rotate the plane of polarization prior to separation into two independent paths generated by splitting into orthogonal polarization components by a polarization splitting cube to enable simultaneous Slimfield illumination and a focused laser bleach illumination path for fluorescence recovery after photobleaching (FRAP) when required. The two paths were reformed into a single common path via a second polarization cube, circularized for polarization via an achromatic $\lambda/4$ plate with fast axis orientated at 45° to the polarization axes of each path and directed at ~ 6 W/cm² excitation intensity onto the sample mounted on an xyz nanostage (Mad City Labs) via a dual-pass green/red dichroic mirror centered at long-pass wavelength 560nm and emission filters with 25nm bandwidths centered at 525nm and 594nm (Chroma).

Fluorescence emissions were captured by a 1.49NA oil immersion objective lens (Nikon) and split into green and red detection channels using a bespoke color splitter utilizing a long-pass dichroic mirror with wavelength cut-off of 565nm prior to imaging each channel onto separate halves of the same EMCCD camera detector (iXon DV860-BI, Andor Technology, UK) at a pixel magnification of 80 nm/pixel using 5ms camera exposure time. We confirmed negligible measured crosstalk between GFP and mCherry signals to red and green channels respectively, using purified GFP and mCherry sampled in an *in vitro* surface immobilization assay (details below).

Microfluidics control of single cell imaging

To investigate time-resolved glucose concentration-dependent changes in Mig1-GFP localization in individual yeast cells, we used bespoke microfluidics and our bespoke control software *CellBild* (LabVIEW, National Instruments), enabling cell-to-cell imaging in response to environmental glucose changes. *CellBild* controlled camera acquisition synchronized to flow-cell environmental switches via a syringe pump containing an alternate glucose environment. Microfluidic flow-chambers were based on an earlier 4-channel design (Gustavsson et al. 2012).

Prior to each experiment flow-chambers were wetted and pre-treated for 15min with 1 mg/ml of concanavalin A (ConA) which binds to the glass surface of the plasma cleaned flow-chamber. Cells were introduced via a side channel and were left bind to ConA for 15min to immobilize cells on the surface. Any remaining ConA and unbound cells were washed out and a steady flow of YNB with 0% glucose provided to one of the central channels by gravity feed. A syringe pump synchronized with image acquisition introduced YNB with 4% glucose in the second central channel. The pumped alternate environment reaches cells within 1-2s at a flow rate of 10 μ l/min, enabling rapid change between two different glucose concentrations.

Slimfield imaging was performed on a similar bespoke microscope setup at comparable laser excitation intensities and spectral filtering prior to imaging onto a Photometrics *Evolve Delta 512* EMCCD camera at 200 frames per second. Alternating frame laser excitation (ALEX) was used to minimize any autofluorescence contamination in the red channel introduced by the blue excitation light.

Foci detection, tracking and stoichiometry determination

Our bespoke foci detection and tracking software objectively identifies candidate bright foci by a combination of pixel intensity thresholding and image transformation

to yield bright pixel coordinates. The intensity centroid and characteristic intensity, defined as the sum of the pixel intensities inside a 5 pixel radius region of interest around the foci minus the local background and corrected for non-uniformity in the excitation field are determined by iterative Gaussian masking. If the signal-to-noise ratio of the spot, defined as the characteristic intensity per pixel/background standard deviation per pixel, is >0.4 it is accepted and fitted with a 2D radial Gaussian function to determine its sigma width, which our simulations indicate single-molecule sensitivity under typical *in vivo* imaging conditions (Adam J M Wollman & Leake 2015). Foci in consecutive image frames within a single point spread function (PSF) width, and not different in brightness or sigma width by more than a factor of two, are linked into the same track. The microscopic diffusion coefficient D is then estimated for each accepted foci track using mean square displacement analysis, in addition to several other mobility parameters.

Cell and nuclear boundaries were segmented from GFP and mCherry fluorescence images respectively using a relative threshold pixel intensity value trained on simulated images of uniform fluorescence in idealized spherical compartments. An optimized threshold value of 0.3 times the mean compartment fluorescence intensity segmented the boundary to within 0.5 pixels.

The characteristic brightness of a single GFP molecule was determined directly from *in vivo* data and corroborated using *in vitro* immobilized protein assays (Leake et al. 2006). The intensity of tracked fluorescent foci in live cells was measured over time as described above. These followed an approximately exponential photobleach decay function of intensity with respect to time. Every oligomeric Mig1-GFP complex as it photobleaches to zero intensity will emit the characteristic single GFP intensity value, I_{GFP} , i.e. the brightness of a single GFP molecule, given in our case by the modal value of all foci intensities over time, and can potentially bleach in integer steps of this value at each sampling time point. This value of I_{GFP} was further verified by Fourier spectral analysis of the pairwise distance distribution (Leake et al. 2006) of all foci intensities which yields the same value to within measurement error in our system.

All foci tracks found within 70 image frames of the start of laser illumination were included in the analysis and were corrected for photobleaching by weighting the measured foci intensity I at a time t following the start of laser illumination with a function $\exp(+t/t_b)$ to correct for the exponential photobleach decay $I_0\exp(-t/t_b)$, to each intensity trace with a fixed time constant, where I_0 is the initial unbleached intensity.

This photobleach time constant t_b was determined from exponential decay fits to the foci intensities and whole cell intensities over time to be 40 ± 0.6 ms. Stoichiometries were obtained by dividing the photobleach estimate for the initial intensity I_0 of a given foci by the characteristic single GFP molecule brightness value I_{GFP} .

Autofluorescence correction was applied to pool quantification by subtracting the red channel image from the green channel image multiplied by a correlation factor. By comparing wild type and GFP cell images we confirmed that when only the GFP exciting 488 nm wavelength laser was used the green channel image contained fluorescence intensity from GFP and autofluorescence, while the red channel contains only autofluorescence pixels, consistent with expectations from transmission spectra of known autofluorescent components in yeast cells. We measured the red channel autofluorescence pixels to be linearly proportional to the green channel autofluorescence pixels. The scaling factor between channels was determined by Slimfield imaging of the wild type yeast strain (i.e. non GFP) under the same conditions and comparing intensity values pixel-by-pixel in each channel. A linear relationship between pixels was found with scaling factor of 0.9 ± 0.1 .

Copy numbers of Mig1-GFP of the pool component were estimated using a previously developed CoPro algorithm (Adam J M Wollman & Leake 2015). In brief, the cytoplasmic and nuclear pools were modelled as uniform fluorescence over spherical cells and nuclei using experimentally measured radii. A model PSF was integrated over these two volumes to create model nuclear and cytoplasmic images and then their relative contributions to the camera background and autofluorescence corrected GFP intensity image determined by solving a set of linear equations for each pixel. Dividing the contributions by the characteristic single GFP molecule intensity and correcting for out-of-plane foci yields the pool concentration.

Stoichiometry distributions were rendered as objective kernel density estimations (Leake et al. 2006) using a Gaussian kernel with bandwidth optimized for normally distributed data using standard MATLAB routines.

Stochastic optical reconstruction microscopy (STORM)

To photoswitch Mig1-mEos2, a 405 nm wavelength laser (Coherent Obis), attenuated to $\sim 1\text{mW}/\text{cm}^2$ was used in conjunction with the 488 nm and 561 nm lasers on the Slimfield microscope, similar to previous super-resolution imaging of yeast cells (Puchner et al. 2013). The 405 nm laser light causes mEos2 to photoswitch from a

green (excitable via the 488 nm laser) to a red (excitable by the 561 nm laser) fluorescent state. Using low intensity 405 nm light generates photoactive fluorophore foci, photobleached by the 561 nm laser at a rate which results in an approximately steady-state concentration density in each live cell studied. The bright foci were tracked similar to the Slimfield data but were used to generate a super-resolved image by the summation of 2D Gaussian functions at each tracked Mig1-mEos2 localization in time with a width of ~40 nm, the measured lateral precision following automated particle tracking (Adam J M Wollman & Leake 2015).

Fluorescent protein brightness characterization

We used a surface-immobilization assay described previously (Adam J M Wollman & Leake 2015; Badrinarayanan et al. 2012) employing antibody conjugation to immobilize single molecules of GFP respectively onto the surface of plasma-cleaned BK7 glass microscope coverslips and imaged using the same buffer medium and imaging conditions as for live cell Slimfield experiments, resulting in integrated single-molecule peak intensity values for mGFP of $4,600 \pm 3,000$ (\pm half width half maximum, HWHM) counts. Similar experiments on unmodified purified Clontech eGFP generated peak intensity values of $4,700 \pm 2,000$ counts, statistically identical to that of mGFP (Student *t*-test, $p < 0.2$) with no significant indication of multimerization effects from the measured distribution of foci intensity values. Similarly, Slimfield imaging and foci stoichiometry analysis on Mig1-mGFP and Mig1-eGFP cell strains were compared *in vivo* under high and low glucose conditions in two separate cell strains, resulting in distributions which were statistically identical (Pearson's χ^2 test, $p < 0.001$). These results indicated no measurable differences between multimerization state or single-molecule foci intensity between mGFP and eGFP which enabled direct comparison between Mig1-eGFP cell strain data obtained from preliminary experiments here and from previous studies (Bendrioua et al. 2014).

Maturation effects of mCherry and GFP were investigated by adding mRNA translation inhibitor antibiotic cycloheximide, final concentration 100 $\mu\text{g/ml}$, for 1h (Hartwell et al. 1970), photobleaching cells, then monitoring any recovery in fluorescence as a metric for newly matured fluorescent material in the cell. Cells were prepared for microscopy as before but using cycloheximide in all subsequent preparation and imaging media and imaged using a commercial mercury-arc excitation fluorescence microscope Zeiss Axiovert 200M (Carl Zeiss MicroImaging) onto an

ApoTome camera using a lower excitation intensity than for Slimfield imaging but a larger field of view, enabling a greater number of cells to be imaged simultaneously.

Surface-immobilized cells using strain YSH2863 were photobleached by continuous illumination for between 3min 40s to 4min until dark using separate filter sets 38HE and 43HE for GFP and mCherry excitation, respectively. Fluorescence images were acquired at subsequent time intervals up to 120min and analyzed using AxioVision software (fig. S6). The background-corrected total cellular fluorescence intensity was quantified at each time point for each cell using ImageJ software. Comparison between Mig1-GFP fluorescence signal and the green channel signal from the parental strain BY4741, and the Nrd1-mCherry signal and the red channel signal from the parental strain, indicate fluorescence recovery after correction above the level of any autofluorescence contributions of <15% for GFP and mCherry over the timescale of our experiments, consistent with previous estimates of *in vivo* maturation times for GFP and mCherry (Khmelniskii et al. 2012; Badrinarayanan et al. 2012; Leake et al. 2006).

Characterizing Mig1-GFP clusters *in vitro*

Using Slimfield microscopy under the same imaging conditions as for live cell microscopy we measured the fluorescent foci intensity of 1µg/ml solutions of purified Mig1-mGFP and mGFP using the normal imaging buffer of PBS, compared with the imaging buffer supplemented with 1kDa molecular weight PEG at a concentration of 10% (w/v) used to reproduce cellular depletion forces (Phillip & Schreiber 2013; Warringer et al. 2011).

Circular dichroism measurements

Purified Mig1-mGFP was placed in 25 mM Na₂HPO₄, pH 7.0, by buffer exchange procedure with a Pur-A-Lyser Maxi dialysis Kit (Sigma Aldrich) for 3h at 4⁰C with constant stirring in 500 ml a buffer. Circular dichroism measurements were performed on a Jasco J810 circular dichromator with Peltier temperature control and Biologic SFM300 stop-flow accessory on 0.16mg/ml Mig1-mGFP samples with or without 20% PEG-1000 at 20⁰C, from 260 to 200 nm, a 2 nm band width, 2 sec response time, at the speed of 100 nm/min. The resulting spectrum represents the average of 5 scans, indicating a typical SD error of ~0.1 mdeg ellipticity. Spectra from 25 mM Na₂HPO₄

and 25 mM Na₂HPO₄ with 20% (w/v) PEG were used as a background and subtracted from spectra of Mig1-mGFP without or with 20% (w/v) PEG respectively.

Bioinformatics analysis and structural modeling

Bioinformatics analysis was used to identify candidate promoter sequences in the budding yeast genome. The Mig1 target pattern sequence was identified based on 14 promoter sequences (Lundin et al. 1994) using the IUPAC nucleotide code. The entire *S. cerevisiae* S288c genome was scanned in order to find all sequences that matched the pattern. The scanning was performed by RNABOB software (Riccitelli & Lupták 2010), and collated for any further analysis and identification of the sequences lying within promoter regions. All information regarding *S. cerevisiae* genes was obtained from SGD database (<http://yeastgenome.org/>).

We used bioinformatics to investigate the extent of intrinsic disorder in the amino acid sequence of budding yeast Mig1 and Msn2 proteins as well as the *E. coli lac* repressor LacI, employing the Predictor of Natural Disordered Regions (PONDR) algorithm (Obradovic et al. 2005) (online tool <http://www.pondr.com/cgi-bin/PONDR/pondr.cgi>) with a VL-XT algorithm. We also used the secondary structure prediction algorithm of PyMOL (<http://www.pymolwiki.org/index.php/Dss>) to highlight disordered and structured regions and display the unfolded protein chain, and used PSI-BLAST multiple sequence alignment to determine conserved structural features of Mig1 for the zinc finger motif in combination with the DISOPRED (Ward et al. 2004) algorithm as a comparison to PONDR, which produced very similar results (online tool <http://www.yeastrc.org/pdr/>).

Oligomerization state of Mig1-GFP in the ‘pool’

Experimental *in vitro* assays of surface immobilized GFP coupled to simulations trained on these single-molecule intensity measurements but using noise levels comparable to *in vivo* cellular imaging conditions (Adam J M Wollman & Leake 2015) indicate single-molecule sensitivity of GFP detection under our millisecond imaging conditions. However, if the nearest neighbor separation of individual GFP ‘foci’ are less than the optical resolution limit w of our microscope (which we measure as ~230 nm for GFP imaging) then distinct fluorescent foci will not be detected and instead will be manifest as a diffusive ‘pool’.

If each GFP ‘foci’ in the pool has a mean stoichiometry S then the mean number of GFP foci, F , in the pool is n_{pool}/S and the ‘pool’ condition for nearest neighbor foci separation s indicates that $s < w$.

The estimated range of mean total pool copy number from nucleus and cytoplasm combined, n_{pool} , is ~ 590 -1,100 molecules depending on extracellular glucose conditions. Approximating the cell volume as equal to the combined volumes of all uniformly separated foci in the pool (equal to the total number of foci multiplied by the volume of an equivalent sphere of radius r) indicates that $F \cdot 4\pi r^3/3 = 4\pi d^3/3$, thus $r = d/F^{1/3}$, where we use the mean measured cell diameter d of $\sim 5 \mu\text{m}$.

However, mobile foci with a microscopic diffusion coefficient D will diffuse a mean two-dimensional distance b in focal plane of $(4D \cdot \Delta t)^{1/2}$ in a camera sampling time window Δt of 5 ms. Using $D \sim 6 \mu\text{m}^2 \text{s}^{-1}$ as a lower limit based on the measured diffusion of low stoichiometry cytoplasmic Mig1-GFP foci detected indicates $b \sim 340 \text{ nm}$ so the movement-corrected estimate for s is $r-b$, thus $s < w$ indicates that $r < b+w$, or $d/F^{1/3} < b+w$.

Therefore, $d(S/n_{pool})^{1/3} < b+w$, and $S < n_{pool}((b+w)/d)^3$. Using ~ 590 -1,100 molecules from the measured mean range of n_{pool} indicates that the upper limit for S is in the range 0.8-1.4; in other words, Mig1-GFP foci in the pool are consistent with being a monomer.

Analysis of the mobility of foci

For each accepted foci track the mean square displacement (MSD) was calculated from the optimized intensity centroid at time t of $(x(t), y(t))$ assuming a tracks of N consecutive image frames at a time interval $\tau = n\Delta t$ is (Gross & Webb 1988; Michalet 2010) where n is a positive integer is:

$$\begin{aligned} MSD(\tau) = MSD(n\Delta t) &= \frac{1}{N-1-n} \sum_{i=1}^{N-1-n} \left\{ [x(i\Delta t + n\Delta t) - x(i\Delta t)]^2 + [y(i\Delta t + n\Delta t) - y(i\Delta t)]^2 \right\} \\ &= 4D\tau + 4\sigma^2 \end{aligned}$$

Here σ is the lateral (xy) localization precision which we estimate as $\sim 40 \text{ nm}$ (Adam J M Wollman & Leake 2015). The microscopic diffusion coefficient D was

then estimated from the gradient of a linear fit to the first four time interval data points of the MSD vs τ relation for each accepted foci track.

To determine the proportion of mobile and immobile Mig1-GFP fluorescent foci we adapted an approach based on cumulative probability-distance distribution analysis (Gebhardt et al. 2013). Here we generated cumulative distribution functions (CDFs) for all nuclear and cytoplasmic tracks, such that the CDF in each dataset is the probability distribution function p_c associated with r^2 , the square of the displacement between the first and second data points in each single track, which was generated for each track by calculating the proportion of all tracks in a dataset which have a value of r^2 less than that measured for that one track. The simplest CDF model assumes a Brownian diffusion propagator function $f(r^2)$ for a single effective diffusion coefficient component of:

$$f(r^2) = \frac{1}{4\pi D\Delta t} \exp\left(-\frac{r^2}{4D\Delta t}\right)$$

Here, D is the effective diffusion coefficient and Δt is image sampling time per frame (i.e. in our case 5 ms). This gives a CDF single component solution of the form:

$$p_c(r^2) = 1 - \exp\left(-\frac{r^2}{4D\Delta t}\right)$$

We investigated both single and more complex multi-component CDF models using either 1, 2 or 3 different D values in a weighted sum model of:

$$p_c(r^2) = \sum_{i=1}^n A_i \left(1 - \exp\left(-\frac{r^2}{4D_i\Delta t}\right) \right)$$

Here n is 1, 2 or 3. Multi-component fits were only chosen if they lowered the reduced χ^2 by >10%. To determine errors on the A_i and D_i parameters we estimated the 95% confidence interval calculated as the R^{-1} factor (the inverse R factor from QR decomposition of the corresponding Jacobian parameter matrix) from each corresponding non-linear regression fit using the MATLAB curve fitting toolbox.

For cytoplasmic foci at *glucose* (+/-) and for nuclear foci at *glucose* (-) this indicated single component fits for diffusion coefficient with a D of $\sim 1-2 \mu\text{m}^2/\text{s}$, whereas nuclear foci at *glucose* (+) were fitted using two components of D , $\sim 20\%$ with a relatively immobile component, $D \sim 0.1-0.2 \mu\text{m}^2/\text{s}$, and the remainder a relatively mobile component, $D \sim 1-2 \mu\text{m}^2/\text{s}$, while using three components produced no statistically significant improvement to the fits. These values of D agreed to within experimental error to those obtained using a different method which fitted two analytical Gamma functions to the distribution of all calculated microscopic diffusion coefficients of tracked foci in the nucleus at *glucose* (+), which assumed a total probability distribution function p_γ of the form: (Stracy et al. 2015)

$$p_\gamma(x, D) = \sum_{i=1}^2 \frac{A_i (m/D)^m x^{m-1} \exp(-mx/D)}{(m-1)!}$$

Here, m is the number of steps in the MSD vs τ trace for each foci track used to calculate D (i.e. in our instance $m=4$). The optimized 2-component Gamma function fit for the nuclear *glucose* (+) dataset generated a good fit with an R^2 goodness-of-fit parameter of 0.85.

We also probed longer time scale effects on foci mobility for each accepted foci trajectory. Here, average MSD values were generated by calculating mean MSD values for corresponding time interval values across all foci trajectories in each dataset, but pooling traces into low stoichiometry (≤ 20 Mig1-GFP molecules per spot) and high stoichiometry (> 20 Mig1-GFP molecules per spot). We compared different diffusion models over a 30 ms time interval scale, corresponding to the shortest time interval range from any of the mean MSD trace datasets.

We found in all cases that mean MSD traces could be fitted well (χ^2 values in the range 1-12) using a subdiffusion model of precision-corrected MSD = $4\sigma^2 + 4D\tau^\alpha$, where α the anomalous diffusion coefficient and D is the microscopic lateral diffusion coefficient. Optimized fits indicated values of D in the range 0.08-0.2 $\mu\text{m}^2/\text{s}$ and those for α of $\sim 0.4-0.8$. Corresponding fits to a purely Brownian diffusion model (i.e. $\alpha = 1$) generated much poorer fits (χ^2 values in the range 4-90).

Analysing trans-nuclear tracks

The segmentation boundary output for the nucleus was fitted with a smoothing spline function, with smoothing parameter $p = 0.9992$ to sub-pixel precision. Trajectories which contained points on either side of the nuclear boundary were considered trans-nuclear. The crossing point on the nuclear boundary was found by linearly interpolating between the first pair of points either side of the nuclear boundary. Coordinates were normalized to this point and the crossing time and were rotated such that y' and x' lie perpendicular and parallel to the membrane crossing point.

Investigating Mig1-GFP molecular turnover

Turnover of Mig1-GFP was investigated using fluorescence recovery after photobleaching (FRAP). In brief a 200 ms 10m W focused laser beam pulse of lateral width $\sim 1 \mu\text{m}$ was used to photobleach the fluorescently-labelled nuclear contents on a cell-by-cell basis and then ≤ 10 Slimfield images were recorded over different timescales spanning a range from 100 ms to $\sim 1,000$ s. The copy number of pool and foci in each image at subsequent time points t post focused laser bleach was determined as described and corrected for photobleaching. These post-bleach photoactive Mig1-GFP copy number values $C(t)$ could then be fitted using a single exponential recovery function:

$$C(t) = C(0)(1 - \exp(-t/t_R))$$

Where t_R is the characteristic recovery (i.e. turnover) time (Reyes-Lamothe et al. 2010b). These indicated a value of 133 ± 20 s (\pm SEM) for nuclear foci at glucose (+), and 3 ± 14 s for nuclear pool at *glucose* (+) and (-).

Modeling the effective diameter of clusters

The effective diameter d of a cluster was estimated from the measured point spread function width p_{spot} (defined at twice sigma value of the equivalent Gaussian fit from our single particle tracking algorithm) corrected for the blur due to particle diffusion in the camera exposure time of Δt as:

$$d = p_{spot} - p_{GFP} - \sqrt{4D\Delta t}$$

Where D is the measured microscopic diffusion coefficient for that track and p_{GFP} is the measured point spread function width of surface-immobilized GFP (i.e. twice the sigma width of 230nm measured in our microscope, or 460nm). We explored a heuristic packing model of $d \sim S^a$ for Mig1-GFP monomers in each cluster, such that a tightly packed spherical cluster of volume V composed of S smaller ca. spherical monomers each of volume V_1 and diameter d_1 varied as $V = S.V_1$ thus $4\pi(d/2)^3 = S.4\pi(d_1/2)^3$, thus in the specific instance of a perfect spherical cluster model $a = 1/3$.

In principle, for general shapes of clusters for different packing conformations we expect $0 \leq a \leq 1$ such that e.g. if clusters pack as a long, thin rod of Mig1 monomers which rotates isotropically during time Δt , then $a = 1$. Whereas, if Mig1 monomers bind to a putative additional ‘anchor’ type structure to occupy available binding sites in forming a cluster, such that the size of the cluster does not significantly change with S but is dependent on the size of the putative anchor structure itself, then $a = 0$. Our optimized fits indicate $a = 0.32 \pm 0.06$ (\pm SEM), i.e. consistent with an approximate spherical shape cluster model.

Modelling the probability of overlap in *in vitro* fluorescent protein characterization

The probability that two or more fluorescent protein foci are within the diffraction limit of our microscope in the *in vitro* characterization assays was determined using a previously reported Poisson model (Llorente-Garcia et al. 2014) to be ~10% at the *in vitro* protein concentrations used here. Such overlapping fluorescent proteins are detected as higher apparent stoichiometry foci.

Software and DNA sequence access

All our bespoke software developed, and Mig1 secondary structure prediction 3D coordinates pymolMig1.pdb, are freely and openly accessible via <https://sourceforge.net/projects/york-biophysics/>. The bespoke plasmid sequence information for the GFP reporter is openly accessible via <https://www.addgene.org/75360/>.

Statistical tests

All statistical tests used are two-sided unless stated otherwise.

SUPPLEMENTAL REFERENCES

Badrinarayanan, A., Reyes-Lamothe, R., Uphoff, S., Leake, M.C., and Sherratt, D.J. (2012). In vivo architecture and action of bacterial structural maintenance of chromosome proteins. *Science* 338, 528–531.

Bendrioua, L., Smedh, M., Almquist, J., Cvijovic, M., Jirstrand, M., Goksör, M., Adiels, C.B., and Hohmann, S. (2014). Yeast AMP-activated Protein Kinase Monitors Glucose Concentration Changes and Absolute Glucose Levels. *J. Biol. Chem.* 289, 12863–12875.

Gebhardt, J.C.M., Suter, D.M., Roy, R., Zhao, Z.W., Chapman, A.R., Basu, S., Maniatis, T., and Xie, X.S. (2013). Single-molecule imaging of transcription factor binding to DNA in live mammalian cells. *Nat. Methods* 10, 421–426.

Geijer, C., Medrala-Klein, D., Petelenz-Kurdziel, E., Ericsson, A., Smedh, M., Andersson, M., Goksör, M., Nadal-Ribelles, M., Posas, F., Krantz, M., et al. (2013). Initiation of the transcriptional response to hyperosmotic shock correlates with the potential for volume recovery. *FEBS J.* 280, 3854–3867.

Gietz, R.D., and Schiestl, R.H. (2007). Frozen competent yeast cells that can be transformed with high efficiency using the LiAc/SS carrier DNA/PEG method. *Nat. Protoc.* 2, 1–4.

Gross, D., and Webb, W. (1988). Cell surface clustering and mobility of the liganded LDL receptor measured by digital video fluorescence microscopy. In *Spectroscopic Membrane Probes*, L. Loew, ed. (CRC Press), pp. 19–45.

Gustavsson, A.-K., van Niekerk, D.D., Adiels, C.B., du Preez, F.B., Goksör, M., and Snoep, J.L. (2012). Sustained glycolytic oscillations in individual isolated yeast cells. *FEBS J.* 279, 2837–2847.

Hartwell, L.H., Culotti, J., and Reid, B. (1970). Genetic control of the cell-division cycle in yeast. I. Detection of mutants. *Proc. Natl. Acad. Sci. U. S. A.* 66, 352–359.

Khmelniskii, A., Keller, P.J., Bartosik, A., Meurer, M., Barry, J.D., Mardin, B.R., Kaufmann, A., Trautmann, S., Wachsmuth, M., Pereira, G., et al. (2012). Tandem fluorescent protein timers for in vivo analysis of protein dynamics. *Nat. Biotechnol.* 30, 708–714.

Leake, M.C., Chandler, J.H., Wadhams, G.H., Bai, F., Berry, R.M., and Armitage, J.P. (2006). Stoichiometry and turnover in single, functioning membrane protein complexes. *Nature* 443, 355–358.

Llorente-Garcia, I., Lenn, T., Erhardt, H., Harriman, O.L., Liu, L.-N., Robson, A., Chiu, S.-W., Matthews, S., Willis, N.J., Bray, C.D., et al. (2014). Single-molecule in vivo imaging of bacterial respiratory complexes indicates delocalized oxidative phosphorylation. *Biochim. Biophys. Acta* 1837, 811–824.

Lundin, M., Nehlin, J.O., and Ronne, H. (1994). Importance of a flanking AT-rich region in target site recognition by the GC box-binding zinc finger protein MIG1. *Mol. Cell. Biol.* 14, 1979–1985.

Michalet, X. (2010). Mean square displacement analysis of single-particle trajectories with localization error: Brownian motion in an isotropic medium. *Phys. Rev. E* 82, 041914.

Obradovic, Z., Peng, K., Vucetic, S., Radivojac, P., and Dunker, A.K. (2005). Exploiting heterogeneous sequence properties improves prediction of protein disorder. *Proteins* 61 Suppl 7, 176–182.

- Phillip, Y., and Schreiber, G. (2013). Formation of protein complexes in crowded environments--from in vitro to in vivo. *FEBS Lett.* 587, 1046–1052.
- Puchner, E.M., Walter, J.M., Kasper, R., Huang, B., and Lim, W.A. (2013). Counting molecules in single organelles with superresolution microscopy allows tracking of the endosome maturation trajectory. *Proc. Natl. Acad. Sci. U. S. A.* 110, 16015–16020.
- Reyes-Lamothe, R., Sherratt, D.J., and Leake, M.C. (2010). Stoichiometry and architecture of active DNA replication machinery in *Escherichia coli*. *Science* 328, 498–501.
- Riccitelli, N.J., and Lupták, A. (2010). Computational discovery of folded RNA domains in genomes and in vitro selected libraries. *Methods* 52, 133–140.
- Rubenstein, E.M., McCartney, R.R., Zhang, C., Shokat, K.M., Shirra, M.K., Arndt, K.M., and Schmidt, M.C. (2008). Access denied: Snf1 activation loop phosphorylation is controlled by availability of the phosphorylated threonine 210 to the PP1 phosphatase. *J. Biol. Chem.* 283, 222–230.
- Stracy, M., Lesterlin, C., Garza de Leon, F., Uphoff, S., Zawadzki, P., and Kapanidis, A.N. (2015). Live-cell superresolution microscopy reveals the organization of RNA polymerase in the bacterial nucleoid. *Proc. Natl. Acad. Sci. U. S. A.* 112, E4390–E4399.
- Ward, J.J., Sodhi, J.S., McGuffin, L.J., Buxton, B.F., and Jones, D.T. (2004). Prediction and functional analysis of native disorder in proteins from the three kingdoms of life. *J. Mol. Biol.* 337, 635–645.
- Warringer, J., Zörgö, E., Cubillos, F.A., Zia, A., Gjuvsland, A., Simpson, J.T., Forsmark, A., Durbin, R., Omholt, S.W., Louis, E.J., et al. (2011). Trait variation in yeast is defined by population history. *PLoS Genet.* 7, e1002111.

Wollman, A.J.M., and Leake, M.C. (2015). Millisecond single-molecule localization microscopy combined with convolution analysis and automated image segmentation to determine protein concentrations in complexly structured, functional cells, one cell at a time. *Faraday Discuss.* 184, 401–424.

APPENDIX C

From Animaculum to single molecules: 300 years of the light microscope

Adam J. M. Wollman, Richard Nudd, Erik G. Hedlund
and Mark C. Leake

Open Biol. 5: 150019. (2015)

<http://dx.doi.org/10.1098/rsob.150019>

My own unique contributions to this work were incorporated into the text with the themes: (i) Bioluminescence, (ii) Fluorescence in microscopy and (iii) Modern imaging techniques, including DH-PSF, astigmatic imaging, TIRF, Super-critical Angle Fluorescence (SAF) microscopy and single cell imaging techniques



Cite this article: Wollman AJM, Nudd R, Hedlund EG, Leake MC. 2015 From *Animaculum* to single molecules: 300 years of the light microscope. *Open Biol.* **5**: 150019. <http://dx.doi.org/10.1098/rsob.150019>

Received: 30 January 2015

Accepted: 1 April 2015

Subject Area:

biophysics/biotechnology/cellular biology

Keywords:

optical microscopy, superresolution, fluorescence

Author for correspondence:

Mark C. Leake

e-mail: mark.leake@york.ac.uk



An invited review to commemorate 350 years of scientific publishing at the Royal Society.

From *Animaculum* to single molecules: 300 years of the light microscope

Adam J. M. Wollman, Richard Nudd, Erik G. Hedlund and Mark C. Leake

Biological Physical Sciences Institute (BPSI), Departments of Physics and Biology, University of York, York YO10 5DD, UK

AJMW, 0000-0002-5501-8131; MCL, 0000-0002-1715-1249

1. Summary

Although not laying claim to being the inventor of the light microscope, Antonj van Leeuwenhoek (1632–1723) was arguably the first person to bring this new technological wonder of the age properly to the attention of natural scientists interested in the study of living things (people we might now term ‘biologists’). He was a Dutch draper with no formal scientific training. From using magnifying glasses to observe threads in cloth, he went on to develop over 500 simple single lens microscopes (Baker & Leeuwenhoek 1739 *Phil. Trans.* **41**, 503–519. (doi:10.1098/rstl.1739.0085)) which he used to observe many different biological samples. He communicated his finding to the Royal Society in a series of letters (Leeuwenhoek 1800 *The select works of Antony Van Leeuwenhoek, containing his microscopical discoveries in many of the works of nature*, vol. 1) including the one republished in this edition of *Open Biology*. Our review here begins with the work of van Leeuwenhoek before summarizing the key developments over the last *ca* 300 years, which has seen the light microscope evolve from a simple single lens device of van Leeuwenhoek’s day into an instrument capable of observing the dynamics of single biological molecules inside living cells, and to tracking every cell nucleus in the development of whole embryos and plants.

2. Antonj van Leeuwenhoek and invention of the microscope

Prior to van Leeuwenhoek, lenses had existed for hundreds of years but it was not until the seventeenth century that their scientific potential was realized with the invention of the light microscope. The word ‘microscope’ was first coined by Giovanni Faber in 1625 to describe an instrument invented by Galileo in 1609. Galileo’s design was a compound microscope—it used an objective lens to collect light from a specimen and a second lens to magnify the image, but this was not the first microscope invented. In around 1590, Hans and Zacharias Janssen had created a microscope based on lenses in a tube [1]. No observations from these microscopes were published and it was not until Robert Hooke and Antonj van Leeuwenhoek that the microscope, as a scientific instrument, was born.

Robert Hooke was a contemporary of van Leeuwenhoek. He used a compound microscope, in some ways very similar to those used today with a stage, light source and three lenses. He made many observations which he published in his *Micrographia* in 1665 [2]. These included seeds, plants, the eye of a fly and the structure of cork. He described the pores inside the cork as ‘cells’, the origin of the current use of the word in biology today.

Unlike Hooke, van Leeuwenhoek did not use compound optics but single lenses. Using only one lens dramatically reduced problems of optical aberration in lenses at the time, and in fact van Leeuwenhoek’s instruments for this reason generated a superior quality of image to those of his contemporaries. His equipment was all handmade, from the spherical glass lenses to their bespoke fittings. His many microscopes consisted mainly of a solid base, to hold the single spherical lens in place,

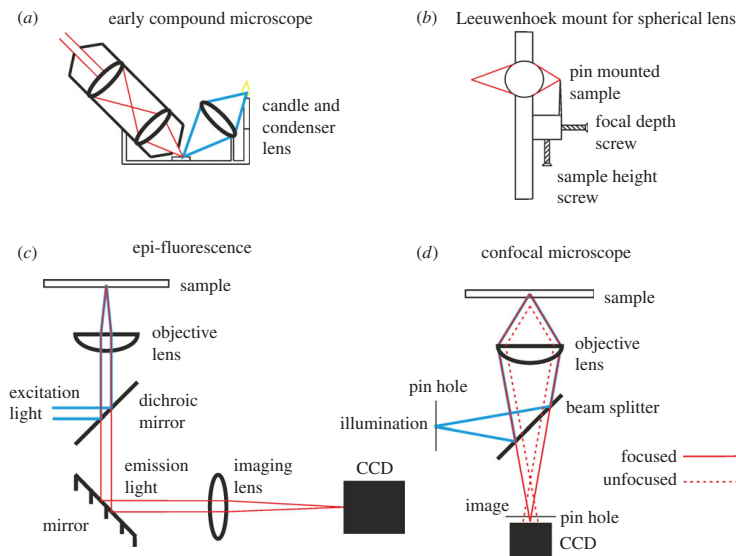


Figure 1. Optical microscope designs through the ages. (a) One design of a simple compound microscope used by Hooke while writing *Micrographia*. (b) An example of the single spherical lens mount system that van Leeuwenhoek used, approximately 5 cm in height. (c) A simple epi-fluorescence system. (d) A simple modern-day confocal microscope.

along with adjusting screws which were mounted and glued in place to adjust the sample holding pin, and sometimes an aperture placed before the sample to control illumination [3] (see figure 1 for an illustration). These simple instruments could be held up to the sun or other light source such as a candle and did not themselves have any light sources inbuilt. His microscopes were very lightweight and portable, however, allowing them to be taken into the field to view samples as they were collected. Imaging consisted of often painstaking mounting of samples, focusing and then sketching, with sometimes intriguing levels of imagination, or documenting observations.

Van Leeuwenhoek's studies included the microbiology and microscopic structure of seeds, bones, skin, fish scales, oyster shell, tongue, the white matter upon the tongues of feverish persons, nerves, muscle fibres, fish circulatory system, insect eyes, parasitic worms, spider physiology, mite reproduction, sheep fetuses, aquatic plants and the 'animalcula'—the microorganisms described in his letter [4]. As he created the microscopes with the greatest magnification of his time, he pioneered research into many areas of biology. He can arguably be credited with the discovery of protists, bacteria, cell vacuoles and spermatozoa.

3. The development of the microscope and its theoretical underpinnings

It was not until the nineteenth century that the theoretical and technical underpinnings of the modern light microscope were developed, most notably diffraction-limit theory, but also aberration-corrected lenses and an optimized illumination mode called Köhler illumination.

There is a fundamental limit to the resolving power of the standard light microscope; these operate by projecting an image of the sample a distance of several wavelengths of light from the sample itself, known as the 'far-field' regime.

In this regime, the diffraction of light becomes significant, for example, through the circular aperture of the objective lens. This diffraction causes 'point sources' in the sample which scatter the light to become blurred spots when viewed through a microscope, with the level of blurring determined by the imaging properties of the microscope known as the point spread function (PSF). Through a circular aperture, such as those of lenses in a light microscope, the PSF can be described by a mathematical pattern called an Airy disc, which contains a central peak of light intensity surrounded by dimmer rings moving away from the centre (figure 2a). This phenomenon was first theoretically characterized by George Airy in 1835 [5]. Later, Ernst Abbe would state that the limit on the size of the Airy disc was roughly half the wavelength of the imaging light [6], which agrees with the so-called Rayleigh criterion for the optical resolution limit [7] which determines the minimum distance between resolvable objects (figure 2b). This became the canonical limit in microscopy for over a hundred years, with the only attempts to improve spatial resolution being through the use of lower wavelength light or using electrons rather than photons, as in electron microscopy, which have a smaller effective wavelength by approximately four orders of magnitude.

Ernst Abbe also helped solve the problem of chromatic aberration. A normal lens focuses light to different points depending on its wavelength. In the eighteenth century, Chester Moore Hall invented the achromatic lens, which used two lenses of different materials fused together to focus light of different wavelengths to the same point. In 1868, Abbe invented the apochromatic lens, using more fused lenses, which better corrected chromatic and spherical aberrations [8]. Abbe also created the world's first refractometer and we still use the 'Abbe Number' to quantify how diffraction varies with wavelength [9]. He also collaborated with Otto Schott, a glass chemist, to produce the first

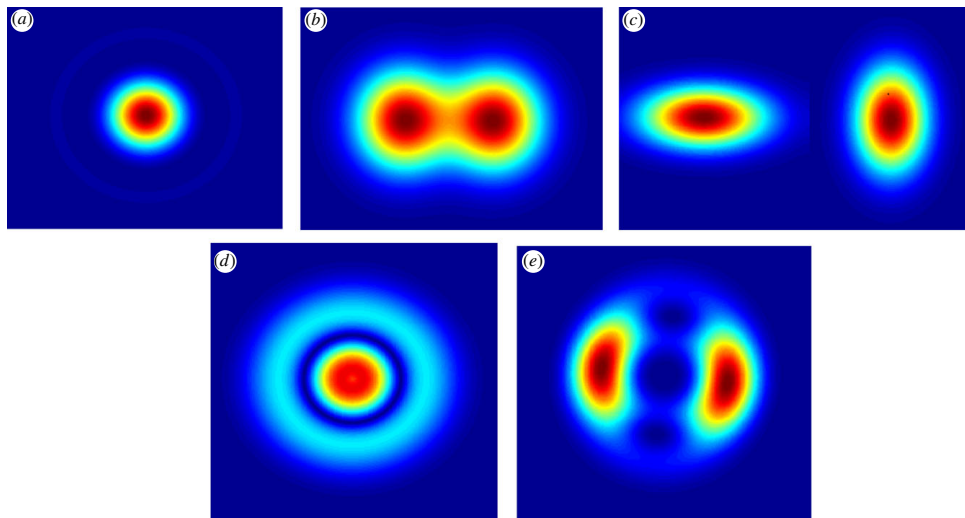


Figure 2. Mathematically generated PSF images from different light microscope designs. (a) The Airy pattern, a disc and one of the rings produced by a point source emitter imaged using a spherical lens. (b) Two such Airy discs separated by less than the Abbe limit for optical resolution. (c) The lateral xy stretching exhibited in astigmatic imaging systems when the height z of a point source emitter is above or below the focal plane, the degree of stretching a metric for z . (d) Expected pattern when a point source emitter is defocused. (e) Two-lobed PSF used in double-helix PSF techniques, where the rotation of the lobes about the central point is used to calculate z .

lenses that were engineered with sufficiently high quality to produce diffraction-limited microscopes [10]. Their work in 1883 set the limits of far-field optics for over a century, until the advent of the 4π microscope in 1994 [11].

Another eponymous invention of Abbe was the Abbe condenser—a unit that focuses light with multiple lenses which improved sample illumination but was quickly superseded by Köhler illumination, the modern standard for ‘brightfield’ light microscopy. August Köhler was a student of many fields of the ‘natural sciences’. During his PhD studying limpet taxonomy, he modified his illumination optics to include a field iris and also an aperture iris with a focusing lens to produce the best illumination with the lowest glare, which aided in image collection using photosensitive chemicals [12]. Owing to the slow nature of photography of the period, good images required relatively long exposure times and Köhler illumination greatly aided in producing high-quality images. He joined the Zeiss Optical Works in 1900, where his illumination technique coupled with the optics already developed by Abbe and Schott went on to form the basis of the modern brightfield light microscope.

4. Increasing optical contrast

One of the greatest challenges in imaging biological samples is their inherently low contrast, due to their refractive index being very close to water and thus generating little scatter interaction with incident light. A number of different methods for increasing contrast have been developed including imaging phase and polarization changes, staining and fluorescence, the latter being possibly the most far-reaching development since the invention of the light microscope.

Biological samples generate contrast in brightfield microscopy by scattering and absorbing some of the incident light.

As they are almost transparent, the contrast is very poor. One way around this, is to generate contrast from phase (rather than amplitude) changes in the incident light wave. Fritz Zernike developed phase contrast microscopy in the 1930s [13] while working on diffraction gratings. Imaging these gratings with a telescope, they would ‘disappear’ when in focus [14]. These observations led him to realize the effects of phase in imaging, and their application to microscopy subsequently earned him the Nobel prize in 1953. Phase contrast is achieved by manipulating the transmitted, background light differently from the scattered light, which is typically phase-shifted 90° by the sample. This scattered light contains information about the sample. A circular annulus is placed in front of the light source, producing a ring of illumination. A ring-shaped phase plate below the objective shifts the phase of the background light by 90° such that it is in phase (or sometimes completely out of phase, depending on the direction of the phase shift) with the scattered light, producing a much higher contrast image.

An alternative to phase contrast is differential interference contrast (DIC). It was created by Smith [15] and further developed by Georges Nomarski in 1955 [16]. It makes use of a Nomarski–Wollaston prism through which polarized light is sheared into two beams polarized at 90° to each other. These beams then pass through the sample and carry two brightfield images laterally displaced a distance equal to the offset of the two incoming beams at the sample plane. Both beams are focused through the objective lens and then recombined through a second Nomarski–Wollaston prism. The emergent beam goes through a final analyser, emerging with a polarization of 135° . The coaxial beams interfere with each other owing to the slightly different path lengths of the two beams at the same point in the image, giving rise to a phase difference and thus a high-contrast image. The resultant image appears to have bright and dark spots which resemble an illuminated

relief map. This faux relief map should not be interpreted as such, however, as the bright and dark spots contain information instead about path differences between the two sheared beams. The images produced are exceptionally sharp compared with other transmission modes. DIC is still the current standard technique for imaging unstained microbiological samples in having an exceptional ability to reveal the boundaries of cells and subcellular organelles.

Contrast can also be improved in biological samples by staining them with higher contrast material, for example dyes. This also allows differential contrast, where only specific parts of a sample, such as the cell nucleus, are stained. In 1858 came one of the earliest documented reports of staining in microscopy when Joseph von Gerlach demonstrated differential staining of the nucleus and cytoplasm in human brain tissue soaked in the contrast agent carmine [17]. Other notable examples include silver staining introduced by Camillo Golgi in 1873 [18], which allowed nervous tissue to be visualized, and Gram staining invented by Hans Christian Gram in 1884 [19], which allowing differentiation of different types of bacteria. Sample staining is still widely in use today, including many medical diagnostic applications. However, the advent of fluorescent staining would revolutionize contrast enhancement in biological samples.

The word 'fluorescence' to describe emission of light at a different wavelength to the excitation wavelength was first made by Stokes in 1852 [20]. Combining staining with fluorescence detection allows for enormous increases in contrast, with the first fluorescent stain fluorescein being developed in 1871 [21]. In 1941, Albert Coons published the first work on immunofluorescence. This technique uses fluorescently labelled antibodies to label specific parts of a sample. Coons used a fluorescein-derivative-labelled antibody and showed that it could still bind to its antigen [22]. This opened the way to using fluorescent antibodies as a highly specific fluorescent stain.

Green fluorescent protein (GFP) was first isolated from the jellyfish *Aequorea victoria* in 1962 [23], but it was not until 1994 that Chalfie *et al.* [24] showed that it could be expressed and fluoresce outside of the jellyfish. They incorporated it into the promoter for a gene that encoded β -tubulin and showed that it could serve as a marker for expression levels. The discovery and development of GFP by Osamu Shimomura, Martin Chalfie and Roger Tsien was recognized in 2008 by the Nobel prize in chemistry.

By mutating GFP, blue, cyan and yellow derivatives had been manufactured [25] but orange and red fluorescent proteins proved difficult to produce until the search for fluorescent proteins was expanded to non-bioluminescent organisms. This led to the isolation of dsRed from *Anthozoa*, a species of coral [26]. Brighter and more photostable fluorescent proteins were subsequently produced by directed evolution [27]. The discovery of spectrally distinct fluorescent proteins allowed multichannel (dual and multi-colour) fluorescence imaging and opened the way to studying the interaction between different fluorescently labelled proteins.

Early work with fluorescent proteins simply co-expressed GFP on the same promoter as another gene to monitor expression levels. Proteins could also be chemically labelled outside of the cell and then inserted using microinjection [25,28]. A real breakthrough, with the discovery of GFP, was optimizing a method to fuse the genes of a protein of interest with a fluorescent protein and express this in a cell—thus leaving

the cell relatively unperturbed. This was first demonstrated [29] on a GFP fusion to the *bcd* transcription factor in *Drosophila* [30].

Fluorescent dyes have been used not just as high-contrast markers, but as part of molecular probes which can readout dynamics between molecules and also environmental factors such as pH. In 1946, Theodore Förster posited that if a donor and acceptor molecule were sufficiently close together, non-radiative transfer of energy could occur between the two, now known as Förster resonance energy transfer (FRET), with efficiency proportional to the sixth power of the distance between them [31]. If such molecules are themselves fluorescent dyes, then fluorescence can be used as a metric of putative molecular interaction through FRET. In 1967, Stryer & Haugland [32] showed this phenomenon could be used as a molecular ruler over a length scale of approximately 1–10 nm. Since then, FRET is used routinely to image molecular interactions and the distances between biological molecules, and also in fluorescence lifetime imaging [33]. Fluorescent probes have also been developed to detect cell membrane voltages, local cellular viscosity levels and the concentration of specific ions, with calcium ion probes, for example, first introduced by Roger Tsien in 1980 [34].

5. The fluorescence microscope

The fluorescence microscope has its origins in ultraviolet (UV) microscopy. Abbe theory meant that better spatial resolution could be achieved using shorter wavelengths of light. August Köhler constructed the first UV microscope in 1904 [35]. He found that his samples would also emit light under UV illumination (although he noted this as an annoyance). Not long after, Oskar Heimstaedt realized the potential for fluorescence and had a working instrument by 1911 [36]. These transmission fluorescence microscopes were greatly improved in 1929 when Philipp Ellinger and August Hirt placed the excitation and emission optics on the same side as the sample and invented the 'epi-fluorescence' microscope [37]. With the invention of dichroic mirrors in 1967 [38], this design would become the standard in fluorescence microscopes. Several innovative illumination modes have also been developed for the fluorescence microscope, which have allowed it to image many different samples over a wide range of length scales. These modes include confocal, fluorescence recovery after photobleaching (FRAP), total internal reflection fluorescence (TIRF) and two-photon and light-sheet microscopy (LSM).

In conventional fluorescence microscopy, the whole sample is illuminated and emitted light collected. Much of the collected light is from parts of the sample that are out of focus. In confocal microscopy, a pinhole is placed after the light source such that only a small portion of the sample is illuminated and another pinhole placed before the detector such that only in-focus light is collected (figure 1). This can reduce the background in a fluorescence image and allow imaging further into a sample. The latter even enables optical sectioning and three-dimensional reconstruction. The first confocal microscope was patented by Marvin Minsky in 1961 [39]. This instrument preceded the laser so the incident light was not bright enough for fluorescence. With laser-scanning confocal microscopes [40], much better fluorescence contrast is achievable, as explored by White who compared the contrast in different human and animal cell lines [41].



Figure 3. By chance, in the last days of finishing this review, the corresponding author was staying approximately 100 m from Leeuwenhoek's final resting place in the Oude Kerk, Delft, and captured these images.

Fluorophores only emit light for a short time before they are irreversibly photobleached, and so microscopists must limit their sample's exposure to excitation light. Photobleaching can be used to reveal kinetic information about a sample by fluorescence recovery. In the earliest fluorescence recovery study, in 1974, Peters *et al.* [42] bleached one-half of fluorescein-labelled human erythrocyte plasma membranes and found that no fluorescence returned, indicating no observable mean diffusive process of the membrane over the experimental time scales employed. Soon after, analytical work by Axelrod *et al.* [43] (on what they termed fluorescence photobleaching recovery) allowed them to characterize different modes of diffusion in intracellular membrane trafficking. The term FRAP appears to have been coined by Jacobson, Wu and Poste in 1976 [44]. With FRAP capabilities commercially available on confocal systems, it is now widely used for measuring turnover kinetics in live cells.

When imaging features that are thin or peripheral such as cell membranes and molecules embedded in these, a widely used method is TIRF microscopy. This technique uses a light beam introduced above the critical angle of the interface between the (normally) glass microscope coverslip and the water-based sample. The beam itself will be reflected by total internal reflection due to the differences in refractive index between the water and the glass, but at the interface an evanescent wave of excitation light is generated which penetrates only approximately 100 nm into the sample, thus only fluorophores close to the coverslip surface are excited, producing much higher signal-to-noise than conventional epi-fluorescence microscopy. It was first demonstrated on biological samples by Axelrod in 1981 to image membrane proteins in rat muscle cells and lipids in human skin cells [45].

In conventional epi-fluorescence or even confocal, there is a limit to how far into the sample it is possible to image because of incident light scattering from the sample, creating a fluorescent background. This is particularly problematic when imaging tissues. Longer wavelength light scatters much less but few fluorophores can be excited by this with standard single photon excitation. In her doctoral thesis, in 1931, Maria Goppert-Mayer theorized that two photons with half the energy needed

can excite emission of one photon whose energy was the sum of the two photons during a narrow time window for absorption of approximately 10^{-18} s [46]. The phenomenon of two-photon excitation (2PE) was not observed experimentally for another 30 years, until Kaiser and Garrett demonstrated it in CaF crystals [47]. The probability of 2PE occurring in a sample is low due to the very narrow time window of coincidence with respect to the two excitation photons, so high-intensity light with a large photon flux is required to use the phenomenon in microscopy. In 1990, Denk used a laser in a confocal scanning microscope to image human kidney cells with 2PE [48]. Since then, it has become a powerful technique for observing molecular processes in live tissues, particularly in neuroscience, where the dynamics of neurons within a live rat brain were first observed by Svoboda *et al.* [49].

Another method of reducing background in fluorescent samples is to only illuminate the sample through the plane that is in focus. This can be achieved by shining a very flat excitation beam through the sample perpendicular to the optical axis. Voie *et al.* [50] first demonstrated this using LSM in 1993. LSM can be used to take fluorescence images through slices of a sample, allowing a stack of images to build a three-dimensional reconstruction. One caveat of LSM is that samples need to be specially mounted to allow an unobstructed excitation beam as well as a perpendicular detection beam, so a bespoke microscope is required. The technique was pioneered and developed by Ernst Stelzer in 2004, and termed selective plane illumination microscopy; it was used to image live embryos in three dimensions [51]. Stelzer's group went on to image and track every nucleus in a developing zebrafish over 24 h [52] and also the growth of plant roots at the cellular level in *Arabidopsis* [53]. LSM has proved itself a powerful tool for developmental biology, the potential of which is only now being realized (figure 3).

6. Improving resolution in length and time

Fluorescence microscopy set new standards of contrast in biological samples that have enabled the technique to achieve

possibly the ultimate goal of microscopy in biology and visualize single molecules in live cells. The Abbe diffraction limit, thought unbreakable for over one hundred years, has been circumvented by ever more inventive microscopy techniques which are now extending into three spatial dimensions.

The first single biological molecules detected were observed by Cecil Hall in the 1950s [54], using electron microscopy of filamentous molecules including DNA and fibrous proteins using metallic shadowing of dried samples in a vacuum. The very first detection of a single biological molecule in its functional *aqueous* phase was made by Boris Rotman, his seminal work published in 1961 involving the observation of fluorescently labelled substrates of β -galactosidase suspended in water droplets. The enzyme catalysed the hydrolysis of galactopyranose labelled with fluorescein to the sugar galactose plus free fluorescein, which had a much greater fluorescence intensity than when attached to the substrate. He could detect single molecules because each enzyme could turn over thousands of fluorescent substrate molecules [55]. A more direct measurement was made by Thomas Hirschfeld, in work published in 1976, who managed to see single molecules of globulin, labelled with approximately 100 fluorescein dyes, passing through a focused laser [56]. Single dye molecules were not observable directly until the advent of scanning near-field optical microscopy (SNOM) developed by Eric Betzig and Robert Chichester, allowing them to image individual cyanine dye molecules in a sub-monolayer [57]. SNOM uses an evanescent wave from a laser incident on an approximate 100-nm probe aperture which illuminates a small section and penetrates only a small distance into the sample. Images are generated by scanning this probe over the sample. This is technically challenging as the probe must then be very close to the sample.

Single molecules were shown to be observable with less challenging methods when, using TIRF microscopy, single ATP turnover reactions in single myosin molecules was observed in 1995 [58]. Other studies observed single F1-ATPase rotating using fluorescently labelled actin molecules in 1997 [59] and the dynamics of single cholesterol oxidase molecules [60]. In a landmark study, the mechanism and step size of the myosin motor was determined by labelling one foot, observing and using precise Gaussian fitting to obtain nanometre resolution (termed 'fluorescence imaging with one nanometre accuracy'—FIONA) [61]. This localization microscopy could effectively break the diffraction limit by using mathematical fitting algorithms to pinpoint the centre of a dye molecule's PSF image, as long as they are resolvable such that the typical nearest-neighbour separation of dye molecules in the sample is greater than the optical resolution limit. These techniques were soon applied to image single molecules in living cells [62,63] and now it is possible to count the number of single molecules in complexes inside cells [64,65].

Stefan Hell showed that it was possible to optically break the diffraction limit with a more deterministic technique which modified the actual shape of the PSF, called Stimulated emission depletion microscopy (STED), which he proposed with Jan Wichmann in 1994 [66] and implemented with Thomas Klar in 1999 [67]. STED works by depleting the population of excited energy state electrons through stimulated emission. Fluorescence emission only occurs subsequently from a narrow central beam inside the deactivation annulus region which is scanned over the sample. The emission region is smaller than the diffraction limit (approx. 100 nm in

the original study), thus allowing a superresolution image to be generated.

The development of STED showed that the diffraction limit could be broken, and many new techniques followed. In 2002, Ando *et al.* [68] isolated a fluorescent protein from the stony coral, *Trachyphyllia geoffroyi*, which they named Kaede. They found that if exposed to UV light its fluorescence would change from green to red, and demonstrated this in Kaede protein expressed in HeLa cells. Photoactivatable proteins such as this were used in 2006 by Hess *et al.* [69] in photo-activated localization microscopy (PALM) using TIRF and by Betzig *et al.* in fluorescence photo-activated localization microscopy using confocal. Both methods use low-intensity long UV laser light to photoactivate a small subset of sample fluorophores then another laser to excite them to emit and photobleach. This is repeated to build a superresolution image. A related method uses stochastic photoblinking of fluorescent dyes, which for example can be used to generate superresolution structures of DNA [70].

Other notable superresolution techniques include structured illumination microscopy [71]. In 1993, Bailey *et al.* showed that structured stripes of light could be used to generate a spatial 'beat' pattern in the image which could be used to extract spatial features in the underlying sample image, which had a resolution of approximately two times that of the optical resolution limit. In 2006, Zhuang and co-workers [72] demonstrated stochastic optical reconstruction microscopy (STORM), which used a Cy5/Cy3 pair as a switchable probe. A red laser keeps Cy5 in a dark state and excites fluorescence, while a green laser brings the pair back into a fluorescent state. Thus, similarly to PALM, a superresolution image can be generated.

Improvements in *dynamic* fluorescence imaging have been significant over the past few decades. For example, using essentially the same localization algorithms as developed for PALM/STORM imaging, fluorescent dye tags can be tracked in a cellular sample in real-time, for example tracking of membrane protein complexes in bacteria to nanoscale precision [73], which has been extended into high time resolution dual-colour microscopy *in vivo* to monitor dynamic co-localization with a spatial precision of approximately 10–100 nm [74]. Modifications to increase the laser excitation of several recent bespoke microscope systems have also improved the time resolution of fluorescence imaging down to the millisecond level, for example using narrowfield and slimfield microscopy [64].

Three-dimensional information can be obtained in many ways including using interferometric methods [75] or multi-plane microscopy [76], which image multiple focal planes simultaneously. Another method of encoding depth information in images is to distort the PSF image in an asymmetrical but measurable way as the light source moves away from the imaging plane. Astigmatism and double-helix microscopy accomplish this using different methods and are compatible with many modes of fluorescence illumination as the equipment used is placed between the objective lens and the camera. As such, it is a viable way to extract three-dimensional data from many currently developed fluorescence microscopes.

Astigmatism microscopy is a simple three-dimensional microscopy technique, first demonstrated by Kao and Verkman in 1994 [77]. An asymmetry is introduced in the imaging path by placing a cylindrical lens before the camera detector. The introduced astigmatism offsets the focal plane along one lateral axis slightly, resulting in a controlled image distortion. When

imaging singular or very small aggregates of fluorophores, the distortion takes the form of an ellipse, extending along either the x - or y -axis in the lateral plane of a camera detector conjugate to the microscope focal plane, depending on whether the fluorophore is above or below the focal plane. Values of 30 nm resolution in the lateral plane and 50 nm in the axial dimension have been reported using astigmatism with STORM [78].

Double-helix PSF (DH-PSF) microscopy is a similar three-dimensional microscopy technique using controlled PSF distortion. It exploits optical vortex beams, beams of light with angular momentum, and works by placing a phase mask—an object which modifies the phase of the beam differently at different points along a cross section—between the camera and the objective lens to turn the laser beam intensity profile from a Gaussian beam to a mixture of higher order optical vortex beams—a superposition of two so-called Laguerre-Gauss (LG) beams. These two beams interfere with each other at the point that the light hits the camera, creating two bright lobes [79]. The fields rotate as a function of distance propagated. As the two beams are superposed, the distance is the same; if the two LG beams are slightly different the electric fields will rotate at different rates thanks to different so-called ‘Gouy Phase’ components. This means that the interference pattern produced rotates as a function of the distance of the point source from the image plane only [80]. The distance from the focal plane can be determined by measuring the rotation angle of the two lobes.

The phase mask can be created using transparent media such as etched glass or using a spatial light modulator (SLM). An SLM is a two-dimensional array of microscale bit components, each of which can be used to change the phase of the incident light across a beam profile. A liquid-crystal-on-silicon SLM retards light as a function of the input voltage to each bit. As such, a phase mask can be applied and changed in real-time using computer control. One major drawback is that they are sensitive to the polarization of light [81], limiting the efficiency of light propagation through the SLM. Alternatively, a fixed glass phase plate can be etched using nanolithography. This is phase-independent and much more photon efficient. The phase is retarded simply by the thickness of the glass at each point in the beam. However, glass phase plates are less precise than SLM due to limitations in the lithography. Still, these are much easier to implement and can be purchased commercially or custom-built and used with almost any microscope set-up with minimal detrimental impact. DH-PSF microscopy has been shown to have some of the smallest spatial localization errors of any three-dimensional localization mode in high signal-to-noise systems [82].

The power of beam-shaping combined with light-sheet illumination has been recently used to create lattice LSM [83]. Using Bessel beams, which focus laser profiles with minimal divergence due to diffraction, they create different bound optical lattices with different properties allowing them to image across four orders of magnitude in space and time and in diverse samples including diffusing transcription factors in stem cells, mitotic microtubules and embryogenesis in *Caenorhabditis elegans*.

7. The future

Although it is over 300 years since the pioneering work of van Leeuwenhoek, many of the major developments in light

microscopy have occurred in just the past few decades and their full impact may not yet be felt. There are several technologies currently in development which may have a profound impact on microscopy. These include, for example, adaptive optics, lens-free microscopy, super lenses, miniaturization and combinational microscopy approaches.

A biological sample itself adds aberration through spatial variation in the refractive index. This is even more of a problem when imaging deep into tissues. Adaptive optics uses so-called dynamic correction elements such as deformable mirrors or SLMs to correct for this aberration, increasing spatial resolution and contrast. There have been many recent developments, reviewed comprehensively by Martin Booth [84], but the technology is still yet to be widely adopted.

The archetypal lens used in light microscopy is made of glass, however this is not the only type of lens available. Optical diffraction gratings (optical gratings) can be used to focus, steer and even reflect light. Recognizing the need for miniaturization, researchers have been investigating the use of diffraction gratings in place of glass to help reduce the necessary size of optical components. While glass is great for large applications, it is extremely bulky when compared with the minimum size of a diffraction grating [85]. Optical gratings can be used as equivalent to lenses under some circumstances, for example a Fresnel zone plate can be used to focus light to a point as a convex lens does. Optical gratings all rely on the interaction of electromagnetic waves as they pass through the spaces in the gratings. This is fundamentally linked to the wavelength of propagating light making achromatic optical gratings very difficult to achieve in practice. Only recently have scientists been able to produce achromatic glass analogues such as an achromatic grating quarter-wave plates, for example, with good operational ranges [86].

Ptychography completely removes the need for imaging optics, lenses or gratings, and directly reconstructs real-space images from diffraction patterns captured from a beam scanned over a sample. In many cases, this allows higher contrast images than DIC or phase contrast and three-dimensional reconstruction [87,88].

All optics currently used in microscopes are diffraction-limited but it is theoretically possible to construct, using so-called ‘metamaterials’, a perfect lens or super lens which could image with perfect sharpness. This was thought to require a material with negative refractive index [89] but it has now been shown that ordinary positive refractive index materials can also be used [90]. Even if super lenses are not achievable, new materials may revolutionize microscope lenses, still mostly composed of the same materials used by van Leeuwenhoek.

It is interesting to note the return of microscopes such as van Leeuwenhoek’s which use only a single lens, in the foldscope developed by Manu Prakash at Stanford University [91]. Using cardboard (an essential and surprisingly cheap component of some of the most advanced bespoke light microscopes found in our own laboratory) and simple filters and lenses, a near indestructible microscope with both normal transmission modes and fluorescence modes has been created that can be used by scientists and physicians working in areas far from expensive laboratory equipment.

Combinatorial microscopy is an interesting recent advance, which shows significant future potential. Here, several different microscopy methods are implemented on the same light microscope device. Many advances are being made at the

level of single-molecule biophysics coupled to light microscopy in this regard. For example, methods are being developed that can permit simultaneous superresolution imaging of DNA coupled to magnetic tweezers manipulation [92].

The ultimate practical limits at the other end of the length scale for imaging tissues and whole organisms in the future are difficult to determine. Recent technological developments such as the light-sheet imaging of *Arabidopsis* or lattice LSM discussed previously have enabled imaging of ever larger samples in greater detail. What limits the largest possible sample and to what level of detail it can be imaged is unknown. And, just as importantly, is computing technology used to store and analyse these data up to the challenge?

It is unquestionable that light microscopy has advanced enormously since the days of Antonj van Leeuwenhoek. The improvements have been, in a broad sense, twofold. Firstly, in length-scale precision: this has been a 'middling-out' improvement, in that superresolution methods have allowed unprecedented access to nanoscale biological features, whereas light-sheet approaches and multi-photon deep imaging

methods in particular have allowed incredible detail to be discerned at the much larger length-scale level of multicellular tissues. Secondly, there has been an enormous advance, almost to the level of a paradigm shift, towards faster imaging in light microscopy, to permit truly dynamic biological processes to be investigated, right down to the millisecond level. Not only can we investigate detailed biological structures using light microscopy, but we can watch them change with time.

And yet, equally so, the basic principles of light microscopy for the study of biology remain essentially unchanged. These were facilitated in no small part by the genius and diligence of van Leeuwenhoek. It is perhaps the finest legacy for a true pioneer of light microscopy.

Funding statement. M.C.L. is supported by a Royal Society University Research Fellowship (UF110111). E.G.H. was supported by Marie Curie EU FP7 ITN 'ISOLATE' ref 289995. R.N. was supported by the White Rose Consortium. The work was supported by the Biological Physics Sciences Institute (BPSI).

Author contributions. All authors contributed to the drafting and revision of the manuscript, and gave their final approval for publication.

References

- Orchard G, Nation B. 2014 *Cell structure & function*, p. 448. Oxford, UK: Oxford University Press.
- Hooke R. 1665 *Micrographia: or some physiological descriptions of minute bodies made by magnifying glasses, with observations and inquiries thereupon*. Courier Corporation.
- Baker H, Leeuwenhoek M. 1739 An account of Mr. Leeuwenhoek's microscopes; by Mr. Henry Baker F. R. S. 1739. *Phil. Trans.* **41**, 503–519. (doi:10.1098/rstl.1739.0085)
- van Leeuwenhoek A, Hooke S. 1800 *The select works of Antony Van Leeuwenhoek, containing his microscopical discoveries in many of the works of nature*, vol. 1. Gale ECCO.
- Airy GB. 1835 On the diffraction of an object-glass with circular aperture. *Trans. Camb. Phil. Soc.* **5**, 239–291.
- Abbe E. 1873 Beiträge zur Theorie des Mikroskops und der mikroskopischen Wahrnehmung. *Arch. Mikrosk. Anat.* **9**, 413–418. (doi:10.1007/BF02956173)
- Lord Rayleigh FRS. 1879 XXXI investigations in optics, with special reference to the spectroscopy. *Phil. Mag. Ser. 5* **8**, 261–274. (doi:10.1080/14786447908639684)
- Mansuripur M. 2002 *Classical optics and its applications*, p. 502. Cambridge, UK: Cambridge University Press.
- Abbe E. 1881 VII.—On the estimation of aperture in the microscope. *J. R. Microsc. Soc.* **1**, 388–423. (doi:10.1111/j.1365-2818.1881.tb05909.x)
- Abbe E. 1883 XV.—The relation of aperture and power in the microscope. *J. R. Microsc. Soc.* **3**, 790–812. (doi:10.1111/j.1365-2818.1883.tb05956.x)
- Hell SW, Stelzer EHK, Lindek S, Cremer C. 1994 Confocal microscopy with an increased detection aperture: type-B 4PI confocal microscopy. *Opt. Lett.* **19**, 222. (doi:10.1364/OL.19.000222)
- Köhler A. 1893 Ein neues Beleuchtungsverfahren für mikrophotographische Zwecke. *Z. Wiss. Mikrosk.* **10**, 433–440.
- Zernike F. 1942 Phase contrast, a new method for the microscopic observation of transparent objects. *Physica* **9**, 686–698. (doi:10.1016/S0031-8914(42)80035-X)
- Zernike F. 1955 How I discovered phase contrast. *Science* **121**, 345–349. (doi:10.1126/science.121.3141.345)
- Smith F. 1955 Microscopic interferometry. *Research* **8**, 385–395.
- Nomarski G, Weill A. 1955 Application à la métallographie des méthodes interférentielles à deux ondes polarisées. *Rev. Met.* **2**, 121–128.
- Gerlach J. 1858 Mikroskopische Studien aus dem Gebiete der menschlichen Morphologie. Enke.
- Golgi C. 1873 Sulla struttura della griglia del cervello. *Gaz. Med. Intalianna Lomb.* **6**, 244–246.
- Gram H. 1884 Über die isolierte Färbung der Schizomyceten in Schnitt- und Trockenpräparaten. *Fortschr. Med.* **2**, 185–189.
- Stokes GG. 1852 On the change of refrangibility of light. *Phil. Trans. R. Soc. Lond.* **142**, 463–562. (doi:10.1098/rstl.1852.0022)
- Baeyer A. 1871 Über eine neue Klasse von Farbstoffen. *Berichte der Dtsch. Chem. Gesellschaft* **4**, 555–558. (doi:10.1002/cber.18710040209)
- Coons AH, Creech HJ, Jones RN. 1941 Immunological properties of an antibody containing a fluorescent group. *Exp. Biol. Med.* **47**, 200–202. (doi:10.3181/00379727-47-13084P)
- Shimomura O, Johnson FH, Saiga Y. 1962 Extraction, purification and properties of aequorin, a bioluminescent protein from the luminous hydromedusa, aequorea. *J. Cell. Comp. Physiol.* **59**, 223–239. (doi:10.1002/jcp.1030590302)
- Chalfie M, Tu Y, Euskirchen G, Ward W, Prasher D. 1994 Green fluorescent protein as a marker for gene expression. *Science* **263**, 802–805. (doi:10.1126/science.8303295)
- Heim R, Prasher DC, Tsien RY. 1994 Wavelength mutations and posttranslational autooxidation of green fluorescent protein. *Proc. Natl Acad. Sci. USA* **91**, 12 501–12 504. (doi:10.1073/pnas.91.26.12501)
- Matz MV, Fradkov AF, Labas YA, Savitsky AP, Zaraisky AG, Markelov ML, Lukyanov SA. 1999 Fluorescent proteins from nonbioluminescent Anthozoa species. *Nat. Biotechnol.* **17**, 969–973. (doi:10.1038/13657)
- Shaner NC, Campbell RE, Steinbach PA, Giepmans BNG, Palmer AE, Tsien RY. 2004 Improved monomeric red, orange and yellow fluorescent proteins derived from *Discosoma* sp. red fluorescent protein. *Nat. Biotechnol.* **22**, 1567–1572. (doi:10.1038/nbt1037)
- Taylor D, Amato P, Luby-Phelps K, McNeil P. 1984 Fluorescent analog cytochemistry. *Trends Biochem. Sci.* **9**, 88–91. (doi:10.1016/0968-0004(84)90098-7)
- Gerdes H-H, Kaether C. 1996 Green fluorescent protein: applications in cell biology. *FEBS Lett.* **389**, 44–47. (doi:10.1016/0014-5793(96)00586-8)
- Wang S, Hazelrigg T. 1994 Implications for bcd mRNA localization from spatial distribution of exu protein in *Drosophila oogenesis*. *Nature* **369**, 400–403. (doi:10.1038/369400a0)
- Förster T. 1946 Energiewanderung und Fluoreszenz. *Naturwissenschaften* **33**, 166–175. (doi:10.1007/BF00585226)
- Stryer L, Haugland RP. 1967 Energy transfer: a spectroscopic ruler. *Proc. Natl Acad. Sci. USA* **58**, 719–726. (doi:10.1073/pnas.58.2.719)
- Clegg RM, Feddersen BA, Gratton E, Jovin TM. 1992 Time-resolved imaging fluorescence microscopy. *Proc. SPIE* **1640**, 448–460. (doi:10.1117/12.58237)

34. Tsien RY. 1980 New calcium indicators and buffers with high selectivity against magnesium and protons: design, synthesis, and properties of prototype structures. *Biochemistry* **19**, 2396–2404. (doi:10.1021/bi00552a018)
35. Köhler A, Rohr MJ. 1905 Photomicrography with ultra-violet light. *J. R. Microsc. Soc.* **25**, 513.
36. Heimstadt O. 1911 Das Fluoreszenzmikroskop. *Z. Wiss. Mikrosk.* **28**, 330–337.
37. Ellinger P, Hirt A. 1929 Mikroskopische Beobachtungen an lebenden Organen mit Demonstrationen (Intravitalmikroskopie). *Arch. Exp. Pathol. Pharmacol.* **147**, 63. (doi:10.1007/BF01946036)
38. Ploem JS. 1967 The use of a vertical illuminator with interchangeable dichroic mirrors for fluorescence microscopy with incidental light. *Z. Wiss. Mikrosk.* **68**, 129–142.
39. Minsky M. 1961 *Microscopy apparatus*. US Patent 3 013 467.
40. Wilke V. 1985 Optical scanning microscopy: the laser scan microscope. *Scanning* **7**, 88–96. (doi:10.1002/sca.4950070204)
41. White JG. 1987 An evaluation of confocal versus conventional imaging of biological structures by fluorescence light microscopy. *J. Cell Biol.* **105**, 41–48. (doi:10.1083/jcb.105.1.41)
42. Peters R, Peters J, Tews KH, Bähr W. 1974 A microfluorimetric study of translational diffusion in erythrocyte membranes. *Biochim. Biophys. Acta Biomembr.* **367**, 282–294. (doi:10.1016/0005-2736(74)90085-6)
43. Axelrod D, Koppel DE, Schlessinger J, Elson E, Webb WW. 1976 Mobility measurement by analysis of fluorescence photobleaching recovery kinetics. *Biophys. J.* **16**, 1055–1069. (doi:10.1016/S0006-3495(76)85755-4)
44. Jacobson K, Wu E, Poste G. 1976 Measurement of the translational mobility of concanavalin A in glycerol-saline solutions and on the cell surface by fluorescence recovery after photobleaching. *Biochim. Biophys. Acta* **433**, 215–222. (doi:10.1016/0005-2736(76)90189-9)
45. Axelrod D. 1981 Cell-substrate contacts illuminated by total internal reflection fluorescence. *J. Cell Biol.* **89**, 141–145. (doi:10.1083/jcb.89.1.141)
46. Göppert-Mayer M. 1931 Über Elementarakte mit zwei Quantensprüngen. *Ann. Phys.* **401**, 273–294. (doi:10.1002/andp.19314010303)
47. Kaiser W, Garrett C. 1961 Two-photon excitation in $\text{CaF}_2: \text{Eu}^{2+}$. *Phys. Rev. Lett.* **7**, 229–231. (doi:10.1103/PhysRevLett.7.229)
48. Denk W, Strickler JH, Webb WW. 1990 Two-photon laser scanning fluorescence microscopy. *Science* **248**, 73–76. (doi:10.1126/science.2321027)
49. Svoboda K, Denk W, Kleinfeld D, Tank DW. 1997 *In vivo* dendritic calcium dynamics in neocortical pyramidal neurons. *Nature* **385**, 161–165. (doi:10.1038/385161a0)
50. Voie AH, Burns DH, Spelman FA. 1993 Orthogonal-plane fluorescence optical sectioning: three-dimensional imaging of macroscopic biological specimens. *J. Microsc.* **170**, 229–236. (doi:10.1111/j.1365-2818.1993.tb03346.x)
51. Huisken J, Swoger J, Del Bene F, Wittbrodt J, Stelzer EHK. 2004 Optical sectioning deep inside live embryos by selective plane illumination microscopy. *Science* **305**, 1007–1009. (doi:10.1126/science.1100035)
52. Keller PJ, Schmidt AD, Wittbrodt J, Stelzer EHK. 2008 Reconstruction of zebrafish early embryonic development by scanned light sheet microscopy. *Science* **322**, 1065–1069. (doi:10.1126/science.1162493)
53. Maizel A, von Wangenheim D, Federici F, Haseloff J, Stelzer EHK. 2011 High-resolution live imaging of plant growth in near physiological bright conditions using light sheet fluorescence microscopy. *Plant J.* **68**, 377–385. (doi:10.1111/j.1365-313X.2011.04692.x)
54. Hall CE. 1956 Method for the observation of macromolecules with the electron microscope illustrated with micrographs of DNA. *J. Biophys. Biochem. Cytol.* **2**, 625–628. (doi:10.1083/jcb.2.5.625)
55. Rotman B. 1961 Measurement of activity of single molecules of beta-D-galactosidase. *Proc. Natl Acad. Sci. USA* **47**, 1981–1991. (doi:10.1073/pnas.47.12.1981)
56. Hirschfeld T. 1976 Optical microscopic observation of single small molecules. *Appl. Opt.* **15**, 2965–2966. (doi:10.1364/AO.15.002965)
57. Betzig E, Chichester RJ. 1993 Single molecules observed by near-field scanning optical microscopy. *Science* **262**, 1422–1425. (doi:10.1126/science.262.5138.1422)
58. Funatsu T, Harada Y, Tokunaga M, Saito K, Yanagida T. 1995 Imaging of single fluorescent molecules and individual ATP turnovers by single myosin molecules in aqueous solution. *Nature* **374**, 555–559. (doi:10.1038/374555a0)
59. Noji H, Yasuda R, Yoshida M, Kinosita K. 1997 Direct observation of the rotation of F1-ATPase. *Nature* **386**, 299–302. (doi:10.1038/386299a0)
60. Lu HP. 1998 Single-molecule enzymatic dynamics. *Science* **282**, 1877–1882. (doi:10.1126/science.282.5395.1877)
61. Yildiz A *et al.* 2003 Myosin V walks hand-over-hand: single fluorophore imaging with 1.5-nm localization. *Science* **300**, 2061–2065. (doi:10.1126/science.1084398)
62. Byassee T, Chan W, Nie S. 2000 Probing single molecules in single living cells. *Anal. Chem.* **72**, 5606–5611. (doi:10.1021/ac000705j)
63. Sako Y, Minoghchi S, Yanagida T. 2000 Single-molecule imaging of EGFR signalling on the surface of living cells. *Nat. Cell Biol.* **2**, 168–172. (doi:10.1038/35004044)
64. Reyes-Lamothe R, Sherratt DJ, Leake MC. 2010 Stoichiometry and architecture of active DNA replication machinery in *Escherichia coli*. *Science* **328**, 498–501. (doi:10.1126/science.1185757)
65. Leake MC, Chandler JH, Wadhams GH, Bai F, Berry RM, Armitage JP. 2006 Stoichiometry and turnover in single, functioning membrane protein complexes. *Nature* **443**, 355–358. (doi:10.1038/nature05135)
66. Hell SW, Wichmann J. 1994 Breaking the diffraction resolution limit by stimulated emission: stimulated-emission-depletion fluorescence microscopy. *Opt. Lett.* **19**, 780–782. (doi:10.1364/OL.19.000780)
67. Klar TA, Hell SW. 1999 Subdiffraction resolution in far-field fluorescence microscopy. *Opt. Lett.* **24**, 954. (doi:10.1364/OL.24.000954)
68. Ando R, Hama H, Yamamoto-Hino M, Mizuno H, Miyawaki A. 2002 An optical marker based on the UV-induced green-to-red photoconversion of a fluorescent protein. *Proc. Natl Acad. Sci. USA* **99**, 12 651–12 656. (doi:10.1073/pnas.202320599)
69. Hess ST, Girirajan TPK, Mason MD. 2006 Ultra-high resolution imaging by fluorescence photoactivation localization microscopy. *Biophys. J.* **91**, 4258–4272. (doi:10.1529/biophysj.106.091116)
70. Miller H, Zhaokun Z, Wollman AJM, Leake MC. In press. Superresolution imaging of single DNA molecules using stochastic photoblinking of minor groove and intercalating dyes. *Methods*. (doi:10.1016/j.ymeth.2015.01.010)
71. Bailey B, Farkas DL, Taylor DL, Lanni F. 1993 Enhancement of axial resolution in fluorescence microscopy by standing-wave excitation. *Nature* **366**, 44–48. (doi:10.1038/366044a0)
72. Rust MJ, Bates M, Zhuang X. 2006 Sub-diffraction-limit imaging by stochastic optical reconstruction microscopy (STORM). *Nat. Methods* **3**, 793–795. (doi:10.1038/nmeth929)
73. Leake MC, Greene NP, Godun RM, Granjon T, Buchanan G, Chen S, Berry RM, Palmer T, Berks BC. 2008 Variable stoichiometry of the TatA component of the twin-arginine protein transport system observed by *in vivo* single-molecule imaging. *Proc. Natl Acad. Sci. USA* **105**, 15 376–15 381. (doi:10.1073/pnas.0806338105)
74. Llorente-García I *et al.* 2014 Single-molecule *in vivo* imaging of bacterial respiratory complexes indicates delocalized oxidative phosphorylation. *Biochim. Biophys. Acta* **1837**, 811–824. (doi:10.1016/j.bbabi.2014.01.020)
75. Shtengel G *et al.* 2009 Interferometric fluorescent super-resolution microscopy resolves 3D cellular ultrastructure. *Proc. Natl Acad. Sci. USA* **106**, 3125–3130. (doi:10.1073/pnas.0813131106)
76. Juette MF, Gould TJ, Lessard MD, Mlodzianoski MJ, Naggure BS, Bennett BT, Hess ST, Bewersdorf J. 2008 Three-dimensional sub-100 nm resolution fluorescence microscopy of thick samples. *Nat. Methods* **5**, 527–529. (doi:10.1038/nmeth.1211)
77. Kao HP, Verkman AS. 1994 Tracking of single fluorescent particles in three dimensions: use of cylindrical optics to encode particle position. *Biophys. J.* **67**, 1291–1300. (doi:10.1016/S0006-3495(94)80601-0)
78. Huang B, Wang W, Bates M, Zhuang X. 2008 Three-dimensional super-resolution imaging by stochastic optical reconstruction microscopy. *Science* **319**, 810–813. (doi:10.1126/science.1153529)
79. Pavani SRP, Thompson MA, Biteen JS, Lord SJ, Liu N, Twieg RJ, Piestun R, Moerner WE. 2009 Three-dimensional, single-molecule fluorescence imaging beyond the diffraction limit by using a double-helix

- point spread function. *Proc. Natl Acad. Sci. USA* **106**, 2995–2999. (doi:10.1073/pnas.0900245106)
80. Schechner Y, Piestun R, Shamir J. 1996 Wave propagation with rotating intensity distributions. *Phys. Rev. E* **54**, R50–R53. (doi:10.1103/PhysRevE.54.R50)
81. Carbone L, Fulda P, Bond C, Brueckner F, Brown D, Wang M, Lodhia D, Palmer R, Freise A. 2013 The generation of higher-order Laguerre-Gauss optical beams for high-precision interferometry. *J. Vis. Exp.* **78**, e50564. (doi:10.3791/50564)
82. Badieirostami M, Lew MD, Thompson MA, Moerner WE. 2010 Three-dimensional localization precision of the double-helix point spread function versus astigmatism and biplane. *Appl. Phys. Lett.* **97**, 161103. (doi:10.1063/1.3499652)
83. Chen B-C *et al.* 2014 Lattice light-sheet microscopy: imaging molecules to embryos at high spatiotemporal resolution. *Science* **346**, 1257998. (doi:10.1126/science.1257998)
84. Booth MJ. 2014 Adaptive optical microscopy: the ongoing quest for a perfect image. *Light Sci. Appl.* **3**, e165. (doi:10.1038/lssa.2014.46)
85. Chrostowski L. 2010 Optical gratings: nano-engineered lenses. *Nat. Photonics* **4**, 413–415. (doi:10.1038/nphoton.2010.143)
86. Passilly N, Ventola K. 2008 Achromatic phase retardation by subwavelength gratings in total internal reflection. *J. Opt. A Pure Appl. Opt.* **10**, 015001. (doi:10.1088/1464-4258/10/01/015001)
87. Marrison J, Rätty L, Marriott P, O'Toole P. 2013 Ptychography—a label free, high-contrast imaging technique for live cells using quantitative phase information. *Sci. Rep.* **3**, 2369. (doi:10.1038/srep02369)
88. Rodenburg JM, Hurst AC, Cullis AG. 2007 Transmission microscopy without lenses for objects of unlimited size. *Ultramicroscopy* **107**, 227–231. (doi:10.1016/j.ultramic.2006.07.007)
89. Pendry J. 2000 Negative refraction makes a perfect lens. *Phys. Rev. Lett.* **85**, 3966–3969. (doi:10.1103/PhysRevLett.85.3966)
90. Leonhardt U. 2009 Perfect imaging without negative refraction. *New J. Phys.* **11**, 093040. (doi:10.1088/1367-2630/11/9/093040)
91. Cybulski JS, Clements J, Prakash M. 2014 Foldscope: origami-based paper microscope. *PLoS ONE* **9**, e98781. (doi:10.1371/journal.pone.0098781)
92. Wollman AJM, Miller H, Zhaokun Z, Leake MC. 2015 Probing DNA interactions with proteins using a single-molecule toolbox: inside the cell, in a test tube, and in a computer. *Biochem. Soc. Trans.* **43**, 139–145.

List of abbreviations, acronyms, protein and gene names

BFP	Back Focal Plane
BY4741	A yeast background strain.
CoPro	Counting Proteins, software to estimate the number of proteins in a cell from unfocussed fluorophores
DAQ	Digital AcQuisition card
DH-PSF	Double Helix Point Spread Function
DIC	Differential Interference Contrast microscopy.
eGFP	Enhanced Green Fluorescent Protein (sometimes written EGFP)
EMCCD	Electron Multiplying CCD (camera technology)
FP	Fluorescent Protein
FRAP	Fluorescence Recovery After Photobleaching
FWHM	Full Width at Half Maximum
<i>GAL</i>	Gene repressed by Mig1
GUI	Graphical User Interface
HWHM	Half Width at Half Maximum
Mig1	Transcription factor localised to DNA in glucose rich environments
mCherry	A monomeric red fluorescent protein
MCL	Mad City Labs, a maker of precision translation stages.
mGFP	monomeric Green Fluorescent Protein
Msn2	Another transcription factor, localising to nucleus under glucose starved conditions

NA	Numerical Aperture
ND1	Neutral Density filter, 1 – attenuates to 1/10 of original intensity
Nrd1	A component in RNA polymerase, normally confined to the nucleus
OD _{600nm}	Optical Density at 600 nm
(F)PALM	(Fluorescence) Photo-Activated Localisation Microscopy
PDMS	PolyDiMethylSiloxane
PSF	Point Spread Function
PTFE	PolyTetraFluoroEthylene, Teflon, a plastic material
ROI	Region Of Interest
SAF	Super-critical Angle Fluorescence, a microscopy technique
STED	STimulated Emission Depletion, a microscopy technique
<i>SUC2</i>	Gene repressed by Mig1
Snf1	AMP kinase homolog in yeast
<i>snf1</i> (Δ)	The gene coding for Snf1, Δ added if gene deleted
STORM	STochastic Optical Reconstruction Microscopy
TTL	Transistor to Transistor Logic
W303	A yeast background strain
YNB	Yeast Nitrogen Base, a minimal medium for yeast growth
YP(D)	Yeast Peptone (D-glucose), a rich medium for yeast growth

References

- Abbe, E., 1873. Beiträge zur Theorie des Mikroskops und der microskopischen Wahrnehmung. *Archiv für Mikroskopische Anatomie*, 9.
- Abbe, E., 1881. VII.-On the Estimation of Aperture in the Microscope. *Journal of the Royal Microscopical Society*, 1(3), pp.388–423.
- Adam, S.A., 2001. The nuclear pore complex. *Genome biology*, 2(9), p.REVIEWS0007.
- Adam, V. et al., 2009. Structural basis of {X}-ray induced transient photobleaching in a photactivable green fluorescent protein. , 131, pp.18063–18065.
- Ahuatzi, D. et al., 2007. Hxk2 regulates the phosphorylation state of Mig1 and therefore its nucleocytoplasmic distribution. *The Journal of biological chemistry*, 282(7), pp.4485–93.
- Almquist, J. et al., 2015. A Nonlinear Mixed Effects Approach for Modeling the Cell-To-Cell Variability of Mig1 Dynamics in Yeast. *PLOS ONE*.
- Avitabile, C. et al., 2014. Circular Dichroism studies on the interactions of antimicrobial peptides with bacterial cells. *Scientific Reports*, 4, pp.337–360.
- Axelrod, D. et al., 1976. Mobility Measurement by Analysis of Fluorescence Photobleaching recovery Kinetics. *Biophysical journal*, 16, pp.1055–1069.
- Axelsson, I., 1978. Characterization of proteins and other macromolecules by agarose gel chromatography. *Journal of Chromatography A*, 152(1), pp.21–32.
- Babazadeh, R. et al., 2013. Osmostress-induced cell volume loss delays yeast Hog1 signaling by limiting diffusion processes and by Hog1-specific effects. *PLoS ONE*, 8(11), pp.1–12.
- Badieirostami, M. et al., 2010. Three-dimensional localization precision of the double-helix point spread function versus astigmatism and biplane. *Applied physics letters*, 97(16), p.161103.

- Badrinarayanan, A. et al., 2012. In vivo architecture and action of bacterial structural maintenance of chromosome proteins. *Science (New York, N.Y.)*, 338(6106), pp.528–31.
- Banaeiyan, A. et al., 2013. Hydrodynamic Cell Trapping for High Throughput Single-Cell Applications. *Micromachines*, 4(4), pp.414–430.
- Barnett, J.A., 1998. A history of research on yeasts 1: Work by chemists and biologists 1789-1850. *Yeast*, 14(16), pp.1439–1451.
- Barnett, J.A., 2000. A history of research on yeasts 2: Louis Pasteur and his contemporaries, 1850-1880. *Yeast*, 16(8), pp.755–771.
- Barnett, J.A., 2003. Beginnings of microbiology and biochemistry: The contribution of yeast research. *Microbiology*, 149(3), pp.557–567.
- Bawendi, M.G., Steigerwald, M.L. & Brus, L.E., 1990. The Quantum Mechanics Of Larger Semiconductor Clusters (. *Annual Review of Physical Chemistry*, 41(4), pp.477–496.
- Bendrioua, L. et al., 2014. Yeast AMP-activated protein kinase monitors glucose concentration changes and absolute glucose levels. *Journal of Biological Chemistry*, 289(18), pp.12863–12875.
- Berg, O.G., Winter, R.B. & Von Hippel, P.H., 1981. Diffusion-driven mechanisms of protein translocation on nucleic acids. 1. Models and theory. *Biochemistry*, 20(24), pp.6929–6948.
- Berkowitz, M., 1996. World's Earliest Wine. *Archeology*, 49(5).
- Beucher, S. & Lantuejoul, C., 1979. Use of Watersheds in Contour Detection. *International Workshop on Image Processing: Real-time Edge and Motion Detection/Estimation*, pp.12–21.
- Botstein, D., Chervitz, S.A. & Cherry, J.M., 1997. Yeast as a Model Organism. *Science*, 277(5330), pp.1259–1260.
- Bruus, H., 2015. Governing Equations in Microfluidics. *Microscale Acoustofluidics*, pp.1–28.

- Chen, M. & Weiss, R., 2005. Artificial cell-cell communication in yeast *Saccharomyces cerevisiae* using signaling elements from *Arabidopsis thaliana*, 23(12), pp.1551–1555.
- Cormack, B.P., Valdivia, R.H. & Falkow, S., 1996. FACS-optimized mutants of the green fluorescent protein (GFP). *Gene*, 173, pp.33–38.
- Costanzo, M. et al., 2010. The Genetic Landscape of a Cell. *Science*, 327(5964), pp.425–432.
- Cremer, C. & Cremer, T., 1978. Considerations on a laser-scanning microscope with high resolution and depth of field. *Microscopica Acta*, 81(1), pp.31–44.
- Cybulski, J.S., Clements, J. & Prakash, M., 2014. Foldscope: Origami-based paper microscope. *PLoS ONE*, 9(6).
- Duan, Z. et al., 2010. A three-dimensional model of the yeast genome. *Nature*, 465(7296), pp.363–7.
- Edelstein, A.D. et al., 2014. Advanced methods of microscope control using μ Manager software. *Journal of Biological Methods*, 1(2), pp.1–10.
- Frolova, E., 1999. Binding of the glucose-dependent Mig1p repressor to the GAL1 and GAL4 promoters in vivo: regulation by glucose and chromatin structure. *Nucleic Acids Research*, 27(5), pp.1350–1358.
- Gallone, B. et al., 2016. Domestication and Divergence of *Saccharomyces cerevisiae* Beer Yeasts. *Cell*, 166(6), p.1397–1410.e16.
- Gebhardt, J.C.M. et al., 2013. Single-molecule imaging of transcription factor binding to DNA in live mammalian cells. *Nature methods*, 10(5), pp.421–6.
- Geijer, C. et al., 2013. Initiation of the transcriptional response to hyperosmotic shock correlates with the potential for volume recovery. *The FEBS journal*, 280(16), pp.3854–67.
- Gertz, J., Siggia, E.D. & Cohen, B.A., 2009. Analysis of combinatorial cis-regulation in synthetic and genomic promoters. *Nature*, 457(7226), pp.215–8.

- Gietz, R.D. & Schiestl, R.H., 2007. Frozen competent yeast cells that can be transformed with high efficiency using the LiAc/SS carrier DNA/PEG method. *Nature protocols*, 2(1), pp.1–4.
- Goffeau, A. et al., 1996. Life with 6000 Genes. *Science*, 274(5287), pp.546–567.
- Gowers, D.M. & Halford, S.E., 2003. Protein motion from non-specific to specific DNA by three-dimensional routes aided by supercoiling. *The EMBO journal*, 22(6), pp.1410–8.
- Greenbaum, L., Rothmann, C. & Lavie, R., 2000. Green Fluorescent Protein Photobleaching: a Model for Protein Damage by Endogenous and Exogenous Singlet Oxygen. *Biol. Chem.*, 381(December), pp.1251–1258.
- Gross, D. & Webb, W., 1988. Cell surface clustering and mobility of the liganded LDL receptor measured by digital video fluorescence microscopy. In L. Loew, ed. *Spectroscopic Membrane Probes*. CRC Press, pp. 19–45.
- Gustavsson, A.-K., 2014. *Glycolytic oscillations in individual yeast cells*. University of Gothenburg.
- Gustavsson, A.-K. et al., 2012. Sustained glycolytic oscillations in individual isolated yeast cells. *FEBS Journal*, 279(16), pp.2837–2847.
- Halford, S.E. & Marko, J.F., 2004. How do site-specific DNA-binding proteins find their targets? *Nucleic acids research*, 32(10), pp.3040–52.
- Hammar, P. et al., 2012. The lac repressor displays facilitated diffusion in living cells. *Science (New York, N.Y.)*, 336(6088), pp.1595–8.
- Harbison, C.T. et al., 2004. Transcriptional regulatory code of a eukaryotic genome. *Nature*, 431(7004), pp.99–104.
- Hartwell, L.H. et al., 1999. From molecular to modular cell biology. *Nature*, 402(6761 Suppl), pp.C47–C52.
- Hartwell, L.H., Culotti, J. & Reid, B., 1970. Genetic control of the cell-division cycle in yeast. I. Detection of mutants. *Proceedings of the National Academy of Sciences of the United States of America*, 66(2), pp.352–9.

- Hedlund, Erik, 2015. *A Fourdimensional Microscope for Single Molecule Studies in Living Cells Using Astigmatic Axial Resolution Enhancement*. Wolfson College, University of Oxford.
- Heim, R., Cubitt, A.B. & Tsien, R.Y., 1995. Improved green fluorescence. *Nature*, 373, pp.663–664.
- Hell, S.W. & Wichmann, J., 1994. Breaking the Diffraction Resolution Limit By Stimulated-Emission - Stimulated-Emission-Depletion Fluorescence Microscopy. *Optics Letters*, 19(11), pp.780–782.
- Hennig, S., Clemens, A. & Rödel, G., 2015. A yeast pheromone-based inter-species communication system. , pp.1299–1308.
- Hetsroni, G. et al., 2005. Fluid flow in micro-channels. *International Journal of Heat and Mass Transfer*, 48(10), pp.1982–1998.
- Hin Yan Tong, A. et al., 2004. Global Mapping of the Yeast Genetic Interaction Network. *Science*, 303(5659), pp.808–813.
- Hink, M.A. et al., 2000. Structural dynamics of green fluorescent protein alone and fused with a single chain Fv protein. *The Journal of biological chemistry*, 275(23), pp.17556–60.
- Huberts, D.H.E.W. et al., 2013. Construction and use of a microfluidic dissection platform for long-term imaging of cellular processes in budding yeast. *Nature protocols*, 8(6), pp.1019–27.
- Höxtermann, E., 1996. Über ‘Gährung’ und ‘gährende Pflänzchen’: Aus den Anfängen der Gärungsforschung im 19. Jahrhundert. *NTM Zeitschrift für Geschichte der Wissenschaften, Technik und Medizin*, 4, pp.31–51.
- Iizuka, R., Yamagishi-Shirasaki, M. & Funatsu, T., 2011. Kinetic study of de novo chromophore maturation of fluorescent proteins. *Analytical Biochemistry*, 414(2), pp.173–178.
- Izeddin, I. et al., 2014. Single-molecule tracking in live cells reveals distinct target-search strategies of transcription factors in the nucleus. *eLife*, 3.
- Jacob, F. & Monod, J., 1961. Genetic regulatory mechanisms in the synthesis of

- proteins. *Journal of Molecular Biology*, 3(3), pp.318–356.
- JSmol, JSmol: an open-source HTML5 viewer for chemical structures in 3D. Available at: <http://wiki.jmol.org/index.php/JSmol>.
- Kaizu, K., Ghosh, S. & Matsuoka, Y., 2010. A comprehensive molecular interaction map of the budding yeast cell cycle. *Molecular Systems Biology*, 6(415), pp.1–11. Available at: <http://dx.doi.org/10.1038/msb.2010.73>.
- Kao, H.P. & Verkman, a S., 1994. Tracking of single fluorescent particles in three dimensions: use of cylindrical optics to encode particle position. *Biophysical journal*, 67(3), pp.1291–1300.
- Kapanidis, A.N. et al., 2005. Alternating-Laser Excitation of Single Molecules. *Accounts of Chemical Research*, 38(7), pp.523–533.
- Karpova, T.S. et al., 2008. Concurrent fast and slow cycling of a transcriptional activator at an endogenous promoter. *Science (New York, N.Y.)*, 319(5862), pp.466–9.
- Khmelniskii, A. et al., 2012. Tandem fluorescent protein timers for in vivo analysis of protein dynamics. *Nature biotechnology*, 30(7), pp.708–14.
- Lampen, O. et al., 1971. Specific Staining of Wall Mannan in Yeast Cells with Specific Staining of Wall Mannan in Yeast Cells with Fluorescein-Conjugated Concanavalin A. , 105(1), pp.1–5.
- Lavoisier, A.-L., 1789. *Traité Élémentaire de Chimie* Robert Ker.,
- Leake, M.C., 2013. *Single-Molecule Cellular Biophysics* First edit., Oxford: Cambridge University Press.
- Leake, M.C. et al., 2006. Stoichiometry and turnover in single, functioning membrane protein complexes. *Nature*, 443(7109), pp.355–8.
- van Leeuwenhoek, A., 1680. Letter 32 to Thomas Gale.
- Lew, M.D. et al., 2011. Corkscrew point spread function for far-field three-dimensional nanoscale localization of pointlike objects. *Optics letters*, 36(2), pp.202–4.

- Li, G.-W. & Xie, X.S., 2011. Central dogma at the single-molecule level in living cells. *Nature*, 475(7356), pp.308–15.
- Liang, L.-F. et al., 2009. [Nucleoplasmic viscosity of living cells investigated by fluorescence correlation spectroscopy]. *Guang pu xue yu guang pu fen xi = Guang pu*, 29(2), pp.459–62.
- Lin, J.C. et al., 2004. A Microdomain Formed by the Extracellular Ends of the Transmembrane Domains Promotes Activation of the G Protein-Coupled alpha-Factor Receptor. *Molecular and Cellular Biology*, 24(5), pp.2041–2051.
- Lin, Y. et al., 2015. Combinatorial gene regulation by modulation of relative pulse timing. *Nature*, 527(7576), pp.54–58.
- Liu, J. et al., 2006. Intrinsic disorder in transcription factors. *Biochemistry*, 45(22), pp.6873–88.
- Llorente-Garcia, I. et al., 2014. Single-molecule in vivo imaging of bacterial respiratory complexes indicates delocalized oxidative phosphorylation. *Biochimica et Biophysica Acta (BBA) - Bioenergetics*, 1837(6), pp.811–824.
- Lowe, A.R. et al., 2010. Selectivity mechanism of the nuclear pore complex characterized by single cargo tracking. *Nature*, 467(7315), pp.600–603.
- Lundin, M., Nehlin, J.O. & Ronne, H., 1994. Importance of a flanking AT-rich region in target site recognition by the GC box-binding zinc finger protein MIG1. *Molecular and cellular biology*, 14(3), pp.1979–1985.
- Lutfiyya, L.L. et al., 1998. Characterization of three related glucose repressors and genes they regulate in *Saccharomyces cerevisiae*. *Genetics*, 150(4), pp.1377–1391.
- Ma, J. & Yang, W., 2010. Three-dimensional distribution of transient interactions in the nuclear pore complex obtained from single-molecule snapshots. *Proceedings of the National Academy of Sciences of the United States of America*, 107(16), pp.7305–7310.

- MacDonald, P.J., Chen, Y. & Mueller, J.D., 2012. Chromophore maturation and fluorescence fluctuation spectroscopy of fluorescent proteins in a cell-free expression system. *Analytical Biochemistry*, 421(1), pp.291–298.
- Mahmutovic, A., Berg, O.G. & Elf, J., 2015. What matters for lac repressor search in vivo--sliding, hopping, intersegment transfer, crowding on DNA or recognition? *Nucleic acids research*, 43(7), pp.3454–64.
- Mappes, T. et al., 2012. The invention of immersion ultramicroscopy in 1912-The birth of nanotechnology? *Angewandte Chemie - International Edition*, 51(45), pp.11208–11212.
- Marks, B., 2011. BioNumbers - *Saccharomyces cerevisiae* - Doubling time of haploid cell. Available at:
<http://bionumbers.hms.harvard.edu//bionumber.aspx?id=101310&ver=16>.
- McKinney, S.A. et al., 2009. A bright and photostable photoconvertible fluorescent protein. *Nature methods*, 6(2), pp.131–3.
- Meyer, F., 1994. Topographic distance and watershed lines. *Signal Processing*, 38(1), pp.113–125.
- Michalet, X., 2010. Mean square displacement analysis of single-particle trajectories with localization error: Brownian motion in an isotropic medium. *Physical Review E*, 82(4), p.41914.
- Michel, R.H., McGovern, P.E. & Badler, V.R., 1992. Chemical evidence for ancient beer. *Nature*, 360(6399), pp.24–24.
- Michels, C.A., 2002. 3 *Saccharomyces* Cell Structure. In *Genetic Techniques for Biological Research*. John Wiley & Sons, Ltd, pp. 43–63.
- Miermont, A. et al., 2013. Severe osmotic compression triggers a slowdown of intracellular signaling, which can be explained by molecular crowding. *Proceedings of the National Academy of Sciences of the United States of America*, 110(14), pp.5725–30.
- Miller, H. et al., 2015. Superresolution imaging of single DNA molecules using stochastic photoblinking of minor groove and intercalating dyes. *Methods*.

- Needham, P.G. & Trumbly, R.J., 2006. In vitro characterisation of the Mig1 repressor from *Saccharomyces cerevisiae* reveals evidence for monomeric and higher molecular weight forms. *Yeast*, 23, pp.1151–1166.
- Needham, P.G. & Trumbly, R.J., 2006. In vitro characterization of the Mig1 repressor from *Saccharomyces cerevisiae* reveals evidence for monomeric and higher molecular weight forms. *Yeast (Chichester, England)*, 23(16), pp.1151–66.
- Nehlin, J.O., Carlberg, M. & Ronne, H., 1991. Control of yeast GAL genes by MIG1 repressor: a transcriptional cascade in the glucose response. *The EMBO journal*, 10(11), pp.3373–7.
- Nehlin, J.O., Carlberg, M. & Ronne, H., 1991. Control of yeast GAL genes by MIG 1 transcriptional cascade in the glucose response. *EMBO Journal*, 10(11), pp.3373–3377.
- NI, National Instruments, NI 660x DAQ, specifications. , (800).
- NI, 2009. National Instruments, NI 660x DAQ User Manual. , (March).
- Nishi, H. et al., 2013. Regulation of protein-protein binding by coupling between phosphorylation and intrinsic disorder: analysis of human protein complexes. *Molecular bioSystems*, 9(7), pp.1620–6.
- Obradovic, Z. et al., 2005. Exploiting heterogeneous sequence properties improves prediction of protein disorder. *Proteins*, 61 Suppl 7, pp.176–82.
- Ormö, M. et al., 1996. Crystal Structure of the *Aequorea victoria* Green Fluorescent Protein. *Science*, 273, pp.1392–1395.
- Otsu, N., 1979. A Threshold Selection Method from Gray-Level Histograms. *IEEE Transactions on Systems, Man and Cybernetics*, SMC-9(1), pp.62–66.
- Ozcan, S. & Johnston, M., 1999. Function and regulation of yeast hexose transporters. *Microbiology and molecular biology reviews : MMBR*, 63(3), pp.554–569.
- Pavani, S.R.P. et al., 2009. Three-dimensional, single-molecule fluorescence imaging beyond the diffraction limit by using a double-helix point spread function. *Proceedings of the National Academy of Sciences of the United States of America*, 106(9), pp.2995–2999.

- Pavani, S.R.P. & Piestun, R., 2008. High-efficiency rotating point spread functions. *Optics Express*, 16(5), p.3484.
- Phillip, Y. & Schreiber, G., 2013. Formation of protein complexes in crowded environments--from in vitro to in vivo. *FEBS letters*, 587(8), pp.1046–52.
- Plank, M., Wadhams, G.H. & Leake, M.C., 2009. Millisecond timescale slimfield imaging and automated quantification of single fluorescent protein molecules for use in probing complex biological processes. *Integrative biology: quantitative biosciences from nano to macro*, 1(10), pp.602–12.
- Prasher, D.C. et al., 1992. Primary structure of the Aequorea victoria green-fluorescent protein. *Gene*, 111(2), pp.229–233.
- Puchner, E.M. et al., 2013. Counting molecules in single organelles with superresolution microscopy allows tracking of the endosome maturation trajectory. *Proceedings of the National Academy of Sciences of the United States of America*, 110(40), pp.16015–20.
- Qin, H. et al., 2003. Evolution of the yeast protein interaction network. , 100(22).
- Reimann, S.M. & Manninen, M., 2002. Electronic structure of quantum dots. *Reviews of Modern Physics*, 74(4), pp.1283–1342.
- Remington, S.J., 2006. Fluorescent proteins: maturation, photochemistry and photophysics. *Current Opinion in Structural Biology*, 16(6), pp.714–721.
- Reyes-Lamothe, R., Sherratt, D.J. & Leake, M.C., 2010a. Stoichiometry and architecture of active DNA replication machinery in Escherichia coli. *Science (New York, N.Y.)*, 328(5977), pp.498–501.
- Reyes-Lamothe, R., Sherratt, D.J. & Leake, M.C., 2010b. Stoichiometry and architecture of active DNA replication machinery in Escherichia coli. *Science (New York, N.Y.)*, 328(5977), pp.498–501.
- Riccitelli, N.J. & Lupták, A., 2010. Computational discovery of folded RNA domains in genomes and in vitro selected libraries. *Methods (San Diego, Calif.)*, 52(2), pp.133–40.

- Rivas, G., Fernández, J.A. & Minton, A.P., 2001. Direct observation of the enhancement of noncooperative protein self-assembly by macromolecular crowding: indefinite linear self-association of bacterial cell division protein FtsZ. *Proceedings of the National Academy of Sciences of the United States of America*, 98(6), pp.3150–5.
- Roy, A. et al., 2011. The nature of transient dark states in a photoactivatable fluorescent protein. *Journal of the American Chemical Society*, 133(46), pp.18586–18589.
- Rubenstein, E.M. et al., 2008. Access denied: Snf1 activation loop phosphorylation is controlled by availability of the phosphorylated threonine 210 to the PP1 phosphatase. *The Journal of biological chemistry*, 283(1), pp.222–30.
- Saito, H., 2010. Regulation of cross-talk in yeast MAPK signaling pathways. *Current opinion in microbiology*, 13(6), pp.677–83.
- Schmidt, H.G. et al., 2014. An Integrated Model of Transcription Factor Diffusion Shows the Importance of Intersegmental Transfer and Quaternary Protein Structure for Target Site Finding. , 9(10).
- Schüller, H.-J., 2003. Transcriptional control of nonfermentative metabolism in the yeast *Saccharomyces cerevisiae*. *Current genetics*, 43(3), pp.139–60.
- Shaner, N.C. et al., 2004. Improved monomeric red , orange and yellow fluorescent proteins derived from *Discosoma* sp . red fluorescent protein. *Nature biotechnology*, 22(12), pp.1567–1572.
- Shaner, N.C., Patterson, G.H. & Davidson, M.W., 2007. Advances in fluorescent protein technology. *Journal of cell science*, 120(Pt 24), pp.4247–60.
- Shaner, N.C., Steinbach, P. a & Tsien, R.Y., 2005. A guide to choosing fluorescent proteins. *Nature methods*, 2(12), pp.905–9.
- Shashkova, S., Welkenhuysen, N. & Hohmann, S., 2015. Molecular communication: crosstalk between the Snf1 and other signaling pathways J. Nielsen, ed. *FEMS Yeast Research*, 15(4).

- Shimomura, O., 1995. A Short Story of Aequorin. *Biological Bulletin*, 189(1), pp.1–5.
- Shimomura, O., Johnson, F.H. & Saiga, Y., 1962. Extraction, purification and properties of aequorin, a bioluminescent protein from the luminous hydromedusan, *Aequorea*. *Journal of cellular and comparative physiology*, 59(165), pp.223–239.
- Sigma-Aldrich, Sigma - Concanavalin A. , (L), pp.3–5.
- Siso-Nadal, F. et al., 2009. Cross-Talk between Signaling Pathways Can Generate Robust Oscillations in Calcium and cAMP. *PLoS ONE*, 4(10), p.e7189.
- Sode, K. et al., 2007. Effect of reparation of repeat sequences in the human alpha-synuclein on fibrillation ability. *International journal of biological sciences*, 3(1), pp.1–7.
- Spring, K.R. & Davidson, M.W., 2016. Depth of Field and Depth of Focus. Available at: <http://www.microscopyu.com/microscopy-basics/depth-of-field-and-depth-of-focus>.
- Stracy, M. et al., 2015. Live-cell superresolution microscopy reveals the organization of RNA polymerase in the bacterial nucleoid. *Proceedings of the National Academy of Sciences of the United States of America*, 112(32), pp.E4390-9.
- Strambio-De-Castillia, C., Niepel, M. & Rout, M.P., 2010. The nuclear pore complex: bridging nuclear transport and gene regulation. *Nature Reviews Molecular Cell Biology*, 11(7), pp.490–501.
- Synge, E.H., 1928. A suggested method for extending microscopic resolution into the ultra-microscopic region. *The London, Edinburgh, and Dublin Philosophical Magazine and Journal of Science*, 6(35), pp.356–362.
- Thastrup, O. et al., 2001. Fluorescent Proteins.
- Toretsky, J.A. & Wright, P.E., 2014. Assemblages: functional units formed by cellular phase separation. *The Journal of cell biology*, 206(5), pp.579–88.
- Towle, H.C., 2005. Glucose as a regulator of eukaryotic gene transcription. *Trends in Endocrinology and Metabolism*, 16(10), pp.489–494.

- Treitl, M.A. & Carlson, M., 1995. Repression by SSN6-TUP1 is directed by MIG1, a repressor/activator protein. *Proceedings of the National Academy of Sciences of the United States of America*, 92(8), pp.3132–6.
- Tsien, R.Y., 1998. The green fluorescent protein. *Annual Review of Biochemistry*, (67), pp.509–544.
- Uversky, V.N. et al., 2015. Intrinsically disordered proteins as crucial constituents of cellular aqueous two phase systems and coacervates. *FEBS letters*, 589(1), pp.15–22.
- Vincent, L. & Soille, P., 1991. Watersheds in Digital Spaces: An Efficient Algorithm Based on Immersion Simulation. *IEEE Transactions on Pattern Analysis and Machine Intelligence*, 13(6), pp.583–598.
- De Vit, M.J., Waddle, J. a & Johnston, M., 1997. Regulated nuclear translocation of the Mig1 glucose repressor. *Molecular biology of the cell*, 8(8), pp.1603–18.
- Ward, J.J. et al., 2004. Prediction and functional analysis of native disorder in proteins from the three kingdoms of life. *Journal of molecular biology*, 337(3), pp.635–45.
- Warringer, J. et al., 2011. Trait variation in yeast is defined by population history. *PLoS Genetics*, 7(6).
- Whiteside, S.T. & Goodbourn, S., 1993. Signal transduction and nuclear targeting: regulation of transcription factor activity by subcellular localisation. *Journal of cell science*, 104 (Pt 4, pp.949–55.
- Wollman, A.J.M. et al., 2015. From Animaculum to single molecules: 300 years of the light microscope. *Open biology*, 5(150019). [Appendix C]
- Wollman, A.J.M. et al., 2016. Transcription factor clusters regulate genes in eukaryotic cells.
- Wollman, A.J.M. & Leake, M.C., 2015. Millisecond single-molecule localization microscopy combined with convolution analysis and automated image segmentation to determine protein concentrations in complexly structured, functional cells, one cell at a time. *Faraday discussions*, 184, pp.401–24.

- Xue, B., Dunker, A.K. & Uversky, V.N., 2012. Orderly order in protein intrinsic disorder distribution: disorder in 3500 proteomes from viruses and the three domains of life. *Journal of biomolecular structure & dynamics*, 30(2), pp.137–49.
- Xue, Q., Jones, N.S. & Leake, M.C., 2010. A general approach for segmenting elongated and stubby biological objects: Extending a chord length transform with the radon transform. *2010 7th IEEE International Symposium on Biomedical Imaging: From Nano to Macro, ISBI 2010 - Proceedings*, pp.161–164.
- Yang, W., Gelles, J. & Musser, S.M., 2004. Imaging of single-molecule translocation through nuclear pore complexes. *Proceedings of the National Academy of Sciences of the United States of America*, 101, pp.12887–12892.
- Zacharias, D.A., Violin, J.D., Newton, A.C., et al., 2002. Partitioning of lipid-modified monomeric GFPs into membrane microdomains of live cells. *Science (New York, N.Y.)*, 296(5569), pp.913–6.
- Zacharias, D.A., Violin, J.D. & Newton, A.C., 2002. Partitioning of Lipid-Modified Monomeric GFPs into Membrane Microdomains of Live Cells. *Science*, 296(May), pp.913–916.
- Zhang, Y. et al., 2011. Reg1 Protein Regulates Phosphorylation of All Three Snf1 Isoforms but Preferentially Associates with the Gal83 Isoform, 10(12), pp.1628–1636.